Lanthanide Functionalised Gold Nanoparticles as MRI Contrast Agents

Muhammad Farooq Warsi

A thesis submitted for the degree of Doctor of Philosophy

The University of York

Department of Chemistry

September 2010

To,

My whole family

Abstract

The aim of this Ph.D project was to synthesize and characterise nanoparticle-based MRI contrast agents. In the first instance, the DTPA (diethylenetriaminepentaacetic acid) based ligand was designed, synthesized and characterised. This ligand was utilised for stabilisation of gold nanoparticles. The gold nanoparticles protected by DTPA based ligand were characterised using UV-Vis, NMR spectroscopies, TGA and TEM. The nanoparticles were then loaded with gadolinium. The relaxivity of gadolinium loaded gold nanoparticles were studied using inversion recovery method and compared with commercially available MRI contrast agents (i.e. Gd-DTPA). The Gd-loaded AuNPs showed only a moderate increase in their relaxivity as compared to the Gd-DTPA complex.

The factors limiting the relaxivity of Gd-loaded AuNPs were explored using EPR spectroscopy. For EPR measurements, Gd^{3+} was replaced with vanadyl (VO^{2+}) which gives EPR spectra sensitive to the rate of molecular tumbling on nanosecond time scale. The EPR measurements of VO^{2+}-loaded AuNPs showed that the nanoparticle attached metal ion retains high molecular mobility. This is likely responsible for only a moderate increase in relaxivity. We next explored different strategies for increasing the relaxivity of gold nanoparticles based MRI contrast agents. In the first strategy, in order to enhance ligand packing at AuNPs surface, the size of the AuNPs was increased from ~2.0 nm to ~6.0 nm. The relaxivity was found to increase with the increased size of the AuNPs. Secondly, polyelectrolyte coating of charged Gd-loaded AuNPs surface also resulted in increase of relaxivity due to better immobilisation of the Gd^{3+} ions.

Gold nanoparticles were also used as templates for nitroxide based redox sensitive MRI contrast agents. The reducing behaviour and relaxivity of nitroxide protected AuNPs was measured and found slightly better than that of free nitroxide.

Finally other useful applications of nanoparticles protected by DTPA based ligand were explored. For example, the DTPA ligand can also chelate strongly with other

lanthanides such as Eu^{3+}, Tb^{3+}etc. The luminescence measurements of lanthanides (Eu^{3+} and Tb^{3+}) loaded onto AuNPs were explored. Lanthanide-loaded AuNPs were also used as model compounds to test an important EPR methodology after labelling with a nitroxide based spin label.

Declaration

This research thesis is my original work (carried out at Chemistry Department, The University of York, Nov. 2006 to Sep. 2010) except where specific references have been made. I have not submitted this work neither as a part nor as a whole for a degree or diploma or other qualification at any other university.

Muhammad Farooq Warsi

Acknowledgements

Firstly, I would like to thank my supervisor Dr. Victor Chechik for his continuous and affectionate support in lab work as well as during writing up this thesis. I would like to thank post doctorate fellows in our group (Dr. Marco Conte, Dr. Brendan Garret, Dr. Xuetong Zhang and Dr. Jamie Gould) for useful suggestions and assistance in the lab work. I would like to thank Dr. Ralph Adams (Prof. S. B. Duckett group) for helping with imaging experiments and relaxation measurements. For technical support and help I would like to thank Dr. Phil Helliwill (for general lab assistance), Dr. Paul Elliott (for TGA analysis) and Miss Heather Fish (for NMR analysis). We also thank Prof. Gunnar Jeschke, Dr. Maxim Yulikov and Ms. Petra Lueders from ETH Zurich (Switzerland) for pulsed EPR measurements.

I would like to thank past (Ricarrdo Grazelli, Eleanor Hurst and Leonie Jones) and present members (James Wallace, Kazim Raza, Thomas Newby and Ma Yun) of research group. My friends (Muddassar Iqbal, Andy Reader, Muhammad Suleman, Alan Burns etc) and staff members (David Lindsey, David Williams, Jason Lynam etc) of the chemistry department with whom I used to play cricket during my stay in York are also thanked. At the end my special thanks will go for my whole family, my uncle Iqbal Javed (Manger Punjab Oil Mills Islamabad-Pakistan) for moral and financial support throughout my educational career.

Higher Education Commission of Pakistan (HEC-Pak) and The University of York (Wild Fund) are thanked for financial support.

Abbreviations

aq	Aqueous
AuNPs	Gold nanoparticles
Ar	Aromatic
BTT	Biotin terminated thiol
Calcd	Calculated
CAs	Contrast agents
Da	Dalton
d	Doublet
DTPA	Diethylenetriamine pentaacetic acid
DCC	Dicyclohexyl carbodimide
DMAP	4-N,N-Dimethylaminopyridine
DMF	Dimethylformamide
DMSO	Dimethylsulfoxide
DCM	Dichloromethane
EPR	Electron paramagnetic resonance
ESI	Electron spray ionization
Eq	Equation
g	Gram
GPC	Gel permeation chromatography
h	Hour
ICP	Inductively Coupled Plasma (Spectrometry)
HR-MS	High Resolution Mass Spectrometry
Ln	Lanthanide
kDa	Kilo Dalton
MRI	Magnetic resonance imaging
M_n	Number average molecular mass
MW	Molecular weight
MWCO	Molecular weight cut off
MS	Mass spectrometry
m/z	Charge to mass ratio

mL	Millilitre
mg	Milligram
min	Minute
NMR	Nuclear magnetic resonance
NMV	Net magnetization vector
NBS	N-bromosuccinimide
nm	Nanometre
o/n	Overnight
Obsd	Observed
ppm	Parts per million
R_1	Spin lattice relaxivity
RF	Radio frequency
RMM	Relative molecular mass
s	singlet , seconds
SPB	Surface Plasmon Band
T_1	Spin lattice relaxation time
T_2	Spin spin relaxation time
TEM	Transmission electron microscopy
TEMPO	2,2,6,6-tetramethyl-1-piperidinyloxyl
TFA	Trifluroacetic acid
TGA	Thermogravimetric analysis
THF	Tetrahydrofuran
TR	Time of repetition
TE	Echo time
t	triplet
UV-Vis.	Ultraviolet visible

Table of Contents

Chapter 4: Gold nanoparticles protected by nitroxide based ligand as redox sensitive MRI contrast agents 142

Chapter 6: Conclusions and Proposed Future Work 202

Chapter 7: Experimental 208

Chapter 1: Introduction

Chapter 1: Introduction

1.1 Magnetic resonance imaging (MRI)

Magnetic resonance imaging (MRI) is a powerful modern diagnostic technique. It is primarily used to produce anatomical images, but physico-chemical state, flow diffusion and other tissue parameters can also be determined using MRI images. MRI can provide excellent soft tissue contrast up to submillimeter resolution, penetrating deep into the tissues. It is frequently used in modern biomedical research.[1-2] The first MRI image was published in 1973 and the first MRI scan of a human body was done on July 3, 1977. [3-4] Paul Lauterbur and Peter Mansfield were awarded a Noble Prize (in 2003) for their major contributions to the invention of MRI. MRI has many advantages over other diagnostic techniques such as X-ray and computed tomography (CT) scanning. The X-ray and CT scan both involve the use of ionizing radiation. MRI, on the other hand, uses a harmless magnetic field and electromagnetic radiation and is therefore referred to as a non-invasive technique.[5]

1.1.1 Principles of MRI

MRI relies on the nuclear magnetic resonance (NMR) phenomenon and was originally termed NMR imaging. The ^1H nucleus is magnetic resonance (MR) active as it contains only one proton and has spin (I) = ½. Most MRI experiments use the ^1H nucleus due to the following reasons:

- It is abundant (>60%) in human body (in the form of water and fat).
- Its solitary proton gives it a large magnetic moment.[6]

MRI gives the spatial distribution of the intensity of water protons in the specific volume of the body, while NMR gives information about chemical shifts and coupling constants.

The signal intensity depends upon the amount of (water) protons and their relaxation times. The basic NMR theory and the relaxation phenomenon are therefore discussed in detail in the following sections.

1.1.2 Basic theory of NMR (creating magnetic resonance signal)

According to the quantum mechanical approach, nuclei with spin "I" possess (quantised) angular momentum P which is further associated with their magnetic moment (μ) (Eq 1.1 and 1.2).

$$P = \sqrt{I(I+1)}\hbar \text{ , where } \hbar = h/2\pi \qquad \text{Eq. 1.1}$$

$$\mu = \gamma P \qquad \text{Eq. 1.2}$$

In equation (1.2), γ is a proportionality constant (i.e. magnetogyric ratio) for the given isotope. In the presence of an applied magnetic field (B_0), the angular momentum component parallel (along z-axis) to the B_0 is given as:

$$P_z = m\hbar \qquad \text{Eq. 1.3}$$

In equation (1.3), "*m*" is the magnetic quantum number that has values from I, I–1,…… to "–I". The number of possible orientations of nuclear angular momentum in the presence of B_0 can be determined from the value of I by the simple formula 2I+1. For example, in the case of ^{1}H nuclei (I = ½), the nuclear angular momentum will have two orientations i.e. either parallel (*m*= +1/2) or antiparallel (*m*= –1/2) to the magnetic field. This classical approach which is used to simplify the NMR picture assumes the magnetic moments of nuclei behave as tiny magnetic bars. In the absence of B_0 tiny magnetic bars are randomly oriented and thus their spins are averaged out. In the presence of B_0, the nuclear spins with relatively higher energy align antiparallel while those with lower energy align parallel to B_0 and the energy difference (ΔE) between these two states is given as:

$$\Delta E = \gamma \hbar B_0 \qquad \text{Eq. 1.4}$$

The energy difference is usually very small and therefore the population difference of nuclei between these two states is also very small. For example the number of excess nuclei in the lower energy level is 1 in 100000 at 3.0 T and 1 in 30000 at 9.4 T. These extra nuclei in the low energy state add together to give a net bulk magnetisation along the direction (z-axis) of the applied magnetic field (B_0) (Figure 1.1). This net magnetisation is usually represented by a vector called the net magnetisation vector (NMV).

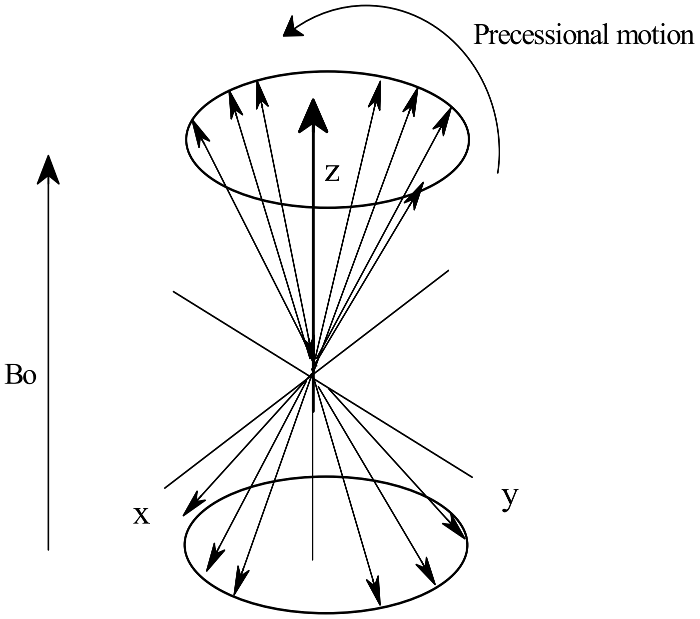

Figure 1.1: Schematic representation of bulk magnetisation (i.e. NMV) in the presence of a magnetic field.

The applied magnetic field imposes a torque on the magnetic moments of nuclei and therefore they are forced to remain at certain angle to the B_0. As a result the magnetic moments of the nuclei wobble around the axis of B_0 with a certain frequency. This motion (wobbling) is called precessional motion and the frequency of this motion is called the Larmor frequency (ω) which is given as:

$$\omega = B_0 \gamma \qquad \text{Eq. 1.5}$$

In above equation, ω is the angular frequency. Equation 1.5 can be modified to give Larmor frequency “ν” (in hertz) as follows:

$$\nu_{precessional} = \frac{\omega}{2\pi} = \frac{\gamma B_0}{2\pi} \qquad \text{Eq 1.6}$$

When radiofrequency (RF) pulses are applied, the transition of nuclei between low and high energy levels occurs as the frequency of the magnetic field component of RF pulses matches the Larmor frequency. The magnetic field (B_1) associated with the RF pulses is in transverse (x-y) plane i.e. B_1 is perpendicular to B_0.

The visualisation of the processes occurring during an NMR experiment can be aided by a simplified formalism known as “rotating frame of reference” which is opposite to the “laboratory (fixed) frame of reference” (which has been used so far) (Figure 1.2). A rotating frame of reference is a non-inertial frame of reference which is rotating relative to an inertial frame of reference. For simplification B_1 is supposed to be composed of two counter rotating magnetic vectors in x-y plane with the frequency equal to Larmor frequency (ν_L). In the rotating frame of reference things can be simplified further. Out of two parts of B_1, one part can be frozen (as in rotating frame of reference both NMV and B_1 are moving) while the other part (moving opposite to NMV) can be ignored as it is moving with frequency far away from the Larmor frequency.

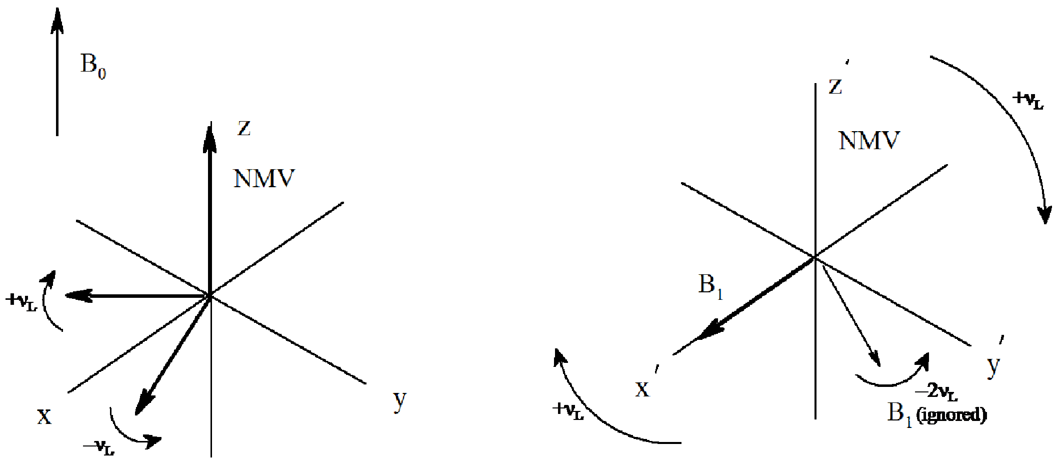

Laboratory frame of reference

Rotating frame of reference

Figure 1.2: Schematic representation of the laboratory frame of reference and the rotating frame of reference.

As the electromagnetic field B_1 imposes a torque on the NMV (i.e. M_z as NMV is parallel to the z-axis) perpendicular to the direction of B_1, the NMV moves from z-axis to the x-y plane (M_{xy}) (depending upon the amplitude and duration of the pulse which will be discussed later). When the RF pulses are turned off, two things occur: (a) the NMV moves back to align along B_0 (this phenomenon is called relaxation), and (b) if a receiver coil is placed in the area of rotating magnetic moments, a voltage (i.e. magnetic resonance signal) is produced; this voltage is responsible for the NMR signal. The NMR signal thus depends upon the amplitude and duration of the pulse. The 90^o and 270^o RF pulses yield the maximum signals while in case of 180^o pulse, NMV will move into the –z-axis and no signal will be detected. [7-9]

The relaxation phenomenon plays an important role in the image formation during MRI. The relaxation phenomenon in NMR is of two types i.e. spin lattice relaxation and spin-spin relaxation, and is discussed in the next section.[10]

1.1.3 Spin-lattice relaxation

The recovery of NMV along the z-axis (i.e. longitudinal axis) after the removal of the RF pulse is called spin lattice or longitudinal relaxation (Figure 1.3) while the loss of M_{xy} is termed transverse or spin-spin relaxation. In the spin lattice relaxation, the absorbed energy is dissipated to the lattice. The lattice may be surrounding molecules or walls of the vessel. Nuclei in the lattice are in rotational and vibrational motion that creates complex magnetic fields. Some of the components of this magnetic field may have a frequency equal to the Larmor frequency. This makes the nuclei relax. The interaction of the lattice nuclei/molecules with the excited nuclei also depends upon the mobility of the lattice; i.e. if mobility is high, there will be more interaction of lattice nuclei with the excited nuclei and vice versa. According to time dependent perturbation theory the relaxation rates depend upon the spectral density functions. The spectral density function is the intensity / concentration of fluctuating magnetic field at the given frequency of motion. In more precise way it indicates the amount of molecular motion which is at correct frequency to cause the relaxation.

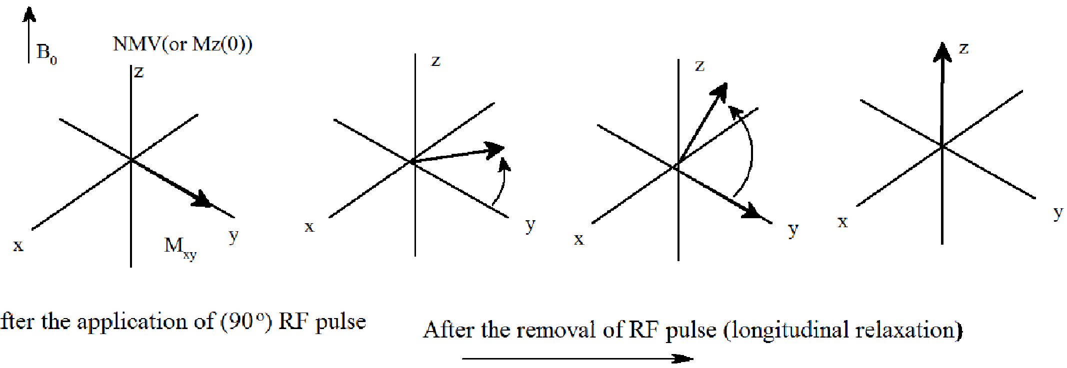

After the application of (90°) RF pulse

After the removal of RF pulse (longitudinal relaxation)

Figure 1.3: Schematic illustration of spin-lattice (longitudinal) relaxation.

The time constant which describes how NMV returns to its equilibrium value $M_z(0)$ is called the spin lattice relaxation time (T_1). Spin lattice relaxation is a first order process and T_1 is the time required to recover ~63% of net magnetization vector of its original value $M_z(0)$ (Figure 1.4).

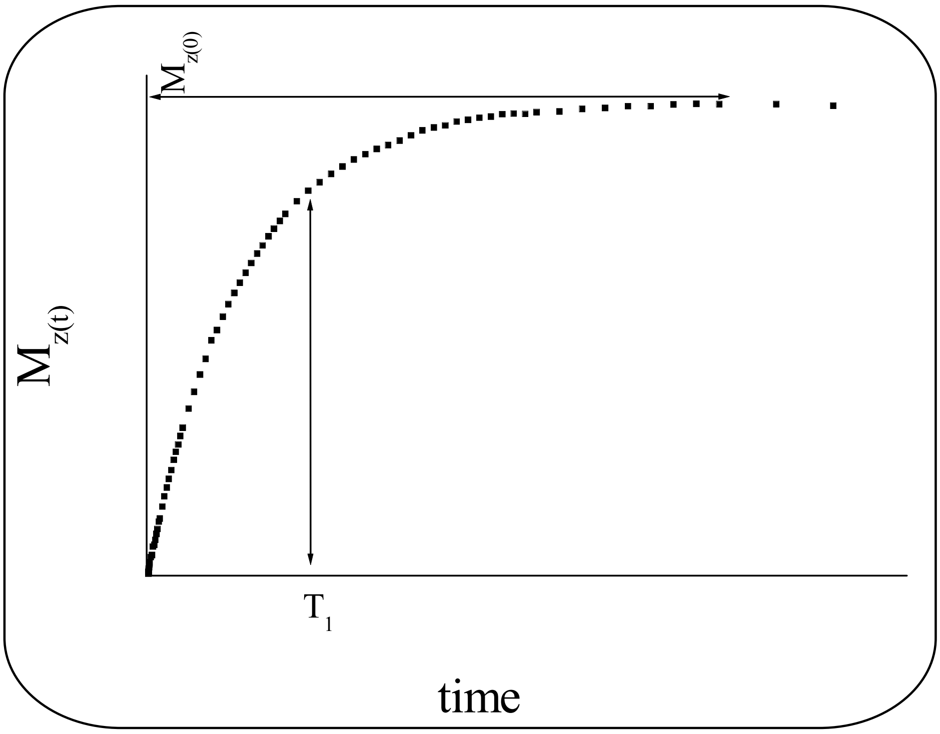

Figure 1.4: Spin-lattice relaxation time (T_1).

Mathematically the recovery of magnetization is given by eq. (1.7)

$$\frac{dM_Z(t)}{dt} = \frac{M_Z(t) - M_Z(0)}{T_1} \qquad \text{Eq. 1.7}$$

In equation 1.7,

$M_z(t)$ = Recovered magnetization vector after the removal of RF pulse at time t.[9-10]

1.1.4 Spin-spin relaxation

Spin-spin relaxation results in the loss of transverse magnetization (M_{xy}) and hence is also called transverse relaxation. In spin-spin relaxation, energy is transferred from one nucleus to another via fluctuating nuclear dipoles. As a result, the energy of one nucleus is increased while for the other is decreased. The net energy remains the same, only the $M_{xy}(t)$ returns to $M_{xy}(0)$. The M_{xy} is the sum of magnetic moments of several nuclei, and all these nuclear magnetic moments are supposed to possess phase coherence in the x-y plane after the application of RF pulse. All these nuclear spins (i.e. magnetic moments) will remain static in the rotating frame if all the nuclear spins in the sample are experiencing exactly the same magnetic field. However, in fact this is not possible; therefore some of the nuclei precess with the frequency slightly higher than Larmor frequency while some exhibit precessional motion with the frequency slightly smaller than the Larmor frequency. Two main factors are responsible for inhomogeneous fields experienced by the sample: (a) static magnetic field inhomogenity which is purely instrumental imperfection and (b) local magnetic field arising from intermolecular and intramolecular interactions in the sample. The second factor is responsible for the genuine or natural transverse relaxation. When RF pulse is switched off, spin-spin interactions between low and high energy nuclei lead to the fanning-out of the individual magnetisation vectors (Figure 1.5).

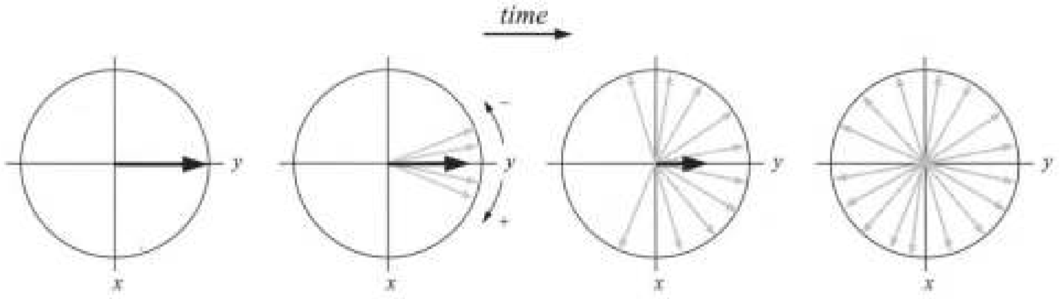

Figure 1.5: Schematic illustration of spin-spin (or transverse) relaxation.

Both longitudinal and transverse relaxation phenomena take place simultaneously. Spin-spin relaxation is characterized by the spin-spin relaxation time constant, denoted by T_2. Spin-spin relaxation time (T_2) is the time required for ~37% of transverse magnetization ($M_{xy}(t)$) to decay from its original value ($M_{xy}(0)$) (Figure 1.6).

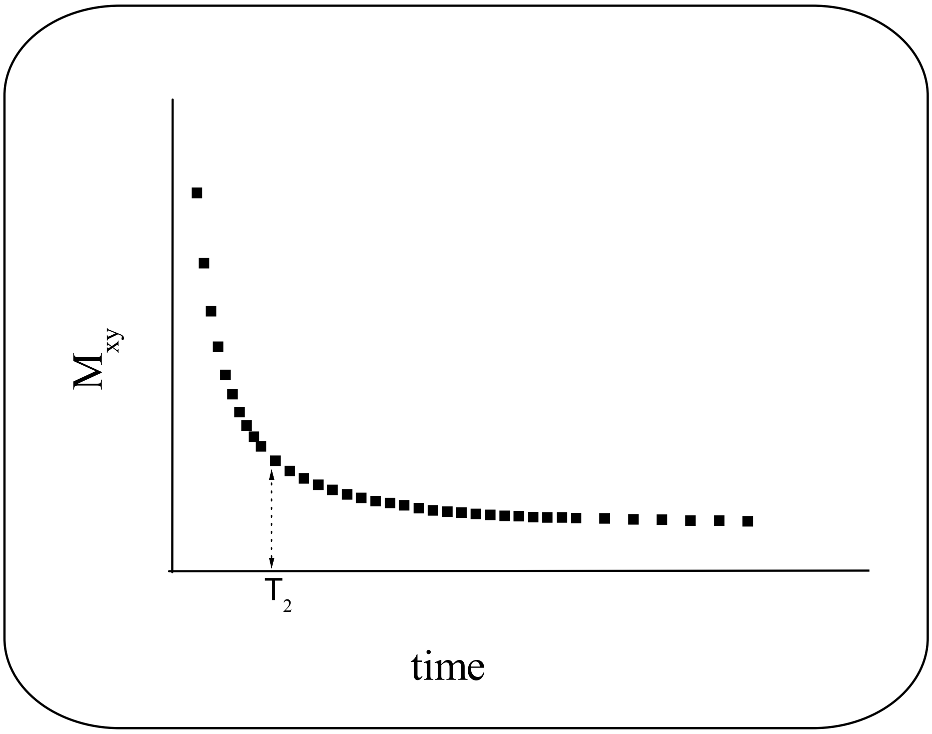

Figure 1.6: Spin-spin relaxation time.

Mathematically the spin-spin relaxation time T_2 is given as:

$$M_{xy}(t) = M_{xy}(0)e^{-t/T_2} \qquad \text{Eq. 1.8}$$

As this thesis mainly deals with T_1 measurements, the next section briefly describes experimental methods for the determination of T_1.

1.1.5 Experimental determination of spin-lattice relaxation time (T_1)

The following three pulse techniques are frequently used for determination of T_1.

1. Inversion Recovery (IR)
2. Saturation Recovery (SR)
3. Null Method

Inversion recovery method was used for measuring T_1 relaxation time in this work, it is discussed in detail in the following section.[11]

1.1.5.1 Inversion-recovery sequence for determination of T_1

The inversion-recovery is the most frequently used method for determination of longitudinal relaxation time T_1. The inversion recovery experiment is a simple two pulse experiment. In the first instance, the $M_z(0)$ is inverted (to –z axis) by applying a 180^o pulse. The $-M_z(t)$ relaxes back to $+M_z(0)$ with the time constant T_1. As the $+M_z$ needs to be observed, it is again moved to the transverse (x-y) plane (M_{xy}) by a 90^o pulse after a suitable delay time τ (Figure 1.7).

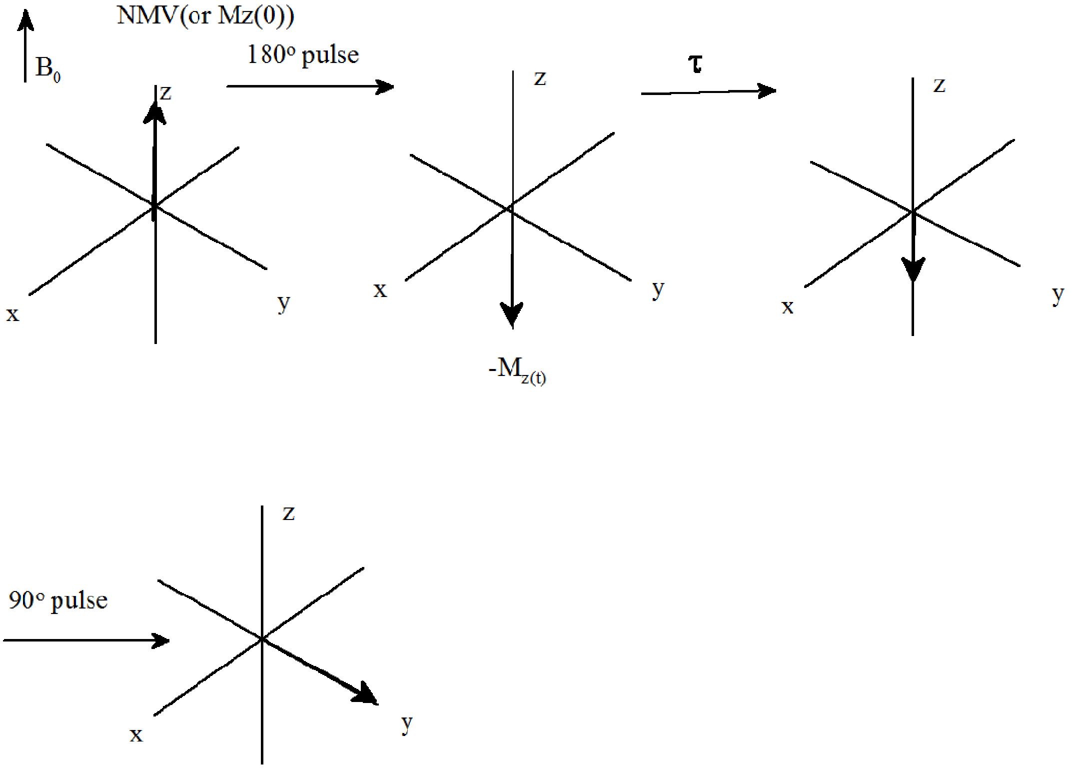

Figure 1.7: Schematic representation of inversion recovery process.

When τ is zero, the $M_z = -M_z$. This experiment is repeated with increasing values of τ and the signal after every 90^o pulse is recorded. Mathematically, magnetisation detected at various values of τ is given as:

$$M_z(t) = M_z(0)(1 - 2e^{-\tau/T_1}) \qquad \text{Eq. 1.9}$$

In equation (1.9), $M_z(0)$ is the equilibrium magnetisation which is recorded at τ_∞. The relaxation time T_1 is determined by fitting the signal intensities (i.e. recovered magnetisation at various time intervals τ) to equation (1.9). The fitting can be done using algorithms which are available in many NMR software packages. Alternatively, T_1 can also be determined from the slope of the plot of $\ln(M_z(0) - M_z(t))$ vs τ.

1.1.6 Obtaining spatial information (for image formation in MRI)[12-14]

In the above section, the basic principles of NMR were discussed i.e. interaction between NMR active nuclei and the RF pulses in the presence of an applied magnetic field. In MRI, magnetic field gradients are applied in addition to the main magnetic field (B_0), which are small perturbations superimposed on B_0. Mathematically, the magnetic field (B_i) at position "r_i" is given as:

$$B_i = B_0 + G_T r_i \qquad \text{Eq. 1.10}$$

In equation (1.10), G_T is the total gradient amplitude. Gradients are generated by coils which are placed within the bore of the magnet and they produce linear variations in one direction only, therefore for 3D imaging three gradient coils located in three different orientations (i.e. along x, y and z-directions) are required. Gradients are usually applied for a short period of time during a scan and hence are called gradient pulses. Gradient pulses, RF-pulses, the data sampling period and the time interval between each of them are collectively referred to as a pulse sequence (discussed in section 1.1.7).

In the presence of magnetic field gradients, the Larmor frequency equation (1.5) will be modified as:

$$\omega_i = \gamma(B_0 + G r_i) \qquad \text{Eq. 1.11}$$

In equation (1.11), ω_i is the Larmor frequency of protons at position i while G represents the total gradient amplitude (expressed in mT/m or G/cm). According to equation 1.11, every proton has a unique Larmor frequency which depends on its location / position within the gradient field.

Gradients perform the following three main tasks in encoding the spatial information.

(a) Slice selection
(b) Frequency encoding
(c) Phase encoding

1.1.6.1 Slice selection

Field gradients change the frequency (ν_L) of body protons in a linear fashion along the direction of the gradients. Therefore, protons in selected slice along the direction of the gradients have a specific range of Larmor frequencies (slice selection gradient G_{SS}). A frequency selective RF pulse having a central frequency and a narrow band of frequencies which coincides with the proton frequencies in the selected slice is applied. As a result, only the protons in the selected slice are excited. The central frequency determines the particular position of the slice. The thickness of the slice can be determined from the slice selected gradient amplitude (G_{SS}) and the bandwidth of frequencies ($\Delta\omega_{ss}$) in the RF pulse as given by following equation (1.12).

$$\Delta\omega = \gamma\Delta(G_{SS} \times \text{Slice Thickness}) \qquad \text{Eq 1.12}$$

$\Delta\omega$ is usually fixed and the amplitude of G_{SS} is changed to get a slice of the desired thickness.

MRI requires multislice imaging, which is achieved by using the same G_{SS} and a unique RF pulse for each slice.

After selecting the slice of desired thickness, the spatial location of MR signal in the slice is determined by the frequency encoding (which tells us the position of the nuclei giving rise to the signal along x-axis on the MR image) and phase encoding (which tells us the position of signal along y-axis on the MR image) which are discussed in the following sections.

1.1.6.2 Frequency encoding or readout process

During signal detection (i.e. read out process) in MRI measurements, frequency encoding is performed which gives us spatial information about MR signal along the x-axis. In an MRI pulse sequence, the signal is always detected in the presence of a gradient known as a readout gradient G_{RO}. The readout gradient G_{RO} is responsible for producing one of the two visual dimensions of the image. Typically, MRI pulse sequences use a slice selective RF pulse (such as 90^o) which excites the protons in the selected slice and make the NMV flip away from the z-direction to the transverse plane. After the RF pulse is applied, the transverse relaxation dephases the NMV. The dephasing can be partially reversed by a 180^o RF pulse which will form an echo. During the formation of the echo, G_{RO} is applied perpendicular to the direction of the slice. Now in the presence of this new gradient field protons will start precessing with different frequencies depending on their positions. Each of these frequencies is superimposed onto the echo and the echo signal is measured at the desired time by the receiver coil. Thus positions of the protons are determined from the G_{RO} magnitude and the corresponding frequency (Figure 1.8).

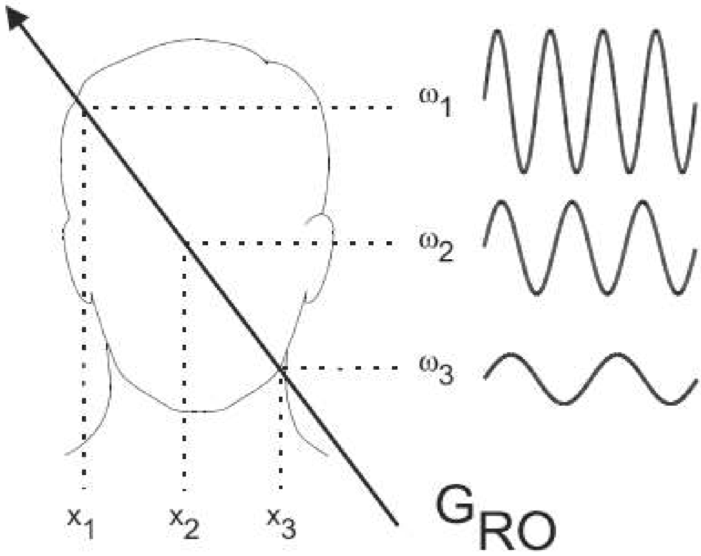

Figure 1.8: Schematic illustration of frequency encoding (or readout process).

In Figure (1.8), x_1, x_2 and x_3 are three different positions of the protons in the selected slice, while ω_1, ω_2, and ω_3 are the corresponding detected frequencies.

1.1.6.3 Phase encoding

Phase encoding is applied before the readout process and it tells us about the MR signal location along y-axis. The phase encoding gradient (G_{PE}) is applied perpendicular to both G_{SS} and G_{RO} which alters the magnetic field strength and the precessional frequencies of the protons. G_{PE} is usually applied just before the 180^o rephasing pulse as mentioned in the previous section. Prior to application of G_{PE}, protons have frequency ω_0 (or Φ_2 as indicated in Figure 1.9) called base frequency. The G_{PE} will increase or decrease this frequency. When the G_{PE} is switched off, protons will resume their base precessional frequency, but the relative phases will be either slightly larger or smaller than Φ_2 as illustrated in Figure 1.9. This change is called induced shift and its magnitude depends on the magnitude and duration of G_{PE}. The induced shift is different for protons located at different positions in the phase encoding direction for the same magnitude of G_{PE}. For example in the Figure 1.9 y_1, y_2 and y_3 are three different locations in the phase encoding direction and they experience three different induced shifts indicated as Φ_1, Φ_2 and Φ_3, respectively.

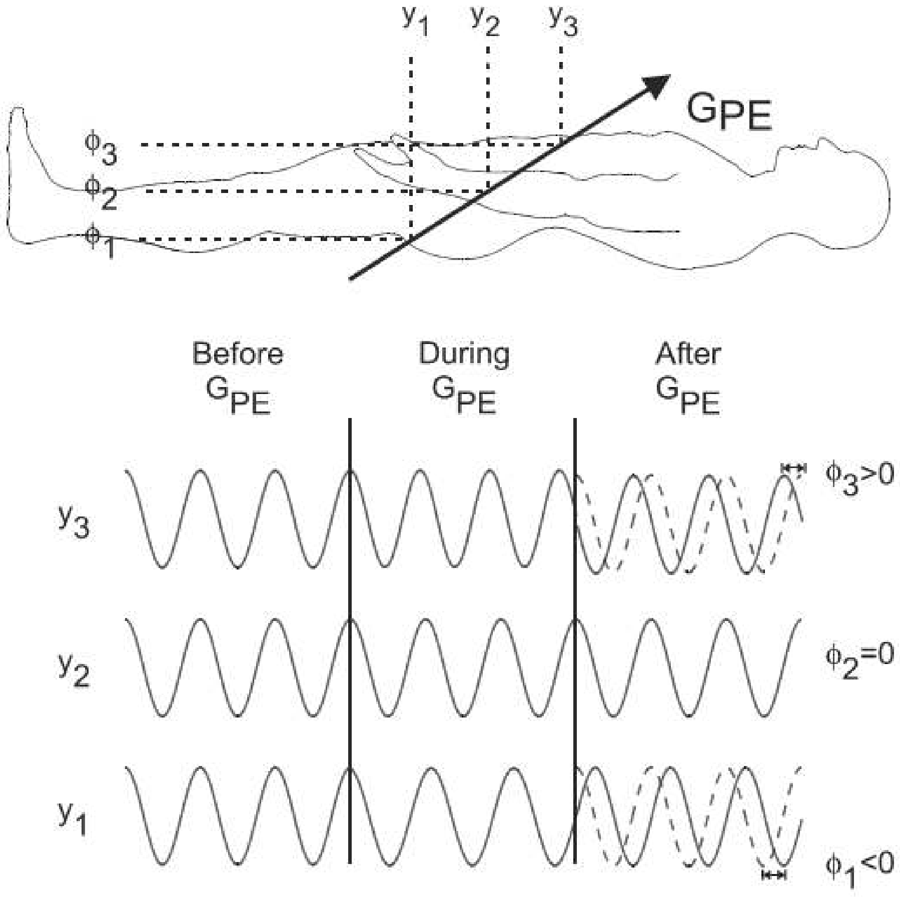

Figure 1.9: Schematic illustration of phase encoding phenomenon.

1.1.6.4 k-Space

Traditionally in MRI the letter "k" is used to represent the coordinate in the Fourier domain, and hence the Fourier domain in MRI is represented as "k-space". This term was introduced by Ljunggren and Twieg in 1983. k-space has two axes i.e. k_x which represents the frequency information and k_y which represents the phase information. This information is then translated into an image using software with the help of computers. Briefly, k-space is a two dimensional matrix of digitized MR data which upon Fourier transformation yields the MR image.

1.1.7 Pulse sequences

A pulse sequence consists of RF pulses, gradient pulses and timings which are applied in a specific order to generate an MR image. Several types of pulse sequence are used in MRI, of which spin echo and gradient echo sequences are the two main methods while echo planar imaging sequence is an example of specialist sequences. Here we will discuss only Spin Echo Sequences, which are commonly used in MRI.

1.1.7.1 Spin echo sequences

Spin echo sequences consist of a 90^o excitation pulse and one or more 180^o refocusing pulses. The 90^o excitation pulse makes the NMV (or $M_z(0)$) flip away from z-axis to the x-y plane(M_{xy}). After the 90^o pulse, the NMV moves back by the T_2 dephasing mechanism. A 180^o pulse is then applied which refocuses the NMV in the x-axis. This produces a spin echo also known as Hartman-Hahn echo. Spin echo sequences are characterised by the timing parameters TR (repetition time) and TE (echo time). TR is the time interval between successive excitation pulses while TE is the time interval from excitation pulse to the echo maximum for a given slice (Figure 1.10). In Figure 1.10, τ is the time taken to rephase the NMV after the application of 180^o (which is equal to time for dephasing NMV by 90^o pulse).

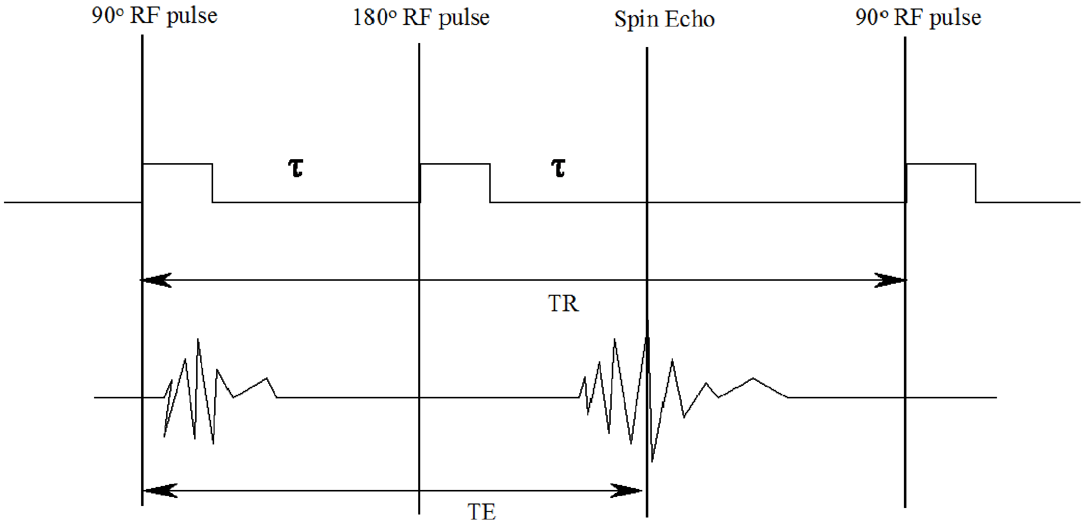

Figure 1.10: Schematic illustration of spin echo pulse sequences.

1.2 Image contrast in MRI

To trace abnormal tissue, the MRI image must produce the contrast between normal (healthy) tissue and abnormal (diseased) tissue. Intensity based image contrast C(A, B) between two tissues A and B may be defined as:

$$C(A,B)=\frac{|I(A)-I(B)|}{I_{ref}} \qquad \text{Eq. 1.13}$$

In eq. 1.13, I_A and I_B are the intensities of tissues A and B, respectively and I_{ref} is the arbitrary reference intensity. In such a simple MRI image there is no external or internal reference, image contrast is simply the difference between intensities of two tissues. An MRI image has contrast if there are areas of high signal intensity (white on the image) and areas of low signal intensity (dark on the MRI image). The images having intermediate signal intensity have grey shades in between white and black.

1.2.1 Contrast mechanism in MRI

Generally three different types of intensity contrast in MR images can be created which are briefly discussed in the following section.

1.2.1.1 T_1 Weighted contrast

The repetition time TR (i.e. time interval between two successive excitation pulses) is the key parameter responsible for T_1 contrast during a pulse sequence. For T_1 contrast a short TR is selected. When a pulse sequence with short TR is applied, the tissues with relatively short T_1 relax quickly (after the application of 90^o pulse) and thus exhibit large signal intensity after the application of next (180^o) pulse. On the other hand, tissues with a long T_1 undergo only little relaxation between two RF pulses and thus yield low signal intensity. For example fat has a shorter T_1 (because it has a relatively slow tumbling rate which is similar to that of the Larmor frequency) and thus will appear with strong signal intensity while water has a relatively longer T_1 (due to relatively high tumbling rate which does not match the Larmor frequency) and will appear with low signal intensity on a T_1 weighted MR image (Figure 1.11).

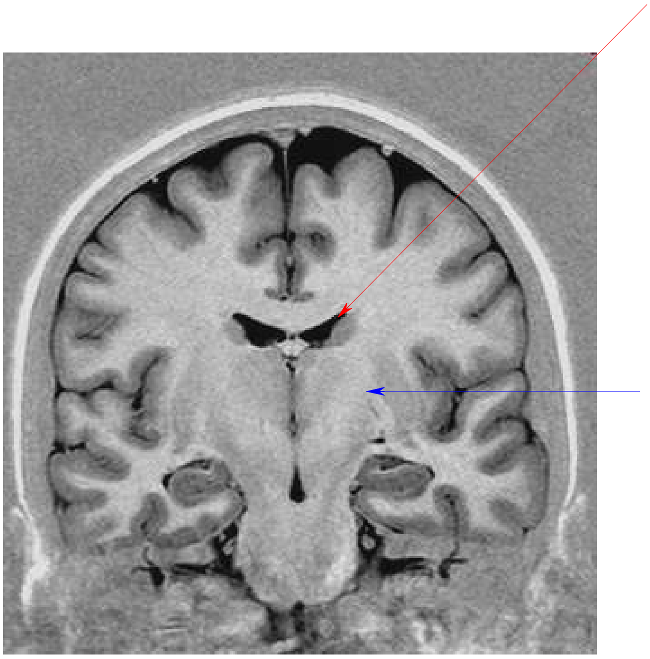

(Water appears dark on T1 image)

(Fat appears bright on T1 image)

Figure 1.11: T_1 weighted image of brain showing contrast between fat and water.[15]

On the other hand, in case of a long TR, both water and fat recover their NMV along the z-axis before the application of the next RF excitation pulse. This results in a very small difference in T_1 contrast which cannot be demonstrated on MR images (Figure 1.12).

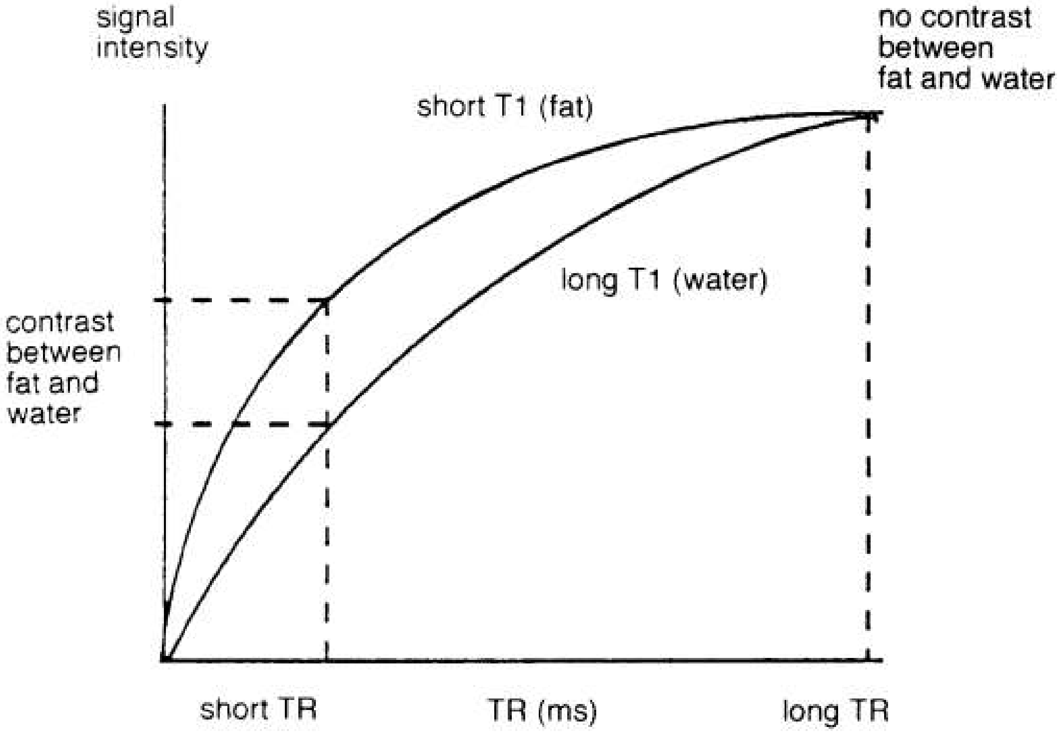

Figure 1.12:T_1 contrast between fat and water in a tissue due to different T_1 values. [15]

1.2.1.2 T_2 Weighted contrast

The effect of T_2 on the image contrast is based on the echo time (TE is the time interval between (90^o) excitation pulse and maximum echo). To create T_2 contrast in MR images, long TE (which must be in the range of T_2 of tissues) is used in spin echo pulse sequences. The tissues with relatively shorter T_2 will lose magnetisation (i.e. NMV) quickly which will yield low signal intensity, while tissues with relatively larger T_2 exhibit high signal intensity. For example fat appears with low signal intensity (as it has short T_2) and water appears with high signal intensity (as it has larger T_2) on T_2-weighted images (Figure 1.13).

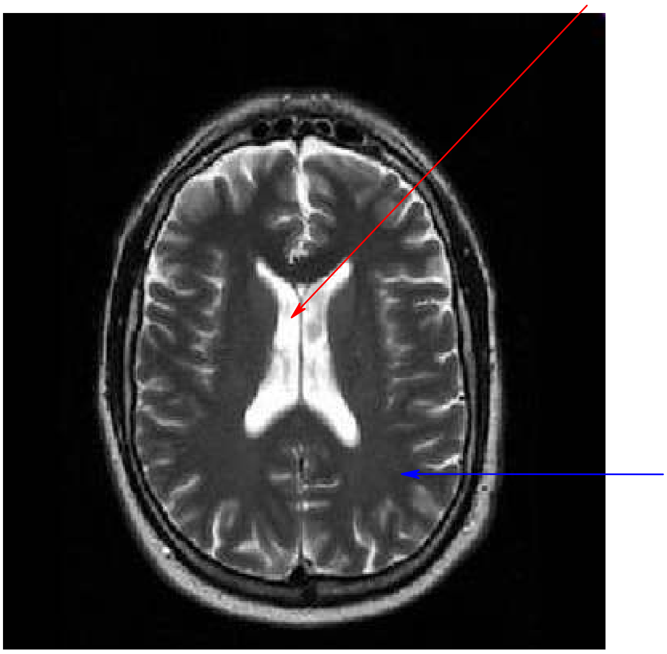

(water appear bright on T2 image)

(fat appear dark on T2 image)

Figure 1.13: T_2 weighted image of the brain showing contrast between fat and water.[15]

On the other hand, if a short TE is used, no contrast will be created because neither the fat nor water transverse magnetization vectors will decay significantly. There will not be much difference in T_2 signals between fat and water as demonstrated in Figure 1.14.

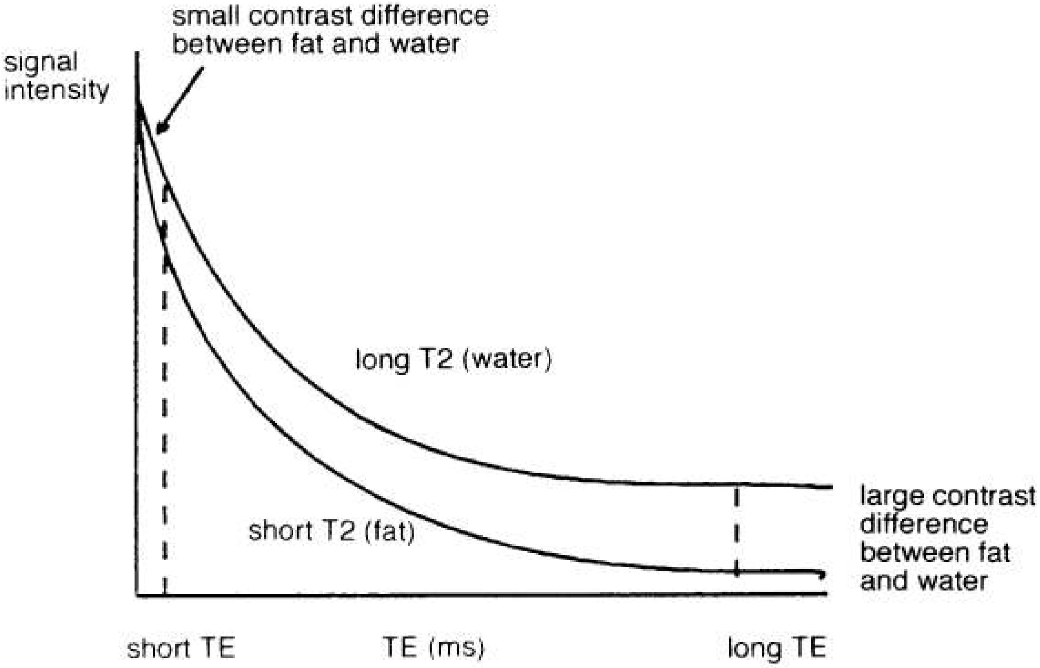

Figure 1.14: T_2 contrast between fat and water in the tissue.[15]

1.2.1.3 Proton density images

Apart from differences in relaxation times in different tissues, the difference in the number of protons per unit volume in different tissues can also create contrast in the MRI images. In proton density images, the extrinsic parameters are selected in the range (TE << T_2 and TR >> T_1) so that they do not significantly affect the image contrast and thus image contrast primarily depends upon the proton density. In proton density images, tissues with higher proton density appear bright (e.g. brain tissues) and the tissues with lower proton density appear dark (e.g. cortical bone) (Figure 1.15).

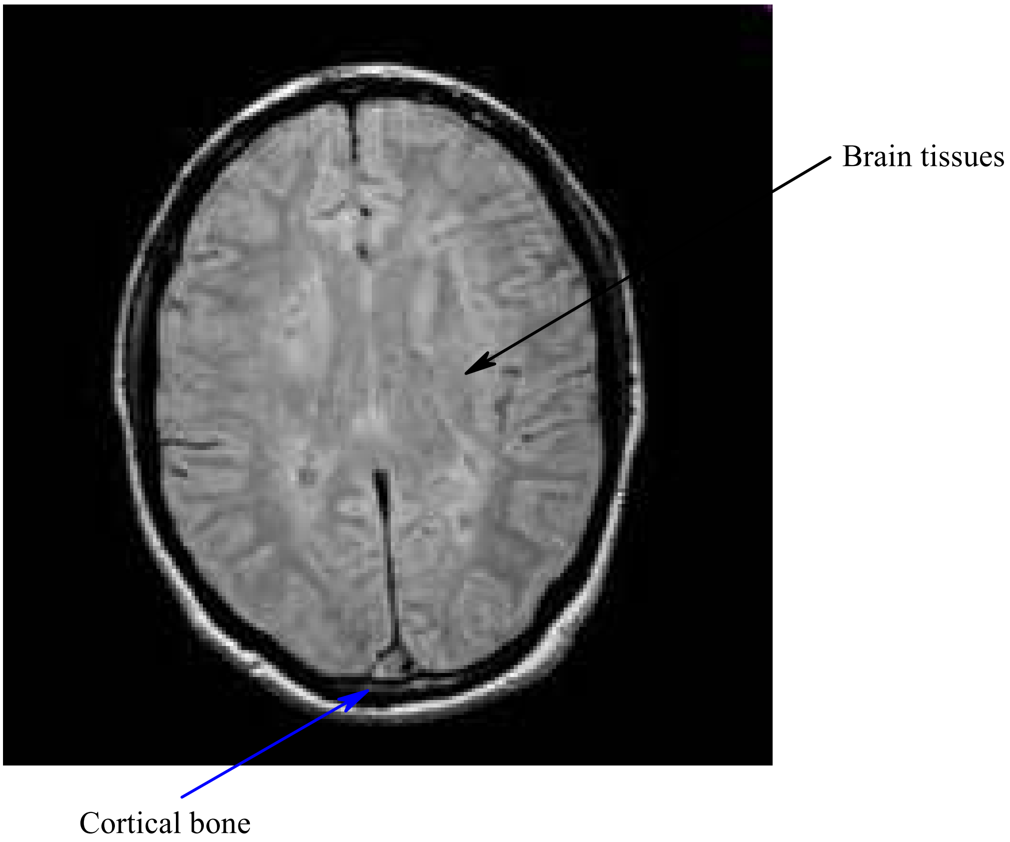

Figure 1.15: Proton density image of the brain. [15]

1.2.1.4 Chemical shift imaging

In conventional MRI, various hydrogen atoms in the body are not differentiated depending upon their chemical environment. However the protons bonded with water have different Larmor frequency than those bonded with aliphatic carbon chains (such as methylene protons in lipids or tissues). The spatial determination of these different protons leads to the chemical shift imaging. Proton chemical shifting imaging may give better results than MRI in diagnostic studies in some situations. For example, chemical shift imaging is reported to diagnose fatty liver disease more efficiently.[16]

1.3 Contrast agents (CAs) in MRI

In the previous sections, it has been discussed that contrast in image can be created / enhanced by altering TR or TE which gives T_1 and T_2 weighted images. The image contrast also depends upon the proton density. However, abnormal tissues under examination may not have significant differences in T_1 and / or T_2 from the surrounding normal tissues which results in very little inherent contrast. The signal difference between normal and diseased tissues can be enhanced through administration of paramagnetic substances called contrast agents. For example in Figure 1.16, the T_1-weighted image without contrast agent lacks some information which is clearly present (i.e. two additional lesions) in the image obtained after the administration of a contrast agent.

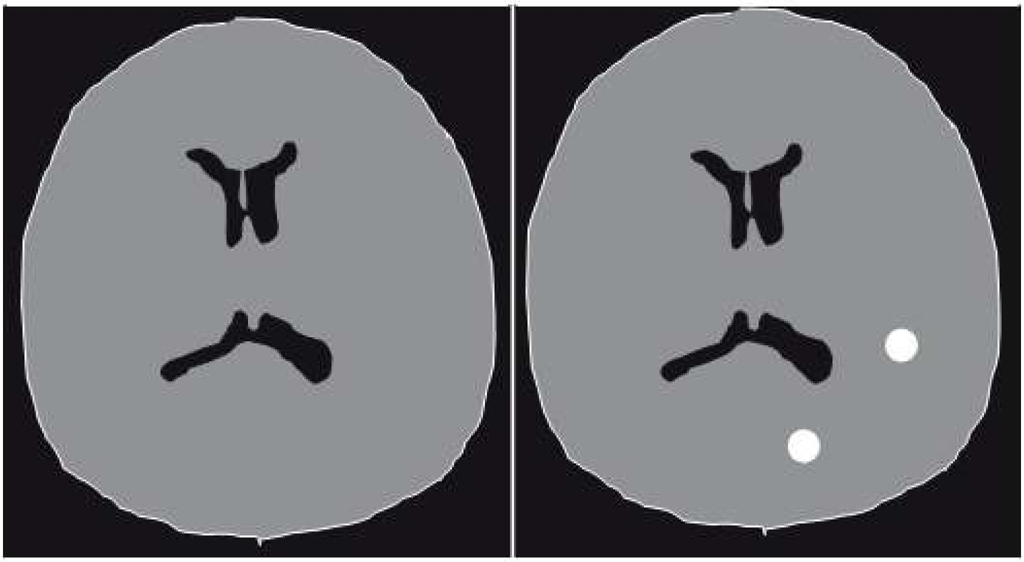

Figure 1.16: T_1 weighted images of transverse orientation of central nervous system (CNS) with (right) and without (left) contrast agent.[13]

In the early years (1948) of NMR, it was found that relaxation of the water protons can be enhanced by paramagnetic substances like $FeCl_3$ etc.[17] 30 years later, Lauterbur *et al.*[18] successfully distinguished different tissues on the basis of different relaxation rate using a Mn(II) salt and thus published the first MRI image. Nowadays, Gd-complexes are widely used as MRI contrast agents and will be discussed in the section 1.5.

1.4 Relaxivity of contrast agents (i.e. Metal Complexes)

The main purpose of the use of contrast agent is to get better contrast so that one can easily distinguish the diseased tissues from the normal ones. The body protons (in the form of water or proteins) are the basis of MRI. The tumbling rate of body water molecules is much higher than the Larmor frequency. As a result, relaxation rate of water protons is very low which results in long relaxation (T_1) times and thus poor / weak MRI signals. By using contrast agents, the relaxation rate is increased resulting in better contrast of the MRI image.[1, 5] The fluctuating magnetic field around the paramagnetic centre due to unpaired electrons is responsible for increasing the relaxation of nearby water protons. There are several mechanisms for affecting the relaxation of surrounding protons by paramagnetic metal complexes; the most dominant is the dipole-dipole interactions between paramagnetic centre and the surrounding water molecules. The dipolar mechanism is orientation dependent i.e. highly dependent on the rate of tumbling of coupled species. The dipolar mechanism of relaxation is discussed in more detail in chapter 3 (section 3.1).

The general theory of solvent nuclear relaxation was developed by the groups of Bloembergen, Solomon and others.[19-21] According to this theory the metal complexes affect both spin lattice relaxation rate ($1/T_1$) and spin-spin relaxation rate ($1/T_2$). The observed relaxation rate of surrounding water protons ($1/T_{1,obs}$) in the presence of paramagnetic substance is generally given by the following mathematical equation.

$$\frac{1}{T_{i,obs}} = \frac{1}{T_{i,d}} + \frac{1}{T_{i,p}} \qquad \text{where } i = 1, 2 \qquad \text{Eq. 1.14}$$

In equation 1.14, $1/T_{i,d}$ is the relaxation in the absence of any paramagnetic substance, while $1/T_{i,p}$ is the relaxation enhancement by the paramagnetic substance. The relaxation enhancement is directly proportional to the concentration of the paramagnetic species [22], equation 1.14 can be modified as:

$$\frac{1}{T_{i,obs}} = \frac{1}{T_{i,d}} + r_i[M] \qquad \text{Eq. 1.15}$$

The concentration of paramagnetic species [M] is usually expressed in mmol/L and relaxation time is in seconds. A straight line is obtained from the plot of various concentrations of paramagnetic species vs relaxation rate; the slope of this plot gives us relaxivity (r_i). Relaxivity is the tendency of contrast agent to increase the relaxation rate of surrounding protons and is usually expressed as $mM^{-1}s^{-1}$.

There are also several other factors which control / limit the relaxivity of contrast agents and are discussed in the section 1.7.

1.5 Gadolinium based contrast agents

Due to the toxicity of many uncomplexed paramagnetic ions at the doses required for imaging, they must be chelated to form thermodynamically and kinetically stable chelates, hence, MRI contrast agents consist of two main parts, i.e. (a) a paramagnetic centre and (b) a chelating ligand. Various paramagnetic ions were considered as paramagnetic centres for MRI CAs as shown in table 1.1.

Table 1.1: Various paramagnetic metal ions with their magnetic moment values.[23]

Atomic No.	***Ions***	***3d***	***4f***	***Magnetic moment / BM***
24	Cr^{3+}	↑ ↑ ↑	-	3.8
25	Mn^{2+}	↑ ↑ ↑ ↑ ↑	-	5.9
26	Fe^{3+}	↑ ↑ ↑ ↑ ↑	-	5.9
29	Cu^{2+}	↑↓ ↑↓ ↑↓ ↑↓ ↑	-	1.7-2.2
63	Eu^{3+}	-	↑ ↑ ↑ ↑ ↑ ↑	6.9
64	**Gd^{3+}**	-	↑ ↑ ↑ ↑ ↑ ↑ ↑	**7.9**
66	Dy^{3+}	-	↑↓ ↑↓ ↑ ↑ ↑ ↑ ↑	10.42
67	Ho^{3+}	-	↑↓ ↑↓ ↑↓ ↑ ↑ ↑ ↑	10.46

Gd^{3+} has received the most attention as a paramagnetic centre for the MRI contrast agent due to its following unique features:

- It has a very high value of magnetic moment due to the seven unpaired electrons present in the “3+” oxidation state.
- The electronic relaxation time for Gd^{3+} is much longer (~10^{-9} s) than for the other lanthanides such as Dy^{3+}, Eu^{3+} and Ho^{3+} (~10^{-13} s).

Lanthanides such as Dy^{3+} and Ho^{3+} have higher magnetic moments than Gd due to a greater orbital angular momentum contribution, but due to their relatively short electronic relaxation time, they are rarely used as paramagnetic centres for MRI contrast agents. The relatively high electronic relaxation time of Gd^{3+} is responsible for changing the relaxation time of the surrounding protons. Another important paramagnetic centre is the Fe^{3+} and iron oxide based MRI contrast agents will be discussed briefly in section 1.6.

The second component of the contrast agent is the ligand which must possess some unique characteristics to form the MRI contrast agents. For example, ligands must be water soluble, form stable complexes with Gd and finally after chelating with Gd^{3+} they must have some exchangeable water molecules. The exchangeable water molecules play a crucial role in increasing the relaxation rate of surrounding water protons by transferring the effect of magnetic moment of the paramagnetic centre to the surrounding protons.

Initially Ethylenediaminetetraacetic acid,(EDTA, a hexadentate ligand) was used for complexation with gadolinium but due to poor in vivo stability, it is unsuitable for clinical use, although Gd-EDTA complex includes three exchangeable water molecules which could significantly contribute to increase the relaxation rate of the surrounding protons (Figure 1.17).

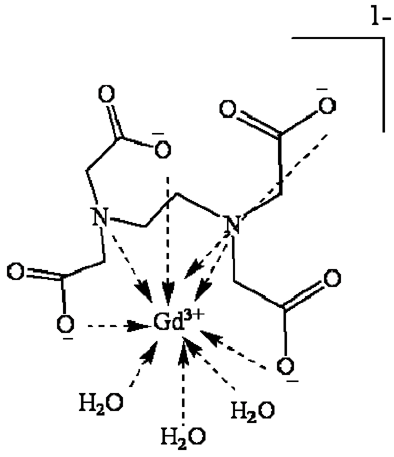

Figure 1.17: [Gd-EDTA]$^{1-}$ chelate.

On the other hand, DTPA and DTPA-like ligands have attracted much attention due to their good in vivo stability (Figure 1.18).[24]

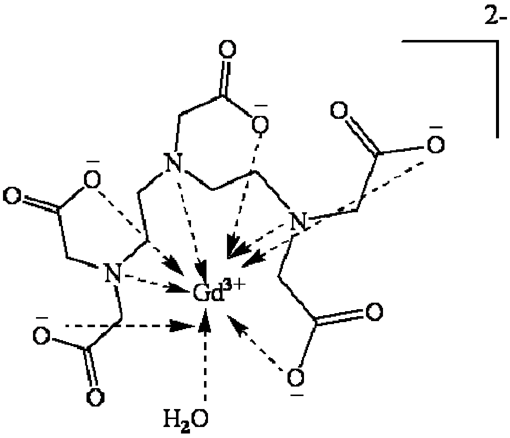

Figure 1.18: [Gd-DTPA]$^{2-}$ chelate.

Macrocyclic ligands can also form stable complexes with lanthanides. For example, DOTA (1,4,7,10-tetraazacyclododecane-1,4,7,10-tetraacetic acid) (Figure 1.19) and similar ligands form complexes which are very stable due to their macrocyclic structure and inert behaviour at physiological pH in blood serum. The main drawback associated with macrocyclic ligands is their synthesis as the synthetic procedure involves several steps. This problem can be solved by synthesizing smaller, cyclen-based ligands such as DOTA (Figure 1.19).

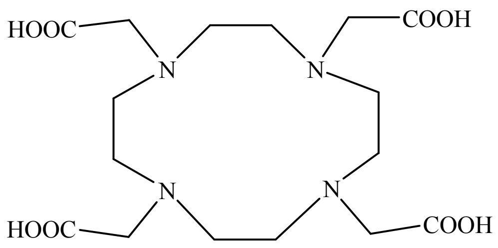

Figure 1.19: Chemical structure of DOTA.

Currently all MRI contrast agents approved for clinical applications are based on Gd-chelates with either DTPA (and DTPA based ligands) or DOTA (and DOTA based ligands) (Figure 1.20).[25]

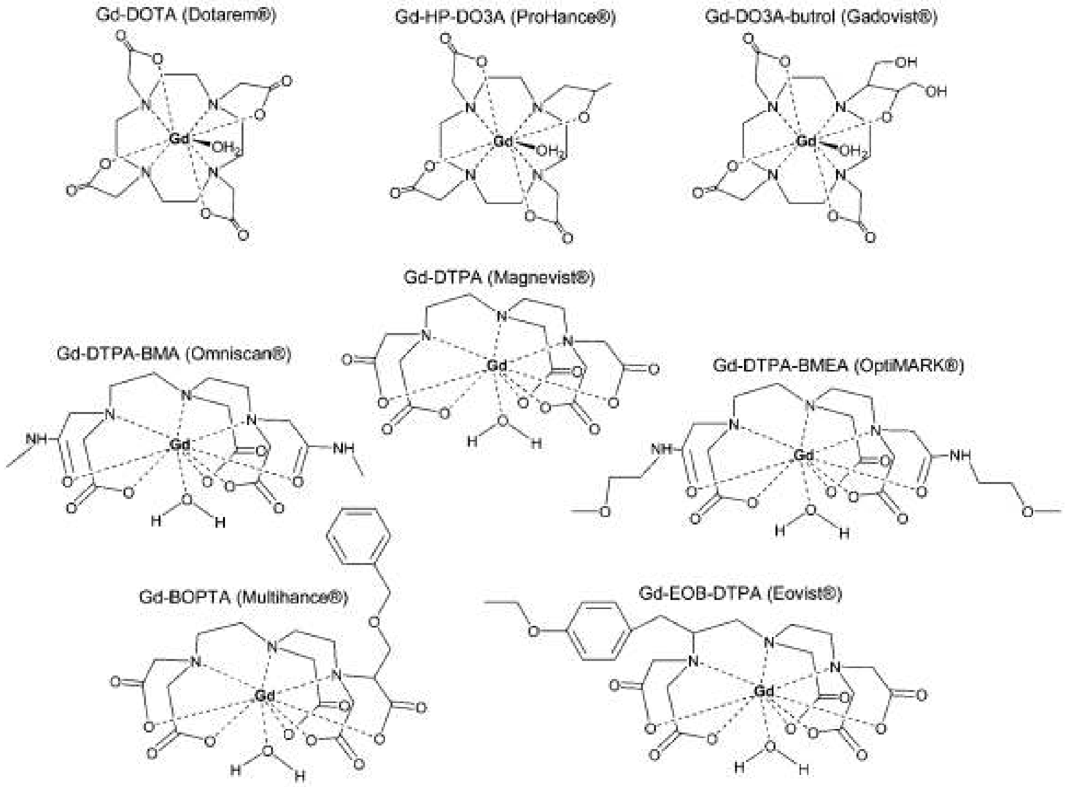

Figure 1.20: Commercially available MRI contrast agents approved for clinical applications.[25]

The main drawback associated with these small molecule based contrast agents is their diffusion to the extravenous area immediately after the intravenous injection because of their low molecular weights. In order to slow down their diffusion, high molecular weight based contrast agents were developed and these will be discussed in section 1.8. Other drawbacks associated with small molecule based contrast agents are that they are non-specific, and have relatively small circulation times due to their fast renal excretion.[26]

1.6 Iron oxide based contrast agents

Iron oxide particles present a major advantage compared to other paramagnetic ions such as Gd^{3+} and Mn^{2+} etc as each iron oxide particle bears a huge magnetic moment as compared to a single paramagnetic ion (Gd^{3+} and Mn^{2+}). Iron oxide particles are superparamagnetic. On the other hand, the main drawback associated with iron oxide based CAs is that they can only be used for T_2-weighted images i.e. negative contrast agents.

As naked iron oxide particles readily aggregate, a range of different ligands is used to stabilise the particles. There are several functional groups, which can be covalently bonded to the surface of iron oxide particles. For example, the presence of the hydroxyl group (Fe-OH) at the surface of iron oxide particles provides the opportunity to attach a wide range of other functionalities which will stabilise the nanoparticles. A range of chemical reactions can be carried out at the Fe-OH surface, via electrostatic or covalent interactions.

Depending upon the size, there are two main classes of iron oxides particles used for MRI applications[27] (a) Superparamagnetic iron oxide nanoparticles (SPIO) and (b) Ultra-small superparamagnetic iron oxide (USPIO). Both SPIO and USPIO have been extensively studied for MRI applications because both types of nanoparticles can be synthesized easily and are bio-compatible.

SPIO are larger particles and have size range 60-350nm. SPIO suspension can be used for oral applications for MRI studies of abdomen. These particles are usually protected by a non-biodegradable and soluble matrix which reduces the aggregation of SPIO particles. A typical example of SPIO is iron oxide crystals coated with dextran having diameter 80-150 nm commercially known as Endorem.[25] USPIO have size smaller than 50 nm.[28] They have prolonged blood half life, therefore they can pass through the capillary walls and can be taken up by lymph nodes and bone marrow. Combidex i.e. iron oxide particles coated with dextran having size 20-40 nm is a typical example of USPIO and it has human blood pool half life more than 24 h.

1.7 Factors affecting the relaxivity of Gd-based contrast agents

Several factors limiting relaxivity of MRI contrast agents are summarised in the Figure 1.21 and are discussed below. There are several mechanisms of relaxivity, however the most dominant is the dipolar relaxation, this mechanism is assumed as the main source of relaxivity for the following discussion. Mathematically inner sphere proton relaxivity is given as;

$$R_1 = \frac{cq}{55.5} + \left(\frac{1}{T_{1m} + \tau_m} \right) \text{................................Eq.1.16}$$

In the above eq.1.16, c = molar concentration, q = number of bound water nuclei per Gd, R_1 = Longitudinal relaxation rate, T_{1m} = Longitudinal relaxation rate for bound water protons and τ_m = Lifetime of water molecule in the inner sphere of the complex

1.7.1 Number of coordinated water molecules (q)

In Figure 1.21, three types of water molecules are associated with the one paramagnetic centre (i.e. Gd^{3+}): (a) inner sphere water molecules which are directly coordinated with the paramagnetic centre; (b) second-sphere water molecules, which are indirectly coordinated with the paramagnetic centre, these water molecules are bonded to the ligand via weak interaction forces; (c) the third type of water molecules are outer sphere molecules which come in contact with the paramagnetic chelate as a result of translational motion of the complex and water molecules. These exchangeable water molecules are responsible for transferring the effect of the magnetic moment from the Gd^{3+} centre to the surrounding water protons. Thus, the observed relaxivity in the presence of paramagnetic centre is the sum of inner sphere relaxivity and outer sphere relaxivity. But it is the inner sphere relaxivity which can be modified and thus for the new generation of contrast agents inner sphere relaxivity plays a crucial role in the overall relaxivity. This mechanism is depicted in the Figure 1.21. The inner-sphere relaxivity is directly proportional to the number of water molecules directly bonded to the paramagnetic centre. Generally, aquated Gd^{3+} can coordinate eight water molecules in its first coordination sphere, but due to toxicity gadolinium has to be chelated with some stable ligand. Several poly(aminocarboxylate) ligands have been approved for medicinal use; they occupy eight coordination sites of gadolinium leaving one free to bind a water molecule. Increasing the hydration number (q) of Gd-chelates is very difficult, as an increased number of inner-sphere water molecules results in a decreased stability of the gadolinium chelate. So far all approved gadolinium chelates for MRI applications have just one water molecule in their first coordination sphere[4] (Figure 1.21).

1.7.2 Metal-H distance (r)

Relaxivity (due to dipolar interactions) is proportional to $1/r^6$, which indicates that an increase in distance between the Gd and the bound water molecule will decrease the relaxivity and vice versa. The average Gd to OH_2 distance (now referred as the Gd-H distance for simplicity) has been found in the range of 2.5-3.3 Å.[29] Theoretically a decrease of 0.1 Å in Gd-H distance will enhance relaxivity by 20 %, and a 0.2 Å decrease results in 50 % increased relaxivity. The Gd-H distance can be decreased by increasing the tilt angle between the plane of bound water molecule with respect to the Gd-O vector.[30] The tilt angle can be increased by H-bonding between H_2O molecule and any suitable side group of the chelate.

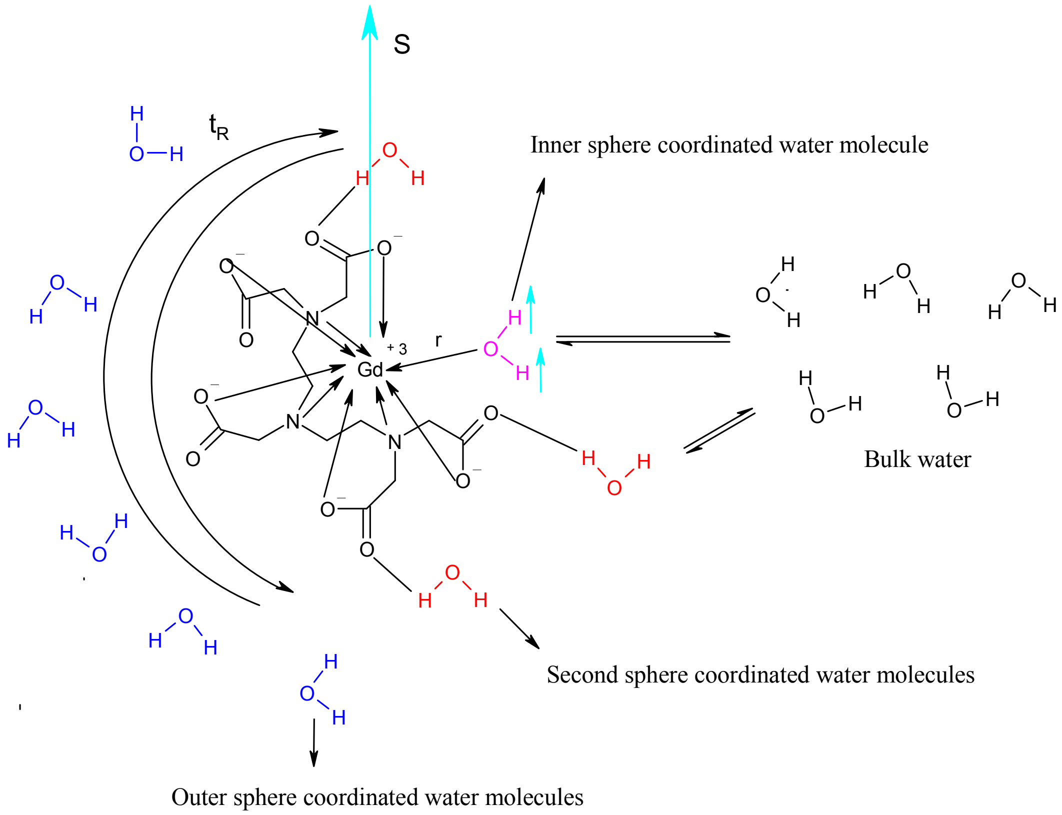

Figure 1.21: Schematic illustration showing various factors which limit the relaxivity.[1]

1.7.3 Rotational correlation time (τ_R)

The time which a species takes to move by one radian is termed its rotational correlation time.[31] This is a very important parameter which controls the relaxivity by controlling dipole-dipole interactions between electronic (Gd^{3+}) and nuclear spins (surrounding protons) as shown below mathematically:

$$\frac{1}{\tau_c} = \frac{1}{\tau_R} + \frac{1}{T_{1e}} + \frac{1}{\tau_m} \text{.................................Eq1.17}$$

In above equation 1.17, τ_c is the reorientational correlational time, τ_R is the rotational correlational tome and T_{1e} is the longitudinal electron spin relaxation time.

The dipolar relaxivity can be enhanced by increasing the τ_R.[1, 4] The increased τ_R will increase the electronic-nuclear dipolar interactions leading to increased relaxivity.

For example, Figure 1.22 shows a typical effect of τ_R on relaxivity for Gd(III) chelates. It is clear from the Figure (1.22) that as the τ_R is increased the relaxivity also increased.

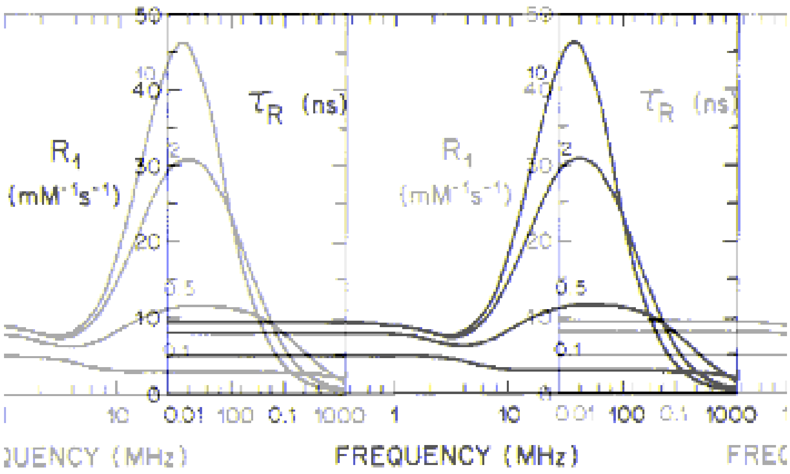

Figure 1.22: Calculated relaxivities vs Larmor frequency for different values of τ_R for Gd(III) complexes. [4]

According to Debye-Stokes theory, τ_R is directly proportional to the viscosity of the medium as given by eq. 1.18.

$$\tau_R = \frac{4\pi a^3 \eta}{3kT} \qquad \text{Eq. 1.18}$$

In eq. 1.16 "a" is the radius of a spherical molecule, k is Boltzman constant, and T is the temperature. Three basic strategies for increasing the τ_R are found in literature.[4]

I. The distribution of the contrast agent into the tissue or compartment of a tissue with high local viscosity.
II. By attaching contrast agents to large molecules, such as proteins etc before injection.

III. By non-covalent binding of the contrast agent molecule to a macromolecule in the tissue.

For example, Meijer *et al.*[32] described the effect of molecular weight on relaxivity by attaching Gd-chelates to various generations of poly(propylene imine). They found that an increase in molecular weight of the contrast agent molecule increases the relaxivity (table 1.2).

Table 1.2: Effect of Molecular Weight on Relaxivity.[32]

Gd-DTPA species	$^{*}r_1$ /mM^{-1}s^{-1}	$^{**}r_2$ / mM^{-1}s^{-1}	MW / Da
Gd-DTPA	4.2 ± 0.1	4.7 ± 0.1	592
Gd-DTPA-Dendrimer (G_o)	8.2 ± 0.2	9.6 ± 0.2	748
Gd-DTPA-Dendrimer (G_1)	11.7 ± 0.2	13.0 ± 0.2	3071
Gd-DTPA-Dendrimer (G_3)	16.0 ± 0.2	19.7 ± 0.2	12705
Gd-DTPA-Dendrimer (G_5)	19.7 ± 0.3	27.8 ± 0.3	51242

$^{*}r_1$ stands for longitudinal relaxivity and $^{**}r_2$ for transverse relaxivity

1.7.4 Water exchange (or residence life time of water molecule τ_M)

Water (protons) exchange is a key factor for relaxivity because through the water exchange between paramagnetic centre and the surrounding bulk water molecules, the relaxation effect is transferred to the surrounding water protons. Relaxivity can be limited either by fast water exchange or too slow water exchange. The fast water exchange will result in a very small residence life time (τ_M) of the water molecule in the paramagnetic centre. As a result of small τ_M values, the water molecule is not coordinated to the paramagnetic centre (e.g. Gd^{3+}) long enough to be relaxed. Too slow water exchange (i.e. higher τ_M) will also result in poor relaxivity due to poor transmission of the relaxation effect from the paramagnetic centre to the bulk water molecules.

1.8 Recent advances / developments in MRI contrast agents

In the previous sections, several factors have been discussed which limit / control of the relaxivity of CAs. Among these factors, the tuning of τ_R is the most frequently reported factor in the recent literature. The τ_R can be tuned easily by bio-conjugation of a small paramagnetic molecule i.e. Gd-DTPA chelate with macromolecules or/and macromolecular species (either) covalently (or non-covalently). There are many reports in the literature of Gd complexes (i.e. Gd-chelates) covalently attached to macromolecules or macromolecular species such as dendrimers, micelles, liposomes, nano-emuslion, carbon nanotubes etc (Figure 1.23)[33-35], in order to enhance the efficiency of MRI CAs. In this section the discussion will focus recent advances in the field of liposomes, micelles, dendrimers and zeolites and silica based contrast agents.

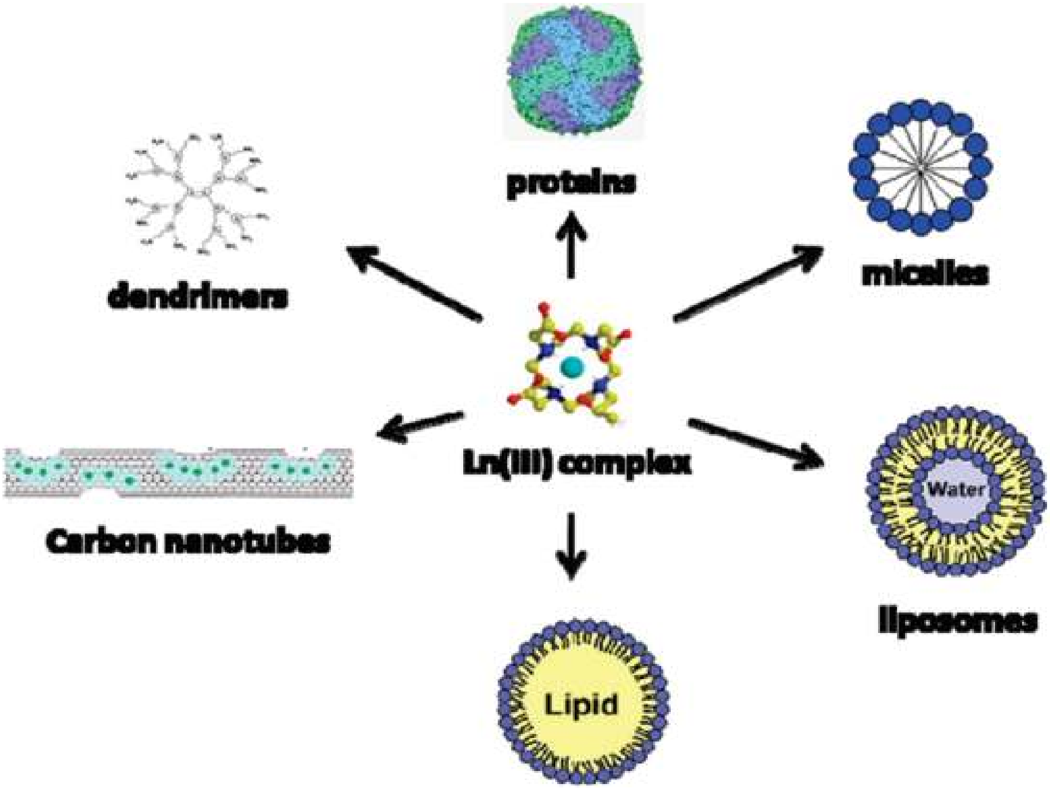

Figure 1.23: Schematic illustration of Gd-loaded species (i.e. dendrimers, micelles, liposomes etc).[33]

1.8.1 Liposome based MRI contrast agents

Liposomes (discovered in early 1960s by Bangham *et al.*[36]) are microscopic spherical vesicles composed of two phospholipids layers with a hydrophilic core and a hydrophobic tail which are often used as drug delivery vehicles.[37-38] Usually they have a size in the range of ~20-400 nm. Recently, they attracted attention for MRI contrast agents' applications due to several favourable features. For example, they can be readily prepared from simple reagents, their size can be easily manipulated and they are biocompatible.[25, 33] Liposome based contrast agents can be further subdivided into the following sections.

1.8.2 Ensomes

The main advantage of selecting liposomes as paramagnetic chelates carriers for the purpose of MRI contrast agents is attributed to their extended circulation time in blood. A short circulation time is the main drawback associated with small molecule based contrast agents. Initially the paramagnetic species were loaded into the interior (hydrophilic) core of the liposome giving rise to the structures called "Ensomes" (Figure 1.24). Various types of paramagnetic species such as Mn-chelates, Gd-chelates etc can be loaded into the liposomes core. A significant decrease in the relaxivity of Gd-chelates was observed after the encapsulation into the liposomes.

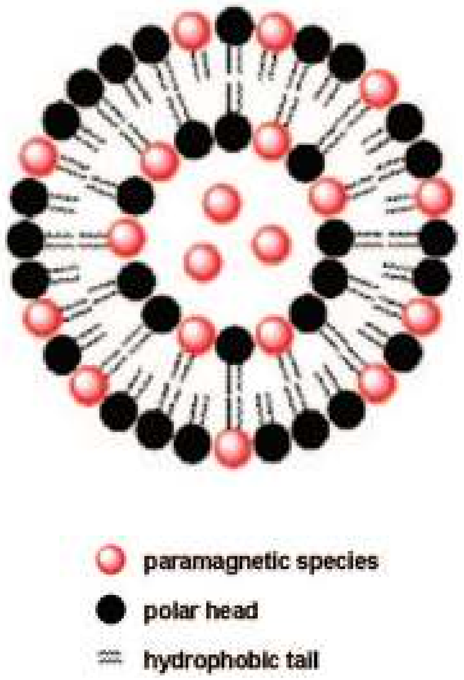

Figure 1.24: Schematic illustration of liposomes containing paramagnetic species.[25]

For efficient relaxivity, the Gd-chelates must have effective contact with bulk water for the efficient transferring of their relaxation effect via water exchange. The water exchange rate is hampered in case of Gd-chelates that are encapsulated into the liposomes. This leads to poor relaxivity (efficiency). The poor water exchange between encapsulated Gd-chelates and bulk water protons was further confirmed by relaxivity measurements at elevated temperatures. At relatively high (~35 ^{o}C) temperature, higher relaxivities values are obtained which are directly attributed to the increased water exchange rate across the liposomes membrane. Different strategies were developed to overcome this problem (i.e. slow water exchange rate) and these are discussed in the following sections.[39]

1.8.3 Memsomes

The rate of water exchange across the liposome layer can be enhanced by incorporating the paramagnetic species into the membrane. In this approach, the metal binding chelates can be attached at hydrophilic heads of the lipids (Figure 1.25). The resulting structure in which metal chelates are incorporated into the liposome leaflets, are called "Memsomes". These memsomes give better relaxivity than the Ensomes due to direct contact with the surrounding water. For example the relaxivity of Gd-DTPA-stearylamide and Gd-DTPA-stearylester incorporated in the lipid membrane was found to be two to five folds higher as compared to relaxivity of paramagnetic chelates (Gd-DTPA-stearylamide etc) in a bulk aqueous solution. This significant increase in relaxivity is due to fast water exchange and restricted motion (which increased τ_R) of the paramagnetic species in the liposome membrane. The increased τ_R of the Gd-chelates that are incorporated into the lipid membrane might be due to increased effective molecular size.

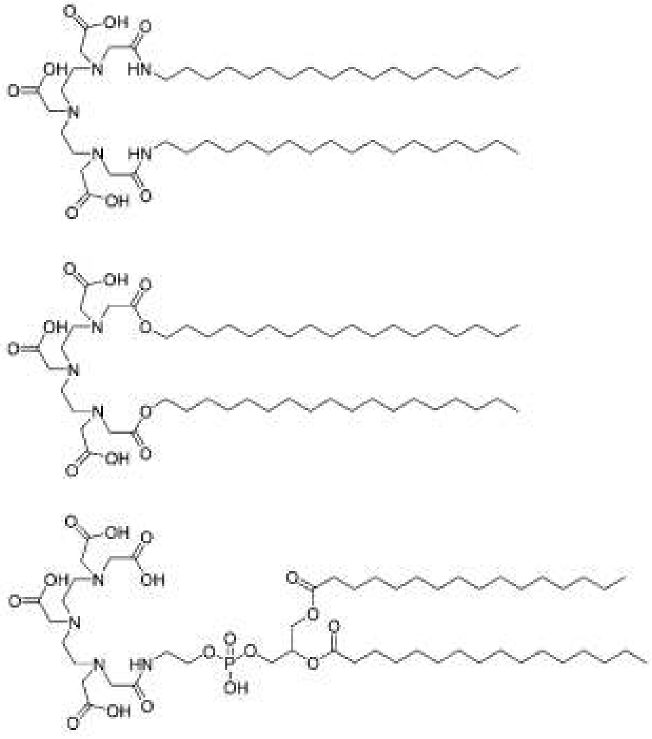

Figure 1.25: DTPA derivatives: (A) stearylamide, (B) stearylester and (C) phosphatidylethanolamine.[25]

However, increasing the size of the memsome did not result in any further increase in relaxivity. This behaviour of memsomes may be due to diffusion of the paramagnetic chelates within the membrane.

1.8.4 Micellar MRI contrast agents

Amphiphilic Gd-chelates with carbon chains that are more than 10 carbons long can self assemble to form colloidal aggregates called micelles. These micelles are much smaller (~5-30 nm) than liposomes (~20-400 nm). Micelles are often used as carriers of poorly soluble pharmaceutical agents.[40-41] As the micelles have hydrophilic heads (i.e. Gd-chelates in our case) that point outwards and hydrophobic tails that point inwards, the water exchange between the paramagnetic centre and the surrounding bulk is not affected. The water exchange rates between the paramagnetic centre and the surrounding bulk as determined for free Gd-chelates and micellar Gd-chelates did not show any difference. Furthermore the supramolecular assembly formed as a result of the micellar phenomenon has a relatively rigid structure. This increased rigidity of supramolecular assembly increases the rotational correlational time τ_{R}, which increases the relaxivity. Further increases in relaxivity could be achieved by further increases in rigidity e.g. rigidity of micelles can be increased by incorporating cholesterol molecules into the hydrophobic interior.[25] Various ligands can be coupled to the surface of such micelles in order to allow them to target specific sites. Alternatively, mixed micelles can be used to get target specific contrast agents. For example Accardo *et al.*[42] described the micellar contrast agent formed from two different surfactants. Both these surfactants have a C18 carbon chain; however one surfactant has Gd-DTPA chelates at its hydrophilic end while the other surfactant has no Gd-DTPA chelates (Figure 1.26). The surfactant without Gd-chelates has a strong affinity for specific receptors (which are over expressed in many tumours).

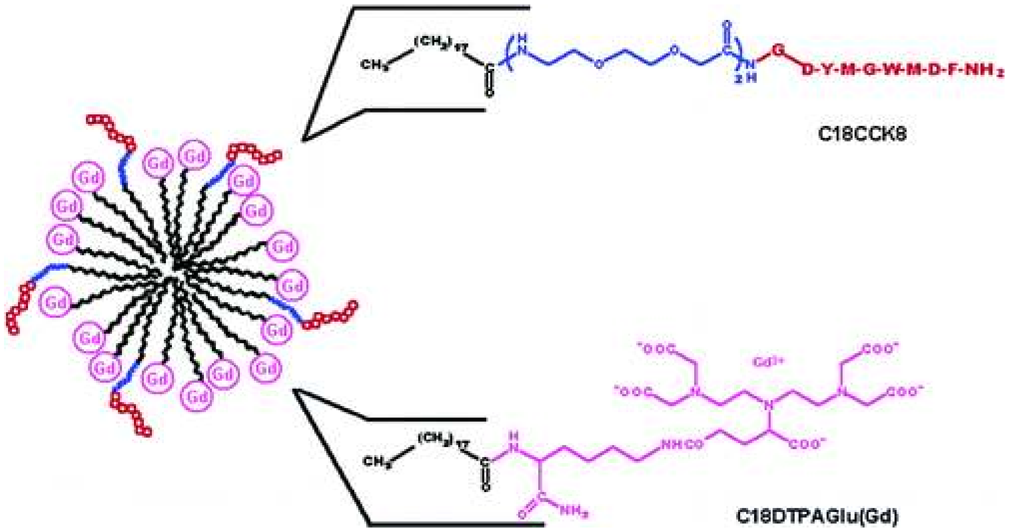

Figure 1.26: Schematic representation of mixed micellar aggregates (C18CCK8 stands for C18 hydrophobic moiety bound to C-terminal of cholecystokinin octapeptied amide) .[42]

The relaxivity of self assembled micelle based contrast agents was found to be four fold higher than the simple complex C18DTPAGlu(Gd). This was attributed to a much longer τ_R (650 ps) for C18DTPAGlu(Gd) than for the corresponding free Gd-chelate (100 ps).

Another big advantage of micellar contrast agents is that they can be designed for the purpose of pH responsive contrast agents because of their pH dependent aggregation behaviour in certain conditions. For example, it has been reported that Gd-DOTA based amphiphilic structures (having tertiary amino group at side chain) (Figure 1.27) exhibit pH dependent relaxivity.

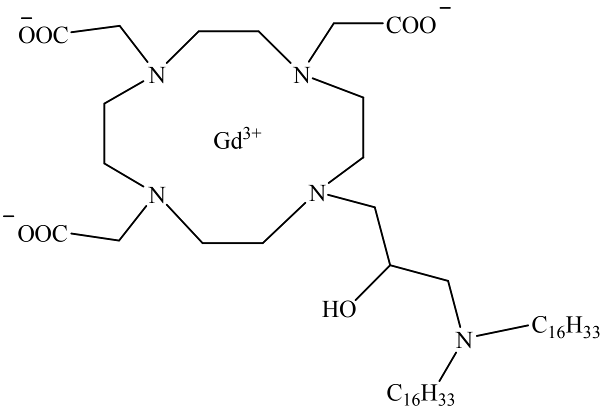

Figure 1.27: Chemical structure of Gd-DOTA based chelate.

At lower pH (3-6) the relaxivity was relatively small (7.9 $mM^{-1}s^{-1}$), at higher pH (8-10) an approximate three fold increase in relaxivity was observed. This increase is attributed to the formation of colloidal aggregates of the deprotonated complex, while no aggregation is suggested at lower pH (i.e. for the protonated or positively charged complex). The presence of the tertiary amino group makes the overall complex pH responsive. Consequently, by modifying the structures of the amphiphilic Gd-chelates they can be made either pH-sensitive or pH-insensitive contrast agents. The pH sensitive contrast agents have potential applications because tumors usually have lower extracellular pH as compared to the normal tissues.

Unfortunately due to poor renal elimination problems associated with the liposomal and micellar contrast agents they could not be approved for clinical use and so researchers turned to dendrimers which are discussed in the next section. So far only small molecule based CAs have been approved for clinical purpose.[26]

1.8.5 Dendritic MRI contrast agents

Dendrimers (discovered in 1980s by Donald Tomalia *et al.*[43]) are repeatedly branched polymeric materials which possess three main parts, (a) core, (b) branches and (c) end groups and usually they have a size in the range 1-10 nm (Figure 1.28).[44]

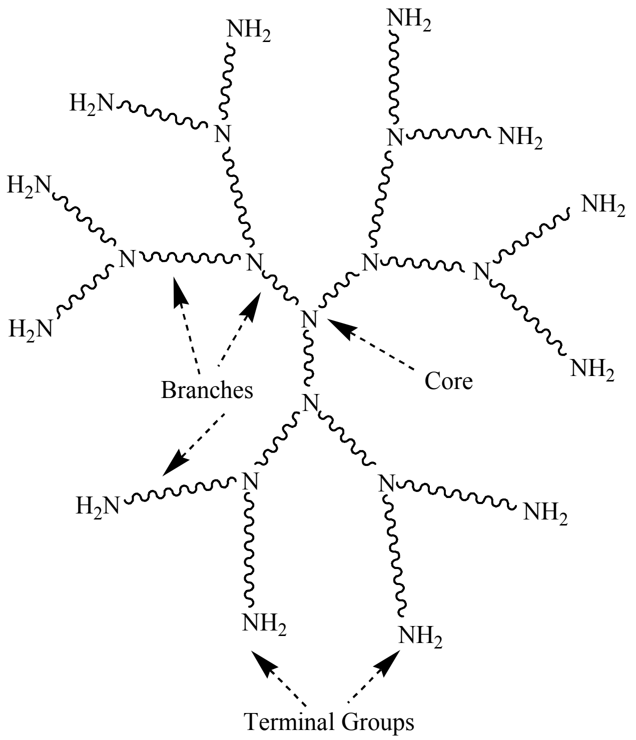

Figure 1.28: Schematic representation of PAMAM (poly(amidoamine)) dendrimer.[44]

Dendrimers are actively used as drug delivery vehicles, in diagnostic studies and tissue engineering etc.[45-46] Due the feasibility of attaching multiple functionalities (for instance, recognition vectors as well as Gd-chelates) to the same dendrimer molecule, dendrimers are promising templates for MRI CAs. As dendritic CAs have paramagnetic chelates at their termini, the water exchange rate will again not be affected. Dendrimers have better efficiency / relaxivity than the liposomes and micelles. Dendrimer relaxivity can be increased by increasing their size, on the other hand the relaxivity of liposomes as well as micelles could not be increased by increasing their size after a certain limit. The first report describing the feasibility of using dendrimers as MRI CAs was published in 1994 by Wiener *et al.*[47] They prepared various generations of dendrimers containing Gd-chelates and described the effect of generation on relaxivity (Figure 1.29).

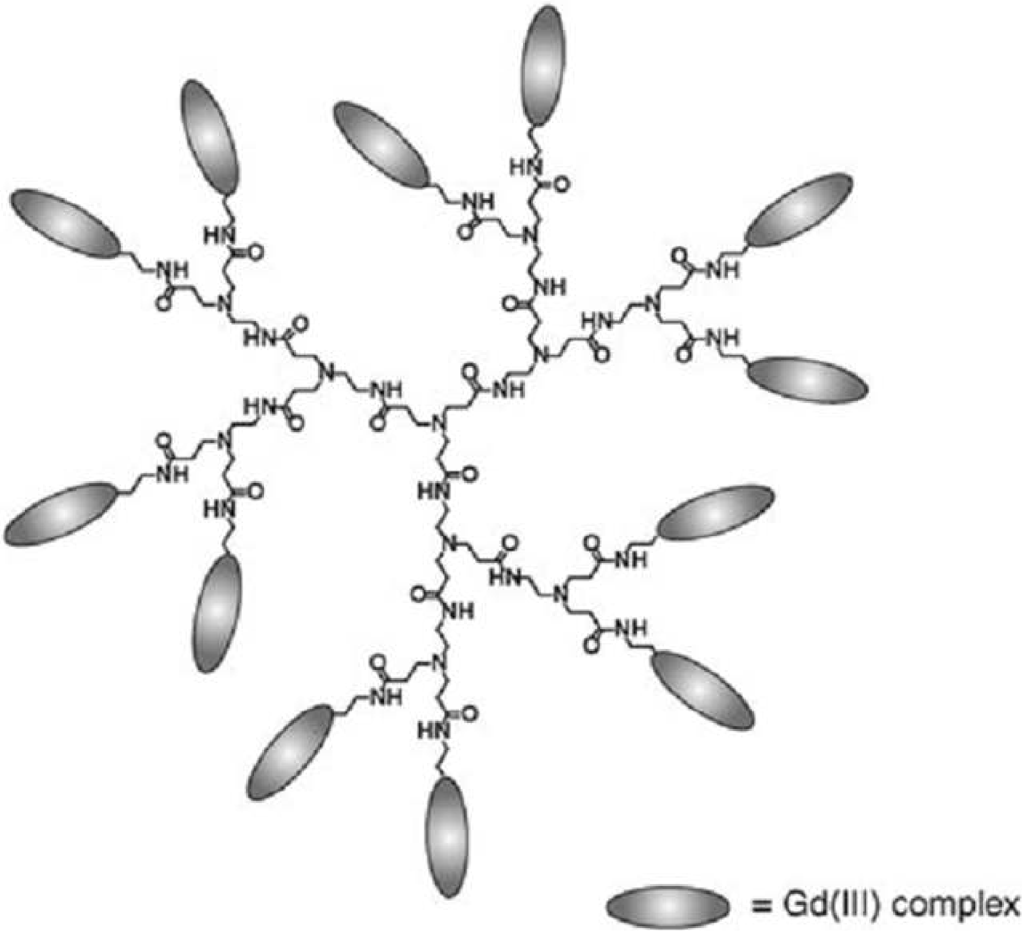

Figure 1.29: PAMAM based MRI contrast agent.

The Gd-DTPA chelates attached to the 6th generation of PAMAM dendrimer (MW: 139 kDa) exhibited about a six fold higher relaxivity than the free Gd-DTPA chelate (0.55 kDa), which is due to restricted tumbling of GD-DTPA chelates at the termini of the dendrimer molecule.[48] The relaxivity measurements of Gd-DTPA chelates attached to flexible polymers with similar MW did not show any increase in relaxivity. There are several other literature reports related to dendrimer based MRI contrast agents.[49-55]

Dendrimer based contrast agents are excellent blood pool agents but their efficiency can be further enhanced by attaching target specific vectors which will enable the contrast agent to accumulate at the target site. Various groups such as polysaccharides[56], oligopeptides[57], proteins[58], antibodies[59] and folic acid[60] can be attached at the periphery of the dendrimers as the recognition units.

There are some future challenges associated with dendrimer based contrast agents and research in this regard is still in progress. For example, the optimal ratio between targeting units and the Gd-chelates at the same dendrimer molecules is very important for efficient output.

Another important class of chemical substances which attracted attention as potential MRI CAs is zeolite and silica based nanomaterials which are discussed in the next section.

1.8.6 Zeolite based contrast agents

Zeolites are microporous aluminosilicates with well defined pores (cavities) and channels which can accommodate a wide variety of cations (such as Na^+, K^+, Mg^{2+}, Ca^{2+} etc). The ability of these materials to easily exchange with other cations[61] led to their applications as ion exchange beds for water purification. Zeolites are also used as food additives as well as in personal care, thus their non-toxicity is already proven and hence they can be used as MRI CA templates.[61-69] Zeolites being microporous in nature, have exceptionally high internal surface area which leads to their high adsorption capacities. The main purpose of selecting zeolites and silica is to increase immobilization of paramagnetic ions by attaching / adsorbing them to the inner side of their cavities / pores. This increase in immobilization will lead to enhanced relaxivity, which might be better than for dendrimer and micelle based contrast agents.[70] For example, Platas-Iglesias and co-workers[64] described the Gd^{3+}-doped zeolite NaY nanoparticles with 80-100 nm diameter as high relaxivity MRI contrast agents. Zeolite NaY is composed of eight sodalite cages which are linked with a large central cavity called a supercage with diameter 0.74 nm (Figure 1.30).

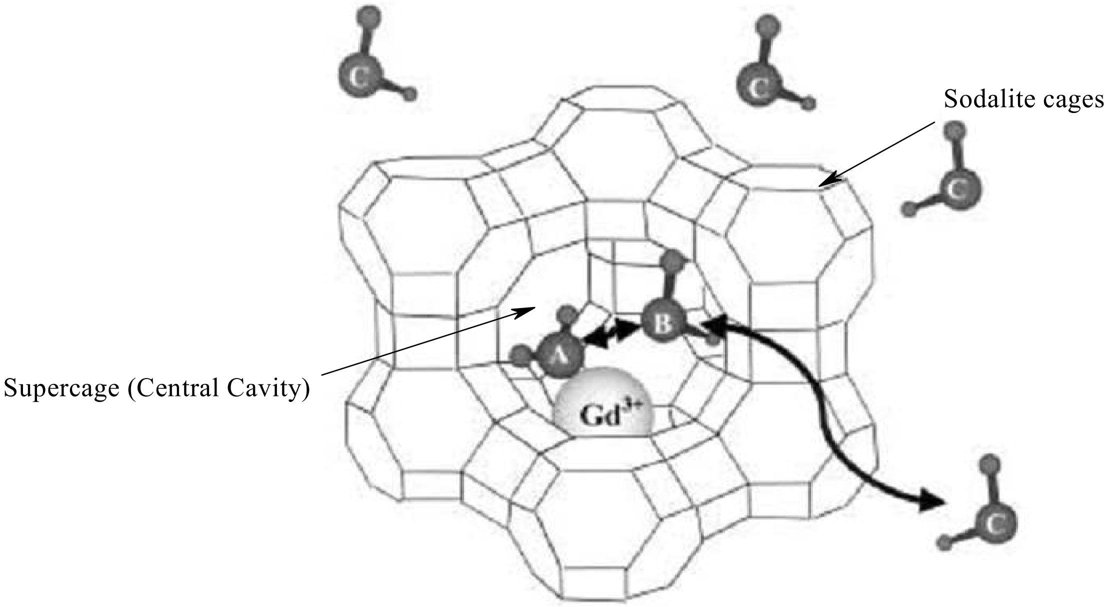

Figure 1.30: Schematic illustration of water exchange between Gd-loaded Zeolites and bulk solvent: "A" represents water coordinated to the Gd, "B" represents an intra-framework water molecule and "C" are bulk water molecules.[64]

Different amounts of Gd^{3+} were incorporated into the central cavity of zeolite NaY and the effect of $[Gd^{3+}]$ on the relaxivity was explored and very interesting observations found. It was reported that relaxivity was decreased with increased Gd^{3+} content. The maximum relaxivity by Gd-doped zeolites was found to be 37.7 $mM^{-1}s^{-1}$ (per Gd ion) for a 1.3 Gd^{3+} Wt% loading which is about nine fold higher than that for the Gd-DTPA (at the same field strength). The increased relaxivity with low Gd^{3+} content was supported by a ca. 25 times longer τ_R for the Gd^{3+} ions which were immobilized in the interior cavity of the zeolite as compared to free Gd^{3+} ions in aqueous. Another important parameter which played a role in the increased relaxivity is the number of Gd^{3+} coordinated water molecules (q). As in the zeolites, the Gd^{3+} ions are immobilized (rather than Gd-chelates), therefore about eight water molecules are expected to coordinate per Gd^{3+} ion. This high number of q, and of course $\tau_{R,}$ are responsible for the higher relaxivity of zeolites based contrast agents. But the decrease in relaxivity with the increased Gd content might be due to several factors. For example, the high Gd content might hinder the water exchange between zeolite central cavity and the surrounding bulk solution. To increase the water exchange rate between the paramagnetic centre and the bulk solution, lanthanides were incorporated into the framework of zeolites rather than into cavities (pores).[67] But still the relaxivity of zeolite based contrast agents was limited by the slow water exchange rate between the paramagnetic centre and the bulk solution. This unexpected behaviour is attributed to the long distance between lanthanide ions in the framework and the water molecules present in the central cavities. Due to this large gap, the magnetic moment propagation between paramagnetic lanthanide ions and the surrounding water protons via water molecules present in the pores of the zeolites was hindered which decreased the relaxivity.

A unique feature of zeolite based contrast agents is the hydration number q. In the zeolites, lanthanide ions (such as Gd^{3+} etc) are incorporated which can have upto eight water molecules, on the other hand in liposomes and micelles Gd-chelates are immobilized which have only one water molecule coordinated to the Gd-chelates.

In general, lanthanide ions (rather than lanthanides chelates) could be immobilized on the interior cavities of the zeolites, but the water exchange rate between the paramagnetic centre and the surrounding bulk water protons via zeolite channels were greatly reduced due to the narrow size of the channels. The reduction in water exchange rate directly affected the relaxivity of lanthanide loaded zeolites. However, this problem can be solved using mesoporous materials (e.g. mesoporous silica) which have relatively wider channel diameters of as discussed in the next section.

1.8.7 Mesoporous silica based contrast agents

Mesoporous silica has pores in the range of 2-50 nm and was first prepared by researchers in Japan in 1990. Due to the relatively large pore size, as compared to zeolites, and several other characteristics like non-toxicity, biocompatibility, surface modification etc, mesoporous silica can be used as MRI contrast agents.[71-74] The relatively large pore size might solve the problem of slow water exchange which was exhibited by zeolite based contrast agents and the immobilization of Gd-chelates on their surface may exhibit better relaxivity than the liposome and dendrimer based contrast agents. Recently, Taylor *et al.*[73] described relaxivity measurements of mesoporous silica based contrast agents. The mesoporous nanospheres (MSNs) particles with diameter ~ 75 nm were prepared and then several Gd-chelates were grafted onto the interior walls (Figure 1.31) of the mesoporous silica nanospheres. The relaxivity (R_1) was found to be 28.8 $mM^{-1}s^{-1}$ which is about seven fold larger than for a commercially available MRI contrast agent (Gd-DTPA). This high value of R_1 can be explained by considering several parameters which optimize the relaxivity of MRI contrast agents. The foremost is the relatively fast water exchange between paramagnetic centre and the surrounding bulk water due to large channels of the mesoporous silica. The second factor is the high τ_R which is due to immobilization of Gd-chelates at the MSNs interior walls. The third factor which also played role in increasing relaxivity of silica based contrast agents is the number of coordinated water molecules q, which was 2 in this Gd-chelate (Figure 1.31).

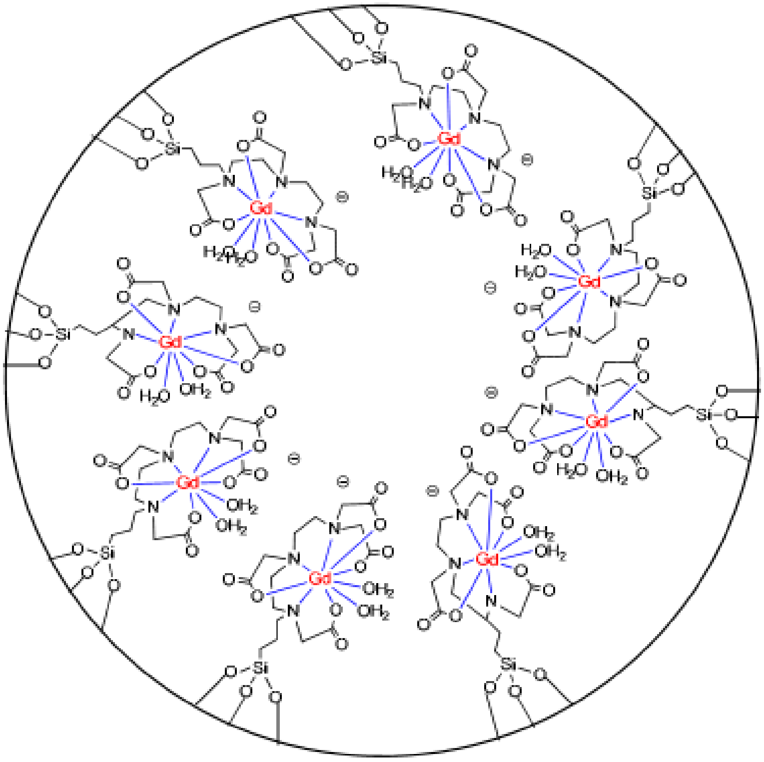

Figure 1.31: Schematic representation of the Gd-chelates grafted onto the interior walls of the mesoporous silica nanoparticles.[73]

These recent observations of zeolite and silica based contrast agents showed that relaxivity / efficiency of contrast agent molecules can be enhanced by immobilizing the Gd^{3+}-chelates on the nanomaterials surface. Metal nanoparticles can also be used as templates for MRI contrast agents because of their several unique features e.g. metal nanoparticles are non-toxic, Gd-chelates can be adsorbed on the surface of the nanoparticles rather than on the interior walls as in zeolites and silica based contrast agents. In addition, various recognition vectors can be attached to Gd-chelates on the surface of metal nanoparticles etc.

1.8.8 Metal nanoparticles based contrast agents in MRI

Metal nanoparticles (or metal colloids) attract much attention due to their unique electronic and optical properties which are highly size dependent. The nanoparticles have large surface to volume ratios and hence the behaviour of surface atoms is different from the atoms inside the nanoparticle. This different behaviour of surface atoms (and hence electrons) is responsible for several unique properties of nanoparticles.[75-76] For example, the optical properties of gold nanoparticles are size dependent. They exhibit a wide range of colours from bright red (smallest particles) to purple and blue (largest particles) depending upon the size of particle. Due to the change in size, the frequency of the oscillating surface electrons is changed which affects the colour of nanoparticle. Interestingly, the colour of the particles not only depends on their size, but also on the shape of the particles and refractive index of the medium. As metal nanoparticles exhibit intense colours, they can be used as pigments for glasses and ceramics.[77-78] They have also many other applications in catalysis, nanoelectronics, medical diagnosis and therapy etc. However, we will limit our discussion to the gold nanoparticle applications in medical diagnosis and therapy, especially as MRI contrast agents.

1.8.9 Gold nanoparticle based MRI contrast agents

Gold nanoparticles (or colloidal gold) have been used in medicine for revitalization and longevity since prehistoric times (i.e. ancient China and India). In Europe they were used as a nerve tonic and as a drug for epilepsy and syphilis.[79-80] In the modern period, gold nanoparticles have a wide range of applications in medical science and in catalysis because of their non-toxic behaviour and good resistance to oxidation. They are easy to synthesize, their size can be tuned easily and a wide range of stabilizing agents can be attached at the gold nanoparticles surface. Gold nanoparticles are the most stable metal nanoparticles.[81] For example, gold nanoparticles modified by gum arabic (GA) were reported[82] as contrast agents for computed tomography (Figure 1.32) after evaluation of their toxicity and stability behaviour.

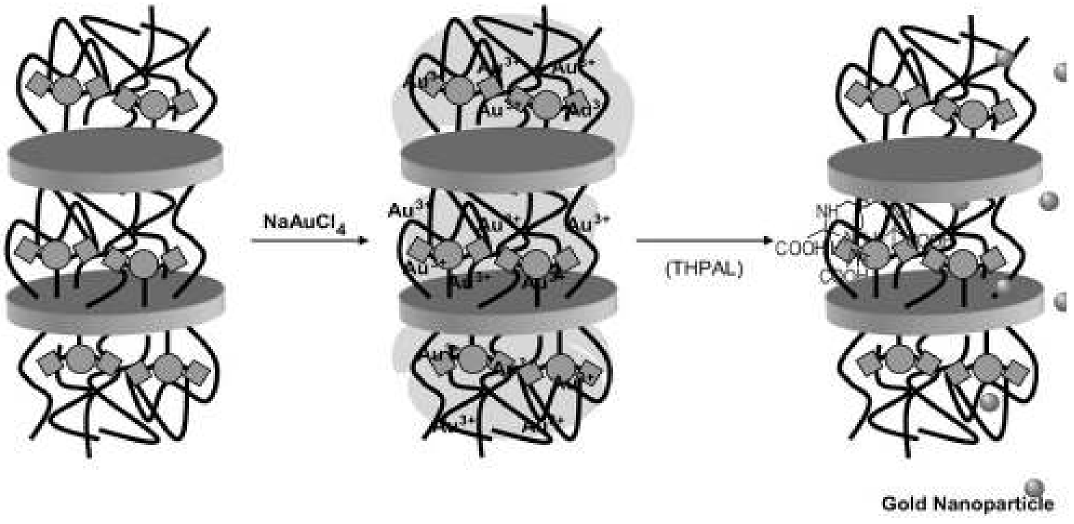

Figure 1.32: Synthesis of gold nanoparticles stabilised by GA.[82]

The contrast enhancement studies showed that gold due to high atomic number (Z) and greater absorption coefficient than iodine can be used as contrast agent in CT imaging. Gold nanoparticles are also reported in cellular imaging studies using light scattering phenomenon,[83] photothermal cellular damage,[84] as DNA carrier for gene therapy[85] etc but we will focus our discussion on the recent reports of gold nanoparticle based MRI contrast agents.

1.8.9.1 Gold nanoparticles protected by multilayered Gd-chelates

In 2006, a group in France (Prof. Roux *et al.*)[86-87] pioneered the design of gold nanoparticles for the purpose of MRI contrast agents. They synthesized dithiolated-DTPA multilayered gold nanoparticles with diameter 2-2.5 nm. These multilayered nanoparticles could accommodate ca. 150 gadolinium ions per nanoparticle (Figure 1.33). The T_1-weighted images and relaxation measurements showed that these gold nanoparticles have better efficiency than the commercially available MRI contrast agent i.e. Gd-DTPA but the enhancement in relaxation was moderate (~30 %). This was attributed to the relatively mobile Gd-chelates at gold nanoparticles surface. Furthermore, the multilayered nanoparticles were not sufficiently stable (i.e. decomposed after one day) at room temperature. Roux *et al.* in their second report[87] regarding Gd-loaded AuNPs explained that the stability of these nanoparticles can be enhanced by decreasing the number of gadolinium ions per particle from 150 to 50.

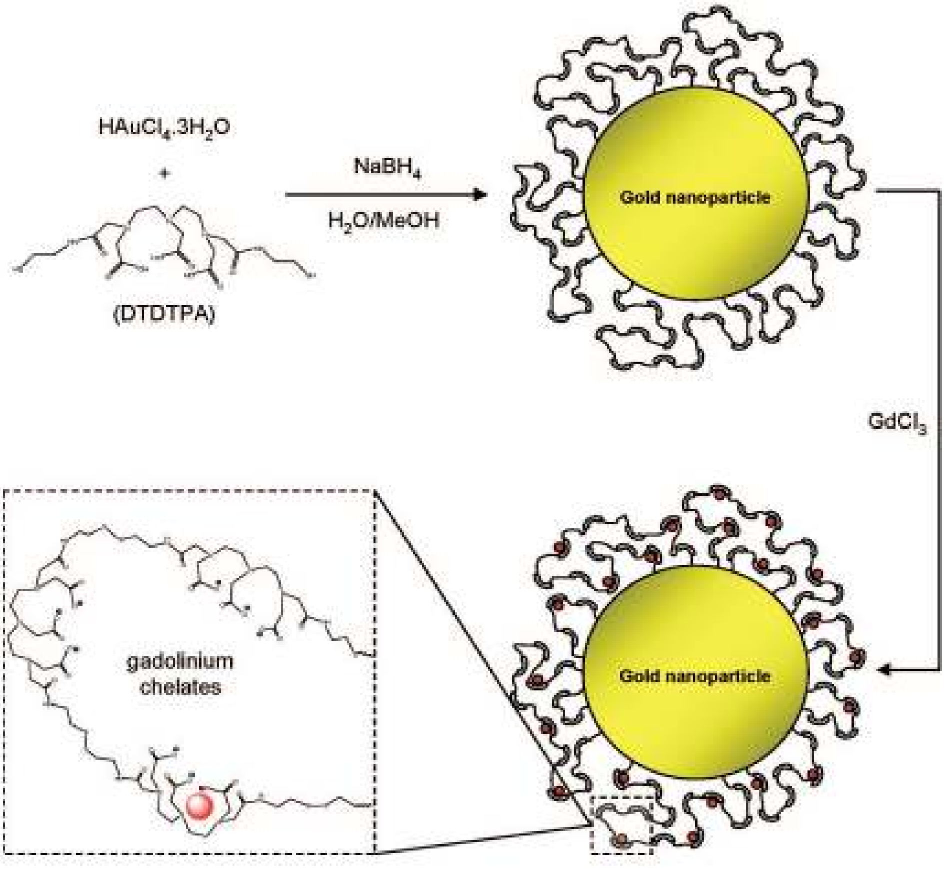

Figure 1.33: Multilayered Gd-loaded AuNPs.[87]

They also used these nanoparticles as contrast agents for X-ray computed tomography studies which showed that very small amount of gold nanoparticles (10 mg / mL) can give contrast equal to relatively large amount of iodine (35 mg / mL).

Park *et al.*[88] reported a similar strategy for gold nanoparticle based MRI contrast agents. They synthesized DTPA conjugated with glutathione protected gold nanoparticles of 5-7 nm in diameter. This report showed quite high number of gadolinium ions (10^4) per nanoparticle, which may be due to formation of multilayers around relatively large nanoparticles as compared to the previous reports of Roux *et al*[86-87]. The relaxivity of these nanoparticles was found to be (17.9 mM^{-1}s^{-1}) five fold higher than for the commercially available MRI contrast agent i.e. Omniscan® (3.30 mM^{-1}s^{-1}). In their recent report[89], they reported bigger (~ 14 nm) gold nanoparticles coated by Gd-DTPA conjugates of cysteine as multimodal (i.e. for X-ray computed and MRI imaging) contrast agents. The cytotoxic studies showed that these nanoparticles are non-toxic and hence are suitable for practical applications. In both reports, multilayers of Gd-chelates (Figure 1.34) were formed at the nanoparticles surface and the stability of these multilayered nanoparticles was not described. In general, the efficiency of these gold nanoparticle based contrast agents can be enhanced by accumulation of the contrast agent at the specific site, which can be achieved by attaching recognition vectors at the surface of gold nanoparticles.

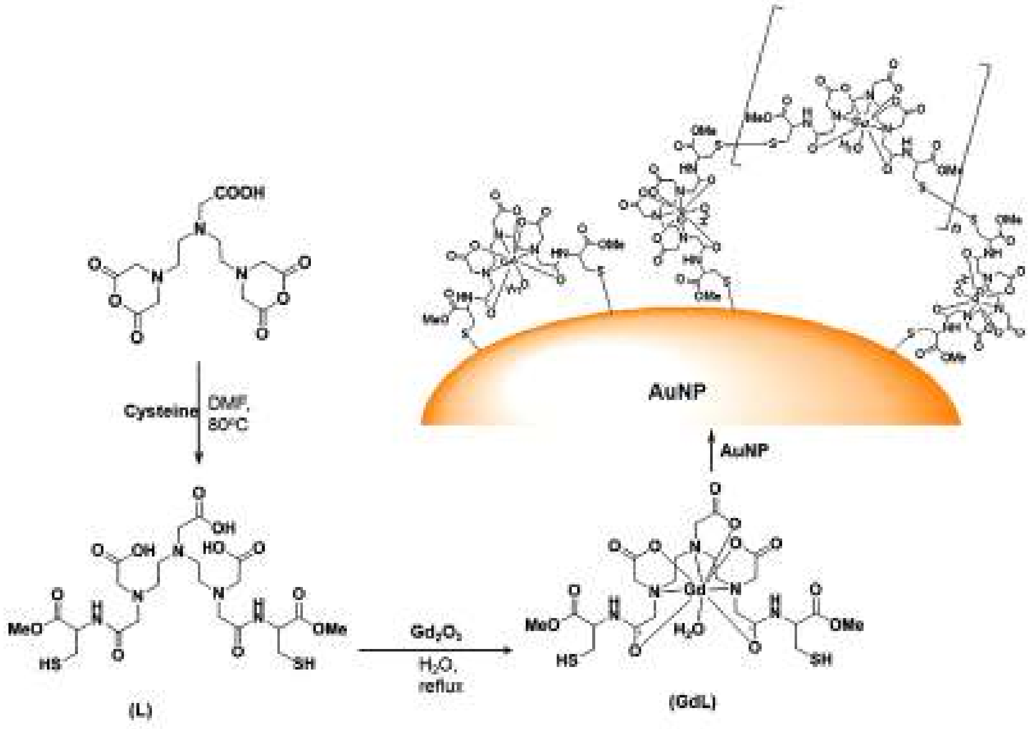

Figure 1.34: Gd-DTPA coated AuNPs.[89]

1.8.9.2 Multifunctional (or target specific) gold nanoparticle based MRI contrast agents

Lim *et al.*[90] reported paramagnetic gold nanostructures as targeted contrast agents for MRI as well as for optical imaging. The cancer targeting antibody (anti-HER2) was reacted with a DTPA based ligand, gadolinium was chelated with DTPA units and finally Gd-chelates modified with the antibody were attached at the gold nanoparticles surface (Figure 1.35). These nanoparticles with Gd and cancer cell targeting units were evaluated for both MRI and optical imaging purpose. The relaxation measurement and the optical imaging studies exhibited better results than commercially available Gd-DTPA chelates. Furthermore, gold nanostructures with cancer targeting antibodies bound to breast cancer cells and due to their absorption in the NIR (near infrared region) by the cancer cells could be destroyed by irradiation. The energy absorbed by gold nanoparticles in the NIR is converted into thermal energy which damaged the cancer cells. These gold nanostructures had diameter of ~60 nm, which might lead to their instability / decomposition. With the increased diameter of the gold nanoparticles, the surface coverage may be incomplete and thus they may have some vacant sites which may lead to aggregation due to interactions with the solvent or/and with other particles.

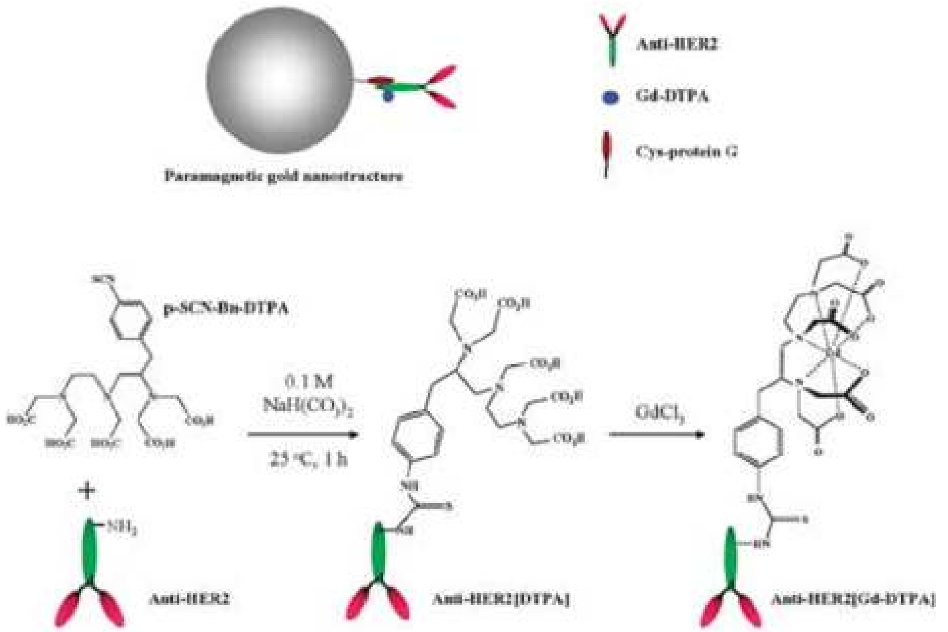

Figure 1.35: Schematic illustration of synthesis of targeted paramagnetic gold nanostructures.[90]

Glyconanoparticles are particles which are protected by carbohydrates. Multifunctional gold nanoparticles (with diameter 2-4 nm) protected by sugar conjugates of β-glucose (*glyc*C_2S and *glyc*C_5S), β-galactcose (*gal*C_5S), and β-lactose (*lac*C_5S) have recently been studied as MRI CAs.[91] Some sugar conjugates have Gd-chelates at their ends while the sugar conjugates without Gd-chelates may serve as recognition vectors. The *in vivo* imaging studies confirmed that *glyc*C_5SAuNPs enhanced the contrast in tumoral zone while the other AuNPs (such as *lac*C_5SAuNPs etc) did not show any affinity for the tumors. The relaxivities of most of these paramagnetic glyconanoparticles was higher than for the corresponding small molecule Gd-chelate. The interesting observation is that the relaxivity of these glyconanoparticles can be tuned by changing the nature of sugar moiety and length of the linker (Figure 1.36).

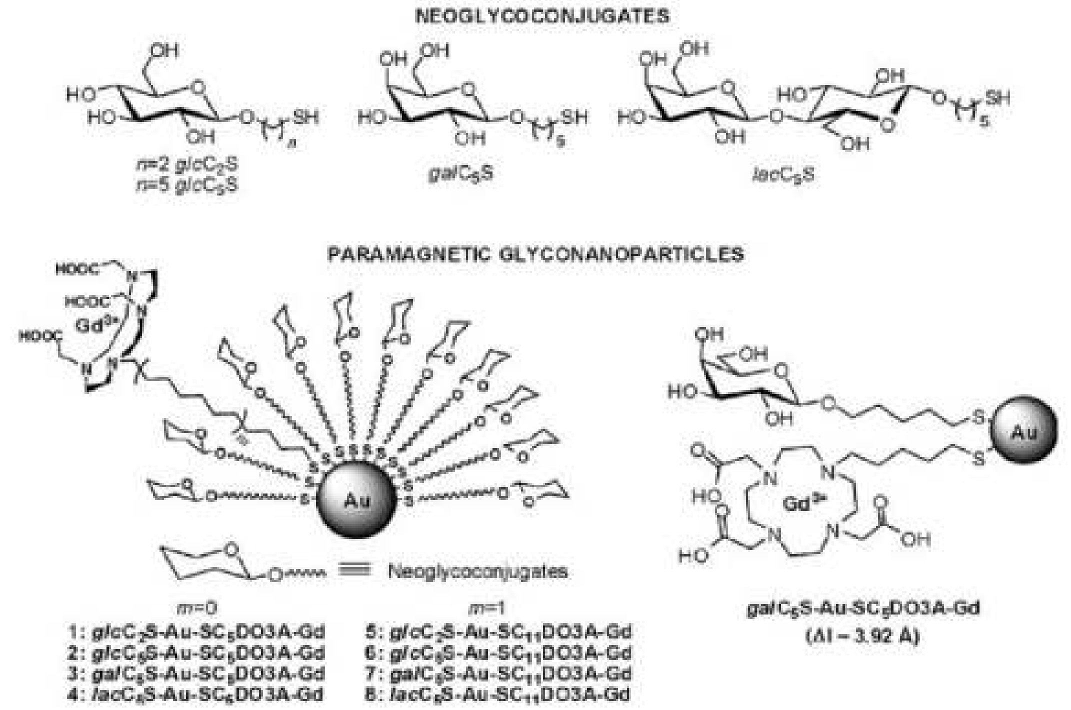

Figure 1.36: Thiol-ending sugar conjugates and the corresponding paramagnetic glyconanoparticles.[91]

It has been found that the gold core of gold nanoparticles can exhibit paramagnetism under certain conditions.[92] This paramagnetism of the gold core may contribute to the overall relaxivity of Gd-chelates attached to the gold nanoparticles surface. In all previous reports on gold nanoparticle based MRI contrast agents[86-88, 90-91], the contribution of this paramagnetism from the gold core to the magnetic moment of Gd^{3+} (and thus to the relaxivity) was not explored. Recently, Moriggi and co-workers[93] reported that gold nanoparticles do not contribute significantly to the magnetic moment of Gd^{3+} ions at the gold nanoparticles surface. They prepared Gd-coated and Ytterbium(Y)-coated gold nanoparticles with diameter ~ 5.0 nm, the magnetic moment (μ_{eff}) of Gd in these Gd-chelated AuNPs was found 7.94BM (which is exactly equal to the magnetic moment of free Gd^{3+}), while no magnetic moment was detected in Y-coated AuNPs. Thus it was proved that in Gd-loaded AuNPs, there is no contribution of gold core paramagnetism to the overall relaxivity of surrounding water protons.

In all reports of gold nanoparticle based contrast agents, it has been found that several gadolinium ions can be loaded per particles and these contrast agents gave better relaxivity (presumably due to relatively slow tumbling of Gd-chelates at nanoparticles surface) and T_1 contrast in MRI images. In many reports[86-89] multilayers of Gd-chelates were formed at nanoparticles surface, which might not favour the stability issues of these nanostructures. Few reports[87, 89] showed the applicability of these gold nanoparticle based contrast agents for X-ray CT imaging because nanoparticles have longer circulation time than iodine, they are non-toxic and various targeting vectors can be attached at the gold nanoparticles surface.

1.9 Aim of the project

Gold nanoparticles as templates for MRI contrast agents were selected due to their highest stability among metal nanoparticles, low toxicity and strong resistance against oxidation. When the projected was started, there were no published reports in the literature regarding gold nanoparticle based contrast agents, hence our main aim was to synthesize and characterize new DTPA ligands which can chelate with gadolinium ions on one end and then can bind to the gold surface on the other end to give us gold nanoparticle based MRI contrast agents. In the very beginning of the project (i.e. in 2006), the first report regarding gold nanoparticles based MRI CAs appeared in the literature.[86] That report dealt with multilayered gold nanoparticles which were highly unstable. We then decided to continue with our aim to synthesize and characterise more stable monolayer protected gold nanoparticles as MRI CAs. Furthermore targeted specific gold nanoparticles based MRI CAs had also not been explored at that time, therefore one direction of our project was to attach some recognition vectors to the Gd-loaded AuNPs and to test their recognition studies. The synthesis of monolayer protected AuNPs with and without recognition vectors and their relaxivity measurements and imaging studies will be discussed in chapter 2.

As the project proceeded, a few more reports[88, 90-91, 93] on gold nanoparticle based MRI CAs were published. The relaxivity measurements of our monolayer Gd-loaded AuNPs were found similar to the recent reports. The relaxivity values of Gd-loaded AuNPs were not found much higher than for small molecule CAs. This relatively low relaxivity of gold nanoparticle based MRI CAs warranted a mechanistic investigation which was lacking in the literature. Therefore, it was decided to explore the main factor responsible for relatively poor relaxivity exhibited by gold nanoparticle based contrast agents which is discussed in chapter 3 of this thesis.

Another important aim of the project was to synthesize and characterise redox sensitive contrast agents for MRI applications. To achieve this goal, nitroxide radical based ligand was used to form monolayer at the surface of gold nanoparticles and then they were characterised and studied for the purpose of redox sensitive MRI CAs and will be discussed in chapter 4.

Apart from applications as MRI contrast agents, the gold nanoparticles were also studied as optical imaging contrast agents after replacing Gd^{3+} with other lanthanides such as Tb^{3+} and Eu^{3+}. The study was finally extended to apply gold nanoparticles as model compounds for heterogeneous systems for distance measurements between paramagnetic radical and metal ions which were attached at the gold nanoparticles surface. The luminescence studies (for the purpose of optical imaging) and some other useful application of lanthanide-loaded nitroxide labelled AuNPs are discussed in chapter 5.

Chapter 6 contains overall conclusions of the project and some possible future directions of the project and chapter 7 describes experimental procedures.

1.10 References

1. P. Caravan, *Chem. Soc. Rev.*, 2006, **35**, 512-523.
2. P. Caravan, *Acc. Chem. Res.*, 2009, **42**, 851-862.
3. P. C. Lauterbur, *Nature*, 1973, **242**, 190-191.
4. R. B. Lauffer, *Chem. Rev.*, 1987, **87**, 901-927.
5. M. Bottrill, L. Kwok and N. J. Long, *Chem. Soc. Rev.*, 2006, **35**, 557-571.
6. C. Westbrook, C. K. Roth and J. Talbot, *MRI in Practice, Blackwell Publishing*, 2006, **3**, Ch. 1.
7. T. D. W. Claridge, *High-Resolution NMR Techniques in Organic Chemistry, Elsevier*, 1999, **19**, Ch. 2.
8. R. S. Macomber, *A complete Introduction to Modern NMR Spectroscopy, Jhon Wiley & Sons*, 1998, Ch.1.
9. J. Keeler, *Understanding NMR Spectroscopy, Wiley*, 2002, Ch. 8.
10. H. Friebolin, *Basic One and Two Dimensional NMR spectroscopy, VCH* 1990, **2**, Ch. 1.
11. I. L. Pykett, B. R. Rosen, F. S. Buonanno and T. J. Brady, *Phys. Med. Biol.*, 1983, **28**, 723-729.
12. M. A. Brown and R. C. Semelka, *MRI Basic Principles and Applications, Jhon Wiley and Sons* 2003, Ch. 4.
13. D. Weishaupt, V. D. Kochli and B. Marincek, *How Does MRI Work?, Springer*, 2006, **2**, Ch. 4.
14. V. Kuperman, *Magnetic Resonance Imaging, Academic Press*, 2000, Ch. 3.
15. C. Westbrook, C. K. Roth and J. Talbot, *MRI in Practice, Blackwell Publishing*, 2005, **3**, Ch. 2.

16. L. Brateman, *Am. J. Roentgenol.*, 1986, **146**, 971-980.

17. F. Bloch, W. W. Hansen and M. Packard, *Phys. Rev.*, 1946, **70**, 474-485

18. P. C. Lauterbur, M. H. Mendoca-Dias and A. M. Rudin, *Frontiers of Biological Energtics, Academic Press, New York*, 1978, p. 752.

19. N. Bloembereg, E. M. Purcell and R. V. Pound, *Phys. Rev.*, 1948, **73**, 678-693.

20. I. Solomon, *Phys. Rev.*, 1955, **99**, 559-565.

21. R. E. Connick and D. Fiat, *J. Chem. Phys.*, 1966, **44**, 4103-4107.

22. R. G. Egdell, M. H. Palmer and R. H. Findlay, *Inorg. Chem.*, 1980, **19**, 1314-1319.

23. V. M. Runge, J. A. Clanton, C. M. Lukehart, C. L. Partain and A. E. James, *Am. J. Roentgenol.*, 1983, **141**, 1209-1215.

24. A. Bianchi, L. Calabi, F. Corana, S. Fontana, P. Losi, A. Maiocchi, L. Paleari and B. Valtancoli, *Coord. Chem. Rev.*, 2000, **204**, 309-393.

25. A. J. L. Villaraza, A. Bumb and M. W. Brechbiel, *Chem. Rev.*, 2010, **110**, 2921-2959.

26. S. Langereis, A. Dirksen, T. M. Hackeng, M. H. P. v. Genderen and E. W. Meijer, *New J. Chem.*, 2007, **31**, 1152-1160.

27. A. E. Merbach and E. Toth, *The Chemistry of Contrast Agents in Medical Magnetic Resonance Imaging, Jhon Wiley & Sons*, 2001, Ch. 10.

28. C. Boyer, M. R. Whittaker, V. Bulmus, J. Liu and P. T. Davis, *NPG Asia Mater*, 2010, **2**, 23-30.

29. P. Caravan, A. V. Astashkin and A. M. Raitsimring, *Inorg. Chem.*, 2003, **42**, 3972-3974.

30. D. Waysbort and G. Navon, *J. Chem. Phys.*, 1978, **68**, 3074-3077.

31. S. F. Oppenheim, G. R. Buettner and V. G. J. Rodgers, *J. Membrane Sci.*, 1996, **118**, 133-139.

32. S. Langereis, Q. G. de Lussanet, M. H. P. van Genderen, W. H. Backes and E. W. Meijer, *Macromolecules*, 2004, **37**, 3084-3091.

33. S. Aime, D. D. Castelli, S. G. Crich, E. Gianolio and E. Terreno, *Acc. Chem. Res.*, 2009, **42**, 822-831.

34. M. Brinkley, *Bioconjugate Chem.*, 1992, **3**, 2-13.

35. P. Caravan, J. J. Ellison, T. J. McMurry and R. B. Lauffer, *Chem. Rev.*, 1999, **99**, 2293-2352.

36. A. D. Bangham, M. M. Standish and J. C. Watkins, *J. Mol. Biol.*, 1965, **13**, 238-252.

37. J. C. Gore, H. D. Sostman and V. J. Caride, *J Microencapsul*, 1986, **3**, 251-264.

38. V. P. Torchilin, *Mol. Med. Today*, 1996, **2**, 242-249.

39. S. L. Fossheim, A. K. Fahlvik, J. Klaveness and R. N. Muller, *Magn. Reson. Imaging*, 1999, **17**, 83-89.

40. V. P. Torchilin, *Cell. Mol. Life Sci.*, 2004, **61**, 2549-2559.

41. W. J. M. Mulder, G. J. Strijkers, G. A. F. v. Tilborg, A. W. Griffioen and K. Nicolay, *NMR Biomed.*, 2006, **19**, 142-164.

42. A. Accardo, D. Tesauro, P. Roscigno, E. Gianolio, L. Paduano, G. D'Errico, C. Pedone and G. Morelli, *J. Am. Chem. Soc.*, 2004, **126**, 3097-3107.

43. D. A. Tomalia, H. Baker, J. Dewald, M. Hall, G. Kallos, S. Martin, J. Roeck, J. Ryder and P. Smith, *Polym. J.*, 1985, **17**, 117-132.

44. F. Zeng and S. C. Zimmerman, *Chem. Rev.*, 1997, **97**, 1681-1712.

45. M. Fischer and F. Vögtle, *Angew. Chem. Int. Ed.*, 1999, **38**, 884-905.

46. S. Hecht and J. M. J. Fréchet, *Angew. Chem. Int. Ed.*, 2001, **40**, 74-91.

47. E. Wiener, M. W. Brechbiel, H. Brothers, R. L. Magin, O. A. Gansow, D. A. Tomalia and P. C. Lauterbur, *Magn.Reson.Med.*, 1994, **31**, 1-8.

48. E. C. Wiener, F. P. Auteri, J. W. Chen, M. W. Brechbiel, O. A. Gansow, D. S. Schneider, R. L. Belford, R. B. Clarkson and P. C. Lauterbur, *J. Am. Chem. Soc.*, 1996, **118**, 7774-7782.

49. G. M. Nicolle, É. Tóth, H. Schmitt-Willich, B. Radüchel and A. E. Merbach, *Chem. Eur. J.*, 2002, **8**, 1040-1048.

50. M. Kawa and T. Takahagi, *J. Polym. Sci. Pt. B-Polym. Phys.*, 2004, **42**, 2680-2689.

51. V. C. Pierre, M. Botta and K. N. Raymond, *J. Am. Chem. Soc.*, 2004, **127**, 504-505.

52. D. A. Fulton, M. O'Halloran, D. Parker, K. Senanayake, M. Botta and S. Aime, *Chem. Comm.*, 2005, 474-476.

53. H. Kobayashi and M. W. Brechbiel, *Adv. Drug Delivery Rev.*, 2005, **57**, 2271-2286.

54. S. D. Swanson, J. F. Kukowska-Latallo, A. K. Patri, C. Y. Chen, S. Ge, Z. Y. Cao, A. Kotlyar, A. T. East and J. R. Baker, *Int. J. Nanomed.*, 2008, **3**, 201-210.

55. K. Nwe, L. H. Bryant and M. W. Brechbiel, *Bioconjugate Chem.*, 2010, **21**, 1014-1017.

56. M. L. Wolfenden and M. J. Cloninger, *J. Am. Chem. Soc.*, 2005, **127**, 12168-12169.

57. I. v. Baal, H. Malda, S. A. Synowsky, J. L. J. v. Dongen, T. M. Hackeng, M. Merkx and E. W. Meijer, *Angew. Chem. Int. Ed.*, 2005, **44**, 5052-5057.

58. R. Kluger and J. Zhang, *J. Am. Chem. Soc.*, 2003, **125**, 6070-6071.

59. C. Wu, M. W. Brechbiel, R. W. Kozak and O. A. Gansow, *Bioorg. Med. Chem. Lett.*, 1994, **4**, 449-454.

60. S. D. Konda, M. Aref, M. Brechbiel and E. C. Wiener, *Invest. Radiol.*, 2000, **35**, 50-57.

61. I. Bresinska and K. J. Balkus, Jr., *J. Phys. Chem.*, 1994, **98**, 12989-12994.

62. S. W. Young, F. Qing, D. Rubin, K. J. Balkus, J. S. Engel, J. Lang, W. C. Dow, J. D. Mutch and R. A. Miller, *JMRI-J. Magn. Reson. Imaging*, 1995, **5**, 499-508.

63. K. J. Balkus and J. M. Shi, *Microporous Mater.*, 1997, **11**, 325-333.

64. C. Platas-Iglesias, L. Vander Elst, W. Z. Zhou, R. N. Muller, C. Geraldes, T. Maschmeyer and J. A. Peters, *Chemistry-a European Journal*, 2002, **8**, 5121-5131.

65. E. Csajbok, I. Banyai, L. Vander Elst, R. N. Muller, W. Z. Zhou and J. A. Peters, *Chemistry-a European Journal*, 2005, **11**, 4799-4807.

66. R. N. Muller, L. Vander Elst, A. Roch, J. A. Peters, E. Csajbok, P. Gillis and Y. Gossuin, in *Advances in Inorganic Chemistry - Including Bioinorganic Studies, Vol 57*, Elsevier Academic Press Inc, San Diego, 2005, vol. 57, pp. 239-292.

67. G. A. Pereira, D. Ananias, J. Rocha, V. S. Amaral, R. N. Muller, L. V. Elst, E. Toth, J. A. Peters and C. Geraldes, *J. Mater. Chem.*, 2005, **15**, 3832-3837.

68. M. Norek, I. C. Neves and J. A. Peters, *Inorg. Chem.*, 2007, **46**, 6190-6196.

69. G. A. Pereira, M. Norek, J. A. Peters, D. Ananias, J. Rocha and C. Geraldes, *Dalton Trans.*, 2008, 2241-2247.

70. J. A. Thomas and B. Ballantyne, *J. Am. Coll. Toxicol.*, 1992, **11**, 259.

71. J. K. Hsiao, C. P. Tsai, T. H. Chung, Y. Hung, M. Yao, H. M. Liu, C. Y. Mou, C. S. Yang, Y. C. Chen and D. M. Huang, *Small*, 2008, **4**, 1445-1452.

72. C.-P. Tsai, Y. Hung, Y.-H. Chou, D.-M. Huang, J.-K. Hsiao, C. Chang, Y.-C. Chen and C.-Y. Mou, *Small*, 2008, **4**, 186-191.

73. K. M. L. Taylor, J. S. Kim, W. J. Rieter, H. An, W. Lin and W. Lin, *J. Am. Chem. Soc.*, 2008, **130**, 2154-2155.

74. B. G. Trewyn, J. A. Nieweg, Y. Zhao and V. S. Y. Lin, *Chem. Eng. J.*, 2008, **137**, 23-29.

75. P. D. C. Burda, *J. Am. Chem. Soc.*, 2009, **131**, 6642-6642.

76. Dmitrii F. Perepichka and F. Rosei, *Angew. Chem. Int. Ed.*, 2007, **46**, 6006-6008.

77. G. Schmid, *Clusters and Colloids: From Theory to Applications, Wiley-VCH*, 1994, Ch. 2.

78. P. Mulvaney, *Langmuir*, 1996, **12**, 788-800.

79. S. Mahdihassan, *Am. J. Chin. Med.*, 1985, **13**, 93-108.

80. D. G. Richards, D. L. McMillin, E. A. Mein and C. D. Nelson, *Int. J. Neurosci.*, 2002, **112**, 31-53.

81. M.-C. Daniel and D. Astruc, *Chem. Rev.*, 2003, **104**, 293-346.

82. V. Kattumuri, K. Katti, S. Bhaskaran, Evan J. Boote, Stan W. Casteel, Genevieve M. Fent, David J. Robertson, M. Chandrasekhar, R. Kannan and Kattesh V. Katti, *Small*, 2007, **3**, 333-341.

83. I. H. El-Sayed, X. H. Huang and M. A. El-Sayed, *Nano Lett.*, 2005, **5**, 829-834.

84. I. H. El-Sayed, X. H. Huang and M. A. El-Sayed, *Cancer Lett.*, 2006, **239**, 129-135.

85. M. Ohsaki, T. Okuda, A. Wada, T. Hirayama, T. Niidome and H. Aoyagi, *Bioconjugate Chem.*, 2002, **13**, 510-517.

86. P.-J. Debouttière, S. Roux, F. Vocanson, C. Billotey, O. Beuf, A. Favre-Réguillon, Y. Lin, S. Pellet-Rostaing, R. Lamartine, P. Perriat and O. Tillement, *Adv. Funct. Mater.*, 2006, **16**, 2330-2339.

87. C. Alric, J. Taleb, G. L. Duc, C. Mandon, C. Billotey, A. L. Meur-Herland, T. Brochard, F. Vocanson, M. Janier, P. Perriat, S. Roux and O. Tillement, *J. Am. Chem. Soc.*, 2008, **130**, 5908-5915.

88. J.-A. Park, P. A. N. Reddy, H.-K. Kim, I.-S. Kim, G.-C. Kim, Y. Chang and T.-J. Kim, *Bioorg. Med. Chem. Lett.*, 2008, **18**, 6135-6137.

89. J.-A. Park, H.-K. Kim, J.-H. Kim, S.-W. Jeong, J.-C. Jung, G.-H. Lee, J. Lee, Y. Chang and T.-J. Kim, *Bioorg. Med. Chem. Lett.*, 2010, **20**, 2287-2291.

90. Y. T. Lim, M. Y. Cho, B. S. Choi, J. M. Lee and B. H. Chung, *Chem. Comm.*, 2008, 4930-4932.

91. M. Marradi, D. Alcantara, J. M. d. l. Fuente, M. L. Garcia-Martin, S. Cerdan and S. Penades, *Chem. Comm.*, 2009, 3922-3924.

92. I. Carmeli, G. Leitus, R. Naaman, S. Reich and Z. Vager, *J. Chem. Phys.*, 2003, **118**, 10372-10375.

93. L. c. Moriggi, C. Cannizzo, E. Dumas, C. d. R. Mayer, A. Ulianov and L. Helm, *J. Am. Chem. Soc.*, 2009, **131**, 10828-10829.

Chapter 2: Synthesis and relaxivity measurements of Gd-loaded gold nanoparticles

Part of the work described in this chapter is published in:

M. F. Warsi, R. W. Adams, S.B. Duckett and V. Chechik, *Chem. Comm.,* 2010, **46** , 451-453.

Chapter 2: Synthesis and relaxivity measurements of Gd-loaded gold nanoparticles

2.1 Introduction

Gadolinium (Gd^{3+}), a highly paramagnetic hard acid needs to be reacted with hard ligands to yield a stable chelate, to be utilised as an MRI contrast agent. Lanthanides form strong complexes with carboxylate ligands due to the hard nature of the carboxylic acid groups.[1] Polyaminopolycarboxylic acids are thus an important class of chelating ligands which are often used to bind lanthanides (such as Gd^{3+}, Eu^{3+} etc) as well as cations of radionuclides e.g. ^{90}Y (III), ^{212}Bi(III) etc. For example, diethylenetriaminepentaacetic acid (DTPA) is an octadentate chelating ligand (Figure 2.1) which forms very stable complexes with metals. The X-ray crystallography of DTPA complexes with metals e.g. Gd-DTPA, show that eight out of the nine coordination sites of Gd^{3+} are occupied by DTPA i.e. three by N atoms and five by COO^- groups. The remaining ninth site is occupied by a water molecule which plays a crucial role in ensuring high relaxivity of Gd-DTPA complexes.[2]

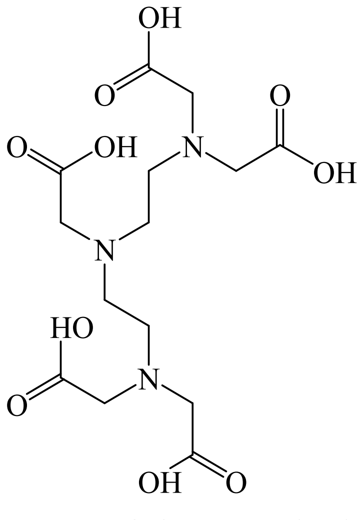

Figure 2.1: Chemical structure of diethylenetriaminepentaacetic acid (H_5DTPA).

Other polyaminopolycarboxylates (as mentioned in chapter 1, section 1.5) can also be used to chelate Gd^{3+}. For instance, ethylenediaminetetraacetic acid (EDTA) is a commercially available hexadentate chelate; in its Gd-EDTA complex, three water molecules are directly bonded to the Gd^{3+} to make it an excellent MRI contrast agent. Due to poor in vivo stability (log K = 17.35) as compared to Gd-DTPA (log K = 22.55), Gd-EDTA have not been subject to significant investigation.[3] Some decadentate polyaminopolycarboxylic acid based chelates are also found in the literature.[4] Despite very strong affinity for metals, however, these lanthanide chelates have no water molecule in the first coordination sphere which makes them unsuitable for applications as MRI contrast agents.

From all the different types of the polyaminopolycarboxylic acid based chelates, DTPA thus attracted the most attention in the field of MRI contrast agents. Therefore in this study we selected DTPA as a primary unit for the preparation of Gd-loaded gold nanoparticles. In order to make the DTPA based ligand attach / adsorb onto a gold nanoparticle surfaces it needs to be functionalised with a disulfide group. The functionalisation of a DTPA based ligand with a thiol or disulfide group can be achieved by selecting a commercially available amino acid i.e. N-ε-CBZ-L-Lysine t-butyl.HCl and dithiobutyric acid as primary building blocks to make a ligand having DTPA units and a disulfide group (Figure 2.2).

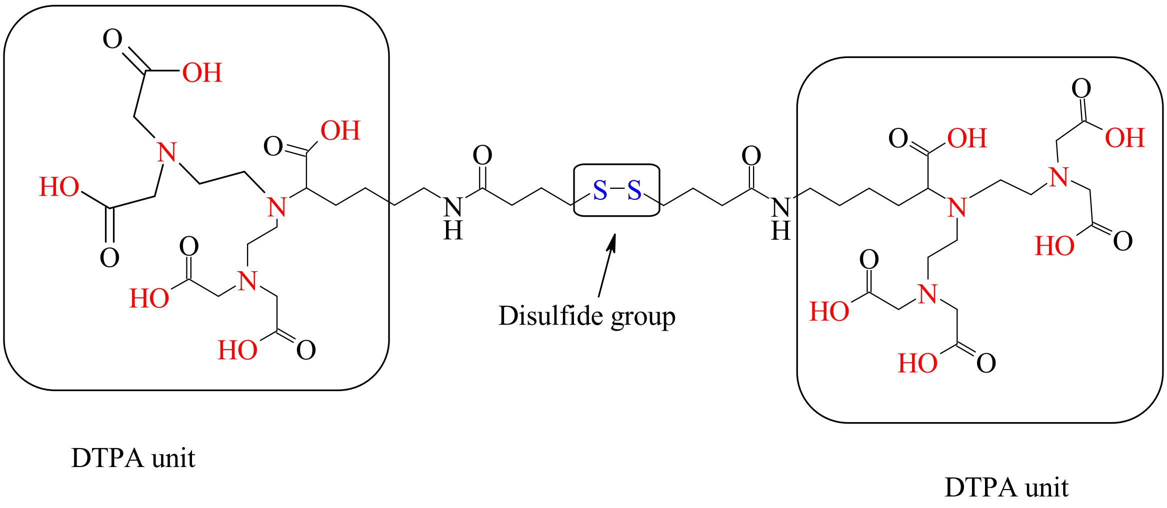

Figure 2.2: Chemical structure of DTPA based ligand 6.

The chain length of the DTPA ligand was relatively long which can give extra stability to the gold nanoparticles as compared to those protected by relatively short chain ligands. The synthesis of ligand **6** is discussed in the following sections.

2.2 Synthesis of DTPA based ligand 6

The synthetic strategy for DTPA ligand **6** is depicted in Scheme **1**. In the first step, dialkylation of ethanolamine with an ester protected bromoacetate yielded compound **1**. The hydroxyl group was then converted into bromide to give compound **2**. The second dialkylation of commercially available N-ε-Cbz-L-Lysine t-butyl ester with bromide **2** produced pentaester protected DTPA analogue. The Cbz (benzoylcarboxy) protection was selected as it is orthogonal to the t-Butyl protection therefore it can be removed easily by catalytic hydrogenolysis to give pentaester protected DTPA analogue **4**. The amino group of the DTPA analogue **4** was then coupled with dithiobutyric acid to give the t-butyl ester protected DTPA ligand **5**. Dithiobutyric acid was selected to avoid extra steps of protection and deprotection of thiol groups. In the last step, the deprotection of t-butyl ester groups gave the target DTPA ligand **6**.

Scheme 1: Synthesis of DTPA based ligand 6

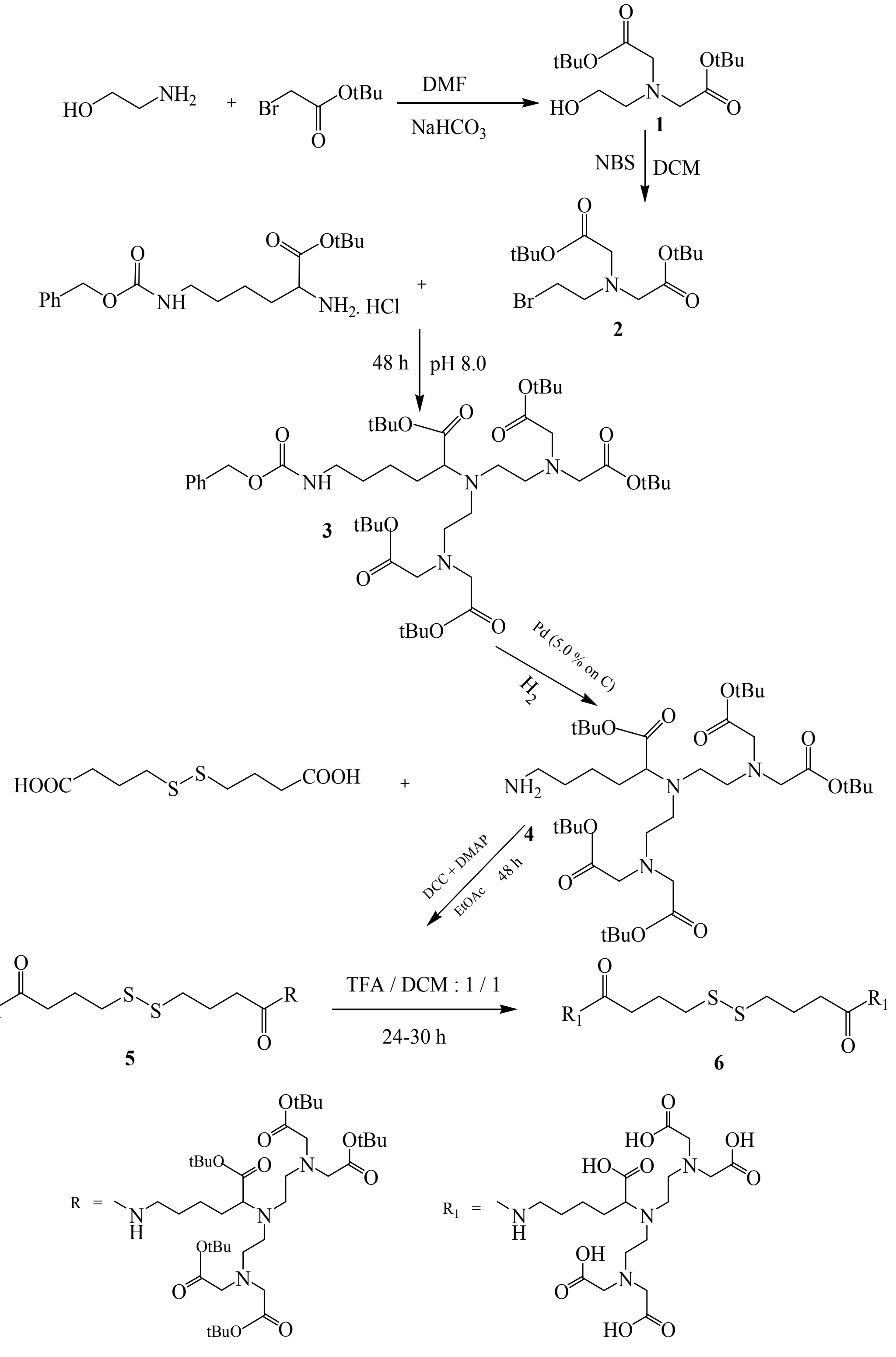

2.2.1 Synthesis of t-butyl ester protected DTPA analogue 3

Compounds **1** and **2** were prepared and purified by following the literature procedure[5] without any significant difference in yield.

Compound **3** was synthesized following the literature[6] procedure. However, the amphiphilic nature of compound **3** created some difficulties in its purification. When the literature procedure was followed and the crude reaction product was dissolved in DCM, washed with water and dried by anhydrous sodium sulphate, ~78 % material was lost. Silica gel flash chromatography led to 92 % loss of product. To trace the lost material, the workup process was analyzed carefully. Compound **3** could be lost during extraction from the aqueous phase. TLC and MS data showed that extracting the crude material from aqueous phase with DCM did not give any target material. NMR and TLC helped to trace the product losses to the drying agent. The product was found to adsorb strongly to anhydrous sodium sulphate. The second problem was traced to silica gel flash chromatography as even after elution with very polar solvents (ethyl acetate and MeOH) no product was collected from the column. But when the same purification was repeated using silica gel of better quality (BDH), NMR, MS and TLC confirmed the successful purification of compound **3** with good yield. The particle size in both grades of silica gel was the same but the differences in the specific pore volume / surface area and defect density might be responsible for irreversible adsorption of ligand by a poorer grade silica gel.[7]

2.2.2 Deprotection of DTPA analogue 3

Hydrogenolysis of the t-butyl ester protected DTPA analogue **3** was carried out by following the literature procedure[6] to get compound **4**. In the literature[6], the flash chromatographic purification of compound **4** was described using pure MeOH as eluent. Compound **4**, i.e. DTPA based primary amine, is basic and therefore could adsorb on acidic sites of silica gel during flash chromatography. Indeed, a TLC of crude product **4** in pure MeOH showed a long tail. However, well separated spots of starting material and product were observed with slightly basic MeOH (i.e. with a few drops of Et_3N). Therefore, compound **4** was purified using slightly basic MeOH. The yield (72%) was higher than in the literature (60%).

2.2.3 Coupling of t-butyl ester protected DTPA analogue 4 with dithiobutyric acid

Compound **5** (t-butyl ester protected DTPA based ligand) was synthesized using a standard coupling procedure.[8] The conversion of the carboxylic acid group into a reactive acylating agent was achieved by using a coupling agent, dicyclohexylcarbodiimide (DCC).[9]

The intermediate O-acyl urea that is formed during peptide coupling can undergo rearrangement to form an N-acyl urea which is not reactive. The solution to this problem is to use a nucleophilic catalyst alongside DCC. The commonly used additives are 1-hydroxybenzotriazole (HOBt) and dimethylaminopyridine (DMAP)[10]. We used DMAP due to its strong nucleophilicity. Compound **5** is a new compound and it was characterized by MS and NMR. NMR peak assignments were facilitated by using "SpecSurf" NMR prediction software that is available via the chemistry database service at www.cds.dl.ac.uk.

2.2.4 Deprotection of t-butyl ester groups of DTPA based ligand 5

The t-butyl ester groups of compound **5** need to be removed in order to make the ligand to chelate with Gd^{3+} ions. The deprotection also made the ligand water soluble.

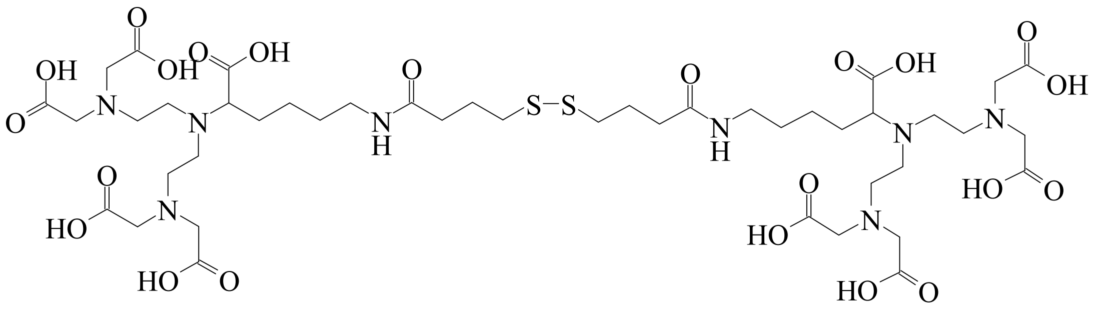

Figure 2.3: DTPA based ligand 6.

The standard[11,12] procedure for the deprotection of the t-butyl ester group includes treatment of the desired reactant with a mixture of trifluoroacetic acid and dichloromethane. We used a 1 / 1 ratio of TFA / DCM for the deprotection of the t-butyl ester groups of DTPA based ligand **5**. The main factor that we had to optimise for the complete deprotection was the reaction time. The reaction was monitored by taking ^{1}H NMR spectra at regular time intervals; the 24-30 h period was optimised for complete deprotection that gave us more than 70 % yield. After the deprotection reaction, the crude product was quite soluble in water, which confirmed the successful deprotection.

Compound **6** was purified by dialysing against deionised water using 500 MWCO dialysis tubing. Purified compound **6** was characterized by MS and NMR spectroscopy.

The ^{1}H NMR spectra of compound **6** showed broadened peaks. This may be due to the restricted tumbling of the large molecule (RMM 1130). The assigned ^{1}H NMR spectrum of compound **6** is shown in Figure 2.4. The complete deprotection is indicated by complete absence of a t-butyl ester peak at 1.40 ppm. The ^{1}H NMR spectrum of compound **6** (Figure 2.4) will be referred to in the next section (2.3.2).

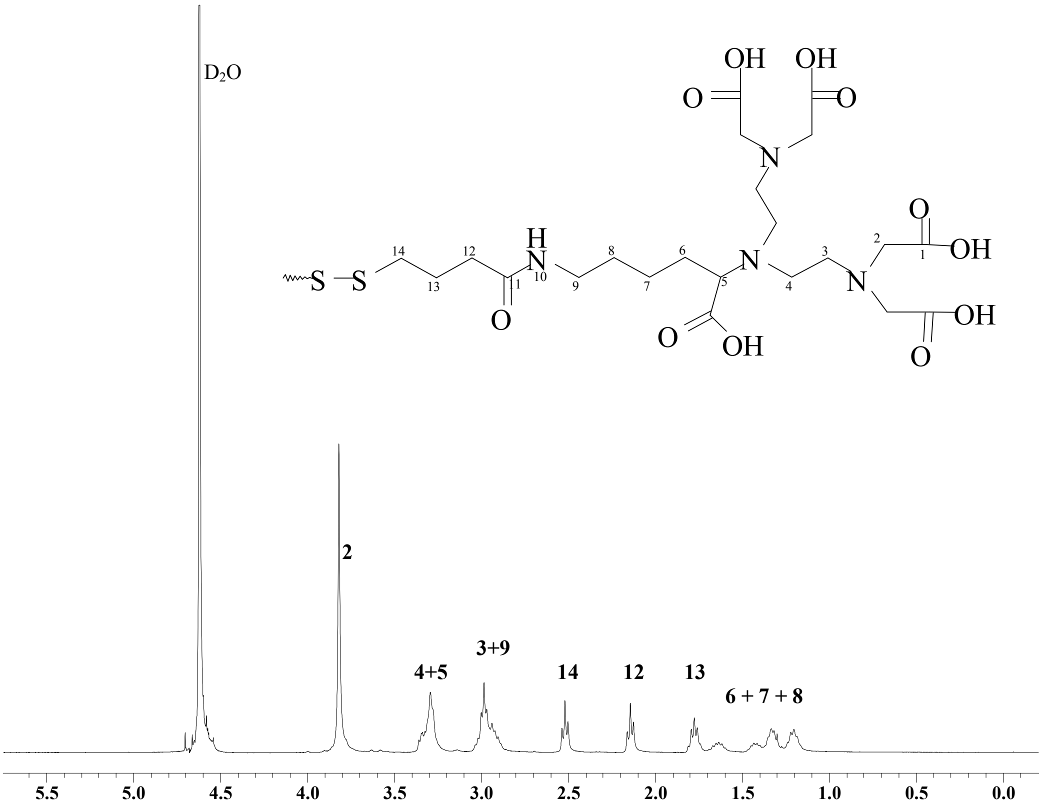

Figure 2.4: ^{1}H NMR spectrum of DTPA ligand 6.

2.3 Synthesis of water soluble AuNPs protected by DTPA based ligand 6

Water soluble gold nanoparticles (AuNPs) protected by DTPA based ligand **6** were prepared by modification of the Brust *et al.* protocol[13] which involves the reduction of metals in the presence of a stabilising agent. Brust's protocol is a biphasic method in which gold ions are transferred from the aqueous phase to the organic phase with tetraoctylammonium bromide, a phase transfer agent. This is followed by reduction of Au^{3+} in the presence of the stabilising / protecting agent in the organic phase. This biphasic method is necessary if the protecting agents are soluble in the organic medium. If the protecting agents are soluble in the aqueous medium, then gold nanoparticles can be prepared by using a single phase method. As the DTPA ligand **6** was water soluble, therefore a single phase method was used.

The gold nanoparticles were thus synthesized by reduction of Au (III) to Au (0) in water in the presence of ligand **6** to ensure the immediate stabilization as shown in the Figure 2.5. Sodium borohydride ($NaBH_4$) was used as a reducing agent.

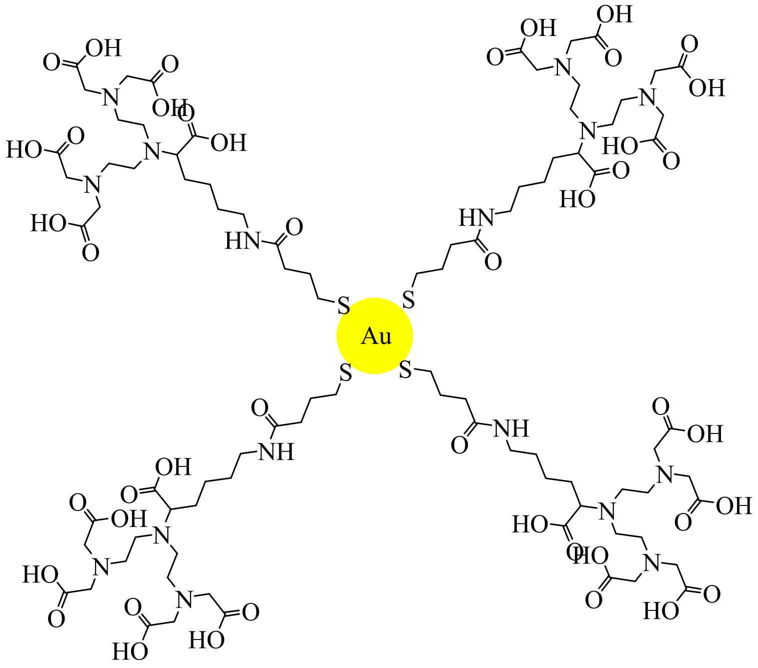

Figure 2.5: Gold Nanoparticles (AuNPs) protected by ligand 6.

The concentration of reducing agent plays a very important role in the stability of gold nanoparticles. Usually the reducing agent is used in a large excess. However, it was found that very high concentration (~ 30 fold excess) of sodium borohydride led to poor stability of the gold nanoparticles. The optimal ratio between gold and reducing agent for the synthesis of gold nanoparticles was found 1:10. After synthesis, the aq AuNPs were dialysed against deionised water to remove water soluble impurities / by-products and also the unbound ligand. Unfortunately the dialysis could not remove the unbound ligand completely (as shown by ^{1}H NMR). The AuNPs were then purified by size exclusion chromatography using Sephadex gel (G 100) as a stationary phase and 0.1M aq NaCl as an eluent to prevent electrostatic binding of the AuNPs to the column. The purified aq AuNPs were again dialysed against deionised water to remove NaCl. The purified AuNPs were characterised by ^{1}H NMR, UV/Vis spectroscopy, TEM and TGA.

2.3.1 UV-Vis spectrum of AuNPs protected by DTPA ligand 6

Surface plasmon band (SPB) is the most distinct feature in the UV-Vis spectra of noble metal (Cu, Ag & Au) nanoparticles. This peak is exhibited by particles having d << λ (where d is the diameter of the nanoparticles and λ is the wavelength of light).[14] When light interacts with nanoparticles, the electric component of the light induces the coherent oscillation of the surface electrons having frequency in the range of visible region. The coherent oscillation of the surface electrons of the nanoparticles is termed the Surface Plasmon Band (SPB). The interaction of the light with the surface electrons of the nanoparticles is represented in Figure 2.6.

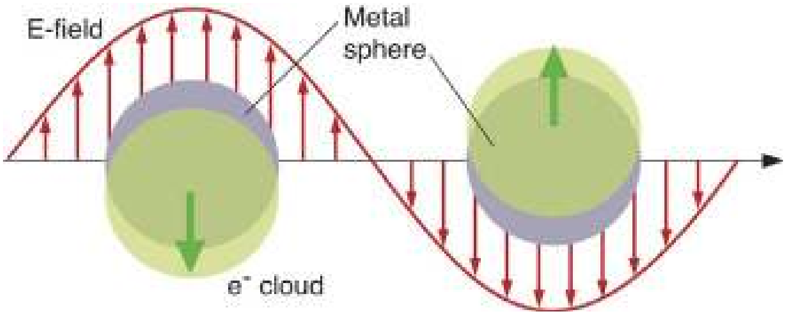

Figure 2.6: Origin of Surface Plasmon Band.[15]

In their UV-Vis spectra, AuNPs usually show a surface plasmon band (SPB) at 520-525 nm.[14-16] The SPB is strongly size dependent: with increase in AuNPs size, the SPB is found to shift towards the longer wavelength. In nanoparticles with size less than 1 nm, SPB is damped; SPB is also absent in bulk gold metal. The UV-Vis spectrum of the AuNPs protected by ligand **6** showed a SPB at 520-525 nm (Figure 2.7) that confirmed the formation of gold nanoparticles. This intensity and position of SPB (Figure 2.7) is typical for small alkanethiol protected AuNPs (~ 2.0 nm).[17]

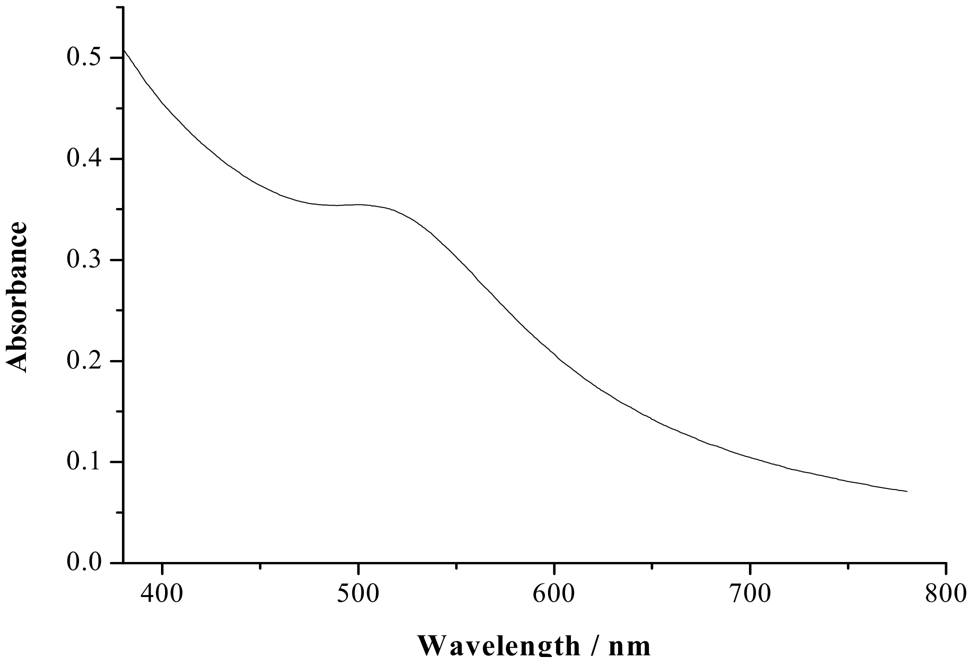

Figure 2.7: UV-Vis Spectrum of Gold Nanoparticles Stabilised by DTPA ligand 6.

2.3.2 ^{1}H NMR spectrum of AuNPs

NMR is a very important technique for the characterization of thiol based gold nanoparticles. The major difference between the ^{1}H NMR spectra of the free thiol based ligand and that adsorbed at the gold nanoparticle surface is the lack of a peak corresponding to the CH_2 group adjacent to the S atom. This is due to the restricted tumbling of ligands adsorbed at AuNPs surface. The peaks of the groups which are further away from the AuNPs surface[18-19] are also broadened. Restricted tumbling leads to incomplete averaging of the anisotropic interactions and hence broadening of peaks of thiol based ligands at AuNPs surface.

In the ^{1}H NMR spectrum of gold nanoparticles protected by DTPA ligand **6**, two major changes were observed as compared with the ^{1}H NMR spectrum of the free ligand (Figure 2.8). The first change is the complete disappearance of the ^{1}H peak of the CH_2S group. Secondly, all peaks became broader. These observations confirmed the successful adsorption of ligand on the AuNPs surface. The peaks of ligand adsorbed on the AuNPs surface appeared at the same chemical shift as the free ligand.

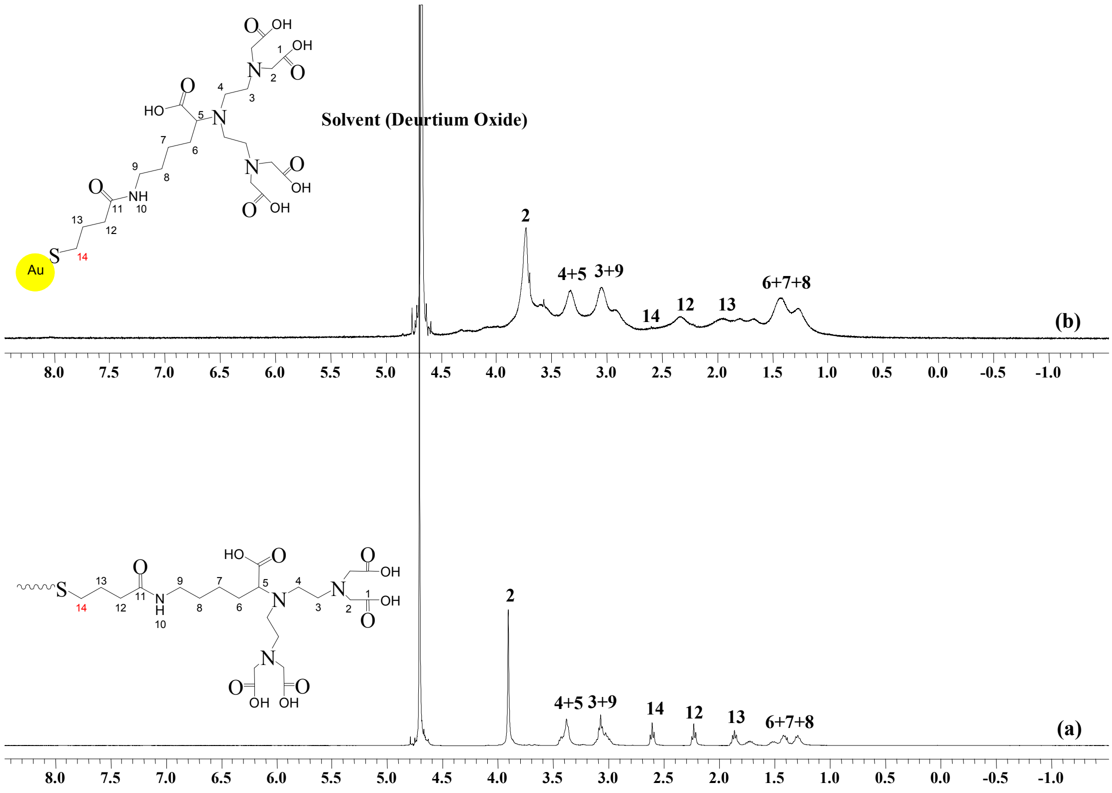

Figure 2.8: ^{1}H NMR Spectra of free ligand 6 (a) and ligand 6 adsorbed on gold nanoparticles surface (b).

2.3.3 TEM analysis of AuNPs

Transmission electron microscopy (TEM) is a standard tool for assessing the core dimensions of metal nanoparticles. Morphology, size, and size distribution of AuNPs can be obtained from the TEM image; therefore this technique is essential for the characterisation of AuNPs. TEM produces a visual image of the gold core of AuNPs. The sample for TEM analysis must be prepared in the form of a thin film which allows the transmission of electrons.[14] The samples of AuNPs protected by ligand **6** were prepared by placing a drop of the AuNP solution in deionised water on a carbon-coated copper grid. The drop was allowed to dry slowly at room temperature and this resulted in the formation of a very thin film. At least six images were taken for each sample. Figure 2.9 shows uniform AuNPs distribution was achieved with reasonable application of dispersity. Nanoparticle diameters were calculated from the particle areas by the mathematical formula

$$\text{Diameter} = [\text{Area} / \pi]^{1/2} \times 2$$

The average diameter of the gold nanoparticles was found to be 1.75 nm ± 0.42, which is comparable with those reported the literature[20] for thiol protected AuNPs prepared by a similar method.

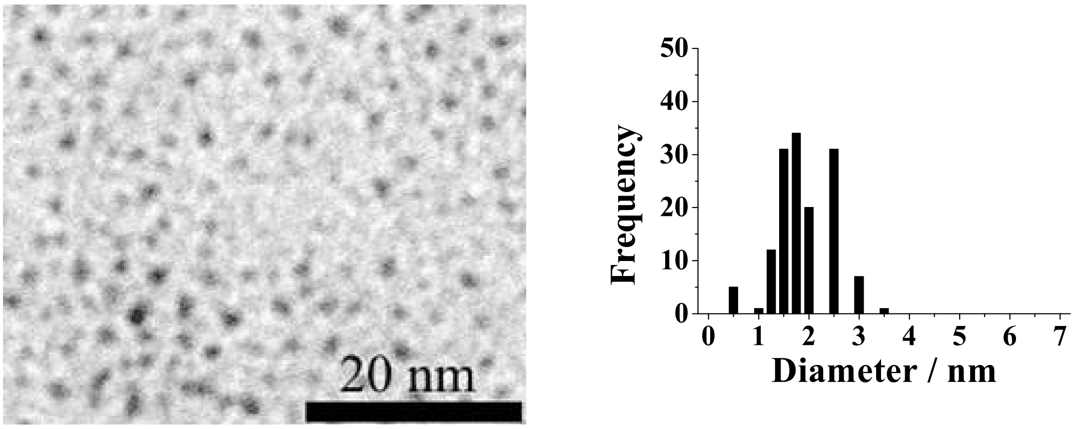

Figure 2.9: TEM image and histogram of AuNPs protected by ligand 6.

2.3.4 Thermogravimetric analysis (TGA) of AuNPs

Thermogravimetric analysis (TGA) determines the rate of change in the weight of a material as a function of temperature in a controlled atmosphere (usually an inert atmosphere). TGA measurements are used primarily to determine the composition of materials and to predict their thermal stability at high temperature. The technique can characterize materials that exhibit weight loss or gain due to decomposition, oxidation, or dehydration. When gold nanoparticles protected by organic ligands are heated, the organic ligands desorb from the AuNPs surface leaving the gold core. The change in weight of AuNPs upon heating gives the amount of organic ligand present on the AuNP surface. The AuNPs protected by ligand **6** were accurately weighed (5.58 mg) and dried under vacuum for ca. 3-4 hours and submitted for TGA analysis. The TGA graph of AuNPs protected by compound **6** is reported in Figure 2.10. The weight loss starts at ca. 200 °C. This value is quite similar to values (200 °C) that are reported in the literature[21] for similar thiol protected AuNPs. Total weight loss calculated from the TGA graph corresponds to the loss of organic ligands from the nanoparticle surface. From TGA analysis, the ratio between the gold and protecting ligand (compound **6**) was determined as 3.98:1 (Au: Ligand). This ratio allowed us to estimate the amount of ligand present at AuNP surface which is needed for calculating gadolinium loading. This composition of gold nanoparticles is similar to the simple alkanethiol-protected gold nanoparticles having similar diameters. [22-23]

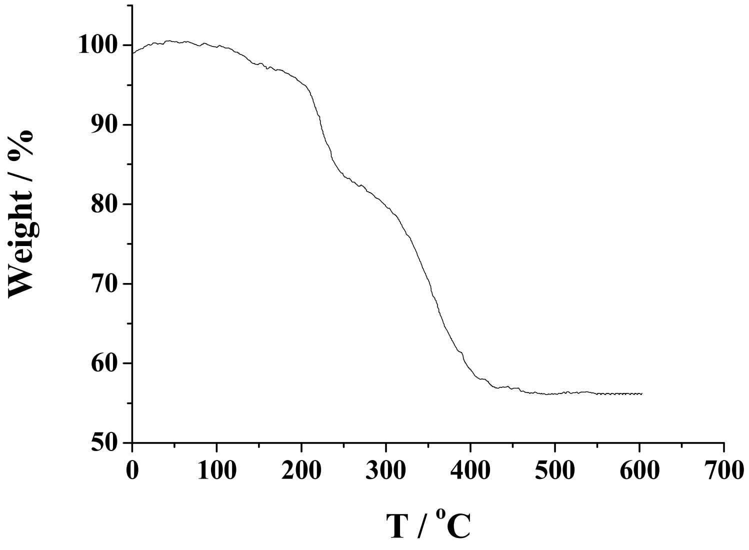

Figure 2.10: TGA graph of gold nanoparticles protected by DTPA ligand 6.

2.4 Complexation of gadolinium (Gd^{3+}) with DTPA ligand 6 at AuNP surface

The characterised AuNPs protected by DTPA ligand **6** were loaded with gadolinium to act as MRI contrast agents. The loaded gadolinium was complexed with DTPA units of the ligand at AuNPs surface as shown in Figure 2.11.

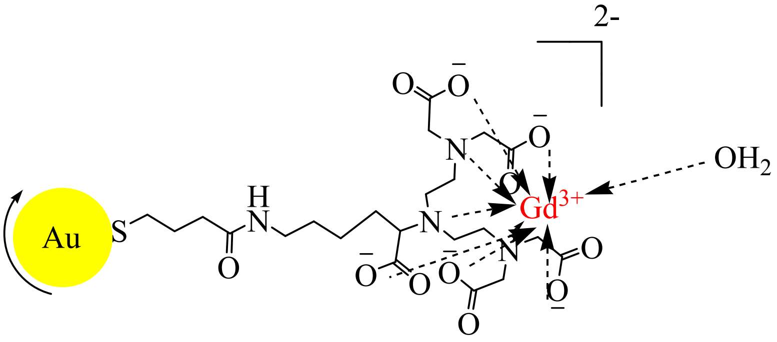

Figure 2.11: Gd-loaded AuNPs.

The amount of gadolinium for loading on AuNPs was calculated using the composition of AuNPs as described in the previous (TGA) section. The protocol was similar to that developed for Gd-complexation with similar AuNPs.[24] To the aqueous AuNPs protected by ligand **6**, aqueous $GdCl_3$ was added portion wise. The excess amount of gadolinium was removed by dialysing the Gd-loaded AuNPs against deionised water. The exact amount of gadolinium in Gd-loaded AuNPs was then determined by ICP and UV-Vis spectroscopy independently and is discussed in the following sections.

2.4.1 Determination of [Gd^{3+}] using xylenol orange titration

A calibration curve for determination of [Gd^{3+}] in Gd-loaded AuNPs was determined by following the literature procedure.[25] Xylenol orange is a weak lanthanide chelating agent that can chelate with free gadolinium ions. Xylenol orange exhibits two absorption peaks at 434 nm and 576 nm in the absence of any lanthanide. In the presence of lanthanides, the intensity of the first peak at 434 nm decreases while that at 575 nm increases. The ratio between the intensities of the two peaks can be used for the quantitative determination of lanthanides (Gd^{3+} in our case). The UV/Vis spectra of xylenol orange in the presence of various concentrations of Gd-atomic standard solutions and the calibration curve built using these spectra are shown in Figures 2.12 and 2.13, respectively.

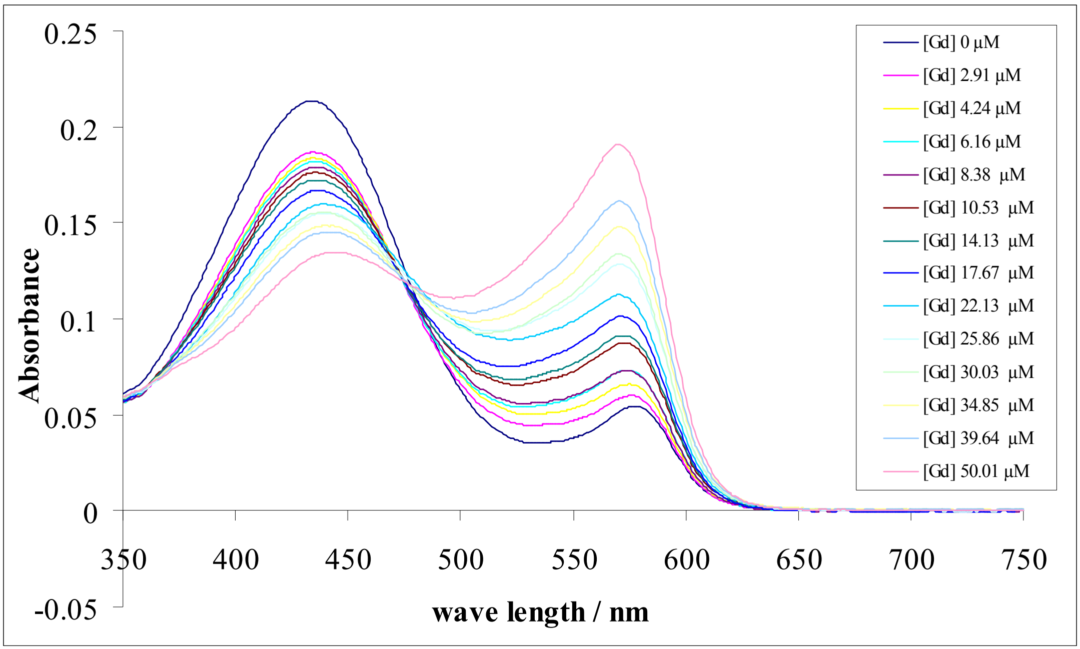

Figure 2.12: UV/Vis spectra of xylenol orange in the presence of Gd atomic standard solution.

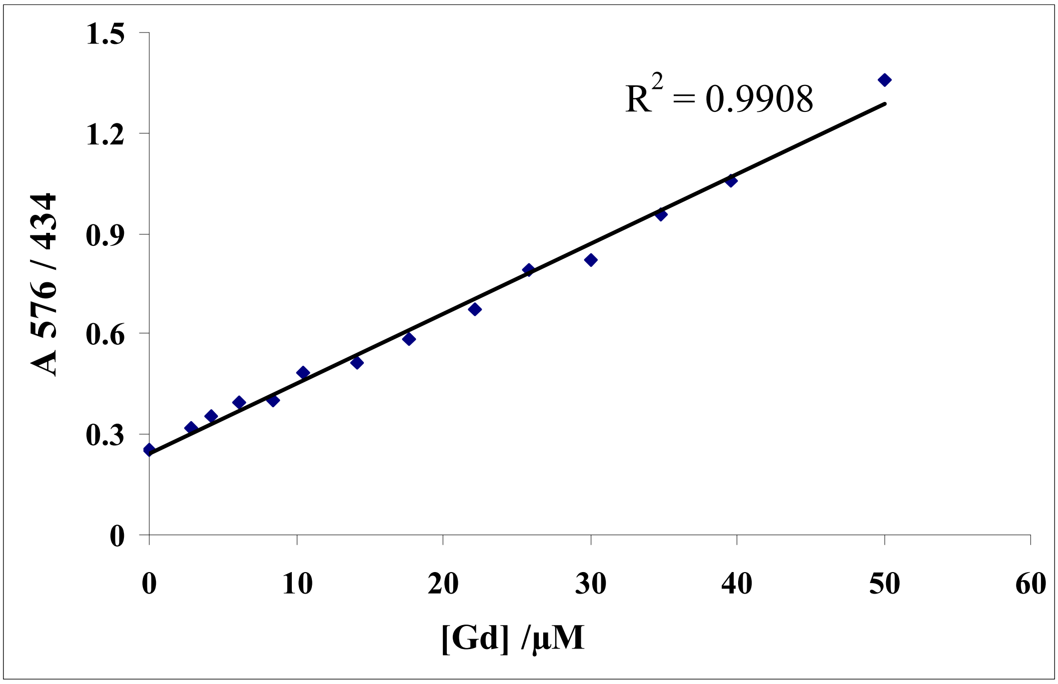

Figure 2.13: Calibration curve for the determination of [Gd^{3+}].

The calibration curve shown in Figure 2.13 was used for the determination of [Gd^{3+}] in Gd-loaded AuNPs. The Gd-loaded-AuNPs were decomposed by treatment with aqua regia at ca. 80 °C for at least 24 h. Under these conditions, the AuNPs and organic ligands are destroyed and Gd^{3+} ions become free. The decomposed Gd-loaded-AuNPs were filtered using syringe filter, pH adjusted (~6) and diluted by the acetate buffer (pH 5.8) to make a solution for analysis (with [Gd^{3+}] in the range 10-50 μM). The unknown concentration of Gd in this solution was determined by adding a 30 μL aliquot to 0.4 mL of xylenol orange and recording UV-Vis spectrum. From the ratio of absorbance at 434 nm and 576 nm, the [Gd^{3+}] could be determined using the calibration curve. For example, in 5.0 mg of Gd-loaded AuNPs, 0.51 mg of Gd content was determined by this method. Using this method, Gd-loaded AuNPs were found to contain ca. 10.13 wt % Gd

.

2.4.2 In situ monitoring of Gd^{3+} loading on AuNPs by UV-Vis titration using xylenol orange as indicator

The gadolinium concentration in Gd-loaded AuNPs was also independently determined by another method which allowed in situ monitoring of Gd-loading. The need for in situ monitoring was realised due to the following reasons.

- Gd determination needs confirmation by an independent method (e.g. to confirm complete decomposition of Gd-loaded AuNPs with aqua regia).
- The in situ monitoring allowed us to determine the exact saturation point of Gd^{3+}, so that the exact amount of gadolinium can be loaded rather than an excess of gadolinium requiring removal by dialysis.

The UV/Vis spectra of xylenol orange in aq AuNPs were recorded after each 20-30 μL addition of aqueous $GdCl_3$. No change in UV-Vis spectra of xylenol orange was observed until all the ligand at AuNPs surface was complexed with gadolinium. As soon as the gadolinium is coordinated by xylenol orange, the sudden changes in peak intensities of xylenol orange were observed as shown in Figure 2.14. Figure 2.14 shows titration results for two different batches of aq AuNPs (2.0 mg dissolved in ca. 5.0 mL of H_2O) that gave saturation point of gadolinium at the AuNPs surface at 235 µL concentration of $GdCl_3$. According to this data, 9.98 % the gadolinium content in AuNPs was determined by this method which is in a very close agreement with that determined by the calibration curve method (10.13 %) as described in the previous section.

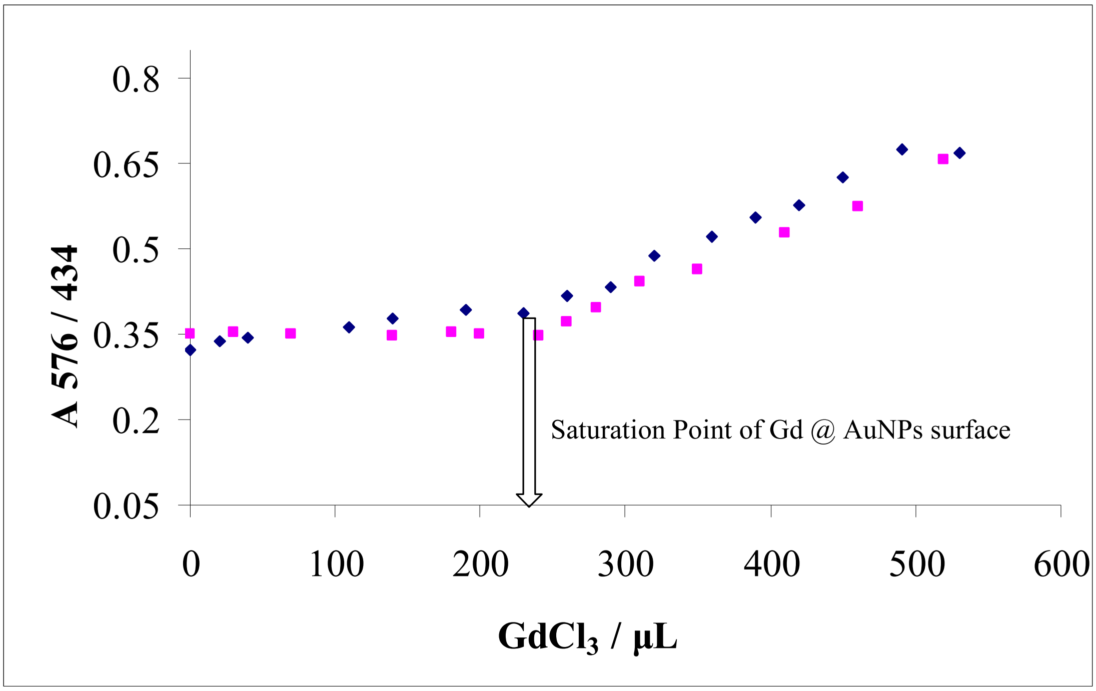

Figure 2.14: Titration of AuNPs with [$GdCl_3$] in the presence of xylenol orange.

2.4.3 Characterisation of Gd-loaded AuNPs by Inductively Coupled Plasma Spectrometry (ICP)

Gd-loaded AuNPs were characterised by ICP to determine the amount of gold and gadolinium. The ICP, TGA and UV/Vis data are summarised in Table 2.1.

Table 2.1: ICP, TGA and UV/Vis data for Gd-loaded AuNPs.

Technique	**Element**	**Composition / %**
ICP	Au	45.64
	Gd	10.95
TGA	Ligand	42.0
UV/Vis	Gd	10.13*
		9.98**

***Determined by Calibration Curve Method, **By In situ monitoring method**

The amount of gadolinium in Gd-loaded AuNPs determined by ICP analysis was compatible with the amount of DTPA ligand **6** at the AuNP surface determined by thermogravimetric analysis (42 %). Similarly, the amount of gadolinium determined by UV/Vis method and ICP are in close agreement with each other. These data were used to derive the composition of Gd-loaded AuNPs which is described in the next section.

2.4.4 Composition of Gd-loaded AuNPs

On the basis of TEM, TGA, ICP and UV-Vis data, the composition of the Gd-loaded AuNPs was determined. The average number of gold atoms per particle (166) were determined from TEM data (i.e. 1.75 nm average diameter of AuNPs) by assuming the same packing density of AuNPs as in bulk gold (eq. 2.1).[17]

$$N_{Au} = \frac{\pi}{6} D^3 n_{Au}^{fcc} \qquad \text{Eq. 2.1}$$

Here N_{Au} is the number of gold atoms in particle, D is the diameter of the AuNPs and n_{Au}^{fcc} is the packing density of gold (59.2 g / cm^3). The ratio between gold and ligand was estimated by TGA and then confirmed by ICP analysis and UV/Vis spectroscopy. The ratio between Au, Gd and ligand was found as $Au_{3.3}$ $Ligand_{1.07}$ $Gd_{1.0}$. As each nanoparticle contains 166 atoms, the composition of Gd-loaded AuNPs was determined as Au_{166} $Ligand_{54}$ Gd_{50}.

2.4.5 Spin lattice relaxivity (r_1) of Gd-loaded AuNPs, Gd-DTPA and $GdCl_3$

The longitudinal relaxation constant for the water ^1H signal, T_1, was measured in the presence of Gd-DTPAligand@AuNPs, Gd-DTPA and $GdCl_3$ using an inversion recovery method (which has been discussed in detail in chapter 1 (section 1.5)).[26] The T_1 (spin lattice relaxation time) can be calculated using equation 2.2.

$$M_z = M_0(1 - 2\exp(-\tau / T_1)) \qquad \text{Eq. 2.2}$$

Here M_z is the longitudinal magnetisation, M_0 is the equilibrium magnetisation and τ is the variable time delay. All the relaxation measurements were carried out at magnetic field 7.0 T with variable time delay "τ" ranging from 0.0001-6.0 s. The inversion recovery curves for Gd-loaded AuNPs are shown in Figure 2.15.

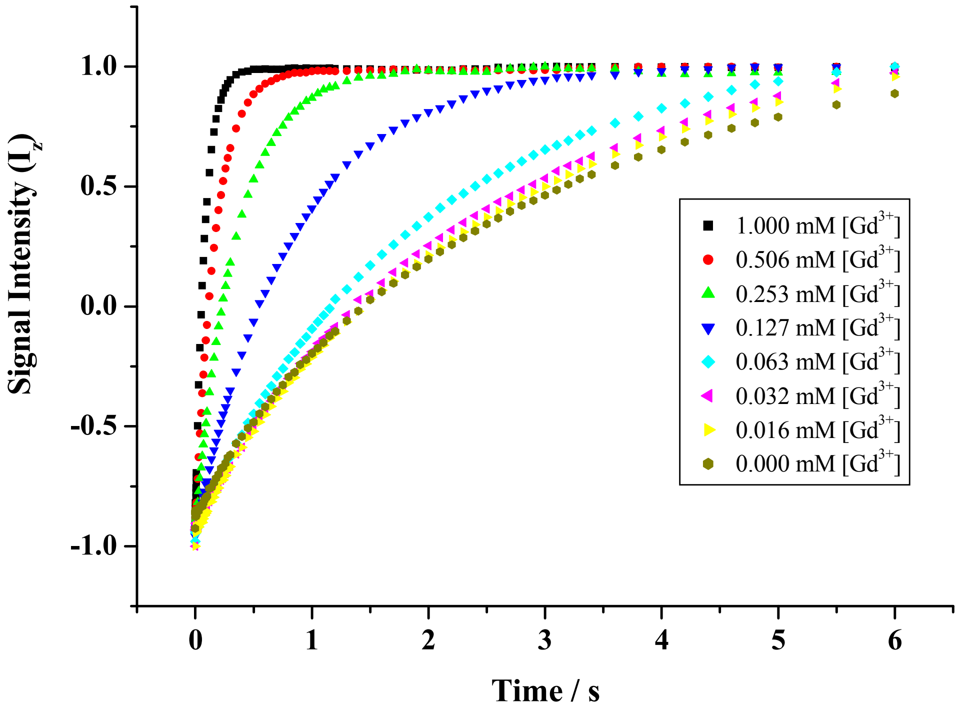

Figure 2.15: Inversion recovery curves for Gd-loaded-AuNPs.

Spin-lattice relaxivity (r_1) was calculated from the slope of the plot $1/T_1$ vs [Gd^{3+}] using equation 2.3.

$$\frac{1}{T_1} = R_1[Gd] \qquad \text{Eq. 2.3}$$

The r_1 curves for Gd-loaded AuNPs, Gd-DTPA and $GdCl_3$ are shown in Figure 2.16.

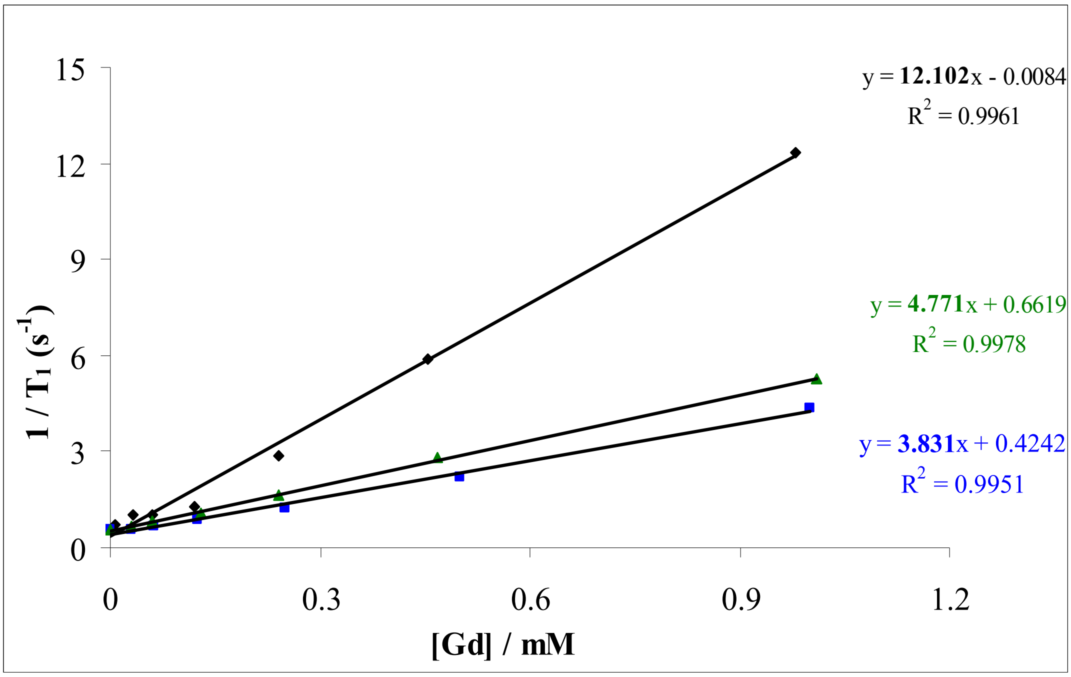

Figure2.16: Spin lattice relaxivity (r_1) curves for Gd-DTPA (blue), Gd-DTPA@AuNPs (green), and $GdCl_3$ (black) at 300 MHz and 298 K

The R_1 of $GdCl_3$ was found to be (12.10 mM^{-1} s^{-1}) much higher than for Gd-DTPA and Gd-loaded AuNPs, but unfortunately due to high toxicity of free Gd^{3+}, it cannot be utilised as an MRI contrast agent. In free Gd^{3+}, eight water molecules are directly coordinated with Gd^{3+} [i.e. $Gd(H_2O)_8]^{3+}$. This water can exchange with surrounding water molecules and thus transfer more magnetic moment from Gd^{3+} centre to the surrounding medium, resulting in high R_1.

The r_1 (at 300 MHz and at 298 K) value for Gd-loaded AuNPs (4.77 mM^{-1} s^{-1}) was found somewhat higher than that of a commercially available MRI contrast agent i.e. $[Gd\text{-}DTPA]^{-2}$ (3.83 mM^{-1} s^{-1}) at the same field strength and same temperature. This increase, however (~25.0%) is not very large. The only moderate increase in R_1 by Gd-loaded AuNPs may be due to several reasons. One possibility is the slow water exchange rate between Gd-DTPA ligand at the AuNPs surface and the surrounding medium. But as the AuNPs are protected by a monolayer of the DTPA ligand, therefore all Gd-DTPA ligand chelates are located at the surface of AuNPs and their water molecules are expected to exchange with surrounding medium easily without any hindrance as shown in Figure 2.17.

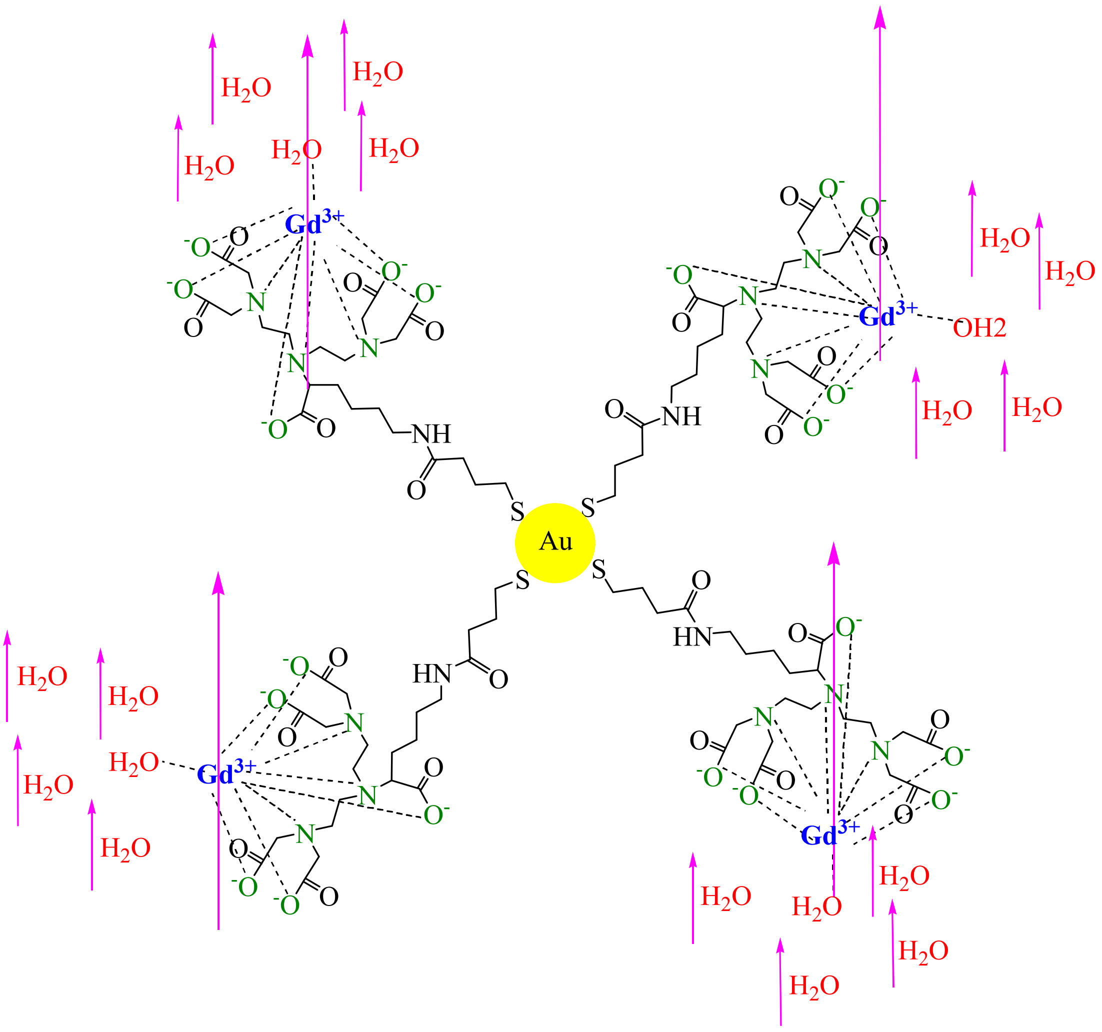

Figure 2.17: Gd-loaded AuNPs.

The second argument for only moderate increase in R_1 is the fairly fast tumbling of the DTPA ligand at AuNPs surface. Fast tumbling will result in averaging of dipole-dipole interactions between the electron spin of Gd^{3+} and the nuclear spin of protons, thus reducing the efficiency of relaxation. We noted that some other reports [27-28] on gold nanoparticle based contrast agents showed similar r_1 values. For example, Roux *et al.*[27] prepared dithiolated DTPA multilayered AuNPs having diameter 2.0-2.5 nm, which also exhibited only moderate increase in r_1 as compared to Gd-DTPA. Furthermore, multilayered Gd-loaded AuNPs were found to decompose within 24 hours.[27] We improved the stability of Gd-loaded AuNPs significantly. Our Gd-loaded AuNPs were stable at room temperature for several months. The relatively long carbon chain (C10) of the DTPA ligand **6** as compared to the dithiolated DTPA[27] ligand may be the major factor improving the stability of Gd-loaded AuNPs.

2.4.6 T_1-weighted images of Gd-loaded AuNPs and Gd-DTPA

The suitability of Gd-loaded AuNPs for MRI applications was evaluated by taking T_1 weighted images of solutions of commercially available MRI contrast agent i.e. Gd-DTPA and Gd-loaded AuNPs. The concentration of gadolinium in both samples for taking T_1-weighted images was kept at 0.25 mM. Figure 2.18 clearly shows the contrast enhancement with increased nanoparticle concentration. Gd-loaded AuNPs have somewhat higher relaxivity than the Gd-DTPA complex as discussed in previous section, which leads to a slightly better contrast in T_1-weighted images (Figure 2.18).

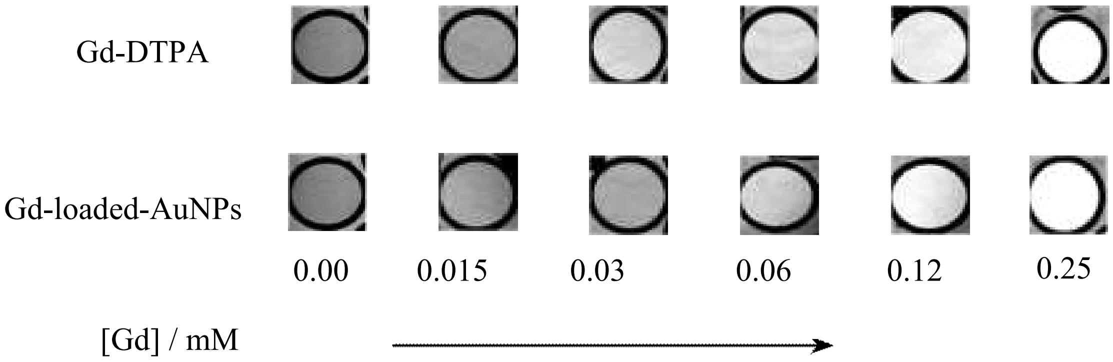

Figure 2.18: T_1-weighted images of Gd-DTPA and Gd-DTPA@AuNPs.

The positive contrast thus confirmed the feasibility of using Gd-loaded AuNPs as MRI contrast agents. The positive contrast in T_1 weighted images by other gold nanoparticles based contrast agent was also reported in the literature.[29]

2.4.7 Attaching a recognition vector to Gd-loaded AuNPs

For applications in medical diagnosis and therapy, the surface modification of gold nanoparticles is important.[30] For example to transport the nanoparticles to a specific tissue / organ, a recognition vector with ability to recognise the specific target is required. Target-specific MRI contrast agents modified with a recognition vector yield better contrast as compared to the non-specific contrast agents due to in situ accumulation at the target place. For example, Dirksen *et al.*[31] recently reported the multivalent target-specific MRI contrast agents for MRI imaging angiogenesis process. They prepared a cyclic peptide (asparagine-glycine-arginine sequence) based MRI contrast agent having Gd-DTPA chelate at one end. The asparagine-glycine-arginine sequence (cyclic peptide) has strong affinity for aminopeptidase (a protein over-expressed by angiogenic endothelial cells).

Biotin (vitamin H) forms an exceptionally strong complex with avidin (association constant $K_a = 10^{15}$ $M^{-1)}$ based on non-covalent interactions. This complex is often used for selective functionalisation or targeting of nanostructures. Figure 2.19 shows how a biotin-avidin complex at a nanoparticle surface can be used for targeting biotinylated ligands via biotin-avidin-biotin complex.

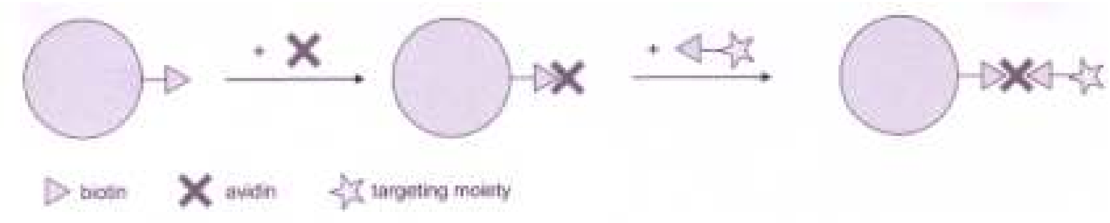

Figure 2.19: Surface functionalisation via biotin-avidin-biotin.[30]

As a proof of principle, we also selected biotin-avidin system for recognition studies of Gd-loaded AuNPs, as described in the following sections.

2.4.7.1 Synthesis of biotin-terminated thiol (BTT)

A recognition vector for the attachment to Gd-loaded AuNPs must have a functional group with strong affinity for AuNPs, and should also be water soluble. Therefore we chose a commercially available hydrophilic biotin derivative NHS-$(PEO)_4$-biotin (Figure 2.20), which can be readily modified with a thiol group (thiols show very strong affinity for gold). A further advantage of this molecule is that the PEO (poly (ethylene oxide)) spacer arm reduces the steric hindrance thus facilitating binding with avidin. In order to introduce the thiol group, NHS-$(PEO)_4$-biotin was treated with cysteamine[32]. Biotin-terminated thiol (BTT) thus prepared (Figure 2.20) has three main functional moieties: (a) thiol for binding to the gold surface, (b) biotin for molecular recognition studies, (c) poly (ethylene oxide) spacer arm for solubility in aqueous medium, and is hence suitable for recognition studies of Gd-loaded AuNPs.

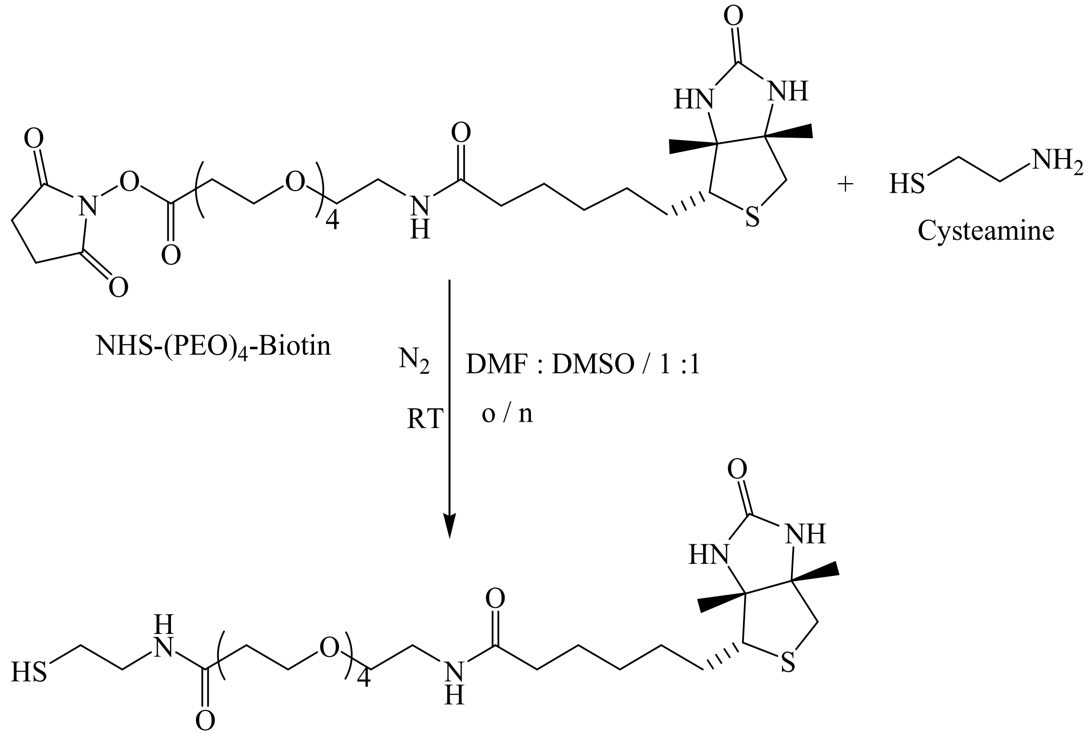

Biotin-terminated Thiol (BTT)

Figure 2.20: Synthesis of biotin-terminated thiol (BTT).

2.4.7.2 Attachment of BTT to Gd-loaded AuNPs

Ligand exchange reaction at AuNPs surface is an efficient way of preparing poly-functionalised nanoparticles. Ligand exchange can be carried out using ligands higher affinity for gold than the ligands already present on the surface. The ligands having similar affinity can also be exchanged.[33] DTPA ligands **6** at Gd-loaded AuNPs surface were exchanged with biotin-terminated thiol (that has similar affinity for gold as the DTPA ligand) by stirring in aqueous medium at room temperature. Biotin terminated thiol (BTT) replaced some of the DTPA ligand molecules on gold nanoparticles (Figure 2.21).

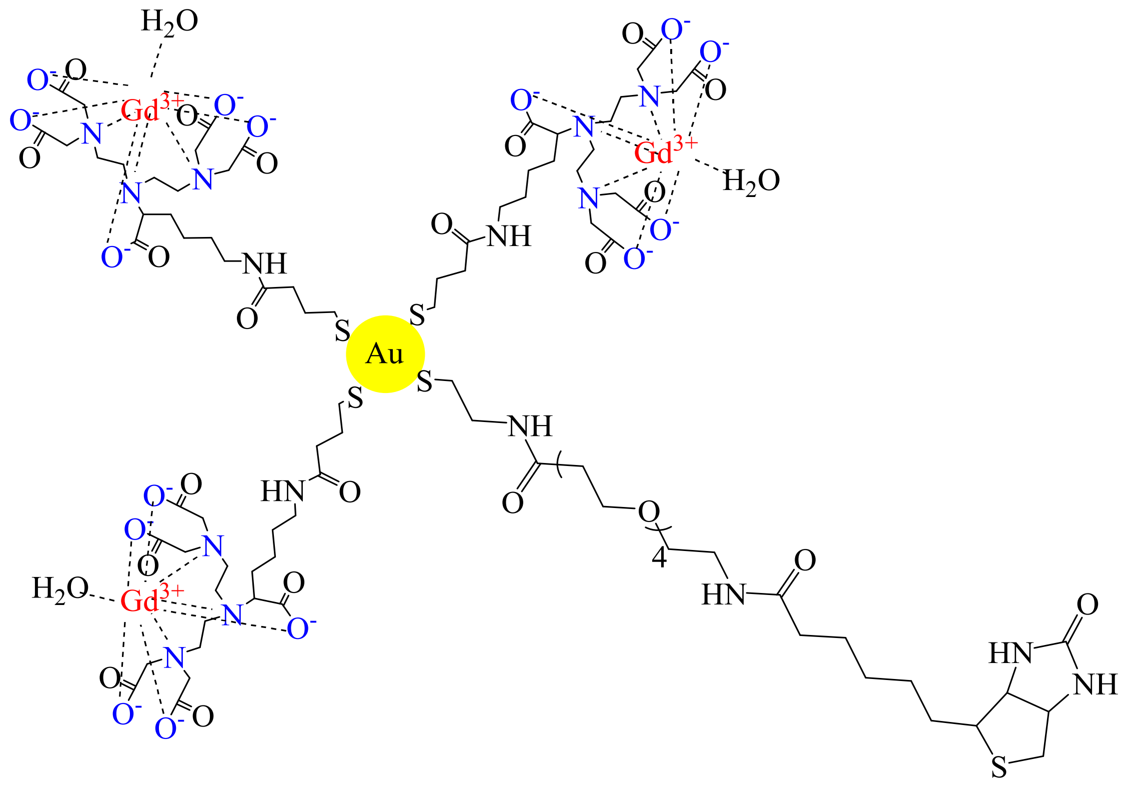

Figure 2.21: BTT-labelled Gd-loaded AuNPs.

The excess of BTT molecules was removed by overnight dialysis against deionised water. The Gd-loaded AuNPs having BTT recognition vectors at their surface were found quite stable and then their recognition studies were carried out (as described in the next section). The gold nanoparticle based targeted MRI contrast agents were thus prepared which contain Gd-DTPA chelates (to act as an MRI contrast agent) and biotin-terminated thiol (a recognition vector) at their surface (Figure 2.21).

2.4.7.3 Molecular recognition of BTT-labelled-Gd-loaded AuNPs

Recognition studies of BTT-labelled-Gd-loaded-AuNPs were carried out by MRI imaging experiments. The avidin-functionalized gel was taken as a target, to which BTT-labelled Gd-loaded AuNPs were expected to bind. Two columns filled with the target gel of identical length and diameters were taken. BTT-labelled-Gd-loaded-AuNPs and Gd-loaded-AuNPs without BTT labelling were passed through the two columns. The BTT labelled Gd-loaded-AuNPs were found to adsorb to the avidin column, while the nanoparticles without BTT labelling do not show any affinity for the avidin column. Although the binding of BTT-labelled Gd-loaded AuNPs with the avidin functionalized gel could be observed easily with a naked eye, it was further confirmed by acquiring T_1-weighted images of the columns and the filtrates (i.e. BTT labelled and unlabelled AuNPs). T_1 weighted MRI images are shown in Figure 2.22. The image "I" (i.e. for avidin column with nanoparticles) is brighter than the image "III" (i.e. for avidin column without nanoparticles).

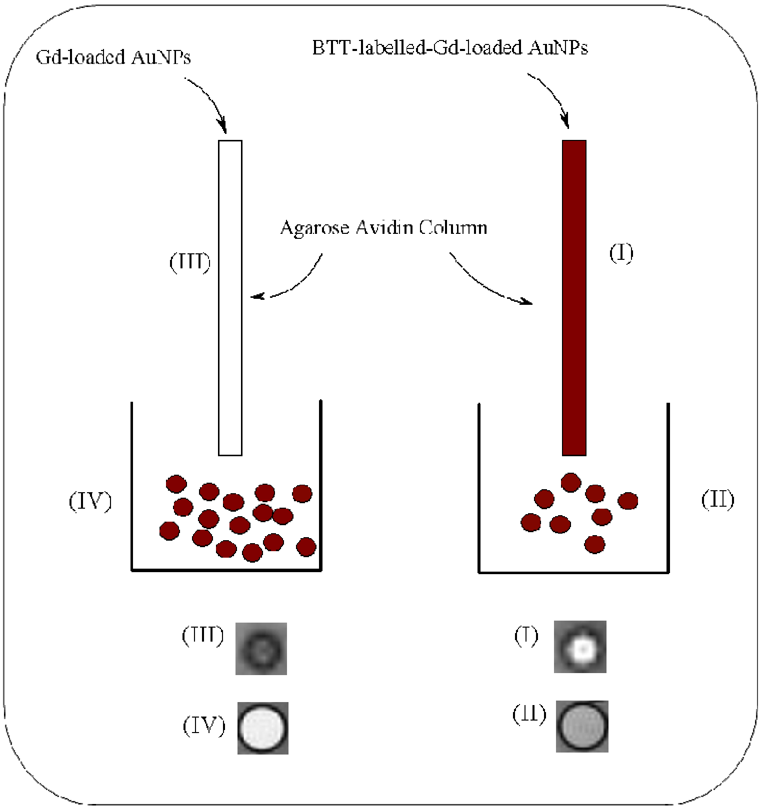

Figure 2.22: T_1-weighted images of BTT labelled and unlabelled Gd-loaded AuNPs, and avidin-functionalized gel columns.

2.5 Conclusions

A DTPA based ligand was synthesized and characterised successfully. The Au nanoparticles protected by the new ligand were synthesized and characterised by UV-Vis spectroscopy, TEM and TGA. The gold nanoparticles were then characterised by ICP after loading with gadolinium. Two different methods based on UV/Vis titrations were established for determination / monitoring of Gd^{3+} loading on

AuNPs. The average composition of Gd-loaded AuNPs was determined as "$Au_{166}Lig_{54}Gd_{50}$". The efficiency of Gd-loaded AuNPs to act as MRI contrast agents was assessed in terms of relaxivity. The gold nanoparticles based contrast agent showed a 25 % increase in relaxivity as compared to the commercially available MRI contrast agent Gd-DTPA. The increase in R_1 for Gd-loaded AuNPs was not very large, possibly due to relatively fast tumbling of nanoparticle-attached Gd-DTPA units.

A recognition vector (biotin terminated thiol) was synthesized and then attached to Gd-loaded-AuNPs. The gold nanoparticles with recognition vector were found to successfully recognize their target (i.e. avidin modified gel). This illustrates that gold nanoparticle based MRI contrast agents can be used as target specific contrast agents.

2.6 References

1. S. Cotton, *Lanthanide and Actinide Chemistry,* John Wiley & Sons, 2006, **1**, pp. 42-43.
2. A. E. Merbach and E. Toth, *The Chemistry of Contrast Agents in Medical Magnetic Resonance Imaging,* John Wiley & Sons, 2001, pp. 45-119.
3. A. Bianchi, L. Calabi, F. Corana, S. Fontana, P. Losi, A. Maiocchi, L. Paleari and B. Valtancoli, *Coord. Chem. Rev.*, 2000, **204**, 309-393.
4. A. E. Merbach and E. Toth, *The Chemistry of Contrast Agents in Medical Magnetic Resonance Imaging,* John Wiley & Sons, 2001, pp. 121-150.
5. M. A. Williams and H. Rapoport, *J. Org. Chem.*, 1993, **58**, 1151-1158.
6. P. L. Anelli, F. Fedeli, O. Gazzotti, L. Lattuada, G. Lux and F. Rebasti, *Bioconjugate Chem.*, 1999, **10**, 137-140.
7. J. Sherma and B. Fried, *Handbook of Thin-Layer Chromatography,* Marcel Dekker, 1996, **2**, 101-107.
8. D. C. Johnson Ii and T. S. Widlanski, *Tetrahed. Lett.*, 2001, **42**, 3677-3679.
9. J. C. Sheehan and G. P. Hess, *J. Am. Chem. Soc.*, 1955, **77**, 1067-1068.
10. Y. Xu, X. Duan, M. Li, L. Jiang, G. Zhao, Y. Meng and L. Chen, *Molecules*, 2005, **10**, 259-264.
11. L. Lattuada and M. Gabellini, *Synth. Commun.*, 2005, **35**, 2409 - 2413.
12. S. Langereis, Q. G. de Lussanet, M. H. P. van Genderen, W. H. Backes and E. W. Meijer, *Macromolecules*, 2004, **37**, 3084-3091.
13. M. Brust, M. Walker, D. Bethell, D. J. Schiffrin and R. Whyman, *J. Chem. Soc.-Chem. Commun.*, 1994, 801-802.
14. M.-C. Daniel and D. Astruc, *Chem. Rev.*, 2003, **104**, 293-346.

15. P. K. Jain, I. H. El-Sayed and M. A. El-Sayed, *Nano Today*, 2007, **2**, 18-29.

16. M. Sastry, *Curr. Sci.*, 2003, **85**, 1735-1745.

17. V. Chechik, *J. Am. Chem. Soc.*, 2004, **126**, 7780-7781.

18. R. H. Terrill, T. A. Postlethwaite, C.-H. Chen, C.-D. Poon, A. Terzis, A. Chen, J. E. Hutchison, M. R. Clark and G. Wignall, *J. Am. Chem. Soc.*, 1995, **117**, 12537-12548.

19. S. Abraham, I. Kim and Carl A. Batt, *Angew. Chem. Int. Ed.*, 2007, **46**, 5720-5723.

20. S. Koenig and V. Chechik, *Langmuir*, 2006, **22**, 5168-5173.

21. S. F. Sweeney, G. H. Woehrle and J. E. Hutchison, *J. Am. Chem. Soc.*, 2006, **128**, 3190-3197.

22. T. Teranishi, S. Hasegawa, T. Shimizu and M. Miyake, *Adv. Mater.*, 2001, **13**, 1699-1701.

23. T. Shimizu, T. Teranishi, S. Hasegawa and M. Miyake, *J. Phys. Chem. B*, 2003, **107**, 2719-2724.

24. P.-J. Debouttière, S. Roux, F. Vocanson, C. Billotey, O. Beuf, A. Favre-Réguillon, Y. Lin, S. Pellet-Rostaing, R. Lamartine, P. Perriat and O. Tillement, *Adv. Funct. Mater.*, 2006, **16**, 2330-2339.

25. A. Barge, G. Cravotto, E. Gianolio and F. Fedeli, *Contrast Med. & Mole. Imag.*, 2006, **1**, 184-188.

26. I. L. Pykett, B. R. Rosen, F. S. Buonanno and T. J. Brady, *Phys. Med. Biol.*, 1983, **28**, 723-729.

27. C. Alric, J. Taleb, G. L. Duc, C. Mandon, C. Billotey, A. L. Meur-Herland, T. Brochard, F. Vocanson, M. Janier, P. Perriat, S. Roux and O. Tillement, *J. Am. Chem. Soc.*, 2008, **130**, 5908-5915.

28. P. J. Debouttiere, S. Roux, F. Vocanson, C. Billotey, O. Beuf, A. Favre-Reguillon, Y. Lin, S. Pellet-Rostaing, R. Lamartine, P. Perriat and O. Tillement, *Adv. Funct. Mater.*, 2006, **16**, 2330-2339.
29. Y. T. Lim, M. Y. Cho, B. S. Choi, J. M. Lee and B. H. Chung, *Chem. Comm.*, 2008, 4930-4932.
30. C. Kumar, *Nanomaterials for Medical Diagnosis and Therapy*, Wiley-VCH, 2007, **1**, 359-379.
31. A. Dirksen, S. Langereis, B. F. M. d. Waal, M. H. P. v. Genderen, T. M. Hackeng and E. W. Meijer, *Chem. Comm.*, 2005, 2811-2813.
32. A. K. Salem, M. Chen, J. Hayden, K. W. Leong and P. C. Searson, *Nano Lett.*, 2004, **4**, 1163-1165.
33. P. Ionita, J. Wolowska, V. Chechik and A. Caragheorgheopol, *J. Phys. Chem. C*, 2007, **111**, 16717-16723.

Chapter 3: Strategies for increasing relaxivity of Gd-loaded gold nanoparticles

Chapter 3: Strategies for increasing relaxivity of Gd-loaded gold nanoparticles

3.1 Introduction

Spin lattice relaxivity (r_1) measurements of Gd-loaded-AuNPs were carried out and discussed in chapter 2 in detail. The r_1 of Gd-loaded-AuNPs (Gd-DTPA@AuNPs) was compared with commercially available MRI contrast agents i.e. Gd-DTPA and only a moderate increase was observed. Although this increase is comparable with some recent literature values[1,2], we decided to explore the strategies for improving the relaxivity. The increase in r_1 may be limited by weaker coupling between Gd-DTPA chelates at the AuNP surface and surrounding water protons (as discussed in chapter 2). In particular, dipole-dipole[3] (dipolar) coupling is the most important mechanism of relaxation. The coupling depends upon the inverse sixth power of the distance between the two nuclei and the direction of the vector joining the two spins (Figure 3.1) e.g. it is proportional to $\frac{3\cos^2\theta - 1}{r_{AB}^6}$.

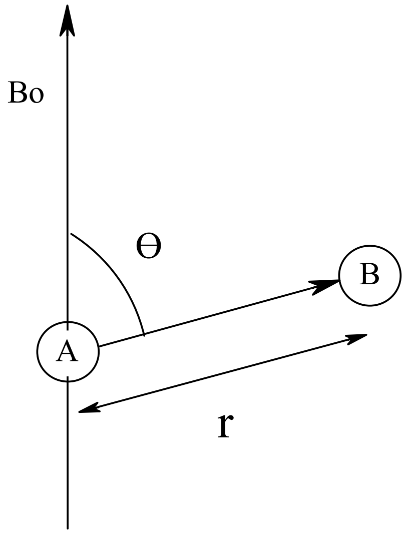

Figure 3.1: Two spins (one is nuclear spin, but the other one is an electron spin) A and B are interacting with each other via dipolar mechanism.

The frequency of rotational motion of tumbling species is also important for effective dipolar coupling and this frequency is usually expressed in terms of so-called correlation time (τ_c). The τ_c is related with spin-lattice relaxation time (T_1) as:

$$\frac{1}{T_1} \propto \frac{\tau_c}{1+(2\pi\nu_o\tau_c)^2} \qquad \text{Eq. 3.1}$$

Here ν_o is the precessional frequency of the target nucleus (e.g A in Figure 3.1). According to this equation, for rapidly tumbling species with $1/\tau_c >> 2\pi\nu_o$, relaxation rate ($1/T_1$) will be proportional to τ_c, while in case of slowly tumbling species ($1/\tau_c << 2\pi\nu_o$) $1/T_1$ will be inversely proportional to τ_c. In rapidly tumbling species ($\tau_c < 10^{-11}$ s), the dipolar interaction averages out, while in slowly tumbling species ($\tau_c > 10^{-11}$ s) the dipolar coupling is significant which can lead to higher relaxivity.[4]

Table 3.1[3] illustrates this effect of τ_c on r_1. For instance, if τ_c is decreased 1000 fold, the r_1 will increase four-fold.

Table 3.1 Effect of τ_c on r_1.

Rotational Correlational Time (τ_c) / ps	Relaxivity (r_1 / $mM^{-1}s^{-1}$)
58	8.0
58,000	32.0

In this chapter, EPR spectroscopy was used to determine the tumbling rate (τ_c) of nanoparticle-attached ligand in order to unravel the main factors responsible for the limited increase in R_1 of Gd-loaded AuNPs as compared to commercially available Gd-DTPA MRI contrast agent.

3.1.1 An introduction to EPR[5-7]

Electron Paramagnetic Resonance phenomenon was discovered by Prof. E. K. Zavoisky in 1944 at Kazan University (Russia) and is abbreviated as EPR and also as ESR (i.e. electron spin resonance). The EPR spectroscopy is used to study materials with unpaired electron(s). EPR is similar to NMR, but EPR is based on the interaction of magnetic field with electron spin, while NMR relies on the nuclear spin.

3.1.1.1 Principles of EPR

Electrons have intrinsic angular momentum called spin (S). Electron has two spin states represented as α and β in the presence of static magnetic field (B_o) (this phenomenon is called Zeeman Effect). These two spin states have different orientations but the same magnitude of spin angular momentum. Electronic angular momentum (S) gives rise to magnetic moment (μ_e). Both μ_e and S are equal in magnitude and opposite in direction (proportionality constant μ_B in negative) and related by following equation.

$$\mu_e = g\mu_B S \qquad \text{Eq. 3.1}$$

In eq 3.1 "g" is a constant called g-factor and μ_B (Bohr magneton) is also a constant. The α and β states of a free electron in the presence of a static magnetic field are shown schematically in Figure 3.2.

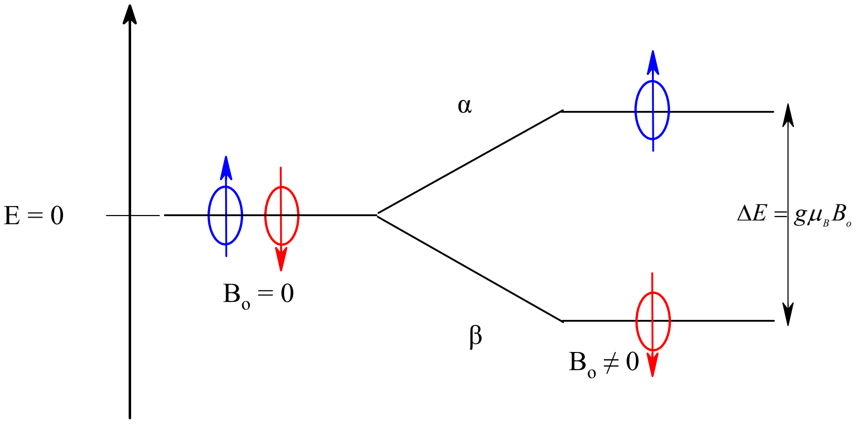

Figure 3.2: Spin states of an electron in the absence and presence of the applied magnetic field B_o.

As electron spin energy is a scalar product of magnetic moment (μ_e) and applied magnetic filed (B), the energy difference between α and β states of a free electron is given by equation 3.2.

$$\Delta E = g\mu_B B_o \qquad \text{Eq 3.2}$$

In EPR, magnetic field is swept keeping the frequency of electromagnetic radiation constant. As the magnetic field strength matches the energy difference between electron spin states (i.e. α and β), the inversion of the spin state occurs. The energy absorbed for inversion / transition of electron from one state to the other is recorded. EPR spectra are usually recorded as first derivative of the absorbed energy against applied magnetic field. The first derivative is used to improve the resolution and to decrease the background noise. An example of a first derivative of absorbed energy vs magnetic field is shown in Figure 3.3.

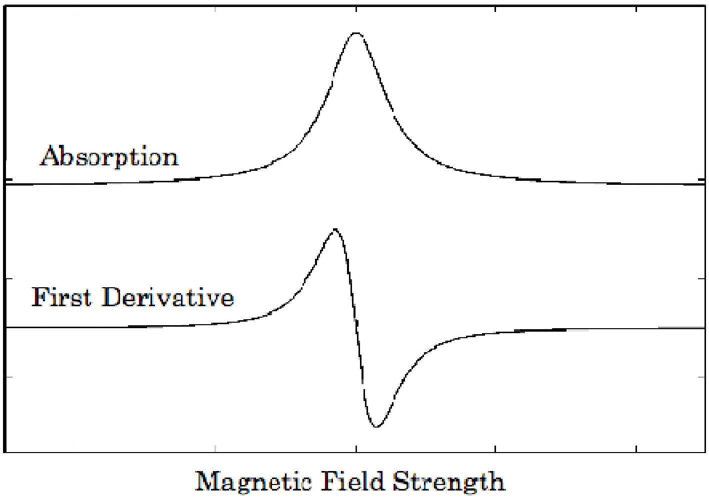

Figure 3.3: EPR absorption curve and its first derivative.

3.1.1.2 The anisotropic g-tensor

“g” factor is a constant and a free electron has “g” (i.e. g_e) value 2.002319.
Equation 3.2 implies that the position of EPR signal depends on the “g” factor for a given field B_o. For example, in the case of organic free radical (especially when they contain only light atoms), the “g” values are very close to “g_e” (i.e. $\Delta g \sim 0$) and hence provide relatively little structural information. On the other hand, Δg may be significant for heavy atoms. The “g” factor becomes more important for structure determination when hyperfine splitting (described in the next section) is not observed.

The value of “g” factor may depend on the direction of magnetic field with respect to molecular axes. In general the “g” factor is a rank 2 tensor defined by the principal values which often correspond to molecular axes. This anisotropic behaviour of “g” factor can be illustrated by TEMPO (2,2,6,6-tetramethyl pyrrolidine-N-oxyl) free radical as shown in Figure 3.4.

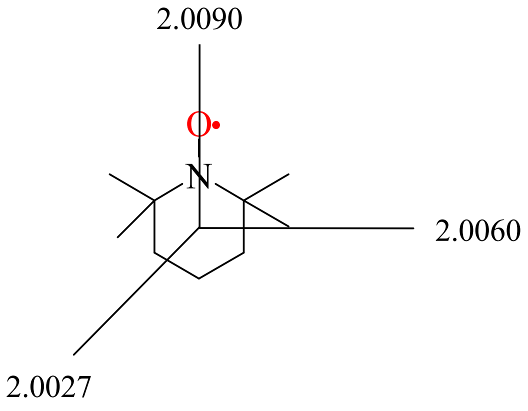

Figure 3.4: Chemical structure of TEMPO radical with anisotropic principal values of the "g" tensor.

3.1.1.3 Hyperfine interactions

The presence of magnetic nuclei with $I \neq 0$ affects the transition of electrons. As a result of this coupling between electron and nuclear spins, EPR signal of unpaired electron is split into more than one line. This splitting is called "Nuclear Hyperfine Splitting" and the strength of the hyperfine interaction is given by a hyperfine constant "A". The spacing between the split lines determines the extent of hyperfine coupling.

The number of lines in a splitting pattern depends upon the nuclear spin and the number of magnetically equivalent nuclei and is determined by eq. 3.5.

$$\text{No of lines} = 2nI + 1 \qquad \text{Eq 3.5}$$

Here n is the number of equivalent nuclei and I is the nuclear spin.

The hyperfine splitting is very helpful for structure elucidation. An example of nuclear hyperfine splitting found in nitroxide radical is shown in the Figure 3.5. The nitroxide EPR spectrum consists of three lines due to hyperfine coupling of unpaired electron with one N atom (I = 1).

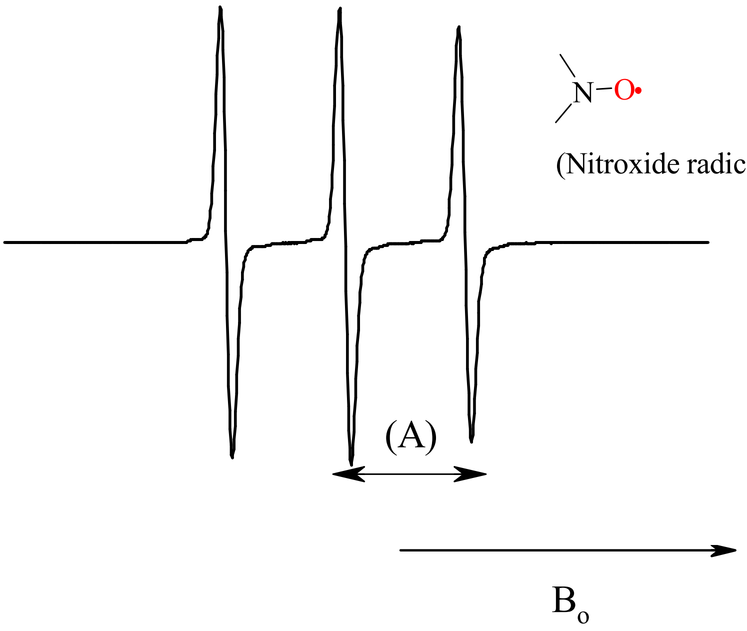

Figure 3.5: EPR spectrum of a free nitroxide in a fluid solution showing isotropic hyperfine coupling ("A" is the hyperfine splitting, B_o is applied magnetic field).

3.1.1.4 Mechanism of the hyperfine interactions

There are two mechanisms of hyperfine interaction.

1. Fermi Contact (isotropic)
2. Dipole-dipole (anisotropic)

The Fermi contact usually dominates in dilute solutions of rapidly tumbling systems. In rapidly tumbling systems, the anisotropic contributions average out to zero and spectra like in Figure 3.5 are observed. The Fermi contact interaction mathematically is given as:

$$U = -\frac{8}{3}\pi(\mu_n.\mu_e)\psi^2(o) \qquad \text{Eq 3.6}$$

In eq 3.6, U is the energy of interaction, μ_n is the nuclear magnetic moment, μ_e is the electron magnetic moment, and $\Psi^2(0)$ is spin density at the nucleus. Fermi contact interaction can occur only for electrons with s-character. Isotropic interactions are also encountered in systems with unpaired electrons in p, d and f-orbitals. In such systems, the isotropic hyperfine is explained by mechanisms like configuration interactions or spin polarization.

Dipole-dipole interactions are classical interactions between electron spin magnetic dipole and nuclear spin dipole moment. The magnetic field generated by nuclear moments is experienced by electron spins. The dipole-dipole hyperfine interactions are usually important for paramagnetic systems in solid, crystal and other cases where molecules are not tumbling very fast. In such systems all orientations are present and anisotropic interaction dominates the spectrum. For example, nitroxide radical is anisotropic i.e. its EPR spectrum depends on its orientation with respect to the direction of the external magnetic field. EPR spectra of an individual nitroxide molecule in different orientations are shown in Figure 3.6.

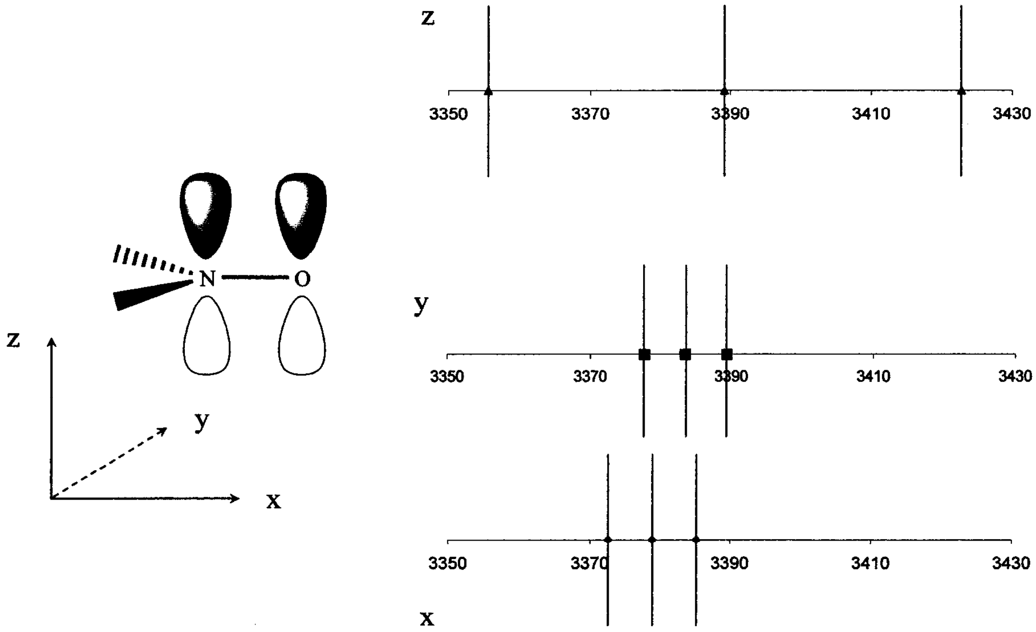

Figure 3.6: Single crystal spectra of nitroxide in three directions of nitroxide frame.[8]

Figure 3.6 shows that when the direction of external magnetic field is changed, the distance between hyperfine extrema and central line (hyperfine splitting) changed uniformly. In the spectra of frozen solutions, spins are orientated randomly with respect to the magnetic field and the resulting spectrum is the sum of the contribution of all the orientations as explained in Figure 3.7. The hyperfine splitting tensor ⟨A⟩ can be obtained by simulation of such powder / frozen spectra.

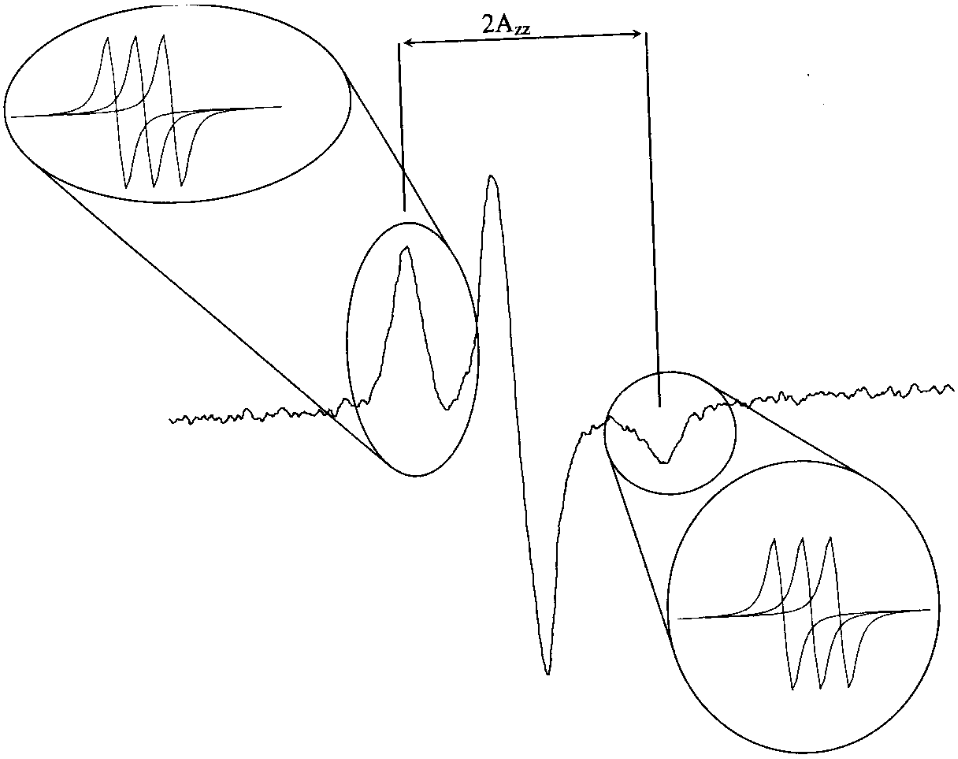

Figure 3.7: Frozen solution spectrum of a nitroxide in toluene. In sets: the overlapping of 1st derivative features yields the positive and negative signals at low and high field respectively.[8]

"g" is also anisotropic but at X-band region of the microwave frequency "A" anisotropy dominates.

Consequently the tumbling rate of species on a ns (nanosecond) time scale has a direct effect on hyperfine interactions, which defines the line shape (and line width) of the EPR spectra. By analysing / simulating line shape of EPR spectra, tumbling rate of species under question can be determined. The tumbling rate of nanoparticle-attached DTPA ligand was determined using EPR spectroscopy and is discussed in the next section.

3.2 Vanadyl complexation with DTPA and DTPA based ligand@AuNPs

To assess the tumbling rate (i.e. rotational correlational time) of nanoparticle-attached DTPA ligand using EPR spectroscopy, Gd^{3+} needed to be replaced with some other paramagnetic ion due to the following reasons:

- Gd^{3+} is paramagnetic (due to seven unpaired electrons), but its EPR spectrum consists of only one broad line due to spin-spin interactions between unpaired electrons (Figure 3.8).
- As no hyperfine splitting is observed in Gd^{3+} EPR spectrum, hence it is isotropic and is not affected by changing the motion of the Gd^{3+}.

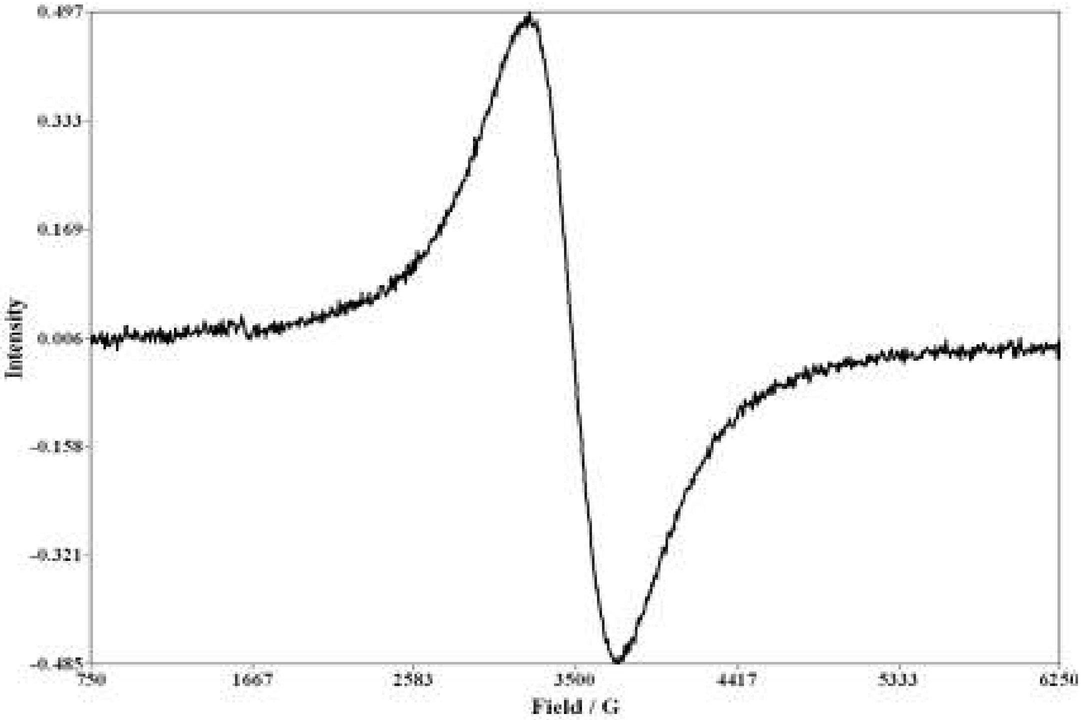

Figure 3.8: EPR spectrum of Gd^{3+} (i.e. aq solution of $GdCl_3$).

The alternative paramagnetic ion must be able to bind with DTPA and DTPA based ligands and its EPR spectrum should be motionally sensitive.[9]

In this work, vanadyl cation (VO^{2+}) was used for this purpose. Vanadium (^{51}V) is a transition metal that exhibits +2 to +5 oxidation state. Vanadyl has coordination number six, one is already occupied by oxygen, the remaining five can chelate with octadentate DTPA and DTPA based ligands[9]. Vanadyl (VO^{+2}) is one of the most stable diatomic cations with a $3d^1$ configuration that makes it EPR active.[10]

Chen *at al.*[10] reported that vanadyl can be used to determine the tumbling rate of MRI contrast agents by replacing Gd^{3+} with vanadyl. As vanadyl possesses very anisotropic hyperfine (A) and Zeeman (g) tensors as well as large nuclear spin (I = 7/2, 100 % natural abundance), it is very sensitive to small changes in the motion.

VO^{2+}-DTPA@AuNPs (Figure 3.9) were prepared using a modified literature[11] procedure and then characterized by EPR spectroscopy to determine the tumbling rate of nanoparticle-attached ligand. The ratio between vanadyl and DTPA based ligand at AuNPs surface was kept 1 : 3, to avoid any spin-spin interactions among vanadyl ions. High concentration of AuNPs was used as VO^{2+} binding to DTPA is weak.

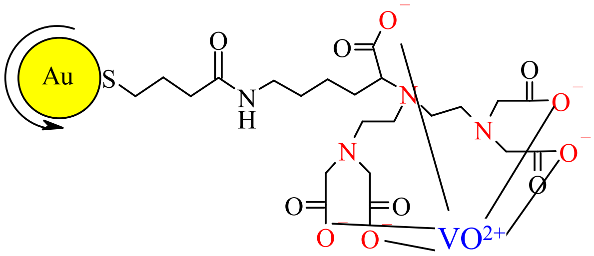

Figure 3.9: Vanadyl complexed with DTPA ligand@AuNPs.

3.2.1 Determination of principal values of “g” and “A” tensors for free VO^{2+} and VO^{2+}-DTPA@AuNPs

Principal values of “g” and “A” tensors need to be accurately known to determine τ_R of nanoparticle-attached ligand by simulating room temperature EPR spectra (discussed in the next section). As described in sections 3.1.1.2-3.1.1.3, the anisotropic “g” and “A” tensors can be obtained by fitting the EPR spectra of frozen solutions (e.g. immobilised). We prepared $VOSO_4$ (free VO^{2+}) and VO^{2+}-DTPA@AuNPs solutions in 10 % glycerol (in deionised water) and recorded their EPR spectra. The 10% glycerol was used as a solvent as it forms good glassy state at low temperature.

The EPR spectra were recorded at 130 K and the magnetic field was calibrated using DPPH (2,2-diphenyl-1-picrylhydrazyl). The EPR spectra of free vanadyl ($VOSO_4$) along with DPPH at 130 K (i.e. in frozen form) are shown in the Figure 3.10.

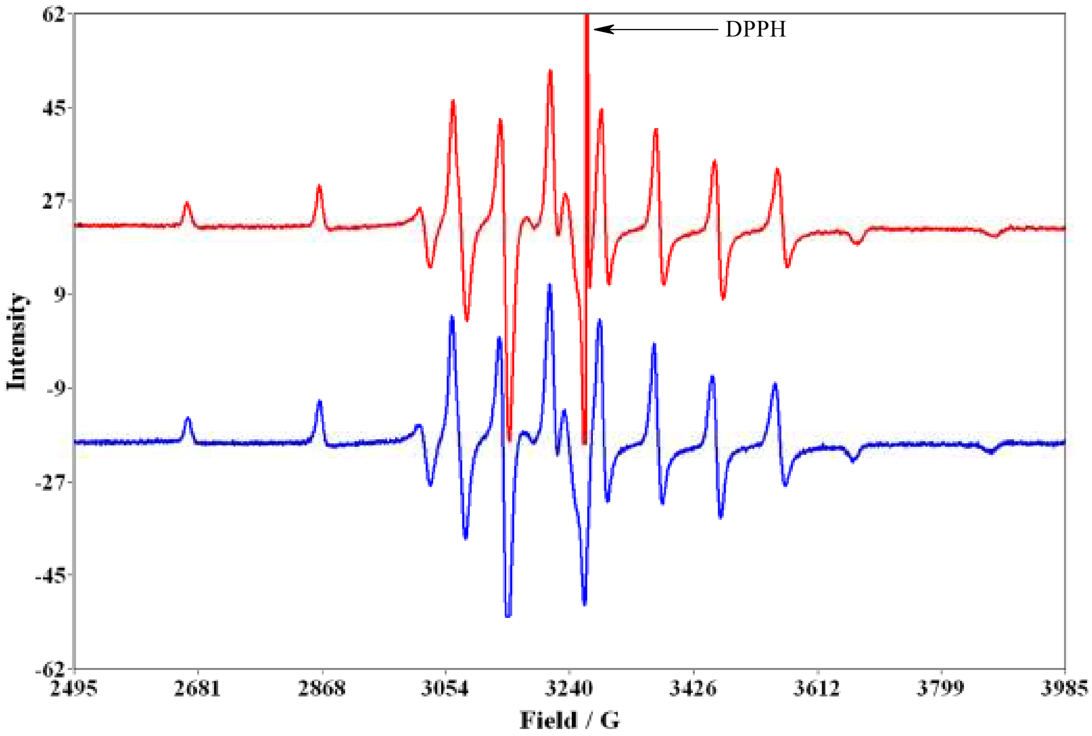

Figure 3.10: EPR spectrum of free vanadyl with (red) and without (blue) DPPH at 130 K.

As discussed earlier (section 3.1.1.4), the EPR spectra depend on molecular orientation with respect to applied magnetic field and the spectra of frozen solutions thus include a sum of spectra in different orientations.

The simulated EPR spectra of vanadyl molecule in different orientations with respect to applied magnetic field and of frozen vanadyl solution are shown in Figure 3.11. For simulation, axial symmetry of the vanadyl molecule was assumed.

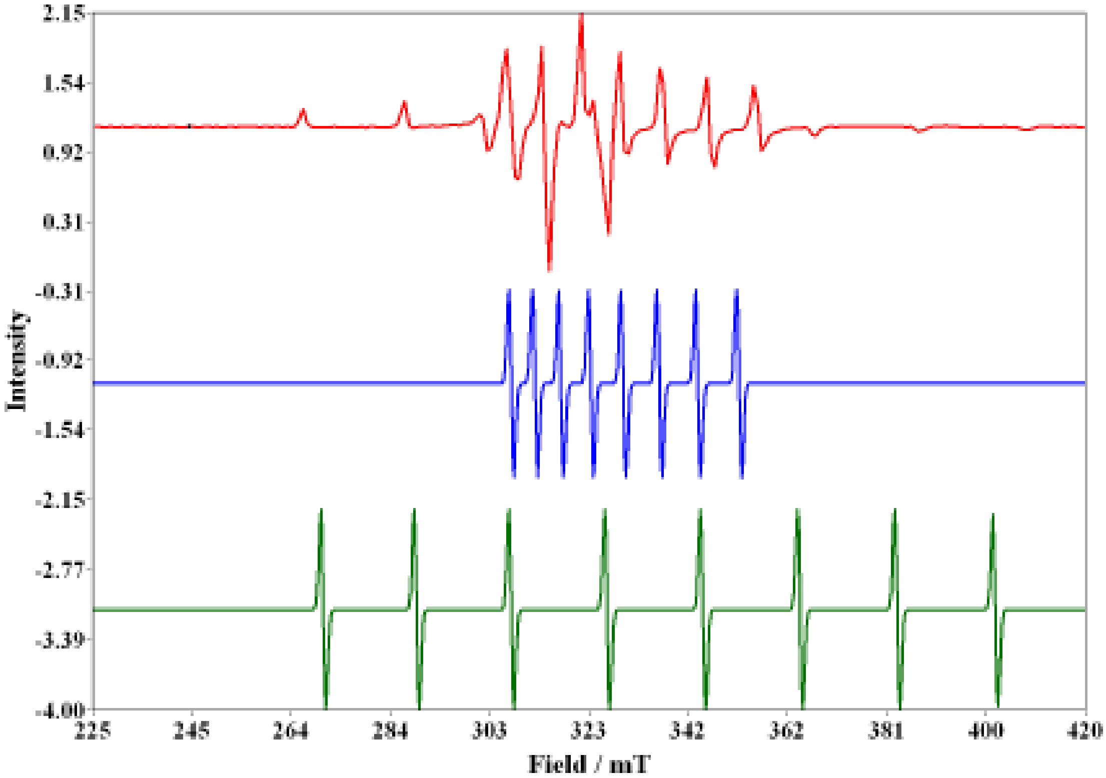

Figure 3.11: Simulated EPR spectra (red for powder, blue for parallel and green for perpendicular orientation of vanadyl to applied magnetic field).

The EPR spectrum of vanadyl exhibits eight lines due to one unpaired electron (and I = 7/2) (Figure 3.11). Due to large value of hyperfine coupling, the hyperfine components are not equally spaced (first order approximation thus cannot be used). The EPR spectrum in frozen form is quite complex (Figure 3.11 red). However certain features in this spectrum correspond to EPR spectra of vanadyl in parallel and perpendicular orientations (Figure 3.11 green and blue). These characteristic features are very important as they allow us to estimate the magnetic parameters (g and A tensors) in parallel and perpendicular orientations of applied magnetic field. These estimates are then used as a starting point for simulations to get accurate values of “g” and “A” tensors.

The experimental EPR spectrum of frozen vanadyl (Figure 3.10) is similar to that of the simulated spectrum (Figure 3.11 red). The fitting of experimental EPR spectra of free vanadyl and VO-DTPA@AuNPs was done using easyspin[12] and the values of g and A-tensors are given in Table 3.2. The experimental and simulated EPR spectra for free vanadyl and VO-DTPA@AuNPs are shown in Figures 3.12.

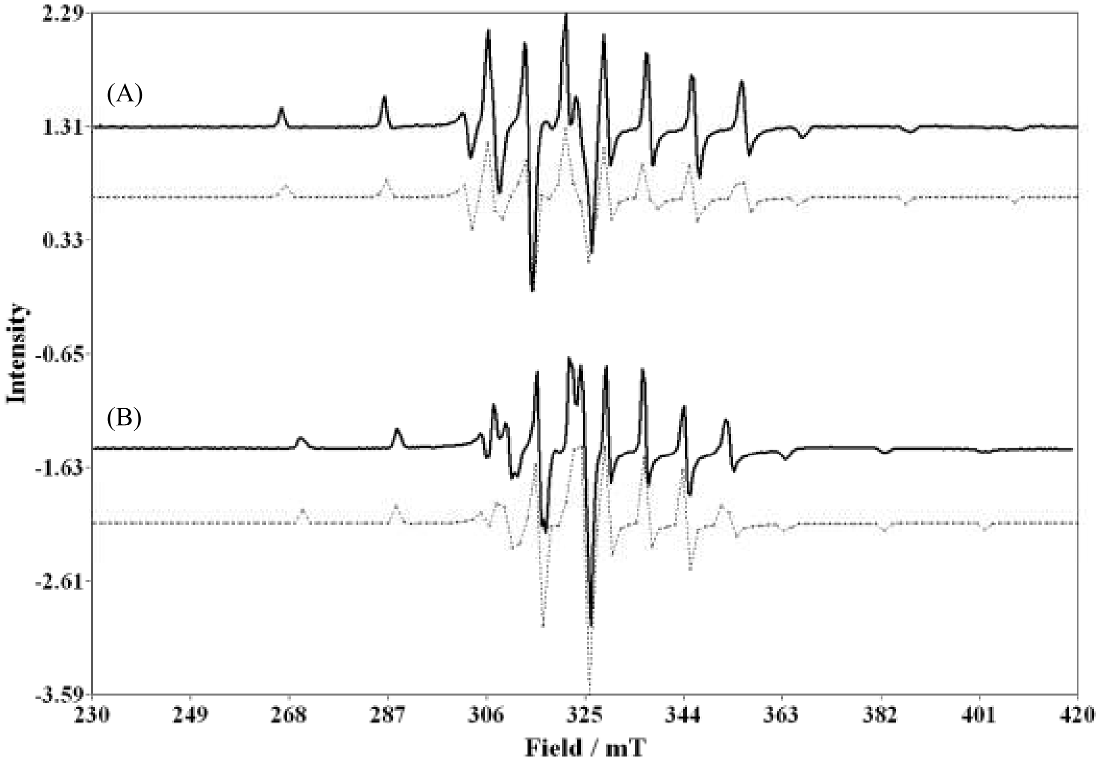

Figure 3.12: Experimental (thick lines) and simulated (thin lines) EPR spectra of free vanadyl (A) and VO-DTPA@AuNPs (B) at 130 K.

Table 3.2 Magnetic parameters of free VO^{2+} and VO-DTPA@AuNPs.

S. No.	**Paramagnetic species**	**A / MHz**			**g**		
		A_{xx}	**A_{xy}**	**A_{zz}**	**g_{xx}**	**g_{xy}**	**g_{zz}**
1	$VOSO_4$	207.3	210.4	543.9	1.9772	1.9708	1.9338
2	VO-DTPA@AuNPs	175.1	187.0	511.7	1.9755	1.9783	1.9412
3	*** VO-DTPA**	186.1	172.0	508.2	1.980	1.978	1.944

***Literature values**

3.2.2 Determination of rotational time from room temperature EPR measurements

Rotational time (τ_R) is defined as the time required for a species to rotate by one radian.[13] The incomplete averaging of “A” and “g” tensors for structures that do not tumble rapidly, affects the line shape. Therefore, simulation of EPR spectra makes it possible to determine τ_R. The τ_R for free vanadyl and VO-DTPA at AuNP surface were thus determined by simulating their room temperature EPR spectra using accurately determined “g” and “A” tensor values from the frozen solution spectra. The tumbling of VO^{2+} species was assumed to be isotropic. The room temperature EPR spectra (Figure 3.13) show a linehape characteristic of fast motion e.g. faster than the Redfield limit $\tau_R^{-1} >> \Delta\omega$. The τ_R^{-1} is the tumbling rate and $\Delta\omega$ is the anisotropy of the hyperfine and Zeeman interactions. Fast motion approximation significantly simplifies simulations.

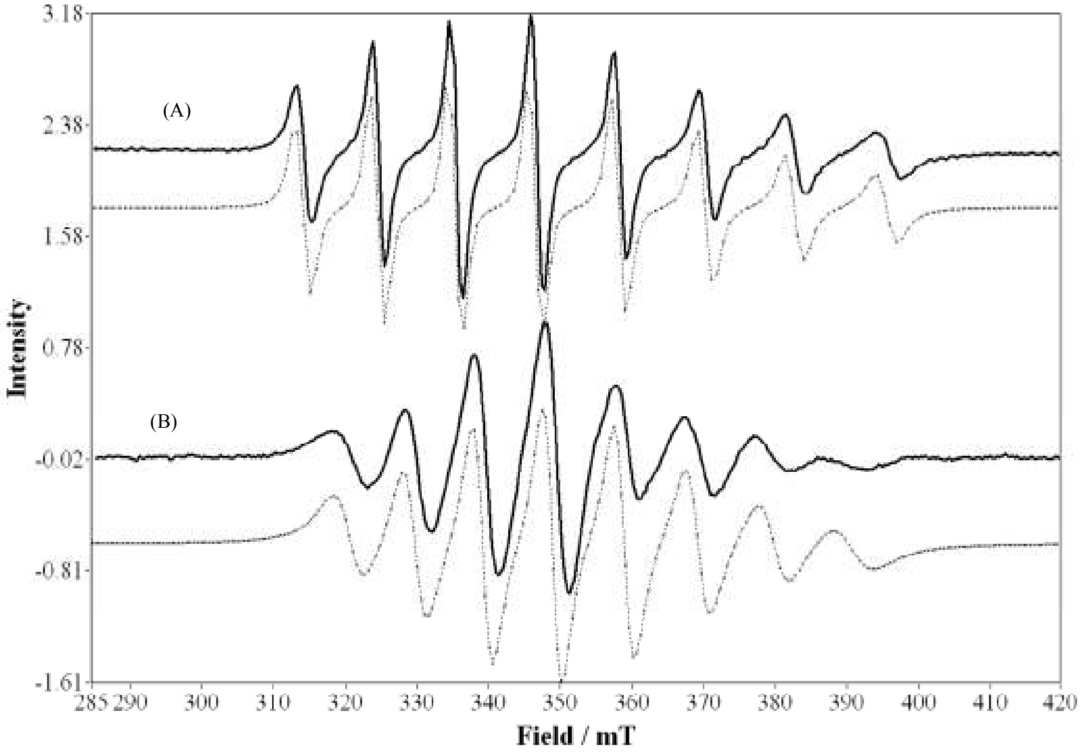

Figure 3.13: Experimental (thick lines) and simulated (thin lines) EPR spectra of free vanadyl (A) and VO-DTPA@AuNPs (B) at 298 K.

The τ_R values for free VO^{2+} and of VO-DTPA@AuNPs are shown in table 3.3. The τ_R of VO-DTPA@AuNPs was found to be only twice as long as for free VO^{2+}. This increase is not very large. The relatively high tumbling rate suggests that ligand molecules are not well packed at AuNP surface (ligand packing at nanoparticles surface is discussed in detail in section 3.4). The branching of DTPA units at the end of ligand molecule might be responsible for preventing tight packing of ligands at the AuNP surface.

Table 3.3 Rotational correlational time of free vanadyl and vanadyl-DTPA@AuNPs.

Paramagnetic Species	τ_R
$VOSO_4$ (Free VO^{2+})	4.52×10^{-11}s
VO-DTPA	4.84×10^{-11}s
VO-DTPA@AuNPs	1.03×10^{-10}s

3.3 Conclusions of EPR results

The EPR results showed that the DTPA based ligand molecules at the AuNP surface tumble relatively fast; attachment of ligands to nanoparticle surface only resulted in slowing down molecular tumbling by a factor of ca. 2. This fast tumbling is probably responsible for the only moderate increase in relaxivity of Gd-loaded AuNPs as compared to commercially available (small molecule based) MRI contrast agents.

The EPR data are important as they show the way to enhance the relaxivity by reducing the tumbling of nanoparticle-attached ligands.

We explored several strategies to reduce the tumbling of nanoparticle-attached ligand which may result in increased relaxivity of gold nanoparticle based MRI contrast agents. They are discussed in the following sections.

3.4 Growth of AuNPs

The first strategy which we used to reduce the tumbling rate of nanoparticle-attached ligand was increasing the core size of nanoparticles. As the size of AuNPs is increased, their curvature is decreased. At the surface of larger particles which have relatively small curvature, ligands are packed more tightly as compared to the surface of small nanoparticles. For example, Mei *et al.*[14] used similar arguments to account for the digestion rate of small and large gold nanoparticles by sodium cyanide. They concluded that the larger gold nanoparticles are digested slower due to smaller curvature leading to more tight packing of the ligands as compared to the smaller nanoparticles (Figure3.14).

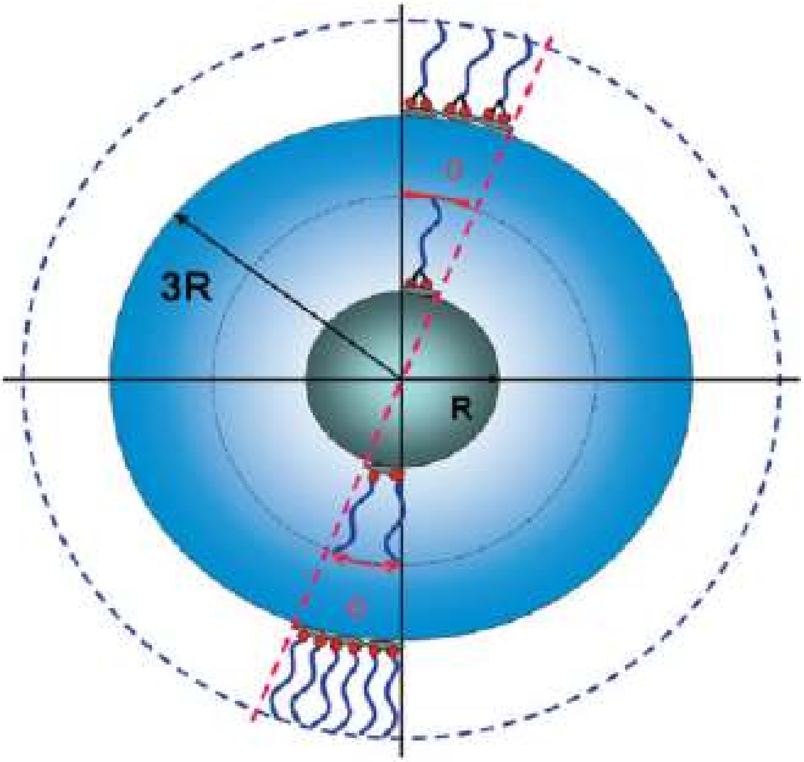

Figure 3.14: Ligand packing density at the surface of AuNPs having various diameters.[14]

It was speculated that the tight packing of ligand will result in reduced tumbling of nanoparticle-attached ligand, which will enhance the relaxivity.

Various methods have been reported in the literature[15-16] for increasing the size of gold nanoparticles based on Ostwald ripening phenomenon. According to this principle, discovered by Wilhelm Ostwald in 1896, larger particles are thermodynamically more stable due to their low surface to volume ratio (that results in lower surface energy). The molecules at the surface of smaller nanoparticles have high surface energy so they detach from the surface and reattach onto the surface of larger particles (Figure 3.15). Thus, the number of smaller particles decreases while larger particles continue to grow.

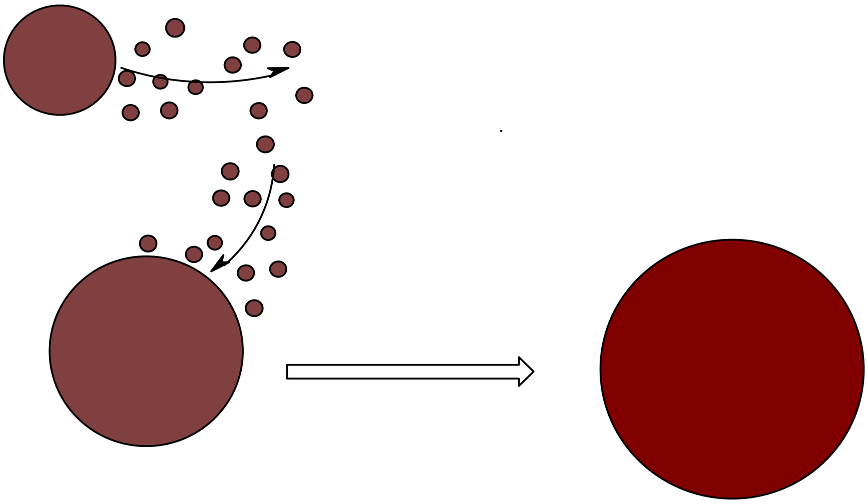

Figure 3.15: Schematic of the Ostwald ripening process.

The most common reported method for AuNP growth involves heating the AuNPs in the solid state. For example, Teranishi *et al.*[15] reported that when the thiol protected AuNPs are heated in the solid state at increased temperatures (i.e. 150, 190, 230 °C etc), their size increases to ~ 3.5, 5.5 and 7.0 nm, respectively. Similar results were observed by Shimizu *et al.*[17]

The alternative one step strategy to prepare gold nanoparticles with larger core sizes is by changing the ratio between Au and Ligand[16] during nanoparticle synthesis. Usually 1:1 ratio is used. By changing this ratio, the size of AuNPs can be tuned / changed. For example, Murray and co-workers[18] described in detail the effect of Au : ligand molar ratio between on the core size of the AuNPs. They reported the size of alkanethiols protected AuNPs was increased by increasing the ratio of gold to alkanethiols. This effect can be explained by slower ligand passivation as compared to the growth of incipient AuNPs at lower ligand / gold ratio.

The change in size of AuNPs can be easily monitored by intensity of surface plasmon band (SPB) using UV-Vis spectroscopy (as discussed in chapter 2, section 2.3.1). The bigger particles have more intense SPB as compared to the smaller particles (Figure 3.17).[15]

We tested several methods for increasing the size of AuNPs protected by DTPA based ligand **6**. In the first instance, freshly prepared AuNPs were heated in the solid state at 90-200 °C, but no significant increase in AuNP diameter (shown by UV-Vis spectra, Figure 3.16) was observed. Even heating for longer period (i.e. for 12-24 h) and at high temperature (i.e. 230-280 °C) failed to increase the size of the small AuNPs.

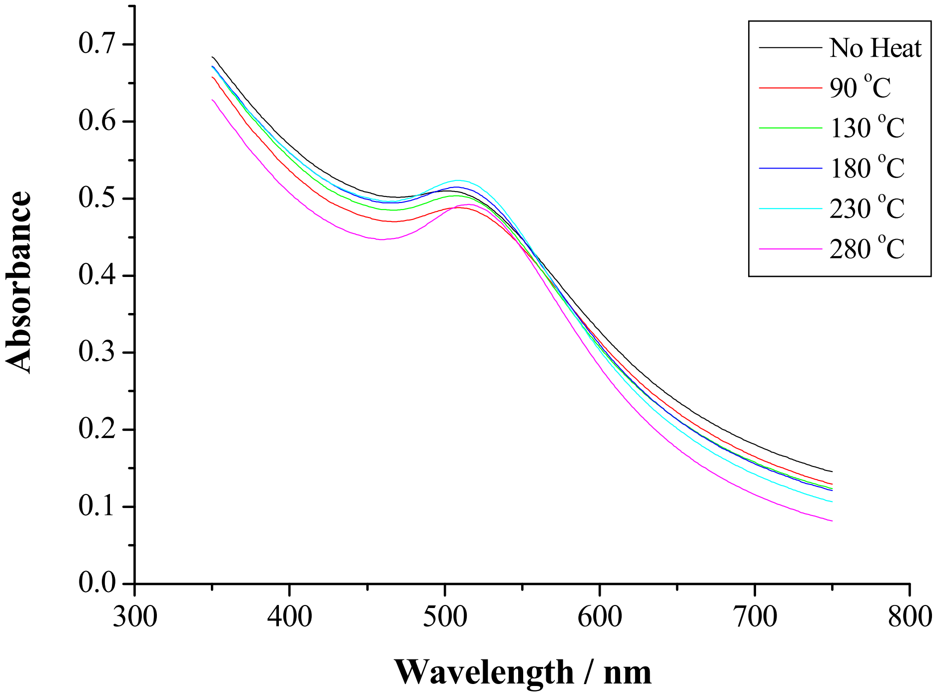

Figure 3.16: UV-Vis spectra of small AuNPs heated at various temperatures in solid state.

The second strategy was to vary the ratio between gold and ligand during synthesis. Various ratios between gold and ligand such as 3/1, 5/1, 7/1 were used. No significant difference in size was observed by UV-Vis spectra, moreover the AuNPs were not very stable. So this method was ruled out for growing the DTPA based ligand protected AuNPs.

In a third approach, the crude aqueous solution of freshly prepared AuNPs was heated at reflux and the increase in nanoparticle size was monitored by UV-Vis spectroscopy. The crude AuNP synthesis mixture contained excess ligands which were needed for stabilisation of AuNPs. The reflux temperature (i.e. boiling point) of aqueous solution of AuNPs was increased by addition of ca. 20% v/v DMF. This method was successful and UV-Vis spectra of grown AuNPs are shown in Figure 3.17. The exact diameter of grown AuNPs was then confirmed by TEM (discussed in next section 3.4.1.1).

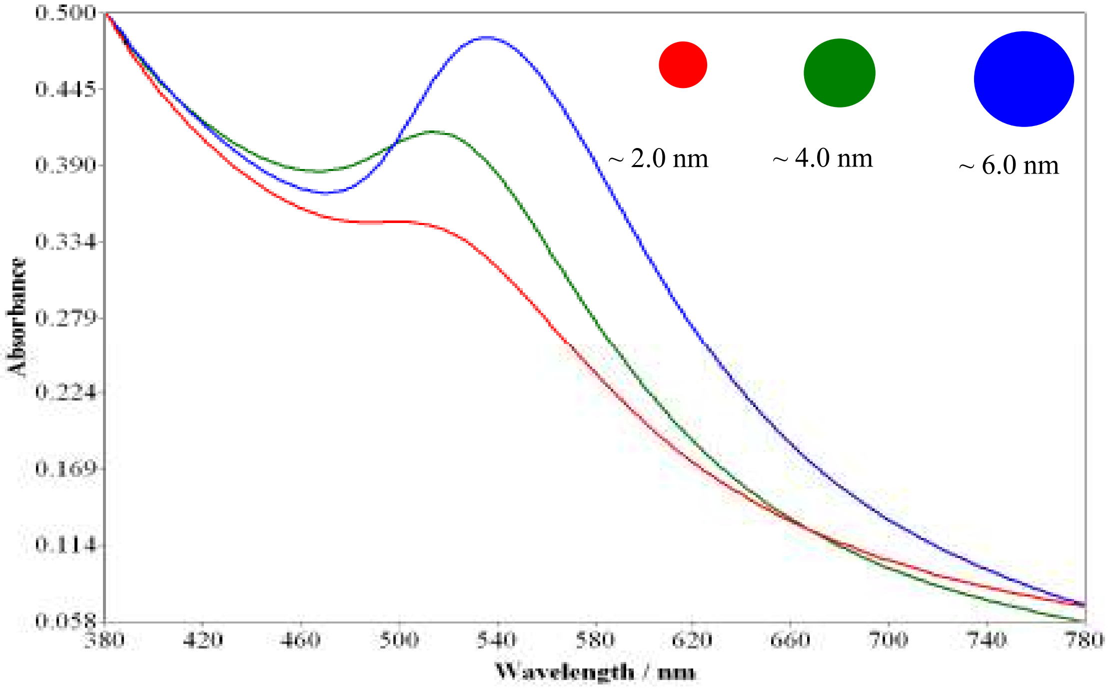

Figure 3.17: UV/Vis spectra of small and large AuNPs.

After the growth of aq AuNPs, DMF was removed by dialysis against deionised water using 12-14 kDa dialysis tubing. The excess ligands were removed by gel permeation chromatography using 0.1 M NaCl as an eluent and Sephadex gel (G-100) as a stationary phase. The purified larger AuNPs were again dialysed against deionised water to remove NaCl. The water was evaporated to get solid grown AuNPs protected by DTPA ligand **6**.

3.4.1 Characterisation of grown AuNPs

The grown AuNPs were characterised by TEM, TGA, AAS and ICP (after loading with Gd).

3.4.1.1 Transmission electron microscopy (TEM) analysis

The TEM analysis of the grown gold nanoparticles was carried out to determine the exact diameter and level of aggregation. The TEM analysis was done in the same way as for small gold nanoparticles (discussed in chapter 2) i.e. by placing a drop of aq solution of grown AuNPs on a copper grid, allowing the solvent to evaporate to dryness and then analysing by TEM. The TEM images along with size distribution histograms for grown AuNPs obtained by refluxing freshly prepared aq AuNPs with addition of DMF are shown in Figures 3.18 and 3.19. The TEM picture also showed that gold nanoparticles are well dispersed.

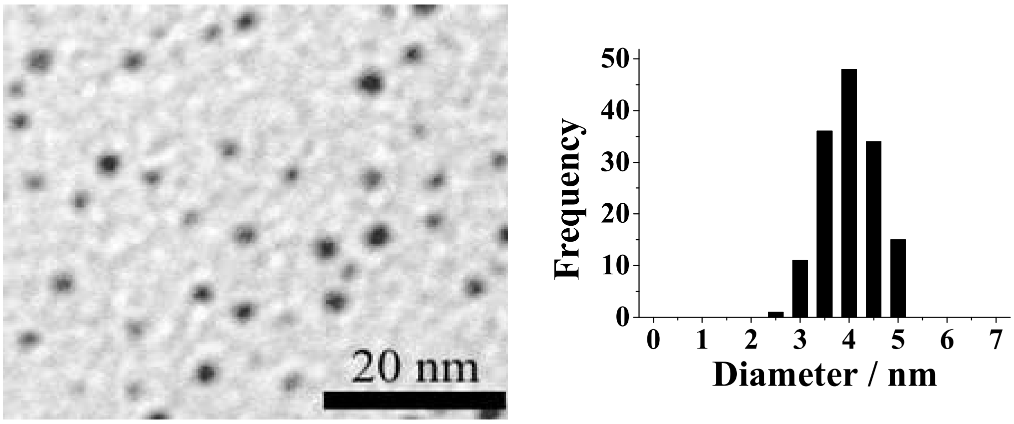

Average Diameter = 3.74 ± 0.58 nm

Figure 3.18: TEM image and size distribution histogram for grown AuNPs (~4.0 nm).

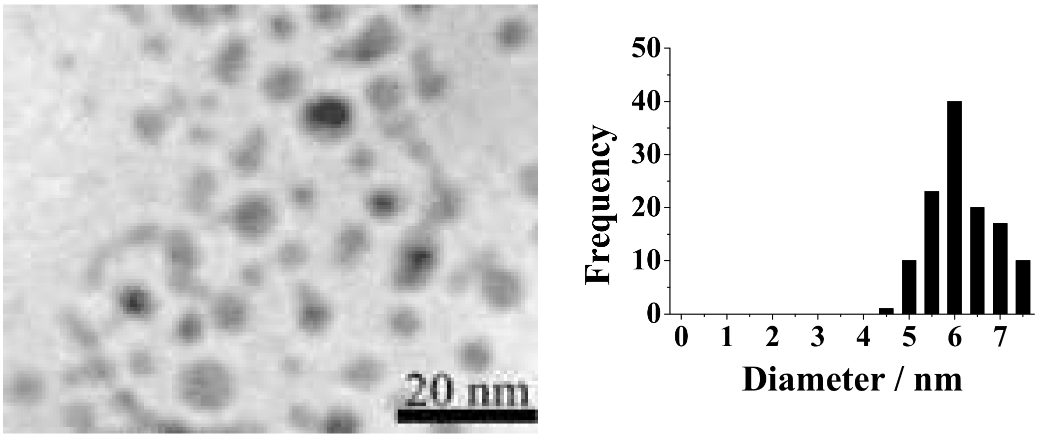

Average Diameter = 6.05 ± 1.07 nm

Figure 3.19: TEM image and size distribution histogram for grown AuNPs (~6.0 nm).

3.4.1.2 Thermogravimetric analysis (TGA) of grown AuNPs

TGA of grown AuNPs was carried out in order to determine the organic content of AuNPs. The TGA data for grown AuNPs along with small AuNPs (~2.0 nm) is shown in the Figure 3.20 which indicates the decreased organic content with increased particle size. The 4.0 nm AuNPs showed ~17 % organic content and 6.0 nm AuNPs showed 8.0 % organic content.

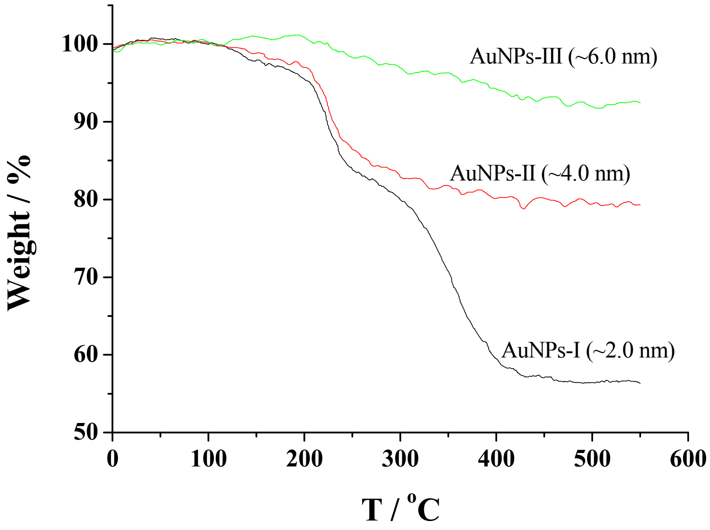

Figure 3.20: TGA graphs of small AuNPs (black) and large (red for 4.0 nm and green for 6.0 nm) AuNPs.

The ratio between gold and protecting ligand (Au / Ligand) was increased with increased particle size because a greater proportion of the Au is located in the core rather than at the surface. Therefore, fewer ligand molecules are required for stabilisation of the larger AuNPs. This is well established in the literature.[15] The TGA graphs for grown AuNPs are shown in Figure 3.20.

3.4.1.3 ICP and AAS analysis of Gd-loaded large AuNPs

The AuNPs were analysed by ICP, AAS and UV-Vis spectroscopy after loading with gadolinium and results are shown in Table 3.4.

Table 3.4: ICP, UV/Vis and AAS data for large (4.0 nm & 6.0 nm) Gd-loaded AuNPs.

Technique	**Element**	**AuNPs diameter**	**Metal content / %**
ICP	Gd	4.0 nm	4.21
		6.0 nm	2.57
UV/Vis	Gd	4.0 nm	4.39
		6.0 nm	2.32
AAS	Au	4.0 nm	70.35
		6.0 nm	82.25

The results of different techniques are quite comparable to each other. The Gd content was later used to determine the relaxivity of Gd-loaded AuNPs. The increased gold content in grown AuNPs as compared to small AuNPs is also confirmed by TGA analysis (as discussed in section 3.4.1.2.).

3.4.2 Composition of grown AuNPs

Composition of large AuNPs was calculated by the same method as for the small AuNPs (discussed in chapter 2). The average nanoparticle composition was calculated for ~4.0 nm and ~6.0 nm Gd-loaded AuNPs:

$Au_{1543}\,Ligand_{160}\,Gd_{128}$ *(~ 4.0 nm AuNPs)*

$Au_{8429}\,Ligand_{65}\,Gd_{65}$ *(~ 6.0 nm AuNPs)*

3.4.3 Rotational time (τ_R) of ligand in large (4.0 and 6.0 nm) AuNPs

The large AuNPs were complexed with vanadyl as described in section 3.3. The ratio between VO^{2+} and DTPA ligand@AuNPs was kept 1 / 3 in order to avoid spin-spin interaction. The τ_R of grown (~4.0 nm and 6.0 nm) gold nanoparticles were determined by simulating room temperature EPR spectra. The τ_R of free vanadyl, VO-DTPA, VO-DTPA@AuNPs (~2.0 nm) VO-DTPA@AuNPs (~4.0 nm) and VO-DTPA@AuNPs (~6.0 nm) are shown in Table 3.5.

Table 3.5: Rotational correlational time of VO^{2+}, VO-DTPA and VO-DTPA@AuNPs.

Paramagnetic Species	**τ_R / s**
$VOSO_4$ (Free VO^{2+})	4.52×10^{-11}
VO-DTPA@AuNPs (~2.0 nm)	1.03×10^{-10}
VO-DTPA@AuNPs (~4.0 nm)	1.25×10^{-10}
VO-DTPA@AuNPs (~6.0 nm)	1.90×10^{-10}

The τ_R of the ligand in large (4.0 & 6.0 nm) AuNPs was not found to be significantly different from the ligands in small AuNPs, but the τ_R in larger AuNPs (~6.0 nm)-attached ligand was found to be reasonably higher (i.e. 4 fold) than that of free vanadyl. The increased τ_R with the increase in nanoparticle size suggested the decreased tumbling of ligand at the surface of relatively larger AuNPs which might give higher relaxivity of nanoparticle based MRI contrast agents. The effect of decreased tumbling rate on relaxivity is discussed in the following section.

3.4.4 Relaxivity measurements of large AuNPs

Relaxivity measurements of large (~4.0 nm and ~6.0 nm) Gd-loaded AuNPs were carried out using the same method as for the small Gd-loaded AuNPs. The R_1 values for small and large Gd-loaded AuNPs are shown in Table 3.6.

It was observed that r_1 increased steadily with increased size of AuNPs. The increase in r_1 is directly attributed to the decreased tumbling of nanoparticle-attached ligand in larger AuNPs as compared to small AuNPs as discussed in section 3.5. In the larger AuNPs, the higher packing density of ligand due to tight packing resulted in higher relaxivity (Figure 3.14).

Table 3.6: Relaxivity values of small and large AuNPs.

Gd-loaded gold nanoparticles	**Relaxivity / $mM^{-1}s^{-1}$**
~ 2.0 nm	4.77
~ 4.0 nm	8.34
~ 6.0 nm	11.04

Although larger AuNP based contrast agents have higher (about 3 fold) relaxivity than the small AuNPs, there are some disadvantages associated with larger AuNPs which might not favour their use for real applications as MRI contrast agents. The larger AuNPs are relatively less stable[19] and hence may be more toxic as compared to the small AuNPs. Overall, our strategy of increasing nanoparticle size for increasing relaxivity was successful but due to disadvantages (associated with large nanoparticles) alternative methods / strategies were explored for increasing relaxivity of small gold nanoparticle based MRI contrast agents. This is discussed in the next section.

3.5 Polyelectrolyte self assembly around nanoparticles

An alternative strategy to decrease the tumbling of nanoparticle-attached ligands (in order to enhance the relaxivity of gold nanoparticle based MRI contrast agents) could include increasing the rigidity of the nanoparticle-attached ligands. The gold nanoparticles protected by DTPA based ligand have overall significant negative charge as each Gd-DTPA chelate has a -2 charge. The flexibility of charged nanoparticle-attached ligands can thus be reduced by adsorbing oppositely charged polyelectrolytes.

Polyelectrolytes are reported[20] to self assemble around charged species i.e. positively charged polyelectrolytes can form self assembled layers around negatively charged species and vice versa. The main driving force for this assembly is electrostatic interactions. Multilayered materials can be prepared by layer by layer (LBL) self assembly technique. The LBL technique was developed in 1997 by G. Decher.[21] The LBL involves the alternating deposition of oppositely charged polyelectrolytes on charged templates. For example as shown in Figure 3.21, the positively charged solid substrate was selected as a template and on this solid substrate the polyelectrolyte layers can be deposited by simply dipping it into solutions containing charged polyelectrolyte of interest. After formation of each layer, the excess / unbound molecules can be removed by washing with a suitable solvent. The multilayer build up based on LBL is schematically shown in Figure 3.21.

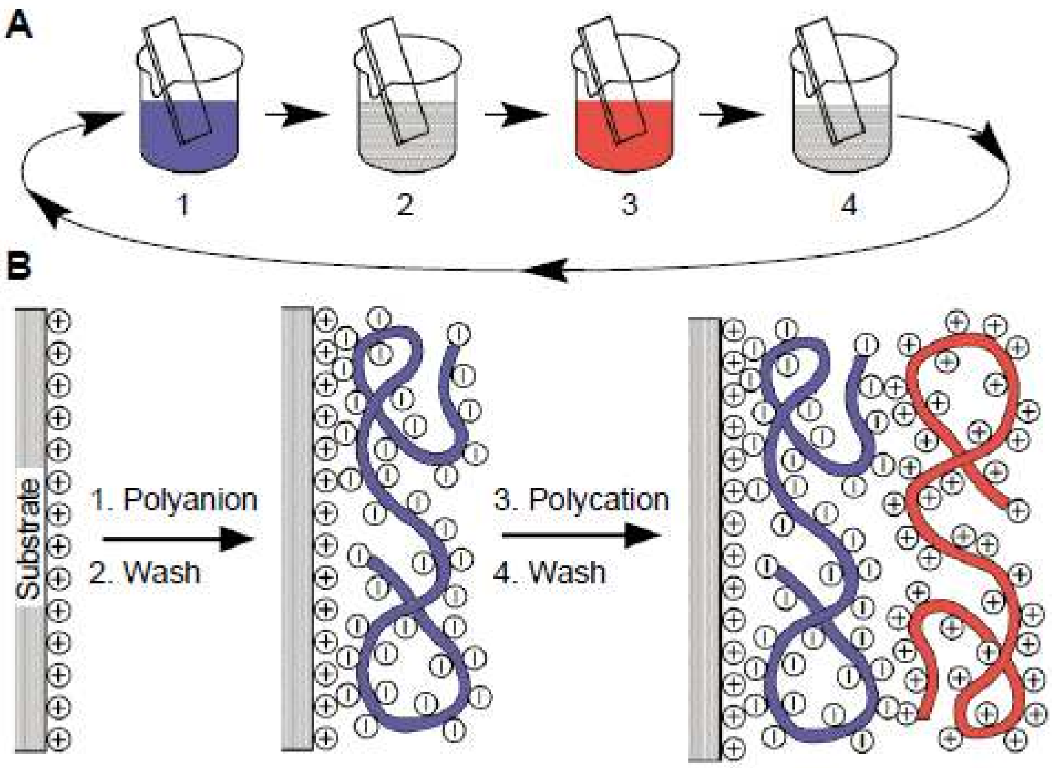

Figure 3.21: Schematic diagram of layer by layer (LBL) self assembly ("A" for film deposition process and "B" for simplified molecular picture) by consecutive adsorption of cationic and anionic polyelectrolytes on positively charged solid substrate.[21]

The LBL principle can also be used to form multilayers of polyelectrolytes using charged particles as templates. The charged particles are usually used to prepare micro- and nanometre sized capsules, as the particle core after formation of polyelectrolytes layers can be destroyed / dissolved by suitable solvents to get hollow microcapsules. The micro- and nanometre sized capsules have wide range of applications in drug delivery systems, gene therapy and biosensor devices. For example, Kotov *et al.*[22] successfully reported polyelectrolyte multilayer formation around nanoparticles (Figure 3.22). Polyelectrolytes have also been reported to self-assemble on the surface of charged gold nanoparticles.[23-24]

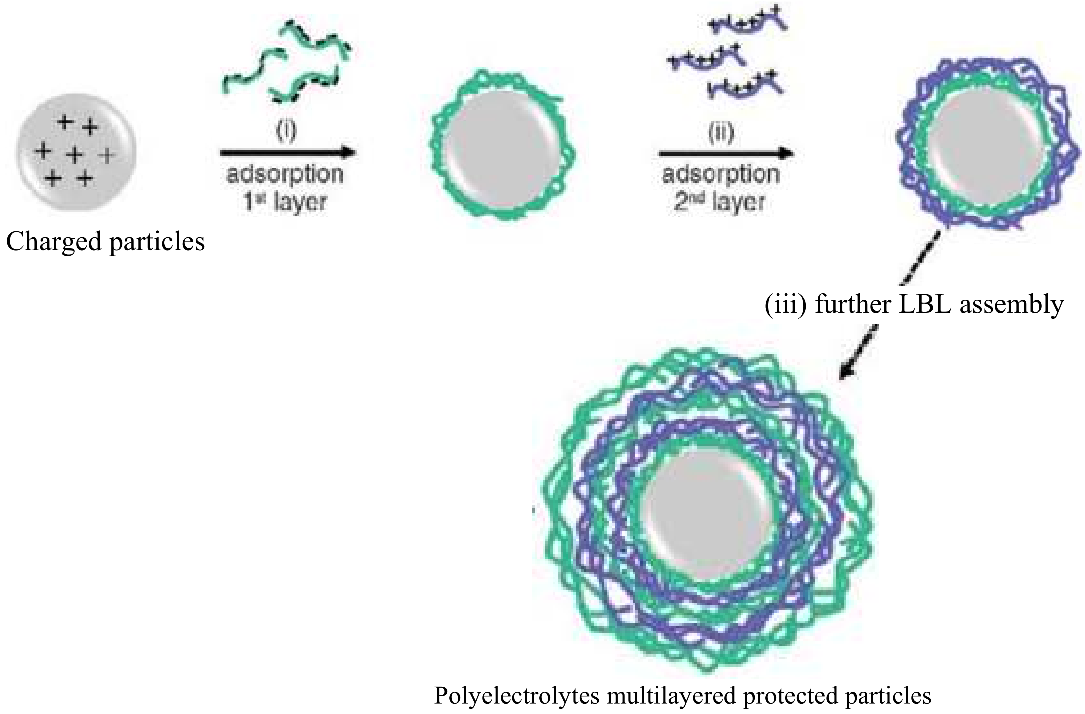

Figure 3.22: Schematic illustration layer by layer self assembly of oppositely charged polyelectrolytes at a charged particle surface.[23]

The negatively charged Gd-loaded AuNPs were reacted with various oppositely (positively) charged polyelectrolytes (discussed in the following sections) to form polyelectrolyte layers around gold nanoparticles. We hoped that adsorption of a polymer layer on the Gd-loaded AuNPs will slow down molecular tumbling (and enhance relaxivity) without adversely affecting the diffusion of water molecules.

3.5.1 Poly (ethyleneimine) (PEI) coating on Gd-loaded AuNPs

PEI is a cheap commercially available organic polymer (Figure 3.23). It is a weakly basic aliphatic water soluble polyelectrolyte. PEI has high density of amino groups that can be protonated at pH lower than 10 and in acidic medium PEI showed maximum protonation (Figure 3.23).[25] As pH was kept slightly basic (7.5-8.0) during PEI coating at AuNPs, so PEI was partially protonated to give polycationic PEI.

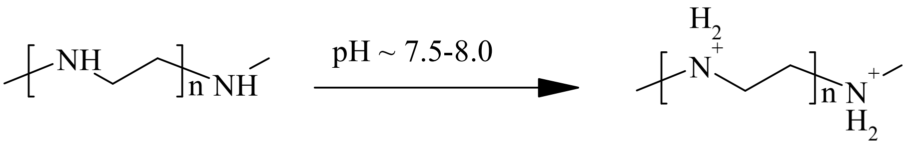

Figure 3.23: Poly (ethyleneimine) (PEI).

The polycationic PEI can adsorb at the surface of negatively charged Gd-loaded AuNPs (Figure 3.24). PEIs are available in different molecular masses.[26] Three different PEIs (PEI-**1**, **2** and **3)** with number average molar masses (M_n) 423, 1800 and 60000 Da, respectively were selected. The ratio between NH^+ and Gd-DTPA@AuNPs$^-$ was kept 2 / 1 to ensure complete adsorption of PEI. The pH of the PEI-protected-Gd-loaded AuNPs (Figure 3.19) was controlled using dilute HCl around physiological range (~7.5-8.0).

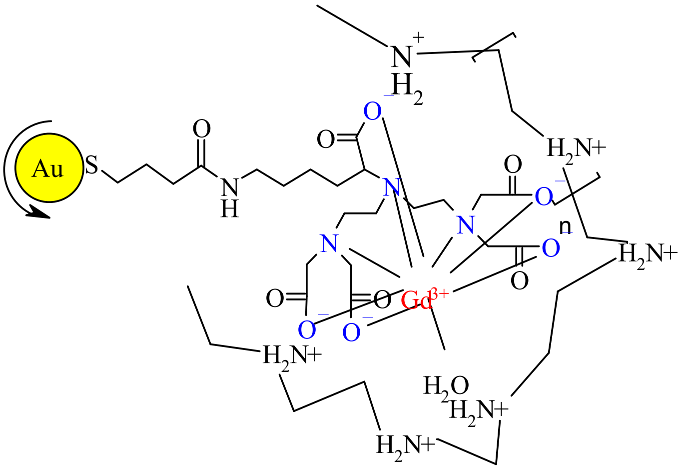

Figure 3.24: PEI-protected Gd-loaded AuNPs.

Before measuring relaxivity of polyelectrolyte coated Gd-loaded AuNPs, their stability was tested as discussed below.

3.5.2 Stability of polyelectrolyte coated Gd-loaded AuNPs

The stability of polyelectrolytes coated AuNPs was tested by UV-Vis spectroscopy and electron microscopy. UV-Vis spectra showed that the PEI-protected Gd-loaded AuNPs exhibited the SPB at the same position as the nanoparticles without any PEI coating (Figure 3.25). Thus, the nanoparticles after polyelectrolyte coating are not aggregated.

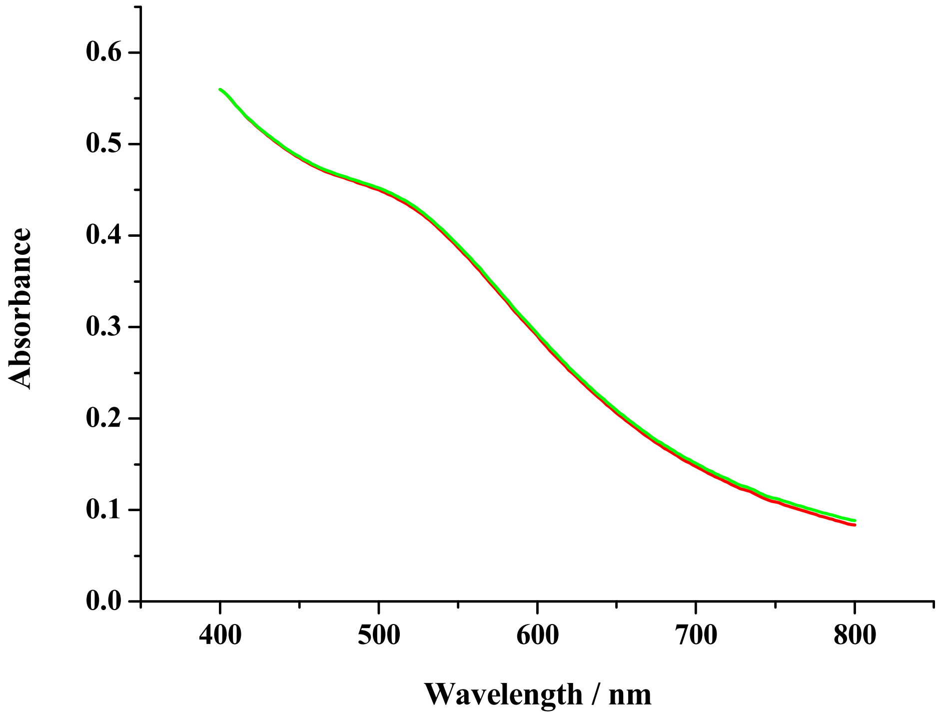

Figure 3.25: UV-Vis spectra of Gd-loaded AuNPs without PEI coating (green) and with PEI (red) coating.

Similarly, the TEM images of polyelectrolyte coated AuNPs also showed that the AuNPs are well dispersed and no aggregation was observed. A typical TEM image with size distribution histogram of PEI-**1** protected AuNPs is shown in Figure 3.26.

Both UV-Vis and TEM data confirmed the stability of nanoparticles after polyelectrolyte coating. The relaxivity of polyelectrolyte coated-Gd-loaded AuNPs is discussed in the next section.

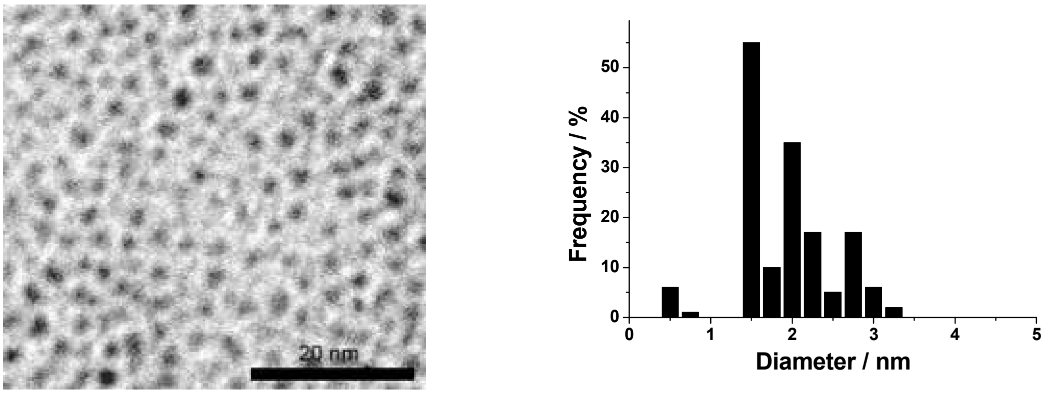

Figure 3.26: TEM image and size distribution histogram of PEI-protected-Gd-loaded AuNPs.

3.5.3 Relaxivity of PEI-protected-Gd-loaded AuNPs

The relaxivity of polyelectrolyte protected Gd-loaded AuNPs was found higher than the nanoparticles without any polyelectrolyte coating (Table 3.7 p.133). The increase in relaxivity confirmed the successful adsorption of polycationic PEI at the negatively charged surface of Gd-loaded AuNPs. The PEI layer increased the rigidity (decreased tumbling) of nanoparticle-attached ligand which resulted in an increase in relaxivity. Furthermore, the relaxivity of PEI protected nanoparticles was increased as the molar mass of the ligand was increased. The charge ratio between positively charged PEI and negatively charged nanoparticles was kept the same, but the length of PEI molecules increased as their molar mass increased. The larger PEI molecules resulted in more rigid structures as compared to smaller PEI molecules.

3.5.4 PAMAM dendrimer layers around AuNPs and their relaxivity

In order to prove the general applicability of polyelectrolyte coating for reducing tumbling of nanoparticle-attached ligand, PAMAM (poly (amido amine)) dendrimers were also used. Dendrimers are reported[27] to be less toxic than PEI.

Dendrimers are repeatedly branched large molecules usually ranging in the size of 1-10 nm. They have very well defined three dimensional architecture. Dendrimers have three main parts: core, branches, and end groups or termini (Figure 3.27).

Generation (G) of a dendrimer is the number of repeated branching cycles as is evident from Figure 3.27. For example if a dendrimer is prepared by performing one branching reaction onto the core, its generation will be one, and if prepared by performing branching reaction twice then it will be a second generation dendrimer and so on.

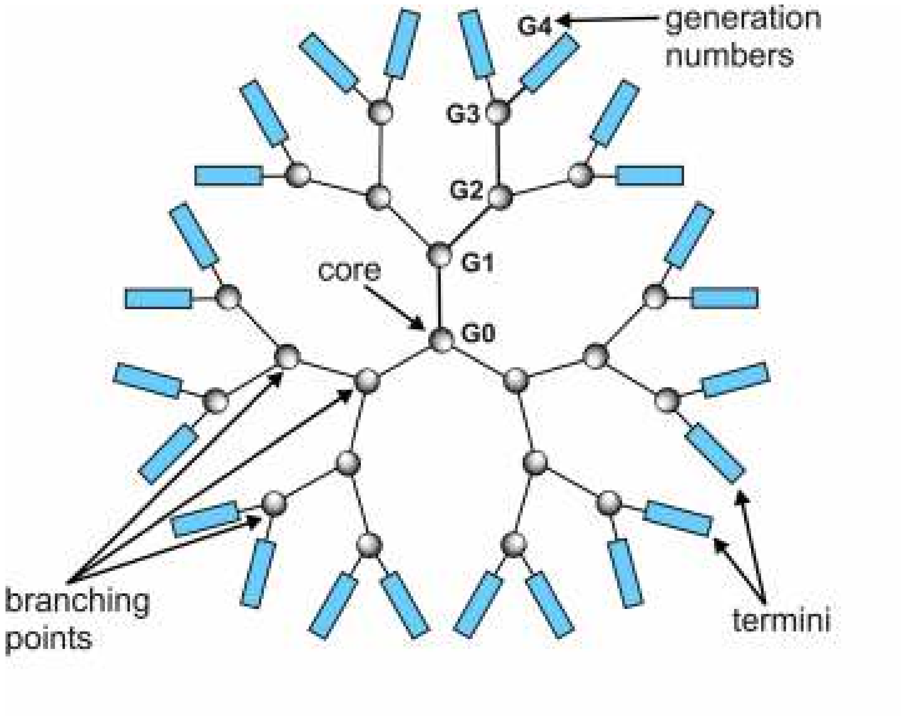

Figure 3.27: Schematic representation of a dendrimer.

Several reports on dendrimer based MRI contrast agents are found in literature. For example nano-sized dendrimers based MRI contrast agents are reported[27] as non toxic materials.

We selected PAMAM (polyamidoamine) dendrimer for coating charged Gd-loaded AuNPs in order to reduce tumbling of nanoparticle-attached ligand that will enhance the relaxivity. PAMAM is the most common class of dendrimers consisting of alkyl-diamine core and tertiary amine branches and is commercially available in generations G_{0-10} (Figure 3.28 shows G_0 PAMAM).

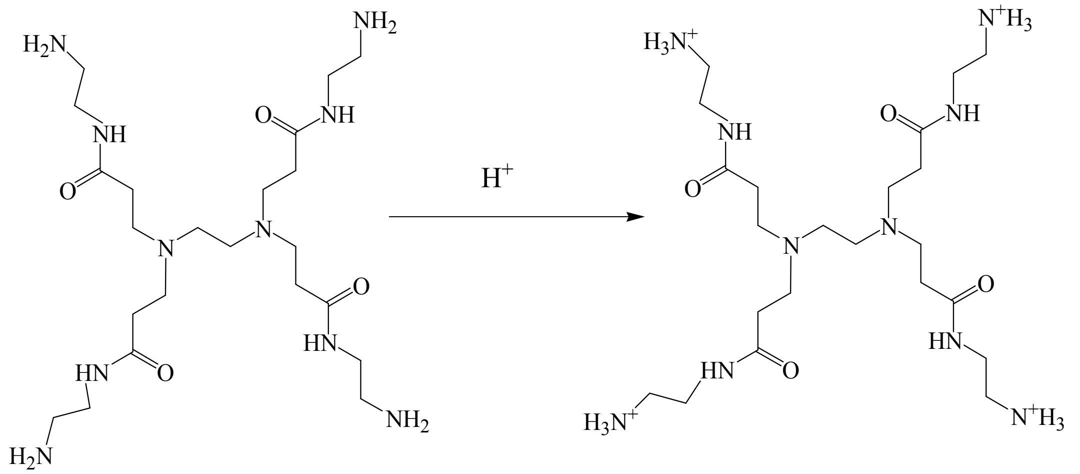

PAMAM dendrimer G0

Positively charged PAMAM in aq solution

Figure 3.28: Zero generation PAMAM dendrimer (in aq solution).

PAMAM is water soluble as it has hydrophilic end groups. In the aq solution, PAMAM gets partially protonated. Two generations of PAMAM i.e. G_0 and G_4 were selected in our study. The PAMAM protected Gd-loaded AuNPs exhibited higher relaxivity as compared to nanoparticles without any dendrimers (Table 3.7). The G_0 PAMAM protected nanoparticles did not show any increase in relaxivity, but G_4 PAMAM showed ~50% increase in relaxivity as compared to nanoparticles without any dendrimers protection. This increase is somewhat (~5%) higher than for the PEI-protected-Gd-loaded AuNPs. The PAMAM dendrimers due to their branched structure resulted in more rigid structure when they adsorbed at the charged surface of Gd-loaded AuNPs. The more rigid structure decreased the tumbling of nanoparticle-attached ligands which enhanced the relaxivity.

Table 3.7: R_1 of polyelectrolyte and dendrimer coated Gd-loaded AuNPs.

Gd-Compound	**Molar Mass of Polyelectrolyte and Dendrimer / Da**	**r_1 / $mM^{-1}s^{-1}$**	**Increase in r_1 relative to Gd-AuNPs / %**
Gd-AuNPs	-	4.77	-
PEI-1-Gd-AuNPs	423	6.50	36
PEI-2-Gd-AuNPs	1800	6.74	41
PEI-3-Gd-AuNPs	60000	7.00	46
PAMAM (G_0)-Gd-AuNPs	517	4.74	-
PAMAM (G_4)-Gd-AuNPs	14000	7.10	50

3.5.5 Layer by layer assembly of polyelectrolytes around Gd-loaded AuNPs

In the above section, the Gd-loaded AuNPs were protected by monolayers of various polyelectrolytes and dendrimers that resulted in reduced tumbling of nanoparticle-attached ligand and consequently an increase in r_1 was observed. In order to further increase relaxivity, multilayers of polyelectrolytes were assembled around AuNPs. The multilayers were formed by LBL technique (discussed in section 3.5) which involves sequential coating by oppositely charged polyelectrolytes.[28-29] PEI (Figure 3.23) and poly (acrylic acid) (PAA) (negatively charged) (Figure 3.29) polyelectrolytes were selected for multilayers formation. Two different PEIs (PEI-**I** and PEI-**II**) with molar masses 1300 and 2000 respectively, and two different PAAs (PAA-**I** and PAA-**II**) with molar masses 1200 and 2100 were selected. On the negatively charged surface of Gd-loaded AuNPs, positively charged PEI layer was coated first. The excess PEI was removed by dialysis against deionised water using 12-14 kDa dialysis tubing. The PAA was then coated on positively charged PEI-Gd-DTPA@AuNPs. The PAA-PEI-Gd-DTPA@AuNPs (Figure 3.30) were again dialysed to remove the excess PAA. The removal of excess polyelectrolytes i.e. PEI and PAA by dialysis was confirmed by a control test. In the control test, ca. 100 mg of each polyelectrolyte dissolved in ca. 10 mL of deionised water was dialysed against deionised water. The dialysis showed complete disappearance of polyelectrolytes which confirmed that the excess polyelectrolytes could pass through the dialysis membrane and thus could be removed. In this way, multilayers of oppositely charged polyelectrolytes were formed at Gd-loaded AuNPs (Figure 3.30).

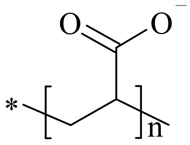

Figure 3.29: Chemical structure of PAA polyelectrolyte.

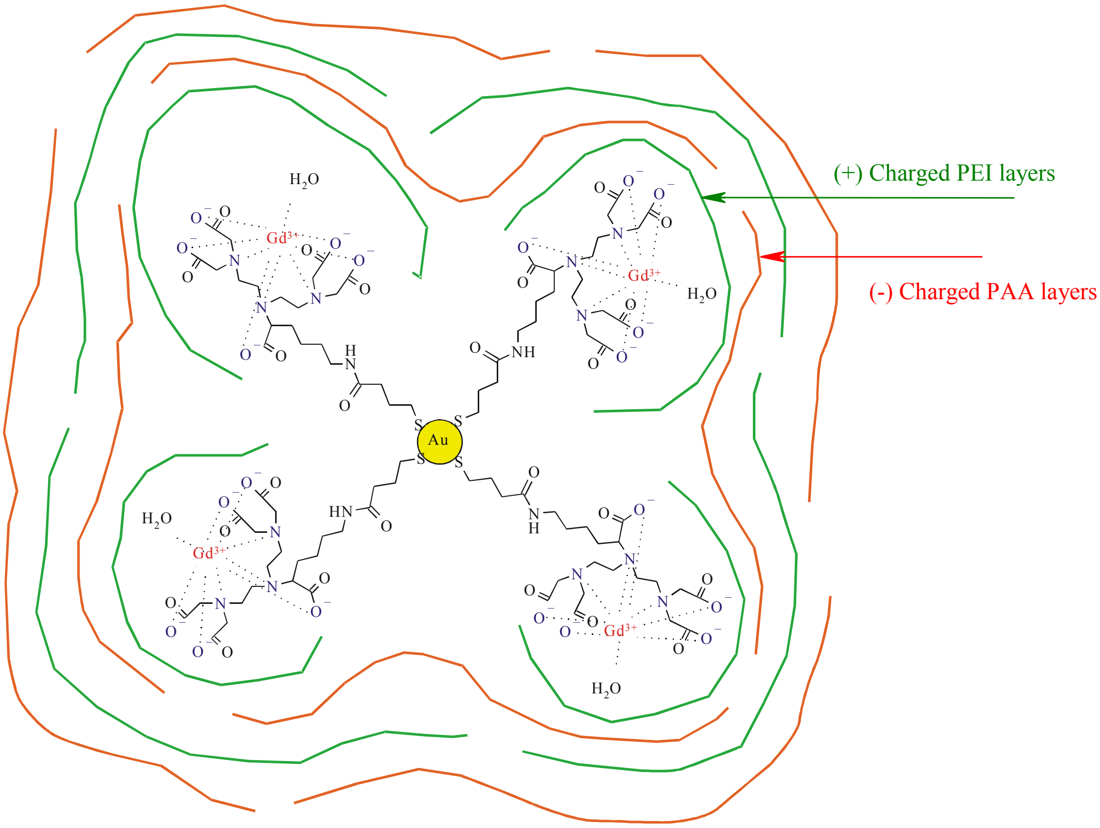

Figure 3.30: Polyelectrolyte multilayers on the surface of Gd-loaded AuNPs

The relaxivity (r_1) was measured after formation of each layer at Gd-loaded AuNPs and a plot of r_1 values against the number of polyelectrolyte layers is shown in Figure 3.31.

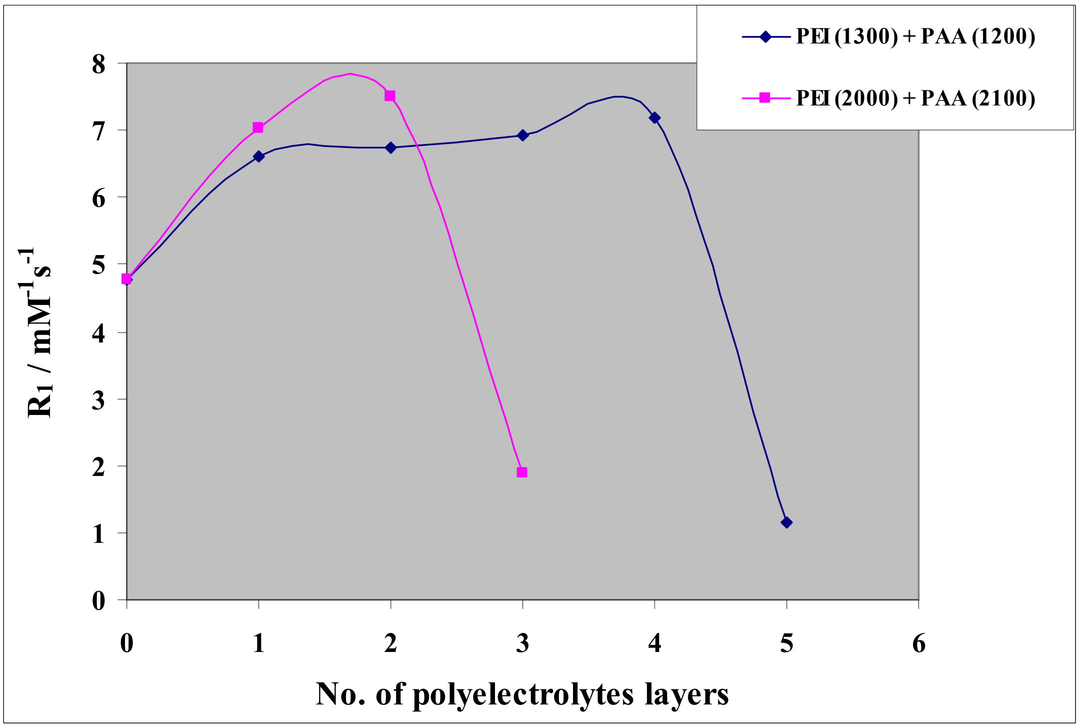

Figure 3.31: R1 values vs no of polyelectrolyte layers@ Gd-loaded AuNPs

Figure 3.31 shows that initially r_1 increased with the increased number of polyelectrolyte layers. The increase in r_1 is due to the progressive reduction in the tumbling of nanoparticle-attached ligand. Interestingly, in case of PEI-I and PAA-I, a plateau was then reached. Despite the reduced tumbling of nanoparticle-attached ligand, presumably the slower water exchange rate between Gd-DTPA chelates at AuNP surface and the surrounding medium also affected the r_1. Furthermore, rapid loss in r_1 was observed after the fourth layer of polyelectrolyte. The rapid loss in R_1 suggested the drop in water exchange rate between Gd at nanoparticle surface and surrounding medium. Peyratout *et al.*[30] reported that the water exchange through polyelectrolyte layers is strongly affected by thickness of the layer. Thus it can be suggested that the rapid loss in r_1 occurred due to increased thickness of polyelectrolyte layers which hindered the water exchange.

The effect of polyelectrolyte multilayers on relaxivity of Gd-loaded AuNPs was further confirmed using another pair of polyelectrolytes with higher molar masses. PEI-II and PAA-II coated AuNPs were prepared and their relaxivity was measured. The relaxivity behaviour of PEI-II-PAA-II is depicted in Figure 3.31. The greater increase in r_1 was observed by PEI-II and PAA-II as compared to PEI-I and PAA-I. The effect of molar mass of polyelectrolyte on relaxivity has already been discussed in section 3.5.1 (Table 3.7). The other difference is the rapid loss in r_1 after formation of only two layers. Presumably the larger polyelectrolytes formed relatively thick layers which hindered the water exchange resulting in sudden decrease in r_1.

3.6 Conclusions

The EPR analysis of vanadyl labelled AuNPs showed that fairly high tumbling rate of nanoparticle-attached ligand limited the increase in relaxivity of Gd-loaded AuNPs as compared to the small molecule based MRI contrast agents. The relaxivity can be increased further by reducing the tumbling of nanoparticle-attached ligand. Two strategies were developed to reduce the tumbling of nanoparticle-attached ligand. The small (~ 2.0 nm) gold nanoparticles were grown into larger nanoparticles (4-6 nm). The larger nanoparticles have more flat surface (smaller curvature). At the more flat surface of larger nanoparticles the tumbling of ligand was decreased due to higher ligand density / tighter ligand packing. The increased nanoparticle size led to higher relaxivity.

The Gd-DTPA chelates have a significant negative charge at AuNPs surface. This negative charge can be neutralised by adsorbing oppositely charged polyelectrolytes. The adsorption of oppositely charged polyelectrolytes at the charged nanoparticles increased the rigidity of nanoparticle-attached ligand. The increased rigidity resulted in an increase in relaxivity.

3.7 References

1. P. J. Debouttiere, S. Roux, F. Vocanson, C. Billotey, O. Beuf, A. Favre-Reguillon, Y. Lin, S. Pellet-Rostaing, R. Lamartine, P. Perriat and O. Tillement, *Adv. Funct. Mater.*, 2006, **16**, 2330-2339.
2. C. Alric, J. Taleb, G. L. Duc, C. Mandon, C. Billotey, A. L. Meur-Herland, T. Brochard, F. Vocanson, M. Janier, P. Perriat, S. Roux and O. Tillement, *J. Am. Chem. Soc.*, 2008, **130**, 5908-5915.
3. A. E. Merbach and E. Toth, *The Chemistry of Contrast Agents in Medical Magnetic Resonance Imaging,* John Wiley & Sons, 2001, pp. 45-119.
4. R. S. Mccomber, *A complete Introduction to Modern NMR Spectroscopy,* John Wiley & Sons, 1998, pp. 13-20.
5. M. Brustolon and E. Giamello, *Electron Paramagnetic Resonance,* John Wiley & Sons, 2009, CH. 1-2.
6. J. A. Weil, J. R. Bolton and J. E. Wertz, *Electron Paramagnetic Resonance: Elementary Theory and Practical Applications,* John Wiley & Sons*,* 1994, CH. 3-5.
7. F. Gerson and W. Huber, *Electron Spin Resonance Spectroscopy of Organic Radicals,* John Wiley & Sons, 2003, pp. 97-153.
8. R. Garzelli, *Ph.D thesis,* The University of York, 2007, pp. 7-11.
9. J. W. Chen, F. P. Auteri, D. E. Budil, R. L. Belford and R. B. Clarkson, *J. Phys. Chem.*, 1994, **98**, 13452-13459.
10. J. W. Chen, R. L. Belford and R. B. Clarkson, *J. Phys. Chem. A*, 1998, **102**, 2117-2130.

11. E. C. Wiener, F. P. Auteri, J. W. Chen, M. W. Brechbiel, O. A. Gansow, D. S. Schneider, R. L. Belford, R. B. Clarkson and P. C. Lauterbur, *J. Am. Chem. Soc.*, 1996, **118**, 7774-7782.
12. S. Stoll and A. Schweiger, *J. Magn. Reson.*, 2006, **178**, 42-55.
13. S. F. Oppenheim, G. R. Buettner and V. G. J. Rodgers, *J. Membrane Sci.*, 1996, **118**, 133-139.
14. B. C. Mei, E. Oh, K. Susumu, D. Farrell, T. J. Mountziaris and H. Mattoussi, *Langmuir*, 2009, **25**, 10604-10611.
15. T. Teranishi, S. Hasegawa, T. Shimizu and M. Miyake, *Adv. Mater.*, 2001, **13**, 1699-1701.
16. X. Sun, X. Jiang, S. Dong and E. Wang, *Macromol. Rapid. Comm.*, 2003, **24**, 1024-1028.
17. T. Shimizu, T. Teranishi, S. Hasegawa and M. Miyake, *J. Phys. Chem. B*, 2003, **107**, 2719-2724.
18. M. J. Hostetler, J. E. Wingate, C.-J. Zhong, J. E. Harris, R. W. Vachet, M. R. Clark, J. D. Londono, S. J. Green, J. J. Stokes, G. D. Wignall, G. L. Glish, M. D. Porter, N. D. Evans and R. W. Murray, *Langmuir*, 1998, **14**, 17-30.
19. T. Stakenborg, S. Peeters, G. Reekmans, W. Laureyn, H. Jans, G. Borghs and H. Imberechts, *J. Nanopart. Res.*, 2008, **10**, 143-152.
20. W. Tong, C. Gao and H. Möhwald, *Polym. Adv. Technol.*, 2008, **19**, 817-823.
21. G. Decher, *Science*, 1997, **277**, 1232-1237.
22. J. W. Ostrander, A. A. Mamedov and N. A. Kotov, *J. Am. Chem. Soc.*, 2001, **123**, 1101-1110.
23. P. R. Gil, L. L. del Mercato, P. del Pino, A. Muñoz Javier and W. J. Parak, *Nano Today*, 2008, **3**, 12-21.

24. C. Lu, H. Möhwald and A. Fery, *J. Phys. Chem. C*, 2007, **111**, 10082-10087.

25. M. Amara and H. Kerdjoudj, *Desalination*, 2003, **155**, 79-87.

26. A. R. Vancha, S. Govindaraju, K. V. L. Parsa, M. Jasti, M. Gonzalez-Garcia and R. P. Ballestero, *BMC Biotechnol.*, 2004, **4**.

27. H. Kobayashi and M. W. Brechbiel, *Adv. Drug Delivery Rev.*, 2005, **57**, 2271-2286.

28. D. Grigoriev, D. Gorin, G. B. Sukhorukov, A. Yashchenok, E. Maltseva and H. Möhwald, *Langmuir*, 2007, **23**, 12388-12396.

29. A. P. R. Johnston, C. Cortez, A. S. Angelatos and F. Caruso, *Curr. Opin. Colloid Interface Sci.*, 2006, **11**, 203-209.

30. C. S. Peyratout and L. Dähne, *Angew. Chem. Int. Ed.*, 2004, **43**, 3762-3783.

Chapter 4: Gold nanoparticles protected by nitroxide based ligand as redox sensitive MRI contrast agents

Chapter 4: Gold nanoparticles protected by nitroxide based ligand as redox sensitive MRI contrast agents

4.1 Introduction

Chapters 2 and 3 discuss the Gd-loaded-gold nanoparticles (Gd^{3+}-based) as MRI contrast agents and various strategies for increasing their relaxivity. Nitroxides are organic paramagnetic molecules which can also be used as MRI contrast agents. This is the focus of this chapter. Nitroxides can also produce T_1 contrast due to the single unpaired electron. However, their use as MRI contrast agents is hampered due to several reasons e.g.

- They are less stable in vivo because they are rapidly reduced (the redox behaviour of nitroxides will be discussed later in this chapter).
- They have a low magnetic moment ~ 1.00 BM, hence their efficiency of T_1 shortening is very low as compared to Gd^{3+} (which has quite high magnetic moment 7.9 BM) based chelates.[1-2]

However, the redox sensitive properties of nitroxides can be exploited to study the redox status of living tissues. Another important feature of nitroxides which attracted researchers, is the ability of nitroxides to pass through the blood brain barrier (BBB), while the other Gd-based contrast agents could not penetrate in this specific area.[3] BBB is a layer of special cells (endothelial cells) which separates the circulating blood from the cerebrospinal fluid of the central nervous system. Generally large species such as bacteria etc and hydrophilic molecules are restricted while endothelial cells permit small hydrophobic molecules to cross the BBB.

4.1.1 Nitroxide based contrast agents

In the early 1980s, nitroxides were identified as potential MRI contrast agents due to the previously mentioned features i.e. paramagnetism and permeability through BBB. In 1983, Brasch and co-workers[4] published a preliminary report on the utilization of nitroxides as contrast agents for MRI. They used a piperidinyl derivative of stable nitroxide radical to study the brains of living animals and found that the nitroxide based free radical crossed the BBB (which was confirmed by MRI). After confirming the feasibility of using nitroxides as MRI contrast agents in animals, their stability was studied. Couet *et al.*[5] described the stability of two different nitroxides (Figure 4.1) (a) a six member ring i.e. N-succinyl-4-amino-2,2,6,6-tetramethylpiperidine-1-oxyl (TES) and (b) a five member ring i.e. 2,2,5,5-tetramethylpyrrolidine-1-oxyl-3-carboxylic acid (PCA), *in vitro* as well as *in vivo*.

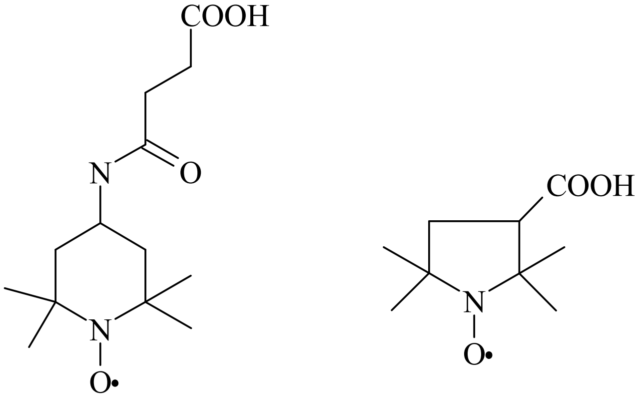

TES

PCA

Figure 4.1: Chemical structures of TES (piperidinyl based nitroxide) and PCA (pyrrolidinyl based nitroxide).[5]

Both the *in vivo* and *in vitro* studies confirmed that PCA is more resistant to reduction and hence is more stable as compared to TES. The five-membered ring based PCA is more stable than six-membered TES because it is planar rather than puckered.

To increase the efficiency of nitroxide based MRI contrast agents, dendrimers were selected as templates. At the termini of dendrimer molecules, several nitroxide moieties can be attached (Figure 4.2).[6-8] It has been found that for higher generation dendrimers, extensive line broadening could be observed due to spin-spin exchange interactions. Yordanov *et al.*[7] reported spin labelled dendrimers in EPR imaging studies. They selected the PAMAM (G 6) dendrimer and different amounts (e.g. 198 and 80) of nitroxides were attached on them. Their studies showed that with the increased number of nitroxides, the tendency of dendrimers to aggregate could increase which hinders the *in vivo* applications. The aggregation of nitroxide-attached dendrimers may be due to highly lipophilic nature of their surface.

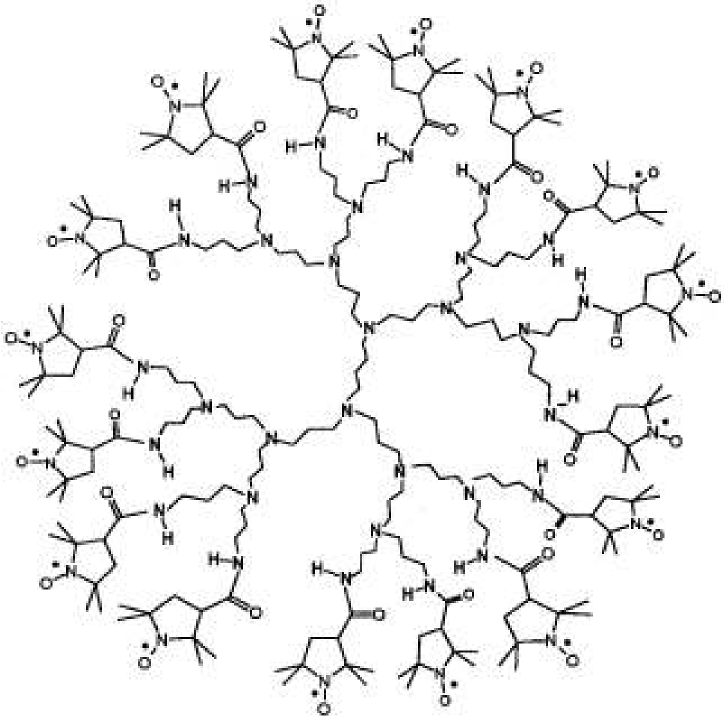

Figure 4.2: G2 DAB dendrimer containing 16 nitroxide moieties.[6]

Winalski *et al.*[152] described the relaxation measurements of different dendrimers functionalised with various numbers of nitroxides. Three different types of dendrimers were selected (a) tris(2-aminoethyl)amine (TREN) (b) DAB and (c) PAMAM. To these dendrimers, nitroxides were attached. The relaxivity of these dendrimer based nitroxides was increased with the increased number of nitroxides to a certain level of dendrimer generation and then became approximately constant. This might be due to sharing of hydration spheres by nitroxides in higher generations. The sharing of hydration spheres may be due to hydrogen bonding between amides of the terminal groups. The relaxivity of PAMAM (G 4) containing 32 nitroxides was found even higher (5.00 $mM^{-1}s^{-1}$) than the Gd-DTPA (4.76 $mM^{-1}s^{-1}$). In fact the relaxivity per nitroxide was 0.18 $mM^{-1}s^{-1}$. Many other reports can be found in the literature describing the utilization of nitroxides as MRI contrast agents.[2, 4, 9-11]

We used gold nanoparticles as a template for nitroxides based MRI contrast agents. Nanoparticles make it possible to attach several nitroxides per particle. The nanoparticle-attached nitroxides were expected to have better relaxivity due to reduced tumbling of nanoparticle-attached nitroxides. Furthermore, gold nanoparticles might be able to pass through BBB after coating with suitable biomolecules such as carbohydrates etc.

Gold nanoparticles protected by nitroxide radical based ligands could not be synthesized by Brust *et al.*[12] protocol, because nitroxide radicals are decomposed during the reduction of Au(III) to Au(0). Therefore the nitroxide protected gold nanoparticles found in literature[13-15] were prepared by a ligand exchange approach using triphenylphosphine (PPh_3@AuNPs) protected AuNPs. The nitroxide protected AuNPs prepared by this strategy could not be utilised for the purpose of MRI contrast agents due to several reasons. Firstly, they were insoluble in aqueous medium (the MRI contrast agents must be water soluble). Secondly the ligand exchange approach may lead to the incomplete exchange reaction particularly at room temperature (Figure 4.3). The elevated temperature could result in complete ligand exchange but may be accompanied by some decomposition of the nitroxide radicals.

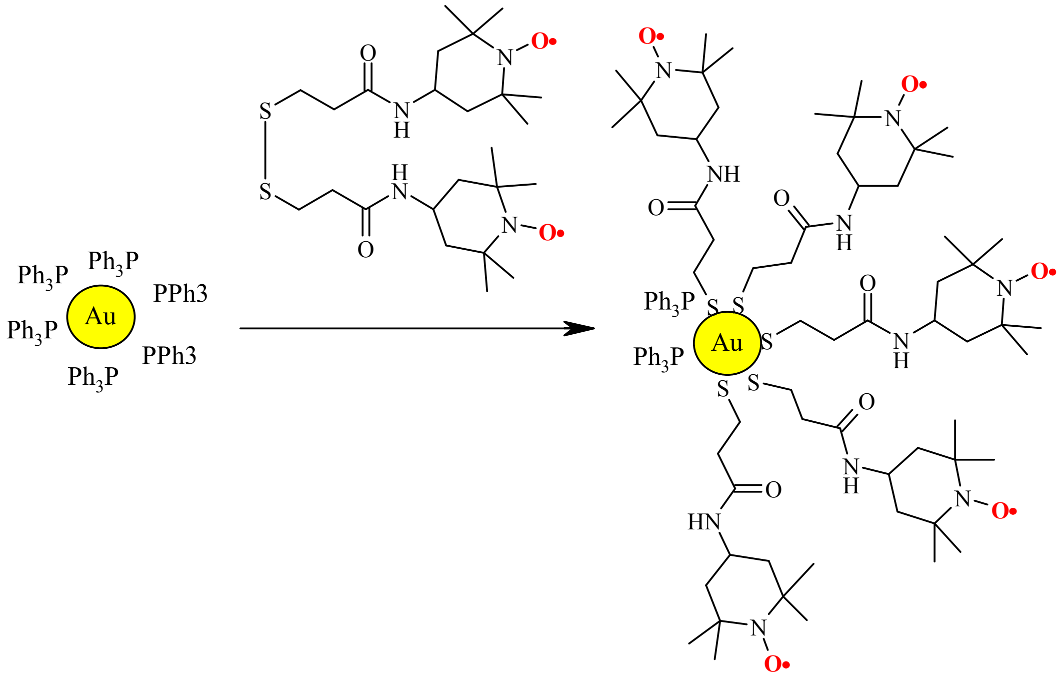

Figure 4.3: Nitroxides spin labelled AuNPs (insoluble in aqueous medium).[16]

Therefore, we developed a different approach to prepare nitroxide protected, water soluble gold nanoparticles. This approach is also based on the ligand exchange reaction; however, it involves two steps and will be discussed in detail in section 4.3.

4.2 Synthesis of triphenylphosphine (PPh_3) protected gold nanoparticles (AuNPs)

Due to relatively weak affinity of phosphorus for gold, PPh_3 can be displaced from the gold nanoparticle surface with sulphur containing ligands and hence it is good starting material for ligand exchange reactions. The PPh_3 protected AuNPs (Figure 4.4) were synthesized and purified by following a literature procedure.[17]

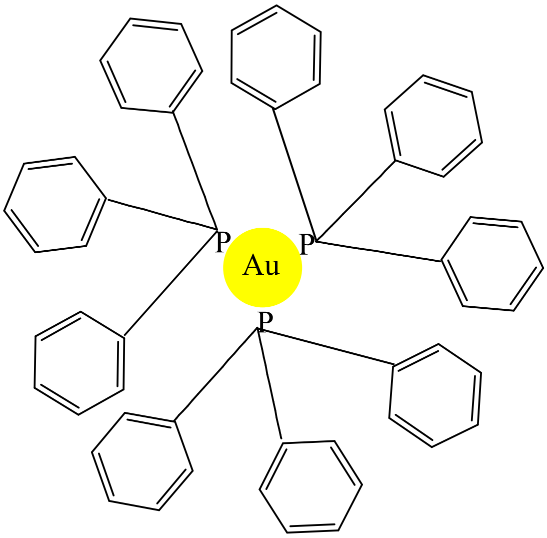

Figure 4.4: Triphenylphosphine protected gold nanoparticles.

PPh_3 protected AuNPs were characterised by conventional techniques e.g. UV-Vis, TEM and TGA. The UV-Vis spectrum showed SPB at 520-525 nm. TGA showed ca. 25 % organic content in the AuNPs. This low amount of ligand corresponds to the large steric bulk of ligand (PPh_3) as compared to straight chain ligands. This amount of organic content (i.e. PPh_3) determined from TGA will be used to calculate the stoichiometry for further ligand exchange reactions. The diameter determined from the TEM image of the PPh_3@AuNPs was found 1.91 ± 0.24 nm.

4.3 Synthesis of gold nanoparticles protected by nitroxide based ligand

We prepared nitroxide protected water soluble AuNPs using a modified ligand exchange approach[18] which involved two steps. In the modified ligand exchange approach, the triphenylphosphine molecules were exchanged with a relatively more stable ligand DSP (dithiobis [succinimdylpropionate]) ligand at relatively elevated temperature (i.e. 50 ^{o}C) in chloroform. The ligand exchange reaction at elevated temperature (i.e. 50 ^{o}C) was done to ensure the complete ligand exchange reaction.

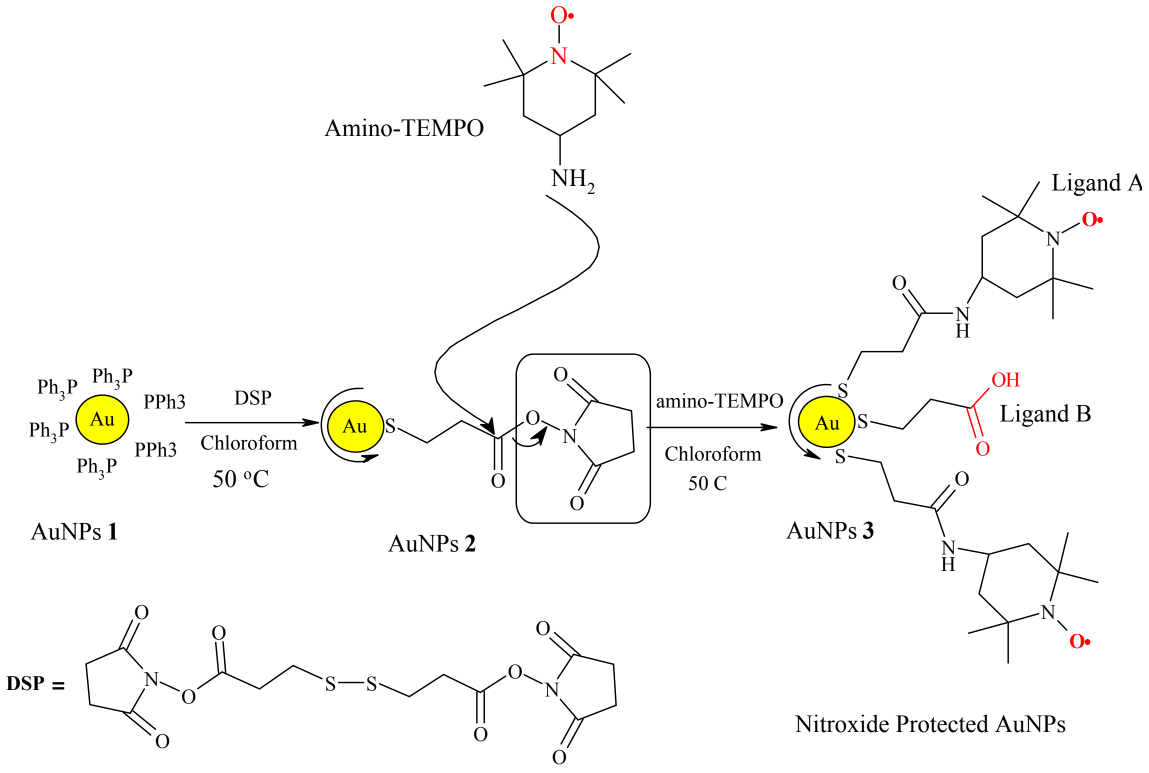

Figure 4.5: Scheme showing synthesis of AuNPs protected by nitroxides based ligand.

The AuNPs protected by DSP (i.e. after first step of ligand exchange approach) could not be purified, because the DSP ligand can be easily hydrolysed during purification. As free DSP ligand was not removed, excess amount of amino-TEMPO was required in the second step. 1.0 min after the addition of DSP to the PPh_3AuNPs, the amino-TEMPO solution in chloroform was added. The amino ($-NH_2$) group of amino-TEMPO reacted rapidly with the activated ester group of the DSP ligand at the AuNP surface to form stable amide linkage (Figure 4.5). NHS esters are easy to hydrolyze by adventitious water; this small amount of carboxylate (Figure 4.5) will make the gold nanoparticles soluble in aqueous media. After stirring the reaction mixture for *ca*. 2h, the solvent was evaporated at room temperature, and AuNPs were purified using Sephadex LH-20 as a stationary phase and MeOH as an eluent. The purified AuNPs protected by nitroxide based ligand were quite soluble in MeOH, and furthermore the concentrated solution of these nanoparticles in MeOH was miscible with deionised water. The miscibility with water confirmed our assumption that some of the NHS groups of DSP ligand were hydrolysed into carboxylic acid (-COOH) groups (Figure 4.5). The purified AuNPs protected by nitroxide based ligand were characterised by UV-Vis, TEM spectroscopies, TGA, elemental analysis and EPR (characterisation is discussed in the next section).

4.3.1 Characterisation of AuNPs protected by nitroxide based ligand

The purified AuNPs were characterised by UV-Vis., TEM, TGA, elemental analysis and EPR spectroscopy which are discussed below.

4.3.1.1 UV-Vis spectrum of AuNPs protected by nitroxide based ligand

The UV-Vis spectrum of gold nanoparticles protected by nitroxide based ligand showed SPB at 520-525 nm (Figure 4.6), which confirmed the formation of gold nanoparticles and its intensity is consistent with the size (~2.0 nm) of the nanoparticles.

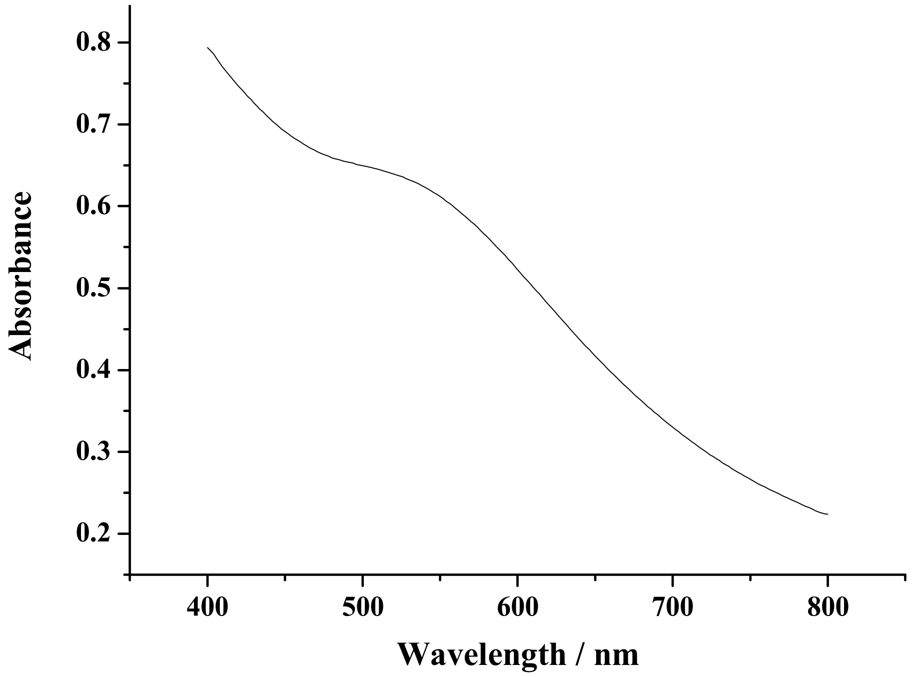

Figure 4.6: UV-Vis spectrum of AuNPs protected by nitroxide based ligand

4.3.1.2 TEM

A TEM image of nitroxide based ligand protected AuNPs was recorded by the same method as for the DTPA ligand protected AuNPs (discussed in ch. 2 and 3). The TEM image shows well dispersed gold nanoparticles with an average diameter 2.12 ± 0.39 nm (Figure 4.7).

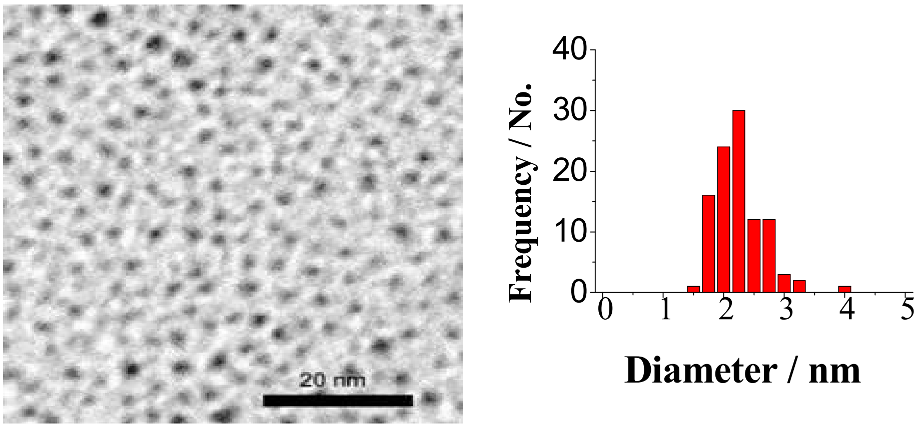

Figure 4.7: TEM image and size distribution histogram of AuNPs protected by nitroxides based ligand

4.3.1.3 TGA of AuNPs protected by nitroxide based ligand

The thermogravimetric analysis (Figure 4.8) showed ca. 32% of total organic matter present on the gold nanoparticle surface. As mentioned in section 4.3, it is possible that two different types of ligands are present at the nanoparticles surface. Hence for the exact determination of nanoparticle composition, elemental analysis of the nanoparticles was carried out and is discussed in the next section.

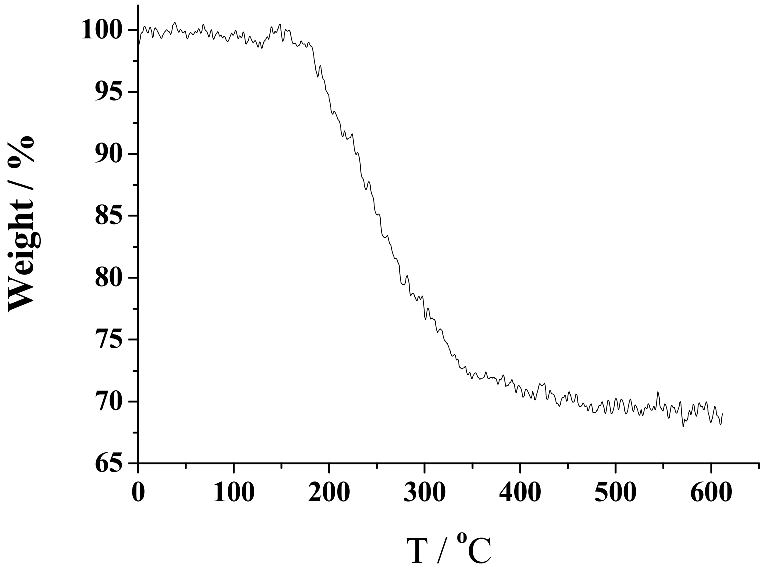

Figure 4.8: TGA graph of AuNPs protected by nitroxide based ligand.

4.3.1.4 Elemental analysis of AuNPs protected by nitroxide based ligand

The elemental analysis was carried out to estimate the nanoparticle composition. The best fit composition (Au : Ligand$_A$: Ligand$_B$ = 34 : 13 : 1) (Table 4.1) (Figure 4.5) determined from elemental analysis was found to be in agreement with the TGA results.

Table 4.1: Percentage composition of various elements present in nitroxide protected AuNPs.

Element	*C*	*H*	*N*	*Au*
% Theory	17.69	2.85	3.15	68
% Found	19.05	2.42	3.08	65

From TEM and elemental analysis data, formula of one nanoparticle is suggested as: $Au_{295}Ligand(A)_{116}\ Ligand(B)_{9}$.

4.3.2 EPR analysis of AuNPs protected by nitroxide based ligand

The nitroxide radical gives three lines in an EPR spectrum due to hyperfine interaction with ^{14}N (I = 1) (as discussed in chapter 3, section 3.1.1.3). Nitroxide-functionalised gold nanoparticles have several nitroxides close to each other. These nitroxides can interact with each other via spin-spin exchange interactions. The spin-spin interaction results in a broad line instead of three lines in the EPR spectrum (Figure 4.9).

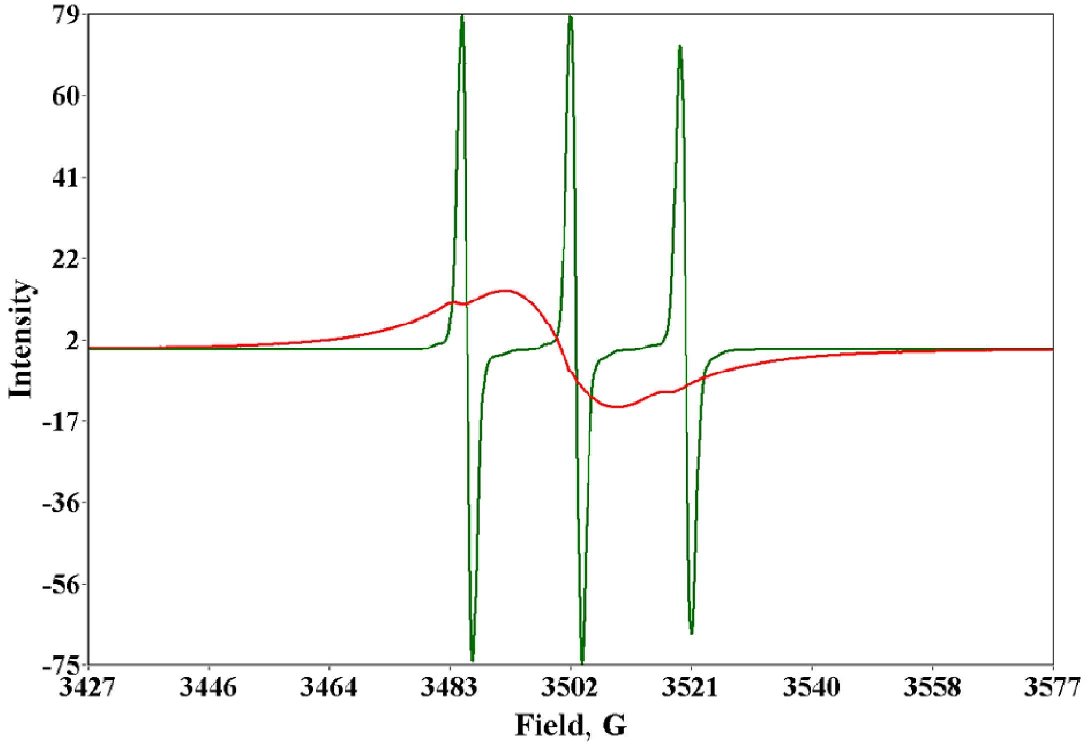

Figure 4.9: EPR spectra of free nitroxide radical (green) and nitroxide based ligand at AuNP surface (red).

The single broad line by nitroxide protected AuNPs has also been reported previously by Chechik *et al*[13]. In their report they described that the single broad line is observed only when the nanoparticle surface is highly covered with nitroxides i.e. more than 20 nitroxides per particle.

The line width of the single broad line is an important parameter to estimate the concentration of nitroxides on the surface of the nanoparticle. As shown in Figure 4.10, nitroxide radicals exhibit three lines at low concentration (e.g. 10^{-4} M); these lines become broader (i.e. due to exchange broadening) and then merge to give a single broad line with the increased concentration of nitroxides. The line width of the single broad line decreases with the further increase in nitroxide concentration (Figure 4.7)[19], this phenomenon is called exchange narrowing.

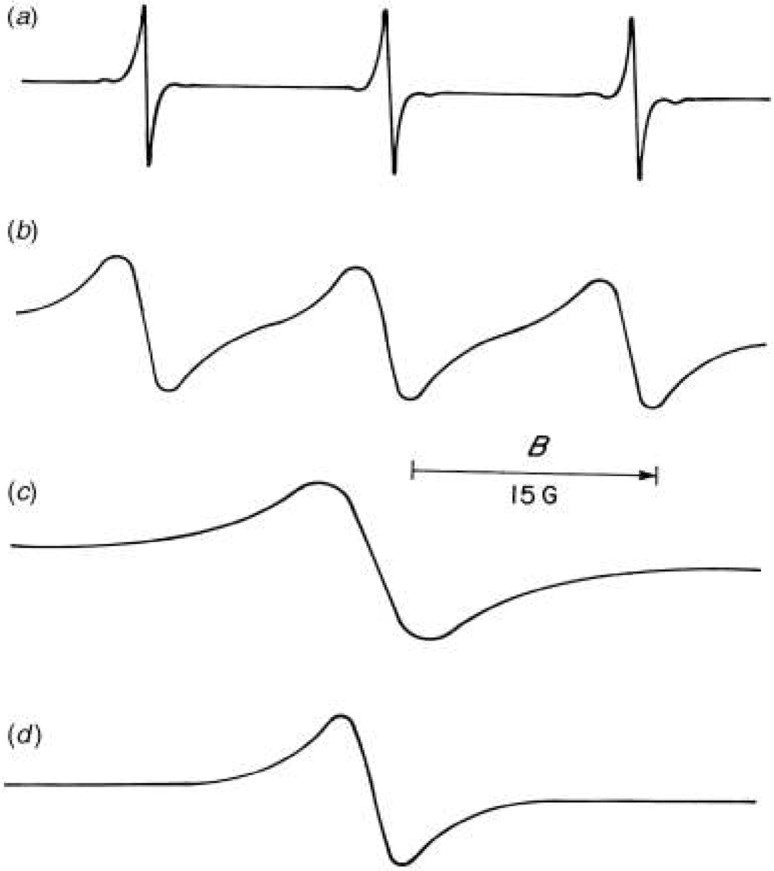

Figure 4.10: EPR spectra of di-t-butyl nitroxide radical in ethanol at room temperature having various concentrations: (a) 10^{-4} M, (b) 10^{-2} M, (c) 10^{-1} M and (d) pure liquid nitroxide.[19]

The line width of EPR spectrum of AuNPs protected by nitroxide based ligand was found to be 16.8 G. Based on the literature, the nitroxide protected gold nanoparticles with similar line width were expected to have ~ 40 nitroxides per particle.[13] Thus EPR confirmed that several nitroxides are closely present at the nanoparticles surface; therefore they can be studied for the purpose of MRI contrast agents. Their relaxation measurements and redox behaviour will be discussed in section 4.3.5 and 4.3.6 respectively.

4.3.3 Quantitative estimation of nitroxide at AuNPs surface by EPR spectroscopy

Unfortunately EPR signal intensity of nitroxide protected AuNPs was not in agreement with the TGA and elemental analysis data. For example, 6.4 mg of nitroxide protected AuNPs dissolved in 2.9 mL of deionised water exhibited EPR spectra with double integral intensity corresponding to ca. 13 wt% of nitroxide based ligand while elemental analysis (and TGA) predicted *ca*. 32 wt % of the nitroxide based ligand. This discrepancy is attributed to the decomposition of some of the nitroxides at the nanoparticles surface. However the total organic content determined by TGA is compatible with the elemental analysis data. This suggests that amino-TEMPO successfully reacted with DSP ligand but nitroxide functionality degraded during the reaction. To check if nitroxide degradation resulted in hydroxylamine, attempts to oxidised hydroxylamine back to nitroxide with PbO_2 failed. In another control experiment, the nitroxide protected AuNPs were decomposed by KI and I_2 solution in MeOH in order to release the nitroxide based ligand which will form a disulphide linkage to give a diradical (Figure 4.11).

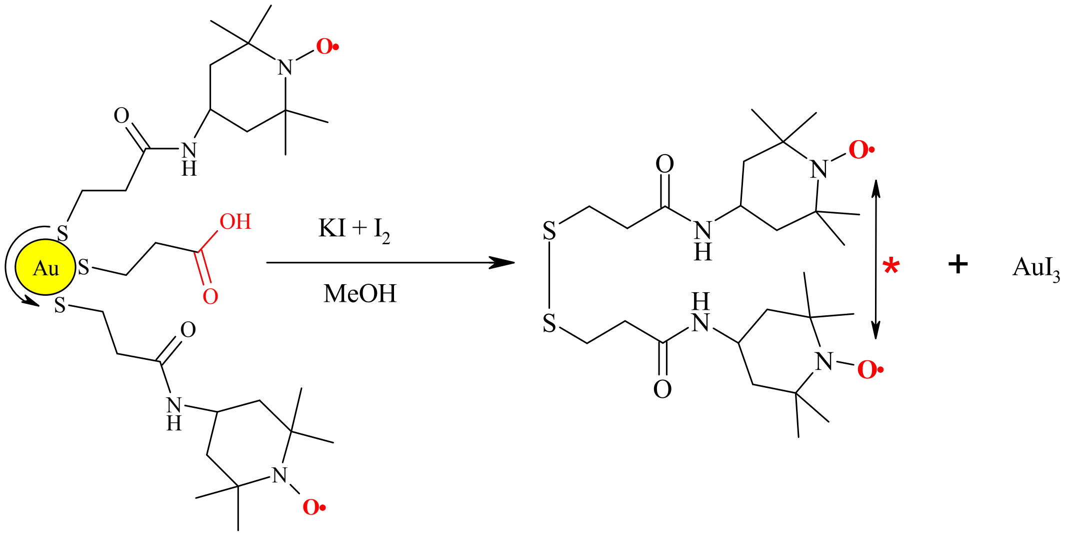

Figure 4.11: Scheme showing control test.

The nitroxide based diradical was expected to exhibit spectra with some additional peaks (*) due to be spin-spin interactions (Figure 4.12). The intensity of the additional peaks (*) was found lower than expected in DCM which confirmed the decomposition of nitroxides. Furthermore, no difference in the EPR signal (double integral) intensity was found before and after decomposing nitroxide protected AuNPs.

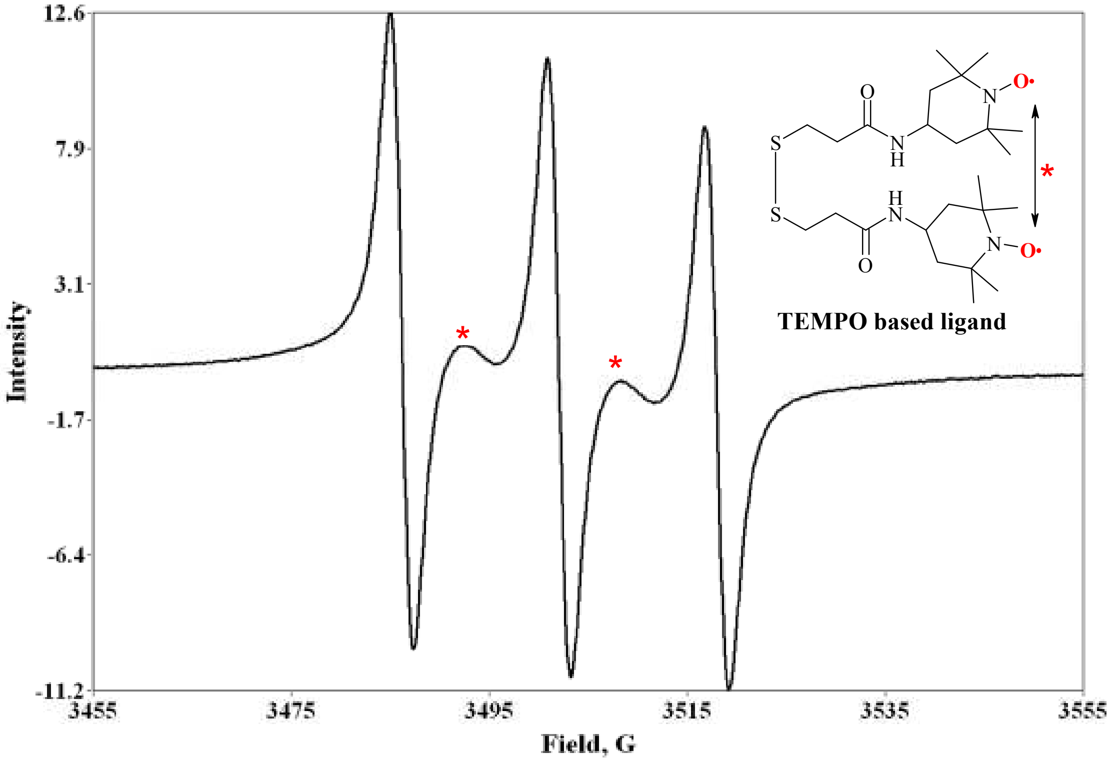

Figure 4.12: EPR spectrum of nitroxide diradicals.

4.3.4 Determination of nitroxide radical concentration

The accurate nitroxide radicals' concentration must be known for determination of relaxivity. The calibration curve was set up using double integral values of EPR spectra of known concentrations of nitroxide radical solutions (TEMPO was used radical for the calibration curve) (Figure 4.13). This calibration curve was then used for determination of nitroxide concentration in nitroxide protected gold nanoparticle solutions.

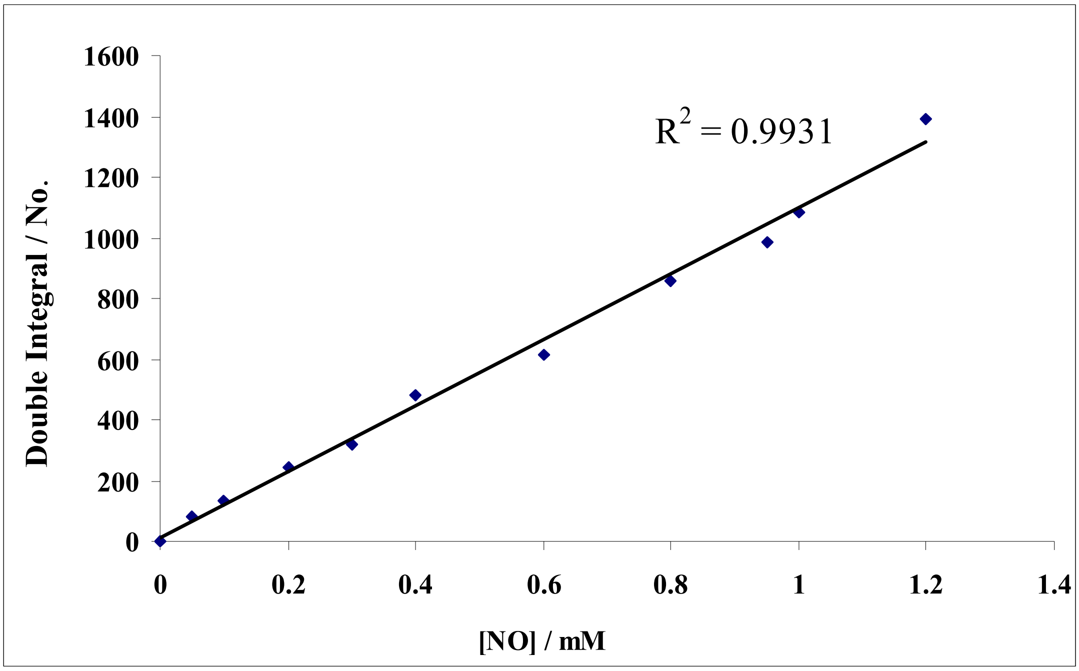

Figure 4.13: Calibration curve for determination of [NO].

4.3.5 Relaxation measurements

The relaxivity of nitroxide protected gold nanoparticles in water was measured using the same method as for Gd-loaded AuNPs. The relaxivity of nitroxide protected AuNPs (0.32 $mM^{-1}s^{-1}$) was slightly higher than that for free nitroxides (0.30 $mM^{-1}s^{-1}$) (Table 4.2). This slight increase may be due to reduced tumbling of nanoparticle-attached nitroxide based ligand. This value of relaxivity for nitroxide based compound is much smaller as compared to Gd^{3+}-based chelates, and is easily justified by the presence of seven unpaired electrons in Gd^{3+}, while the nitroxide contain only one unpaired electron. The similar values of relaxivity for nitroxide based contrast agents have also been reported previously[3]. However, unlike the Gd^{3+} based contrast agents, relatively hydrophobic nitroxides can pass through the BBB and they can report on redox status of the brain tissues. Furthermore, nitroxides are non-toxic, while Gd^{3+} ions are extremely toxic and they must be chelated before utilisation for MRI applications. Gd^{3+} may also leach from the chelates which can cause serious problems.

Table 4.2: Comparison of R_1 values of Nitroxides@AuNPs with Gd-DTPA@AuNPs.

Compound	***Relaxivity / $mM^{-1}s^{-1}$***
Free Nitroxides	0.29
Nitroxides@AuNPs	0.32
Gd-DTPA	3.83
Gd-loaded AuNPs	4.77

4.3.6 Redox behaviour of nitroxide at the surface of AuNPs

It was hoped that attaching several nitroxides to the gold nanoparticles surface would increase their stability towards reducing agents. Nitroxides can undergo redox transformation i.e. either to oxoammonium cation by gaining one electron or hydroxylamine by losing one electron[2], but in biological media they are reduced (e.g. by ascorbic acid). This limits their applications as T_1-contrast agents in MRI imaging. However their redox behaviour can be exploited to study the redox status of the living tissues.

Nitroxides are cell permeable and depending upon the presence of abnormal amounts of oxidising or reducing species in the cells, the cell status can be studied by measuring the rate of nitroxide transformation reactions and then comparing with the rate of reduction of nitroxides in the normal cells. For example in the tumour cells, the nitroxides are reduced more rapidly as compared to normal tissues.

The rate of reduction of free nitroxides and nitroxides at the surface of gold nanoparticles was studied *in vitro*. Sodium ascorbate, a commonly used reducing agent, was used as a reducing agent. Sodium ascorbate was selected rather than ascorbic acid in order to avoid the decomposition of gold nanoparticles in acidic medium. Ascorbate ions can reduce nitroxide radicals as they possess a labile H-atom (Figure 4.14). The ascorbate radical formed is relatively persistent.

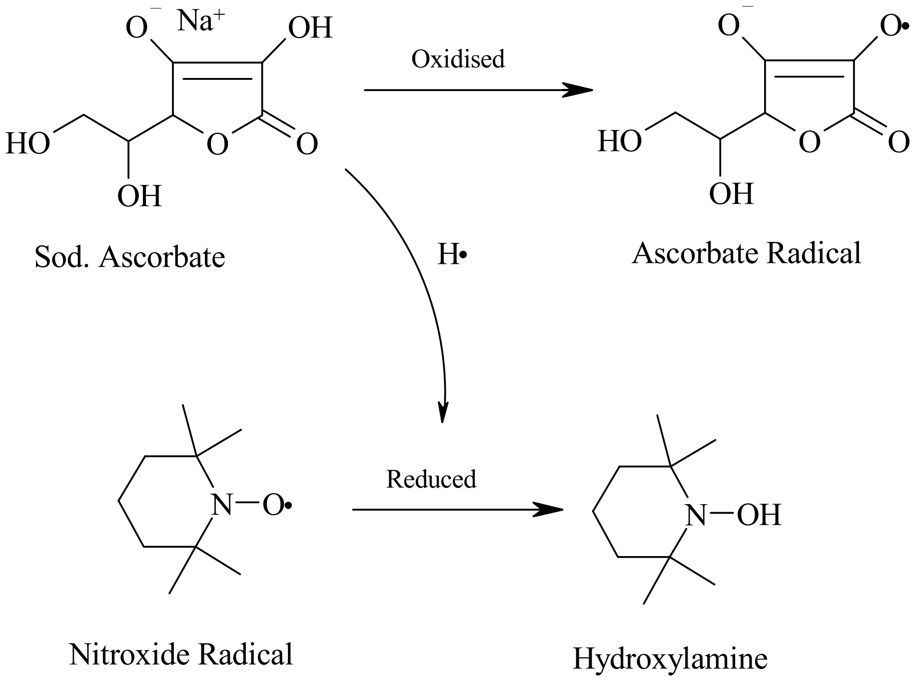

Figure 4.14: Mechanism of reduction of nitroxide radicals by sodium ascorbate.

The rate of reduction of free as well as nanoparticle-attached nitroxides was monitored by recording EPR spectra at regular intervals. EPR spectra of nanoparticle-attached nitroxides and free nitroxides in the presence of sodium ascorbate (4-fold excess) are shown in Figures 4.15 and 4.16 respectively. In Figure 4.15, the two sharp lines are assigned to ascorbate radical. The intensity of the single broad line exhibited by gold nanoparticle-attached nitroxides (Figure 4.15) and of three lines exhibited by free nitroxides (Figure 4.16) was reduced over time. The decrease in intensity was due to reduction of nitroxides by sodium ascorbate (Figure 4.14). During the reduction of surface-bound nitroxides, very weak evolution of ^{14}N hyperfine interactions (**) (i.e. three lines) was observed due to decrease in the number of nitroxides attached to the same nanoparticle (Figure 4.15). The decreased number of nitroxides per particle decreased the spin-spin interactions which resulted in appearance of three lines (**).

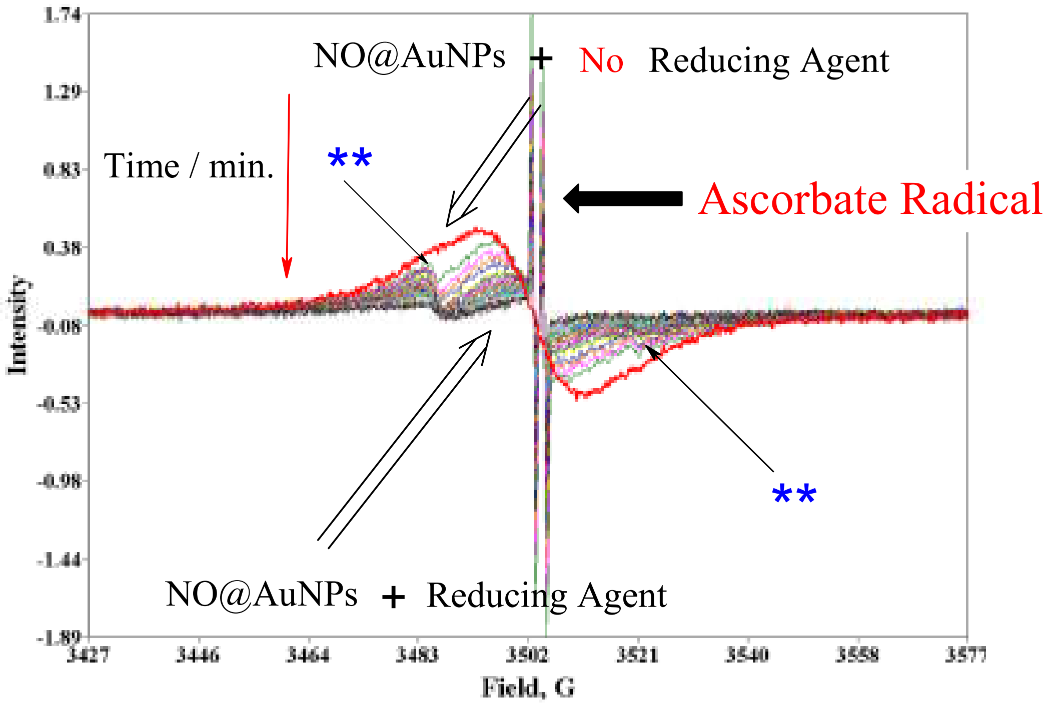

Figure 4.15: EPR spectra of Nitroxides@AuNPs in the presence of reducing agent at various intervals of time.

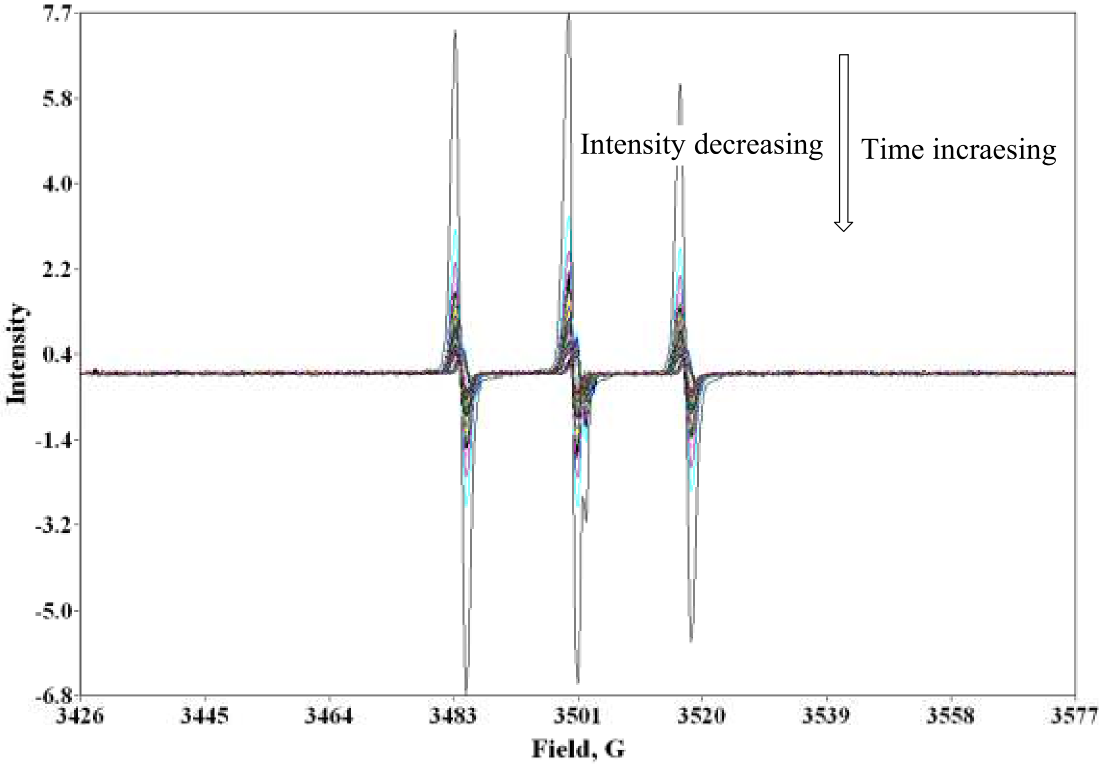

Figure 4.16: EPR spectra of free nitroxides (i.e. amino-TEMPO) in the presence of reducing agent at various intervals of time.

The rate of reduction of free as well as nanoparticle-attached nitroxides was determined by plotting the double integral intensity of their EPR spectra vs time (Figure 4.17). Figure 4.17 shows that free nitroxides are reduced more rapidly as compared to the nitroxides adsorbed at the surface of gold nanoparticles. The nitroxides at gold nanoparticle surface have compact packing and hence access of ascorbate to the nitroxides is restricted as compared to the access to the free nitroxides. The nanoparticle-attached nitroxides follow the first order decay while the first order decay was not well fitted for the free nitroxides (Figure 4.17). This difference in the reduction behaviour might be attributed to the different compositional changes as the reaction proceeds.

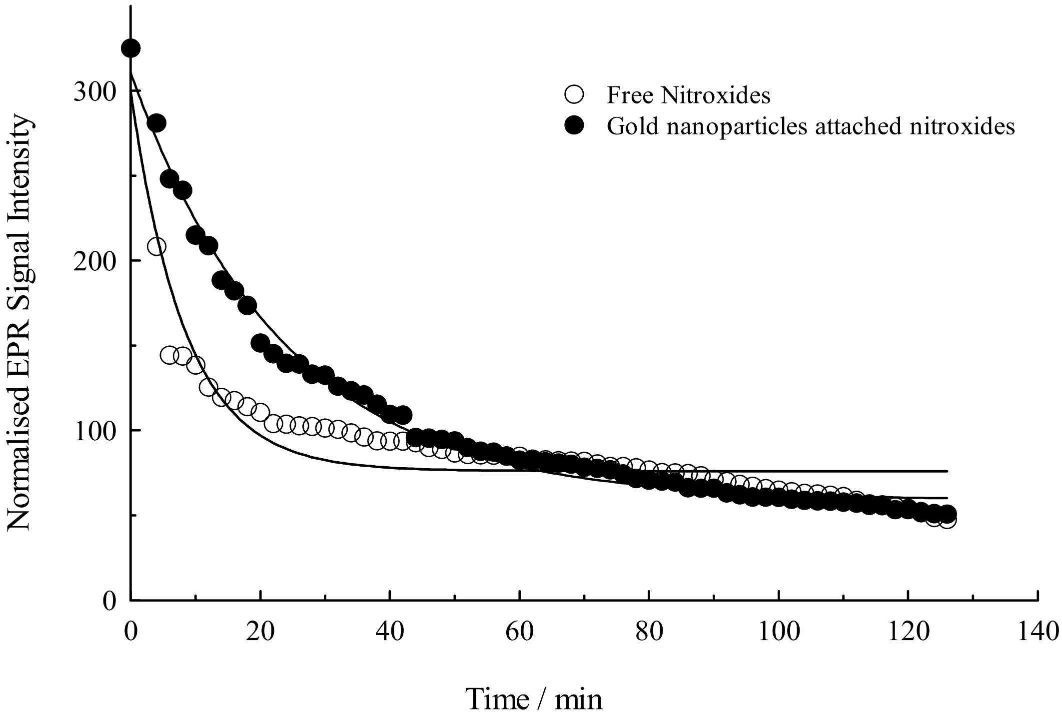

Figure 4.17: Rate of reduction of free nitroxides and nanoparticles-attached nitroxides.

4.4 Conclusions

Water soluble gold nanoparticles protected by nitroxide based ligand were prepared and characterised. After characterisation, the relaxivity measurements and oxidising behaviour of nitroxide protected gold nanoparticles was studied and compared with free nitroxides *in vitro*. The nitroxide protected gold nanoparticles showed a slightly higher relaxivity than the free nitroxides. This increase in relaxivity is attributed to the slower tumbling of nitroxide ligand at the nanoparticle surface as compared to the free nitroxides. The nitroxides at nanoparticles surface also showed slow reduction as compared to the free nitroxides due to compact packing, which may encourage their *in vivo* applications as MRI contrast agents.

4.5 References

1. V. M. Runge, J. A. Clanton, C. M. Lukehart, C. L. Partain and A. E. James, *Am. J. Roentgenol.*, 1983, **141**, 1209-1215.
2. K.-i. Matsumoto, F. Hyodo, A. Matsumoto, A. P. Koretsky, A. L. Sowers, J. B. Mitchell and M. C. Krishna, *Clin. Cancer Res.*, 2006, **12**, 2455-2462.
3. K.-i. Matsumoto, H. Yakumaru, M. Narazaki, H. Nakagawa, K. Anzai, H. Ikehira and N. Ikota, *Magn. Reson. Imaging*, 2008, **26**, 117-121.
4. R. C. Brasch, D. E. Nitecki, M. Brantzawadzki, D. R. Enzmann, G. E. Wesbey, T. N. Tozer, L. D. Tuck, C. E. Cann, J. R. Fike and P. Sheldon, *Am. J. Roentgenol.*, 1983, **141**, 1019-1023.
5. W. R. Couet, U. G. Eriksson, T. N. Tozer, L. D. Tuck, G. E. Wesbey, D. Nitecki and R. C. Brasch, *Pharm. Res.*, 1984, **1**, 203-209.
6. A. W. Bosman, R. A. J. Janssen and E. W. Meijer, *Macromolecules*, 1997, **30**, 3606-3611.
7. A. T. Yordanov, K. Yamada, M. C. Krishna, J. B. Mitchell, E. Woller, M. Cloninger and M. W. Brechbiel, *Angew. Chem.-Int. Edit.*, 2001, **40**, 2690-2692.
8. A. J. Maliakal, N. J. Turro, A. W. Bosman, J. Cornel and E. W. Meijer, *J. Phys. Chem. A*, 2003, **107**, 8467-8475.
9. J. F. W. Keana and F. L. Vannice, *Physiol. Chem. Phys. Med. NMR*, 1984, **16**, 477-480.
10. F. Hyodo, K.-i. Matsumoto, A. Matsumoto, J. B. Mitchell and M. C. Krishna, *Cancer Res.*, 2006, **66**, 9921-9928.

11. H. C. Chan, K. Sun, R. L. Magin and H. M. Swartz, *Bioconjugate Chem.*, 1990, **1**, 32-36.

12. M. Brust, M. Walker, D. Bethell, D. J. Schiffrin and R. Whyman, *J. Chem. Soc.-Chem. Commun.*, 1994, 801-802.

13. V. Chechik, H. J. Wellsted, A. Korte, B. C. Gilbert, H. Caldararu, P. Ionita and A. Caragheorgheopol, *Faraday Discuss.*, 2004, **125**, 279-291.

14. P. Ionita, A. Caragheorgheopol, B. C. Gilbert and V. Chechik, *J. Am. Chem. Soc.*, 2002, **124**, 9048-9049.

15. P. Ionita, A. Caragheorgheopol, B. C. Gilbert and V. Chechik, *Langmuir*, 2004, **20**, 11536-11544.

16. M. Zachary, *Ph.D thesis,* The University of York, 2005, Ch. 5.

17. M. Conte, H. Miyamura, S. Kobayashi and V. Chechik, *J. Am. Chem. Soc.*, 2009, **131**, 7189-7196.

18. S. Durocher, A. Rezaee, C. Hamm, C. Rangan, S. Mittler and B. Mutus, *J. Am. Chem. Soc.*, 2009, **131**, 2475-2477.

19. J. A. Weil, J. R. Bolton and J. E. Wertz, *Electron Paramagnetic Resonance,* John Wiley & Sons, 1994, Ch. 10.

Chapter 5: Other applications of lanthanide-loaded gold nanoparticles

Chapter 5: Other applications of lanthanide-loaded gold nanoparticles

5.1 Introduction

Previous chapters (2-3) describe the preparation of gold nanoparticles protected by DTPA based ligand and their applications as MRI contrast agents. The DTPA ligand protected AuNPs have also some other useful and interesting applications apart from MRI contrast agents. For example, the DTPA based ligand is a strong chelate which can also bind other lanthanides such as terbium (Tb^{3+}), europium (Eu^{3+}), dysprosium Dy^{3+} etc. As Tb^{3+} and Eu^{3+} both exhibit luminescence (discussed in the next section), therefore Tb^{3+} or Eu^{3+}-loaded AuNPs in principle can be used as optical imaging contrast agents. By loading Gd^{3+} (as MRI contrast agent) and Tb^{3+} (as optical imaging contrast agent) on the same nanoparticle, dual imaging contrast agents can be obtained.[1] MRI usually provides high spatial resolution to give physiological and anatomical information while optical imaging allows the rapid screening i.e. accurate delineation between the targeted (diseased) and the surrounding (normal) tissues.[2] Currently a lot of effort is being devoted to the development of dual modal imaging probes.[3-5] For example, Lee and co-workers[5] described iron oxide particles conjugated to fluorescent dye doped silica nanoparticles for dual optical and magnetic resonance imaging (Figure 5.1).

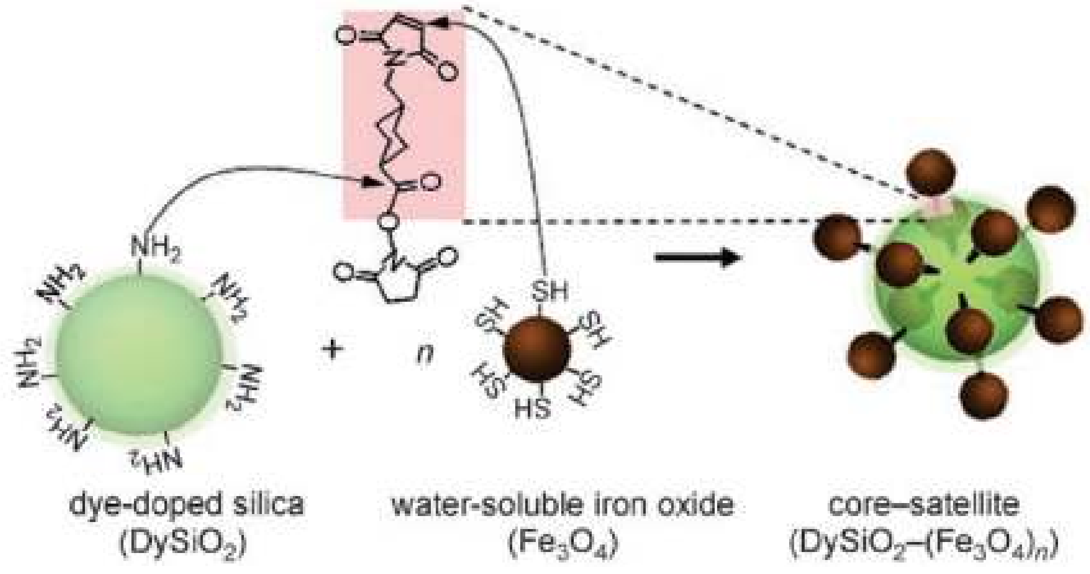

Figure 5.1: Schematic representation of dual imaging contrast agents i.e. core-satellite $DySiO_2$-$(Fe_3O_4)_n$ nanoparticles.[5]

Dye (Rhodamine) doped silica nanoparticles acted as optical imaging contrast agents while iron oxide particles were used as MRI contrast agents.

Furthermore, gold nanoparticles protected by DTPA ligand can also be used to test an important EPR methodology. The relaxation of unpaired electrons of paramagnetic species can be enhanced by other paramagnetic lanthanide metal ions which are close to each other. So, if we attach a nitroxide radical to the gold nanoparticles which already have lanthanides, the relaxation enhancement of nitroxide radical by paramagnetic lanthanide ion can be monitored by EPR spectroscopy. The EPR methodology which was tested using nitroxide-labelled-lanthanide-loaded gold nanoparticles will be discussed in the second part of this chapter.

5.1.1 Luminescence

Luminescence is the emission of light by a substance and it occurs when excited electron returns to the ground state from the excited state. Luminescence phenomena are divided into two classes depending upon the nature of the excited state:

- Fluorescence
- Phosphorescence

In fluorescence the electrons in the excited orbital have opposite spin as compared to the electrons in the ground state. Therefore they return to the ground state rapidly by emission of photons as this transition is spin allowed (paring of opposite spins). The emission rates of fluorescence are usually in the range of 10^8 s^{-1} (typical florescence life times are near 10 ns). Phosphorescence is the emission of light from triplet excited states. In phosphorescence the excited electron has the same spin orientation as the ground state electron. The transition to the ground state is thus forbidden and hence emission becomes slow. The phosphorescence life times are typically in milliseconds to seconds.[6]

In lanthanides, 4f orbitals are shielded by outer lying $5s^25p^6$ filled sub shells, and hence the spectral properties of Ln^{III} are minimally affected by the external field, caused by counter ions or ligands. As a result, very narrow f→f absorption bands are observed as compared to d→d absorption bands of transition metals. The f→f absorption bands are observed mostly in visible or near infrared regions. The f→f transitions have very low molar absorptivities i.e. typically <3 M^{-1} cm^{-1}. Therefore both absorption and emission bands are weak for lanthanides. The radiative life times for f-f transitions are in the range of 0.1-1.0 ms. [7-8]

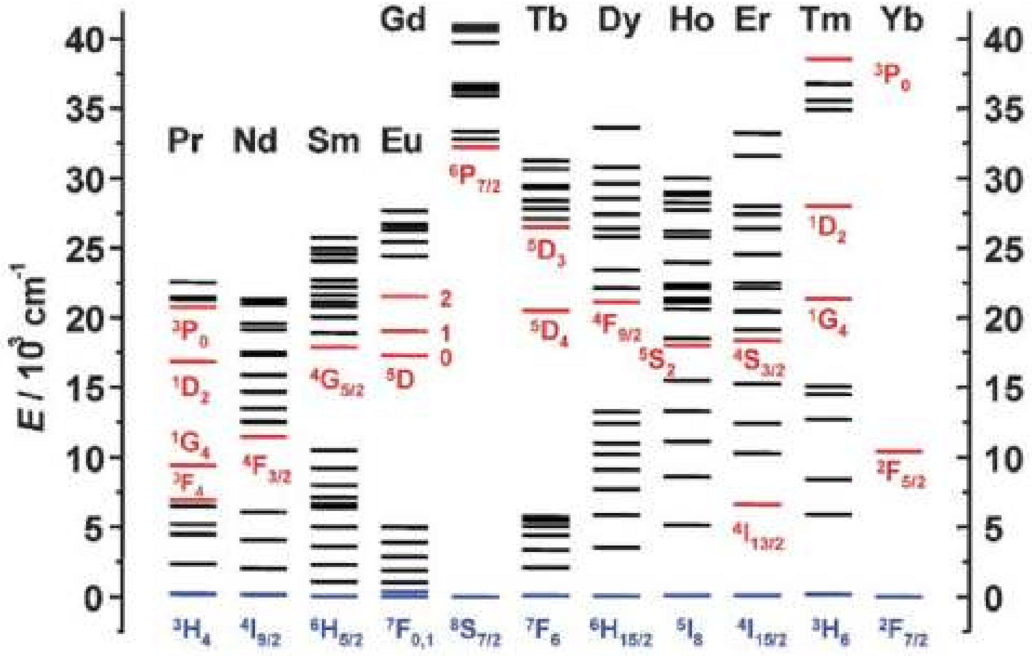

Figure 5.2: Partial energy diagram for lanthanide aqua ions (the main luminescent levels are drawn as red and fundamental levels are indicated as blue).[9]

Most lanthanides are luminescent, but some exhibits stronger emission than the others (Figure 5.2). Lanthanides can be either fluorescent (Pr^{III}, Nd^{III}, Ho^{III}, Er^{III}, Yb^{III}) or phosphorescent (Sm^{III}, Eu^{III}, Gd^{III}, Tb^{III}, Dy^{III}, Tm^{III}, Pr^{III}). Some lanthanide ions (e.g. Pr^{III}) exhibits both fluorescence and phosphorescence transitions. The emission of the lanthanides covers the entire spectrum i.e. from UV (Gd^{III}) to visible (e.g. Tb^{III}, Sm^{III} etc) and near-infrared (Pr^{III}, Yb^{III} etc).[8]

5.1.2 Sensitization (antenna effect)

Electronic transitions of lanthanides take place by redistribution of electrons within the 4f-subshell. These transitions are forbidden by electric dipole selection rules (i.e. there is no change of parity from the ground state to the excited state).[7] However these rules are relaxed by several factors / mechanisms. For example, mixing / coupling of vibrational states (i.e. J-mixing) and mixing with opposite parity wave functions, such as 5d orbitals, ligand orbitals or charge transfer states, results in breaking of the selection rules. For example for Eu^{3+}, $^7F_0 \leftrightarrow {}^5D_0$ transition is not allowed according to the selection rule, but in actual practice this transition is observed weakly due to J-mixing. The coupling between these electronic and vibrational states and the 4f wave functions depends on the interaction between 4f-orbitals and surrounding ligands.[8] As mentioned above, f-orbitals are shielded, and hence very weak absorption and emission bands are obtained by direct excitation of lanthanides.

The weak f→f oscillator strength can be overcome by indirect excitation. The indirect excitation phenomenon is also termed "sensitisation or antenna effect". The indirect excitation process involves three steps as depicted in Figure 5.3:

- The light is absorbed by surroundings of the lanthanide ions which may be either inorganic matrix or organic ligands (chromophores).
- Energy is then transferred onto the lanthanide ions.
- The lanthanide ions show luminescence by emitting absorbed energy in the form of photons.

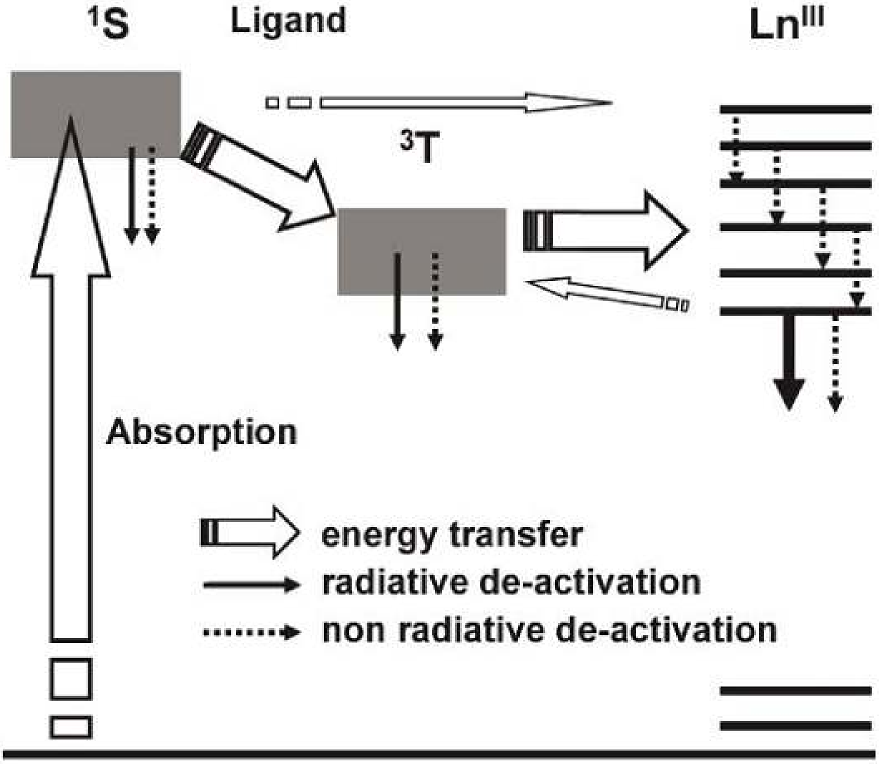

Figure 5.3: Block diagram showing energy flow paths during sensitisation of lanthanide luminescence.

Usually organic ligands (chromophores) are used as sensitisation agents. Many organic chromophores have very strong absorption and emission characteristics i.e. they have very high value of molar absorptivities ($>10^4\ M^{-1}cm^{-1}$).

As lanthanide ions or / and lanthanide chelates need a sensitizer in close proximity which can enhance lanthanide luminescence, gold nanoparticles can be used as a template to achieve this target because:

- More than one functional group / ligand can be attached on the surface of AuNPs easily.
- The sensitizer species / ligand can be attached on the nanoparticle surface in the same ligand shell as the lanthanide-DTPA chelate.
- There is no need to make a separate linker molecule to bring lanthanide chelate close to the sensitizer species.
- The ratio between sensitizer and lanthanide chelates at the nanoparticle surface can be tuned depending upon the requirement.

On the other hand, as gold absorbs light in the visible region strongly, this might affect the luminescence of lanthanide chelates at its surface. In order to test the feasibility of gold nanoparticles as dual imaging contrast agents, a ligand containing sensitizer group was designed which can be attached on gold nanoparticles protected by DTPA ligand and is discussed in the next section.

5.2 Design and synthesis of tryptophan based ligand 7

Tryptophan contains an indole group which absorbs light in UV-Vis region. The absorbed energy can be transferred to lanthanide ions if the tryptophan and lanthanide ion are in close proximity. Recently, Duhme-Klair and co-workers[10] reported the long lived luminescence of Tb-containing amphiphile which was sensitised by a tryptophan based compound. The Tb-chelate and the sensitizer were brought close to each other in a micelle via non-covalent interactions (Figure 5.4).

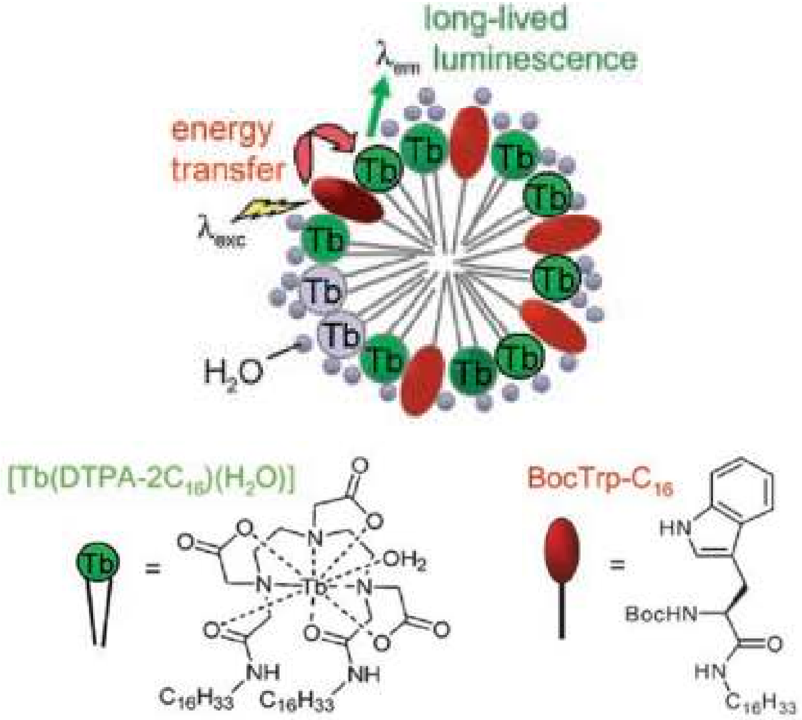

Figure 5.4: Schematic illustration of the intermolecular sensitisation process.[10]

Thus it was confirmed that covalent linkage between lanthanide ion and the sensitizer is not necessary for efficient transfer of energy. This report[10] strongly supports the idea of attaching tryptophan based ligand and lanthanide ion on the gold nanoparticle surface in the same ligand shell.

The tryptophan based ligand **7** (Figure 5.5) was synthesised by DCC coupling of L-amino tryptophan ester hydrochloride with dithiobutyric acid.

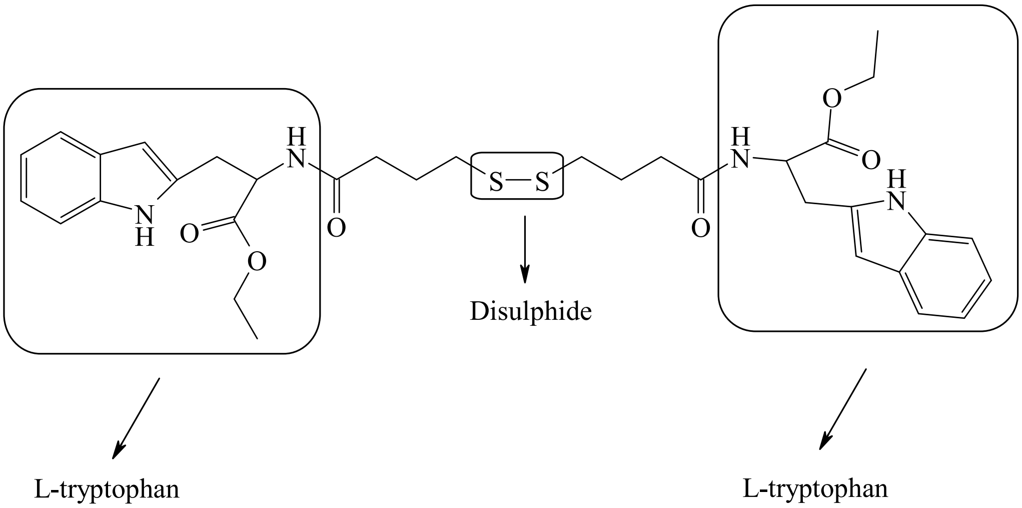

Figure 5.5: Chemical structure of tryptophan based ligand 7

The dithiobutyric acid was selected as it contains disulphide group which will make the ligand attach at the gold nanoparticle surface. The other important advantage of dithiobutyric acid selection was to maintain the chain length of ligand **7** in the same range as DTPA ligand **6**. The Tryptophan ligand **7** was characterised by MS and NMR spectroscopies (data shown in experimental chapter 7).

5.3 UV-Vis absorption and emission spectra of tryptophan ligand 7

After characterisation, the absorption and emission spectra of tryptophan based ligand **7** were recorded and compared with L-tryptophan ester hydrochloride. The UV-Vis absorption spectra (Figure 5.6) show λ_{max} = 282 nm for L-tryptophan and tryptophan ligand. The absorbance of tryptophan ligand **7** in the normalised UV-Vis spectra was twice as high as for L-tryptophan. This is due to the presence of two tryptophan units in the tryptophan ligand molecule. The UV-Vis spectra were used to determine the wavelength for excitation of tryptophan ligand.

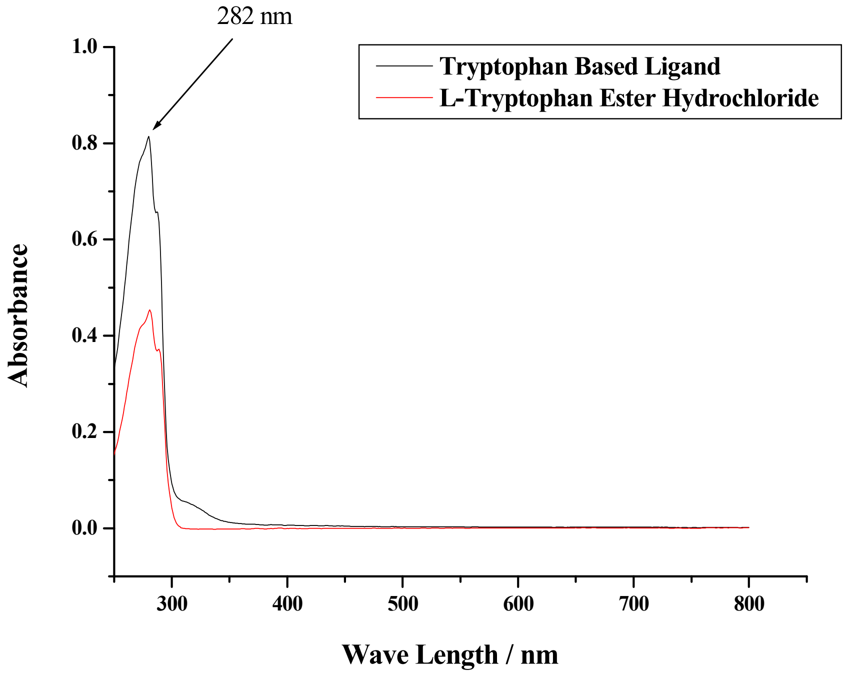

Figure 5.6: UV-Vis spectra of L-tryptophan and tryptophan based ligand 7.

The fluorescence emission spectra of tryptophan ligand were recorded by exciting at 282 nm. The emission spectrum of tryptophan ligand shows very strong emission in the range of 330-430 nm (Figure 5.7).[11]

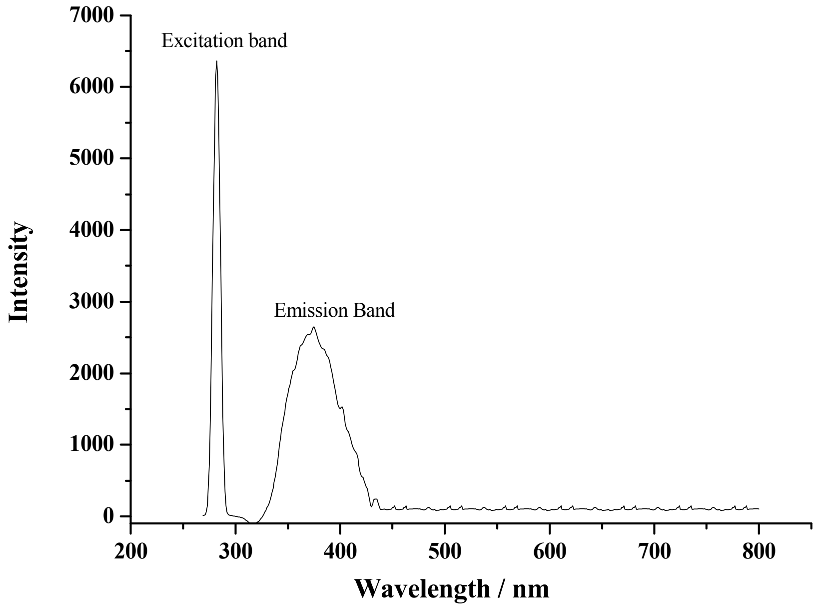

Figure 5.7: Fluorescence emission spectrum of tryptophan ligand 7.

The UV-Vis absorption and emission spectra of tryptophan ligand **7** thus confirmed that the tryptophan ligand can be used for sensitisation of lanthanide ion.

5.4 Synthesis of gold nanoparticles stabilised by DTPA based ligand 5

Gold nanoparticles stabilised by ester-protected DTPA ligand **5** were selected, because of their solubility in organic media. The solubility of gold nanoparticles in organic medium rather than aqueous medium was preferred for ease of the ligand exchange reaction. In aqueous medium, the rate of ligand exchange reaction at gold nanoparticles surface was negligible. After ligand exchange reaction in organic medium, the t-butyl ester groups of DTPA ligand at nanoparticles surface can be removed easily by TFA / DCM deprotection (and will be discussed in section 5.5.1) so that DTPA ligand can chelate lanthanides.

Gold nanoparticles protected by DTPA ligand **5** (Figure 5.8) were synthesized by Brust's biphasic method[12] and then purified by size exclusion chromatography. The biphasic approach was used because DTPA ligand **5** is soluble in organic medium while the gold salt (used for AuNPs preparation) is soluble in aqueous medium. Brust's protocol has been discussed in detail previously (chapter 2 section 2.3). Tertiary (t)-butyl ester protected DTPA ligand **5** was selected to get the gold nanoparticles which should be soluble in organic medium. In organic medium ligand exchange reaction at gold nanoparticles surface with other thiol based ligands can be done easily as compared to the aqueous medium.[13-14]

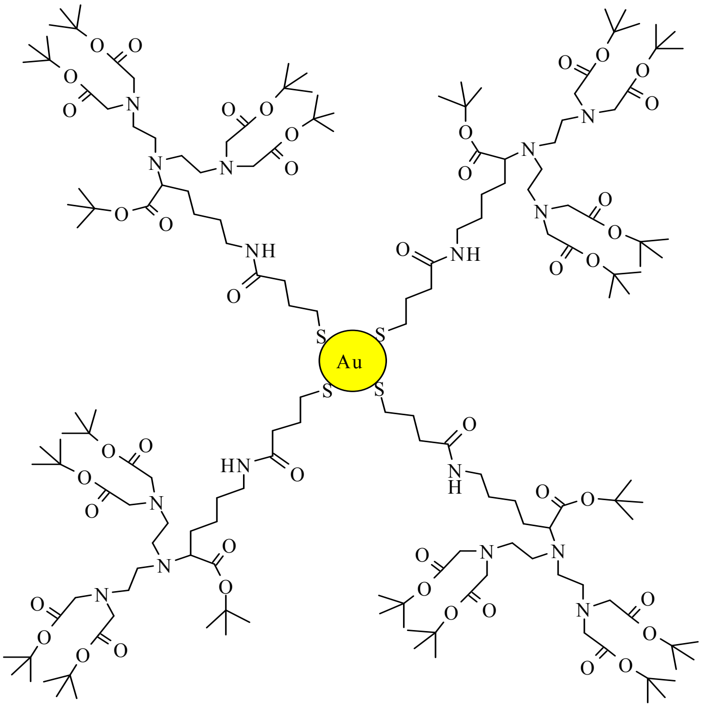

Figure 5.8: Gold nanoparticles protected by DTPA ligand 5.

The purified gold nanoparticles protected by DTPA ligand **5** were characterised by ^{1}H NMR, UV-Vis (SPB at 520-525 nm), TGA and TEM.

5.4.1 ^{1}H NMR characterisation of AuNPs protected by DTPA ligand 5

The AuNPs protected by DTPA ligand **5** were characterised by ^{1}H NMR spectroscopy to confirm the successful adsorption of the ligand at the nanoparticles surface and the complete removal of tetraoctylammonium bromide (which was used as a phase transfer agent) and any free ligand during purification. The proton peaks of ligand at the surface of nanoparticles become broader due to incomplete averaging of anisotropic interactions (discussed in chapter 2, section 2.3.2). The ^{1}H NMR spectra of free DTPA ligand **5** and the ligand adsorbed on the gold nanoparticle surface are shown in Figure 5.9.

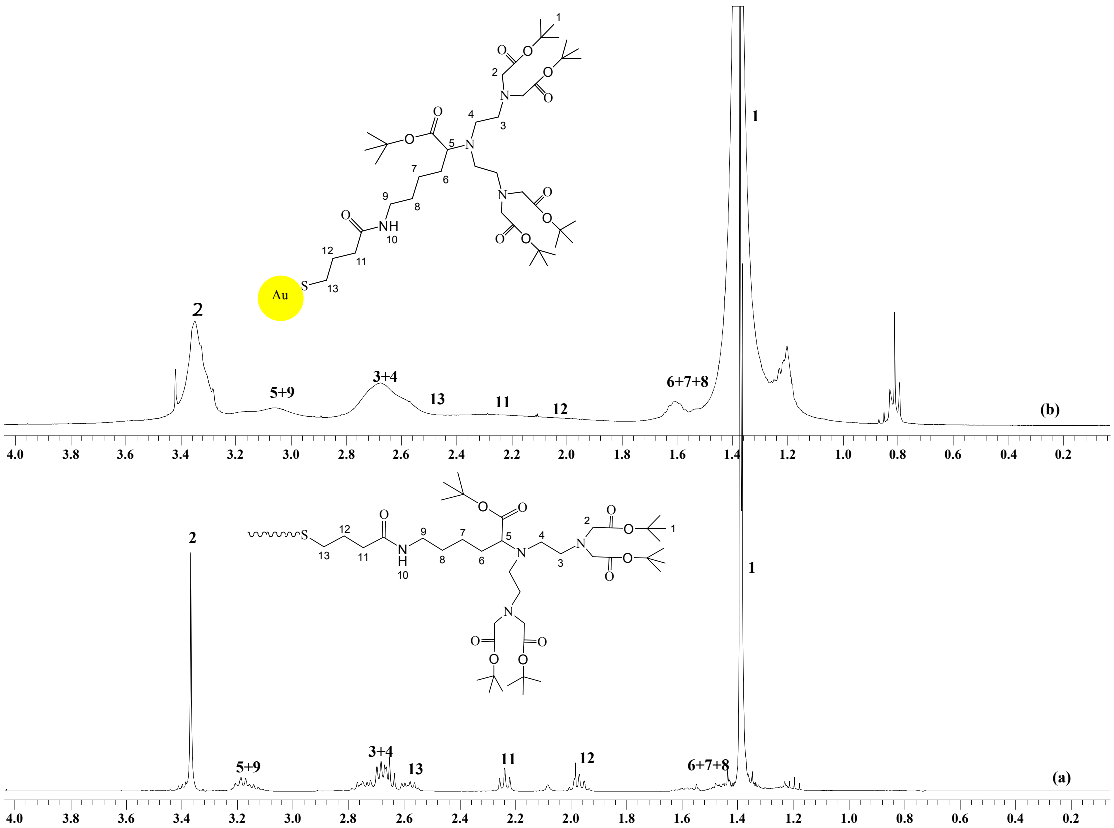

Figure 5.9: ^{1}H NMR spectra of free DTPA ligand 5 (a) and ligand 5 adsorbed at AuNPs surface (b).

Figure 5.9 shows significant broadening of the ^{1}H peaks consistent with the successful adsorption of ligand at the nanoparticle surface. Furthermore, no evidence of any free ligand is observed in ^{1}H NMR spectrum. After NMR characterisation of gold nanoparticles, the DTPA ligand coverage at nanoparticle surface was estimated by TGA and is discussed in the next section.

5.4.2 TGA of AuNPs protected by DTPA ligand 5

Thermogravimetric analysis (TGA) was carried out by the same method as for the AuNPs protected by DTPA ligand **6** (discussed in chapter 2 section 2.3.4) to determine the amount of organic content (DTPA ligand **5**) present at gold nanoparticle surface. Organic content was needed to estimate the composition of AuNPs. The TGA graph of AuNPs protected by DTPA ligand **5** (Figure 5.10) shows about 47 % of the organic content. This amount is compatible with similar type of AuNPs protected by thiol based ligands.[15]

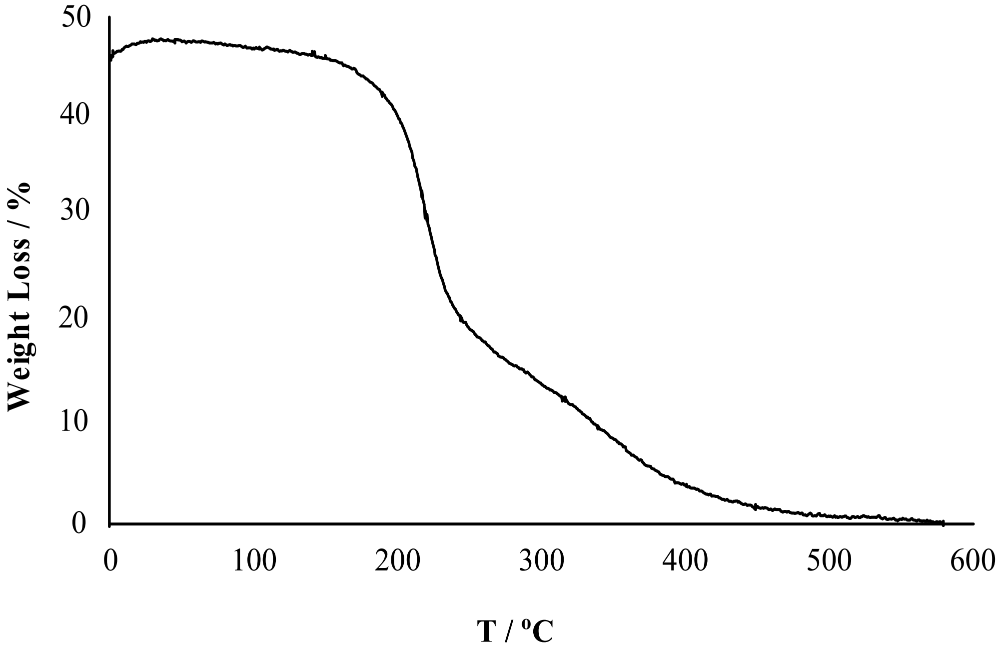

Figure 5.10: TGA plot of AuNPs protected by DTPA ligand 5.

5.4.3 TEM of AuNPs protected by DTPA ligand 5

TEM was carried out by the same method as for the gold nanoparticles discussed in previous chapters. TEM image (Figure 5.11) of AuNPs showed well dispersed nanoparticles with average diameter 2.42 ± 0.34 nm.

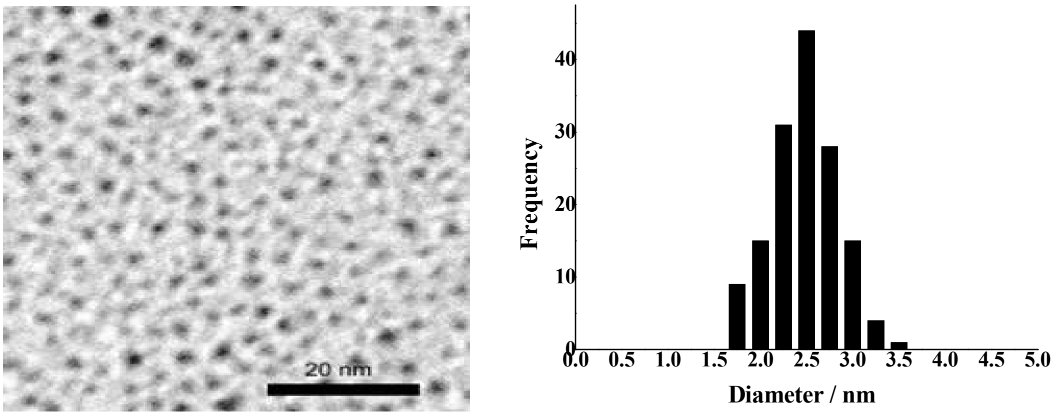

Figure 5.11: TEM image and size distribution histogram of AuNPs protected by DTPA ligand 5.

From TGA and TEM data, the composition of the gold nanoparticles protected by DTPA ligand was estimated (Au_{439} $Ligand_{88}$) which was used for tryptophan labelling and then lanthanide loading onto the nanoparticles.

5.5 Ligand exchange of tryptophan ligand 7 with DTPA ligand 5 at AuNP surface

By ligand exchange approach, the ligands with higher affinity than the ligands already present at gold nanoparticle surface, can be replaced. Some DTPA ligands from the AuNP surface were replaced with tryptophan ligand **7** (Figure 5.12) using a ligand exchange approach. As both tryptophan and DTPA ligands have similar affinity for gold, the reaction mixture was stirred overnight for successful ligand exchange reaction. The ratio between tryptophan and DTPA ligand was kept 1 / 6. It is difficult to determine the exact extent of ligand exchange, however the feasibility of ligand exchange of one thiol based ligand with another thiol based ligand at gold nanoparticle surface was confirmed by EPR spectroscopy with a spin labelled ligand and will be discussed in section 5.8.2 in this chapter.

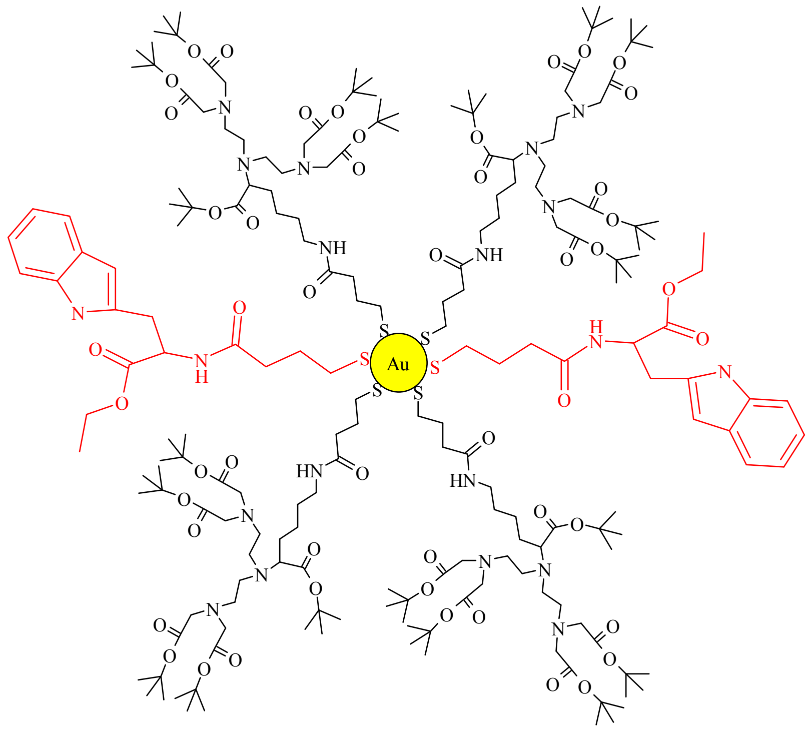

Figure 5.12: Tryptophan labelled AuNPs

5.5.1 Deprotection of t-butyl ester groups of DTPA and tryptophan ligand at AuNPs

The deprotection of t-butyl ester groups of DTPA ligand **5** at AuNP surface was carried out to generate the chelating unit. The deprotection was carried out using 1:1 mixture of TFA and DCM by a modified literature procedure[16] as described in detail in chapter 2 (section 2.2.4). To avoid the decomposition of gold nanoparticles in acidic medium, the deprotection reaction was carried under the inert (N_2) atmosphere. After deprotection, the AuNPs were water soluble which is a sign of successful deprotection.

5.5.2 Lanthanide (Tb^{3+} and Eu^{3+}) loading on tryptophan labelled AuNPs and their fluorescence emission spectra

From several luminescent lanthanides, Tb^{3+} and Eu^{3+} were selected as they exhibit the most intense emission band in the visible region. Lanthanide loading onto the AuNPs protected by DTPA ligand was monitored by UV-Vis titration using xylenol orange as an indicator as described in detail in chapter 2 (section 2.4.2).

The fluorescence emission spectra of Tryptophan labelled Tb-loaded gold nanoparticles were recorded by exciting the tryptophan at 282 nm and then at 375 nm (i.e. direct excitation of Tb^{3+}). It was expected that the energy absorbed by tryptophan molecule will be transferred to the Tb^{3+} ion which will exhibit strong emission band, but unfortunately Tb^{3+} did not show any emission band (Figure 5.13). This absence of emission band of Tb^{3+}-chelate at gold nanoparticle surface may be due to several reasons. Gold absorbs light in the UV-Vis region; hence it is possible that much of the incoming light is absorbed by gold nanoparticles rather than sensitizer molecule or lanthanide ions. Second possibility might be the chemical decomposition of tryptophan ligand during deprotection step, because if the tryptophan was decomposed, there will be no alternative way by which energy was absorbed and then transferred to Tb^{3+}. The third possibility is the quenching of the fluorescence by gold nanoparticles.

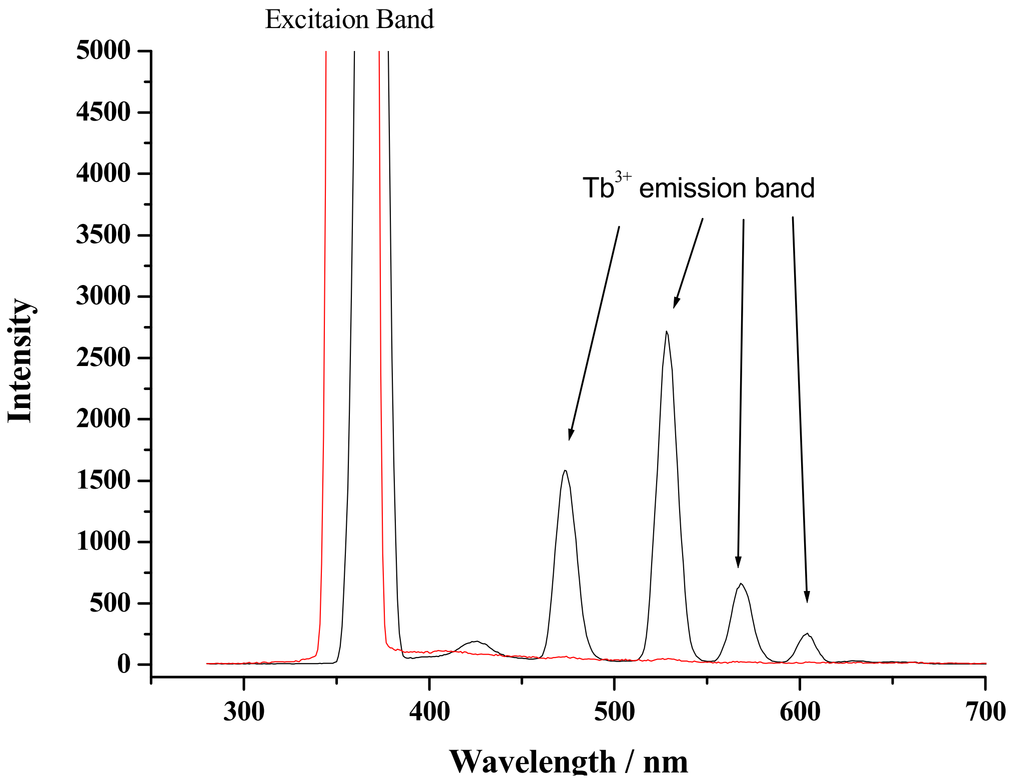

Figure 5.13: Fluorescence emission spectra of Tb-DTPA chelates at the surface of AuNPs (red) and free Tb-DTPA chelates in aq solution (black).

5.6 Control experiments to confirm the quenching of lanthanide ion fluorescence by AuNPs

Two independent control experiments were carried to explore the reason for the absence of Tb^{3+} emission band at gold nanoparticle surface.

5.6.1 Ligand exchange approach (first control experiment)

In the first control experiment, most lanthanide-DTPA chelates were displaced from the gold surface using a large (100 fold) excess of an alkane thiol (Figure 5.14).

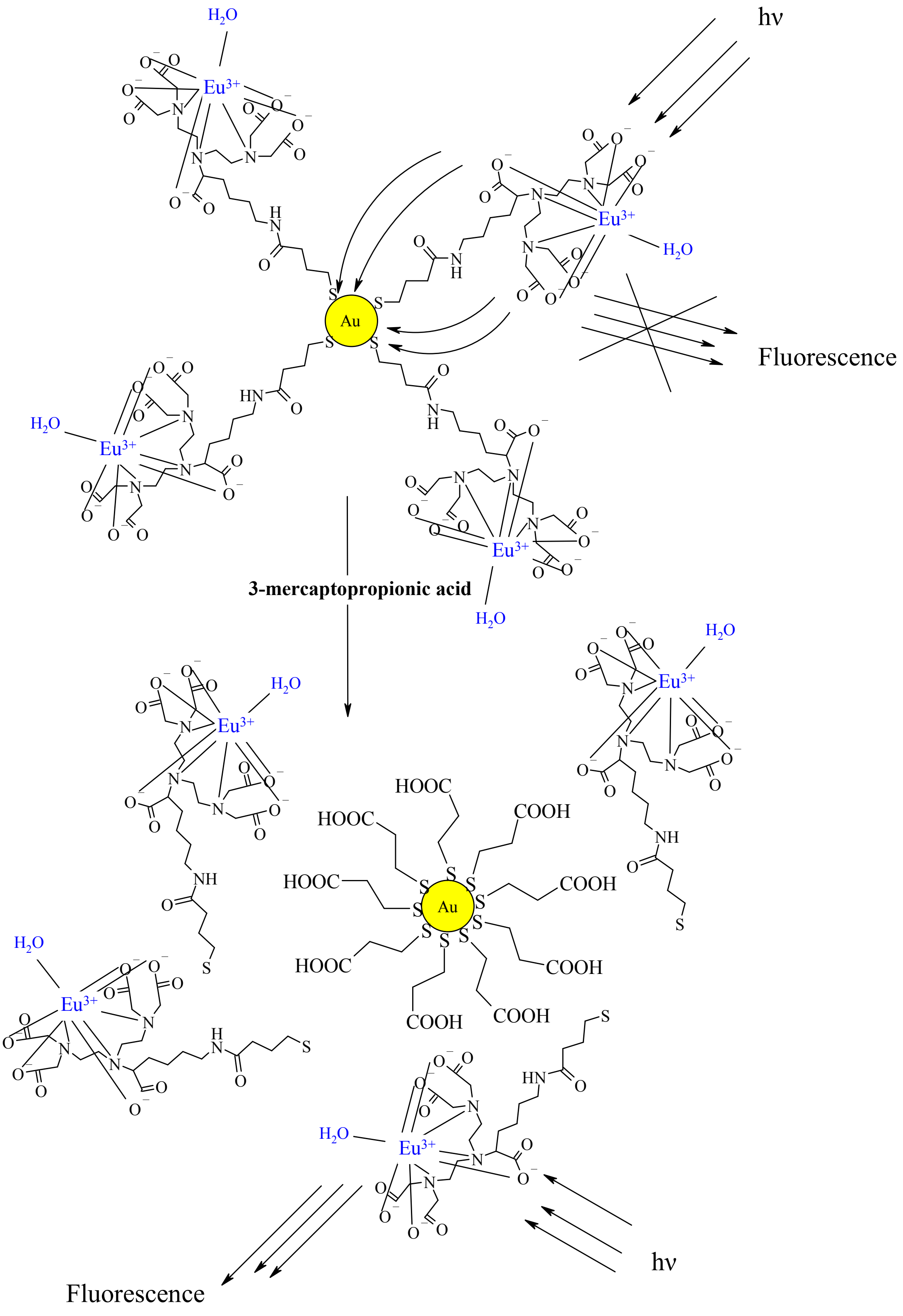

Figure 5.14: Schematic representation of the first control experiment.

The purpose of removing all lanthanide -DTPA chelates from the gold surface was to remove the possibility of quenching the fluorescence of lanthanide-chelates by gold nanoparticles. Mercaptopropionic acid was used for ligand exchange as it is water soluble and has strong affinity (due to thiol group) for gold. The fluorescence emission spectra of Eu^{3+}-loaded AuNPs were recorded before and after ligand exchange. When the lanthanide-DTPA chelates were replaced from the nanoparticle surface, they exhibited intense fluorescence emission spectra (Figure 5.15) upon excitation at 400 nm. This confirmed that Eu-DTPA chelate fluorescence was quenched by gold nanoparticles.

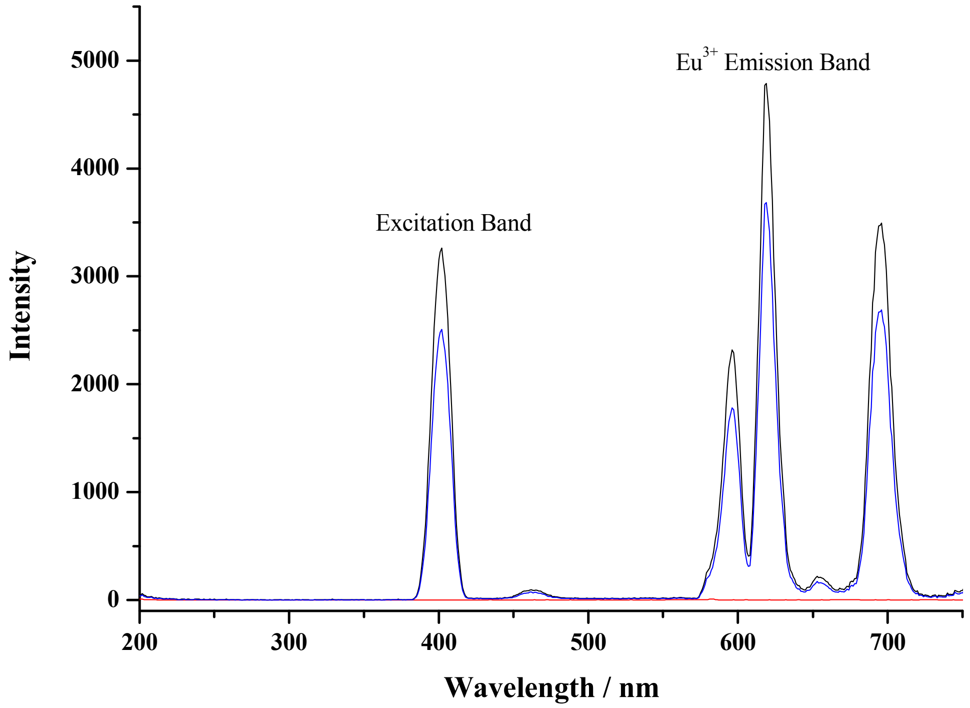

Figure 5.15: Fluorescence emission spectra of Eu^{3+}-DTPA@AuNPs, first control experiment (black) and second control experiment (blue).

5.6.2 Second control experiment (decomposition of AuNPs)

The second control experiment confirmed the observations of the first control experiment independently. In this experiment, gold nanoparticles were decomposed in order to release the lanthanide-DTPA chelates from nanoparticle surface. It is well established in literature[17] that gold nanoparticles can be destroyed / aggregated by treatment with a mixture of KI (a good ligand in the form of iodide) and I_2 (strong oxidizing agent) in MeOH. When the lanthanide-loaded AuNPs were treated with a mixture of KI and I_2 in MeOH, gold nanoparticles were decomposed immediately; the lanthanide-DTPA chelates desorbed from the nanoparticles surface. The desorbed lanthanide-DTPA chelates exhibited fluorescence (Figure 5.15). This confirmed the observations of first control experiment i.e. the fluorescence of lanthanide-DTPA chelates at gold nanoparticles surface was quenched by gold nanoparticles.

In the literature, many researchers described the gold nanoparticles as fluorescence quencher,[18-20] while some[21-22] reported opposite observations. The fluorescence quenching by metal nanoparticles is generally ascribed to the enhanced nonradiative relaxation of the excited state. For example, Agulia *et al.*[19] described the quenching of fluorescence of dansyl cadaverine attached to the gold nanoparticle surface. Sometimes the fluorescence emission range of a fluorescent substance overlaps with the absorption band (i.e. SPB) of metal (gold) nanoparticles. This may also result in diminishing or quenching fluorescence.[23] On the other hand, if the chromophores or lanthanide chelates are separated (by bulky groups / spacers) about 10-15 nm from the nanoparticles surface, the nanoparticles do not quench the fluorescence. For example it has been reported that CdSe(ZnS) particles do not show any luminescence at the surface of gold nanoparticles, but when polyelectrolyte layers of ~11 nm thickness were formed between gold nanoparticles and CdSe(ZnS) nanocrystals, a strong luminescence was observed.[24]

In tryptophan labelled lanthanide-loaded AuNPs, fluorescence of tryptophan or lanthanide chelate or of both may be quenched. But as the lanthanide-DTPA chelates showed fluorescence even without tryptophan, the lanthanide fluorescence is likely to be quenched by gold nanoparticles.

5.7 Conclusions

Multifunctional gold nanoparticles bearing a fluorophore were prepared. Various fluorescent lanthanides were chelated with DTPA based ligand at AuNPs surface. A tryptophan based ligand (sensitizer for lanthanides) was prepared and adsorbed at the nanoparticle surface via ligand exchange approach. Unfortunately tryptophan-labelled lanthanide-loaded AuNPs did not show any fluorescence. The fluorescence was found to be quenched by gold nanoparticles as confirmed by two independent control experiments.

The next section of this chapter describes the other applications of lanthanide-functionalised gold nanoparticles.

5.8 Distance measurements by EPR spectroscopy

The second part of this chapter describes another important area of applications of lanthanide-loaded gold nanoparticles which deals with the use of gold nanoparticles as a model system for distance measurements. Interradical distance measurements have wide spread applications in dynamics and structural studies of biomacromolecules and their complexes.[25] For example site-directed spin labelling (SDSL), discovered in 1994, is a technique used for probing protein local environment using EPR spectroscopy. To study with EPR, a spin label is attached to the proteins, which exhibit EPR spectra depending upon the dynamical and local chemical behaviour of proteins. In most SDSL, nitroxide based spin labels are used (Figure 5.16). Furthermore, two spin labels can also be attached at two different sites of the protein, the distance between these two spins can be determined on the basis of dipolar interactions using EPR spectroscopy. Most important applications of SDSL is to study the membrane proteins as these proteins represent more than 50% of all proteins and future drug targets, and are difficult to crystallize.[26]

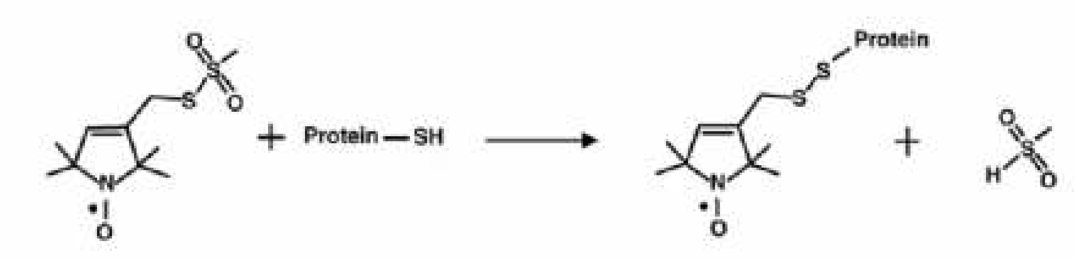

Figure 5.16: Reaction of the methanethiosulfonate spin label with cysteine to generate the disulfide-linked side chain to a protein.[26]

The following four techniques were developed for distance measurements in various ranges.

1. Exchange interaction ESR
2. Dipolar cw-EPR
3. DEER (double electron-electron resonance)
4. Double quantum coherence

The first two methods (based on continuous wave (cw) EPR) are limited to only short distance measurements (0.4-2.5 nm) as they rely on the line shape analysis for which strong interactions are required. The remaining two methods (3 and 4) are based on pulsed EPR, and are much more sensitive than the cw-EPR spectroscopy. These methods can extract dipolar interactions of weaker intensity and are thus sensitive to long range distances between 1.7-8.0 nm.[27] A new method for distance measurements is being developed based on relaxation enhancement by paramagnetic metal ions.[28] For example, recently Jeschke and co-workers described the distance measurement between nitroxide spin label and lanthanide chelate which are attached at two ends of a model compound (Figure 5.17).[25] The lanthanide chelate was used for relaxation enhancement of nitroxide spin label.

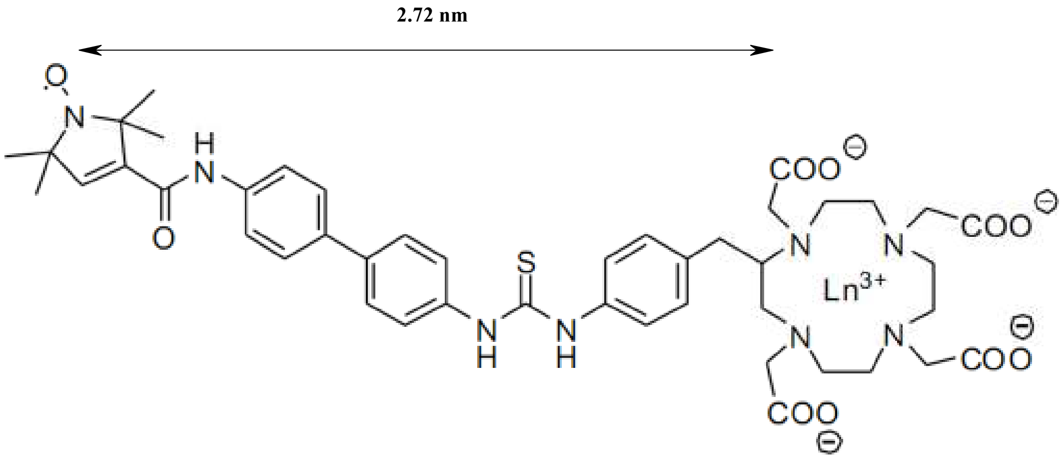

Figure 5.17: Structure of a model compound having lanthanide chelate and nitroxide spin label.[25]

Gold nanoparticles protected by DTPA ligand were selected as a model system for distance measurements by DEER due to several reasons. For example nanoparticles having good size range (i.e. 1.5 nm to 15 nm) can be prepared easily with predictable size distribution. Their size can be determined independently by TEM. Furthermore more than one ligand can be attached at gold nanoparticle surface easily. For distance measurements based on relaxation enhancement method, a spin label and a lanthanide ion are needed. The DTPA ligand which is used for stabilisation of gold nanoparticles can chelate lanthanides easily, while the spin label was synthesized separately and then attached at gold nanoparticles surface by ligand exchange approach. Thus these nanoparticles; a model system can be used to test the application of pulsed EPR method for distance measurements to the heterogeneous systems. The synthesis and characterisation of TEMPO based ligand **8** (i.e. nitroxide based spin label) by EPR is discussed in next section.

5.8.1 Synthesis of TEMPO based ligand 8

TEMPO based ligand **8** was synthesized by peptide coupling of dithiodipropionic acid with amino-TEMPO. Dithiodipropionic acid contain disulphide group which will make the ligand adsorb at the gold nanoparticle surface, while amino-TEMPO has a stable nitroxide radical (Figure 5.18). The TEMPO based ligand was characterised by MS (data shown in experimental chapter) and EPR spectrum. The EPR spectrum showed characteristic features due to spin-spin interactions between the two nitroxide radicals. A free nitroxide exhibit three lines, but if two nitroxides are placed close to each other (as in TEMPO based ligand **8**), some extra lines of low intensity (marked as * in Figure 5.18) are observed, which confirmed the successful synthesis of TEMPO based ligand **8**.

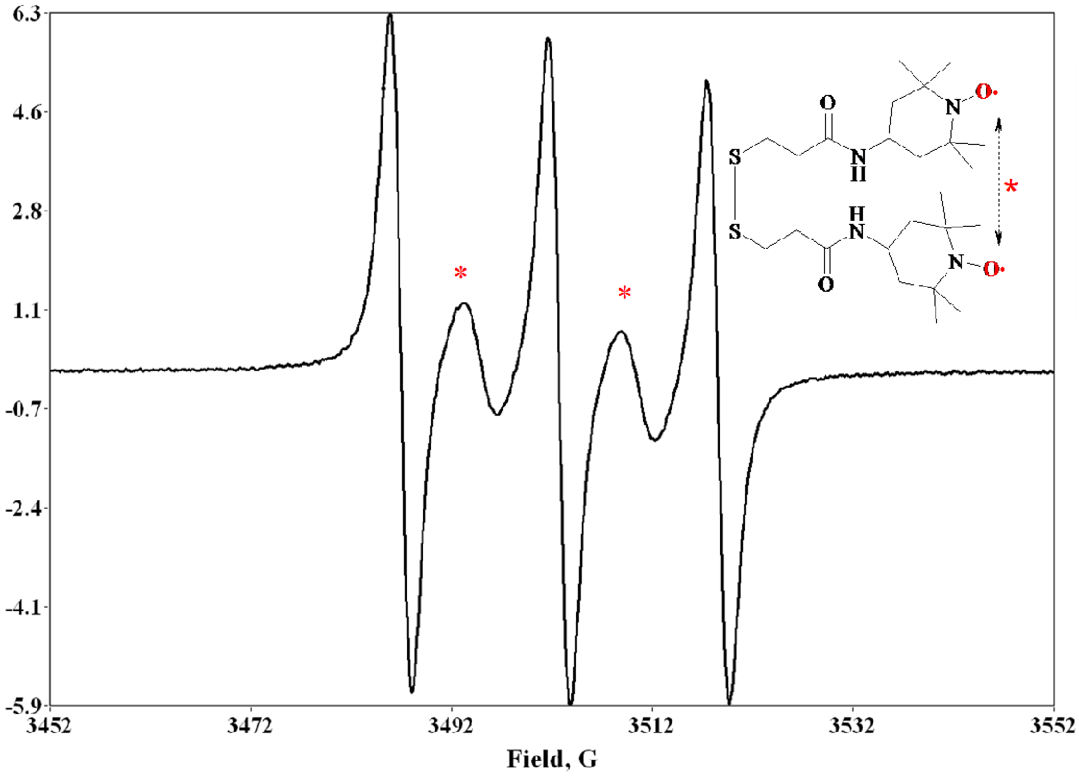

Figure 5.18: EPR spectrum of TEMPO based ligand 8 in DCM.

5.8.2 Spin-labelling of AuNPs by TEMPO based ligand 8

Spin labelling of gold nanoparticles with TEMPO based ligand i.e. nitroxide spin label was carried out at 60-65 °C. The number of spin labels per nanoparticle can be controlled by controlling stoichiometric ratio between gold nanoparticles and spin label (i.e. TEMPO based ligand **8**). To avoid multiple distances, on average 2-3 spin labels were adsorbed per nanoparticle. The spin labelling was monitored using EPR spectroscopy. After spin labelling, the free ligand could be removed by size exclusion chromatography. When the nitroxide spin labels were adsorbed at gold nanoparticles surface, the characteristic features (*) in their EPR spectrum disappeared (Figure 5.20). Another important change in an EPR spectrum of nitroxide adsorbed at the nanoparticle surface was the line broadening. The line broadening occurs due to slower motion of the nitroxide at the nanoparticle surface than the free nitroxide (Figure 5.20). These two changes in EPR spectrum of TEMPO based ligand at gold nanoparticle surface confirmed the successful spin labelling of gold nanoparticles.

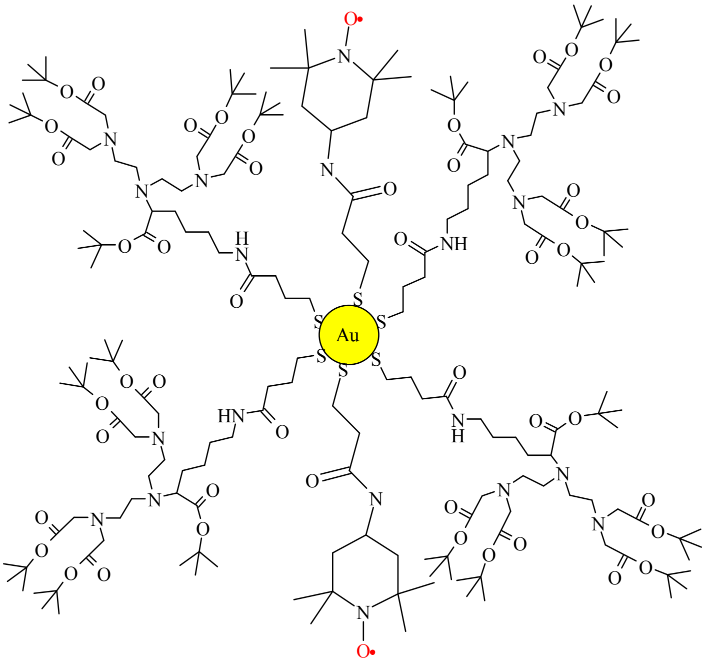

Figure 5.19: Spin labelled AuNPs protected by DTPA ligand 5.

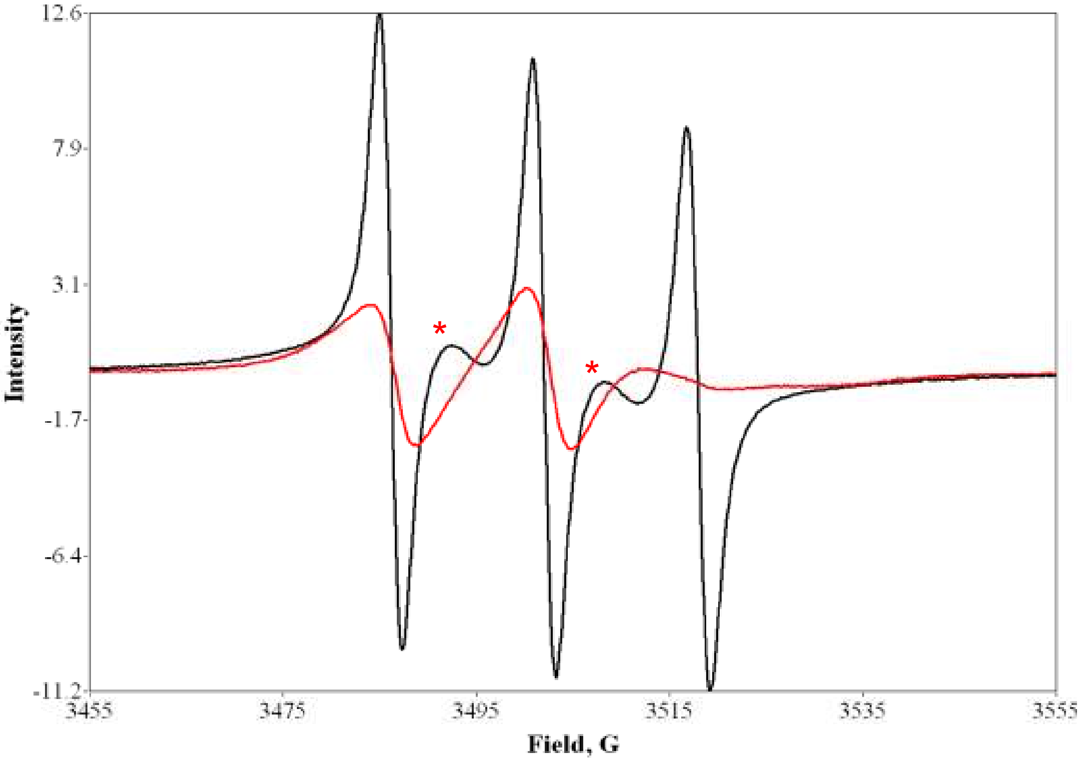

Figure 5.20: EPR spectra of free nitroxide spin label (black) and adsorbed at AuNP surface (red).

5.8.3 Deprotection of t-butyl ester groups of DTPA ligand at AuNP surface

The t-butyl esters groups of DTPA ligand were removed in order to chelate with lanthanides. As deprotection involves the use of acid (TFA) and DCM (discussed previously in chapter 2, section 2.2.4), the reaction was carried out under inert atmosphere in order to avoid the decomposition of nitroxide radical. Furthermore, use of excess (about 2 fold) DCM as compared to TFA, also helped to avoid nitroxide radical decomposition. The nitroxide radical can disproportionate in the presence of acid. During deprotection reaction, about half of nitroxide radicals at the nanoparticle surface were found to decompose as evident from the EPR spectra shown in Figure 5.22. The deprotected spin-labelled gold nanoparticles (Figure 5.21) were water soluble, and were purified by size exclusion chromatography.

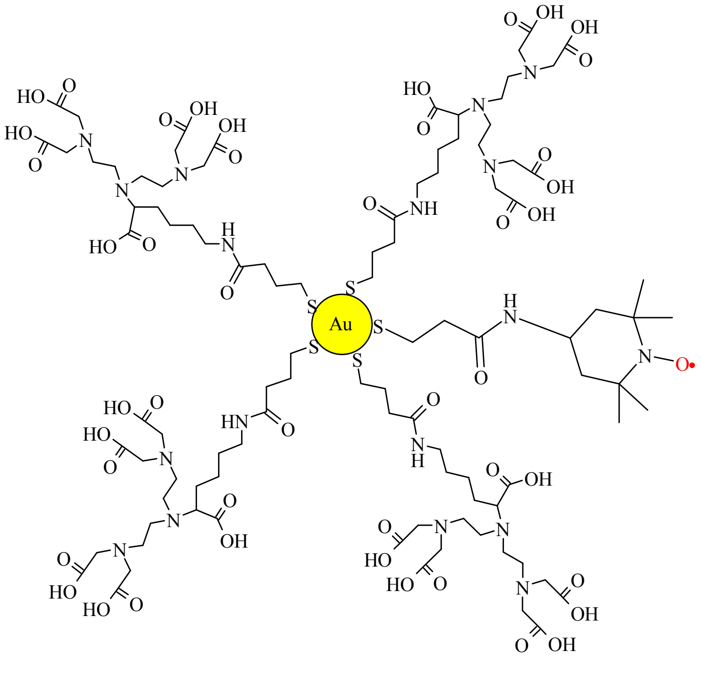

Figure 5.21: Water soluble spin-labelled AuNPs protected by DTPA ligand 6.

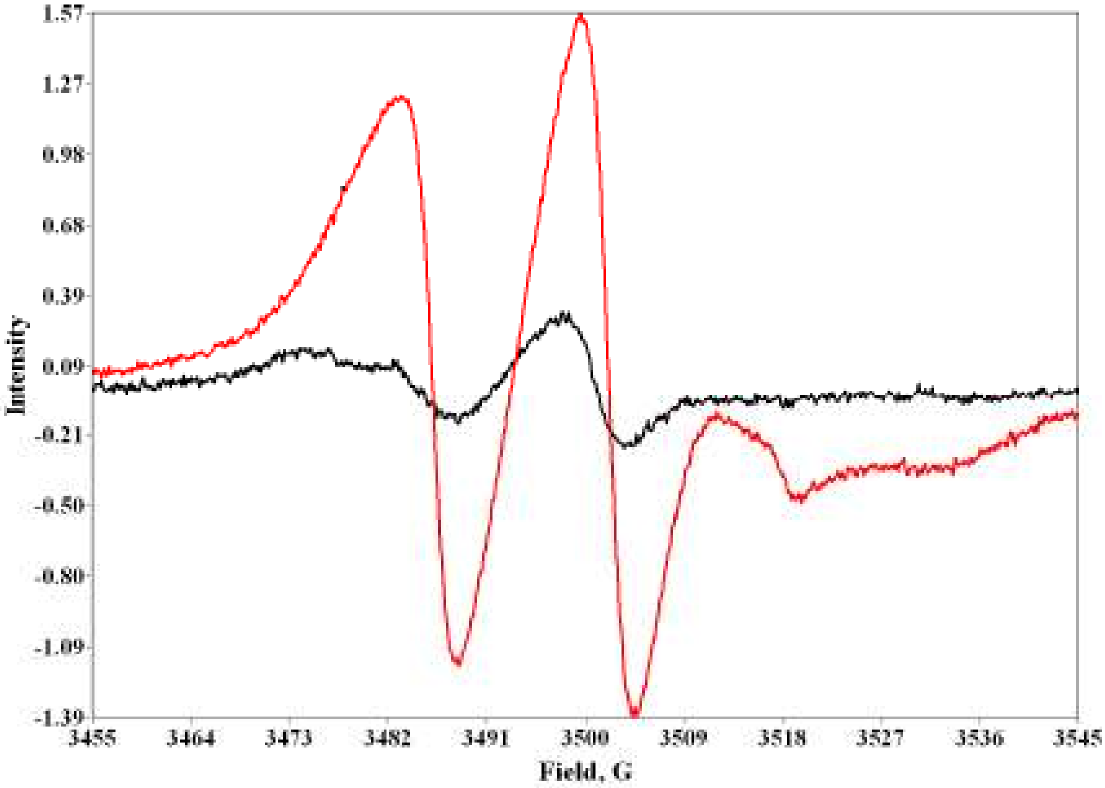

Figure 5.22: EPR spectra of nitroxide spin labelled AuNPs before (red) and after (black) t-butyl ester deprotection.

5.8.4 Lanthanide loading on nitroxide spin labelled AuNPs and their cw and pulsed-EPR measurements

Various lanthanides (Gd^{3+} and Dy^{3+}) were loaded at the gold nanoparticle surface (Figure 5.23). The loading was monitored using xylenol orange titration using UV-Vis spectroscopy (as discussed in chapter 2, section 2.4.2).

The lanthanides loaded spin-labelled gold nanoparticles were characterised by cw-EPR and pulsed-EPR spectroscopy. In cw-EPR spectra, line broadening of the nitroxides was observed, which was increased with the increased concentration of lanthanides as shown in Figure 5.24. The line broadening occurs due to relaxation enhancement of nitroxide radical by the paramagnetic lanthanide ion. Some sharp lines are also observed in the Figure 5.24 (marked as **), these signals are due to nitroxides leaching from the nanoparticle surface (i.e. free nitroxides). As the amount of lanthanides was increased, the intensity of sharp lines was not affected, which confirmed that lanthanides only enhance the relaxation rate of nitroxides which are close to lanthanides.

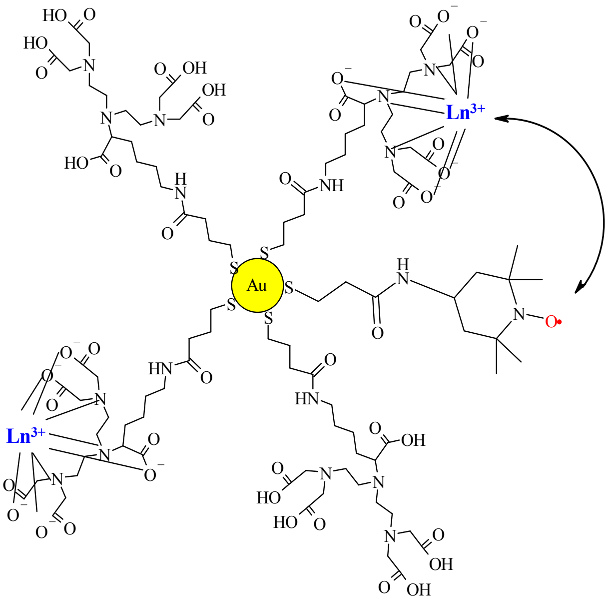

Ln^{3+} = Gd^{3+} , Dy^{3+} and La^{3+}

Figure 5.23: Lanthanide loaded spin-labelled AuNPs

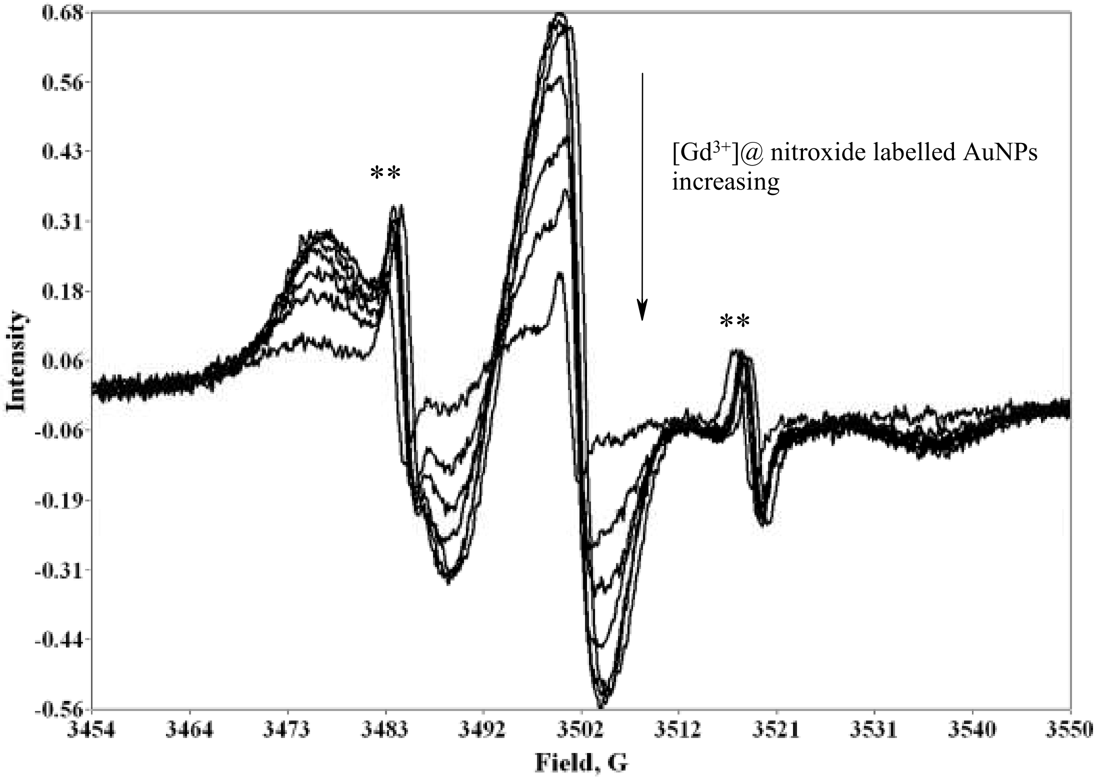

Figure 5.24: CW-EPR spectra of nitroxide spin labelled AuNPs in the presence of various [Gd^{3+}] concentrations.

5.8.5 Pulsed-EPR experiments

All the pulsed-EPR experiments were carried out in the laboratory of Prof. Gunnar Jeschke at ETH Zürich (Switzerland). The pulsed EPR experiments consist of two main parts: (a) distance measurements by Double Electron-Electron Resonance (DEER), and (b) relaxation enhancement of nitroxide electron by lanthanides (pulse EPR measurements).

5.8.5.1 Distance measurements (by DEER experiments)

The four pulse DEER experiment has become the most frequently used approach to measure the nitroxide-nitroxide distances in the range between 1.6 and 8 nm. Recently the same experiment has been performed on the Gd^{3+} ion as a detection spin and with a nitroxide radical as a pumped species[25, 29]. The nitroxide-nitroxide distance and Gd^{3+}-

nitroxide distance at the surface of gold nanoparticle measured by DEER experiments are shown in Table 5.1.

Table 5.1: Mean distance and the width of distance distribution obtained from the fit of DEER data.

Gd and La at spin labelled AuNPs	NO-NO distance		Gd^{3+}-NO distance	
	r / nm	Distribution width (r) / nm	r /nm	Distribution width (r) / nm
0.0 % Gd^{3+}	2.40	0.53	-	-
2 % Gd^{3+}	2.46	0.53	2.85	0.57
4 % Gd^{3+}	-	-	2.85	0.67
32 % La^{3+}	2.45	0.57	-	-

The mean distance data are completely consistent and provide the averaged nitroxide-nitroxide distance of approx. 2.44 nm and the Gd^{3+}-nitroxide distance of 2.85 nm (Table 5.1). Gd^{3+}-nitroxide distance was found slightly larger than the nitroxide-nitroxide distance because the DTPA ligand which chelated Gd^{3+} is bigger than the nitroxide spin label (i.e. ligand **8**).

5.8.5.2 Relaxation enhancement measurements

Relaxation enhancement (T_1) of nitroxides by paramagnetic lanthanide ions at gold nanoparticle surface was determined by fitting of inversion recovery traces. For Dy^{3+}-loaded spin labelled AuNPs, the relaxation enhancement depends on the amount of Dy^{3+}. The optimal enhancement contrast is achieved at 50-60 K (Figure 5.25). The enhancement is one order of magnitude less than that observed previously for the nitroxide and lanthanide labelled membrane inserting polypeptide. This unexpectedly small relaxation enhancement of nitroxide by Dy^{3+} might be due to some underlying relaxation mechanism at the surface of gold nanoparticles.

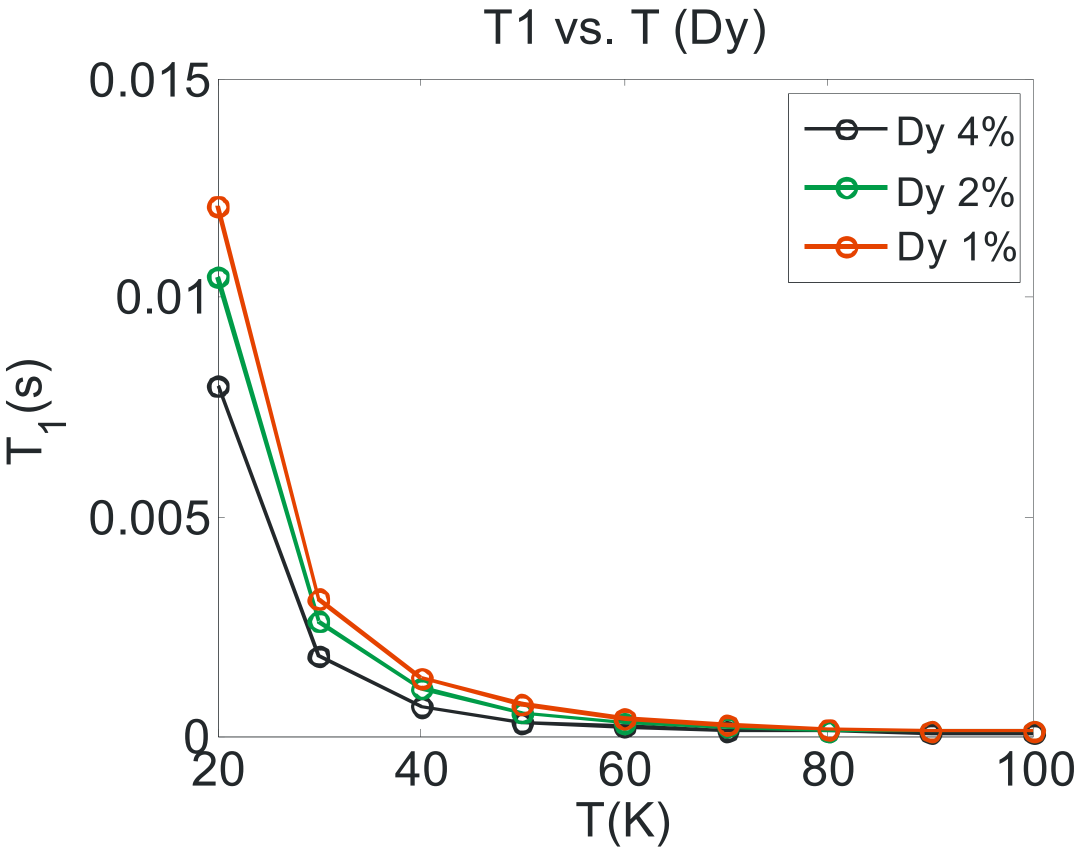

Figure 5.25: Relaxation time vs temperature curves for Dy^{3+}-loaded spin labelled AuNPs.

The relaxation enhancement for Gd^{3+}-loaded spin labelled AuNPs was also found similar in behaviour as for Dy^{3+} (Figure 5.26).

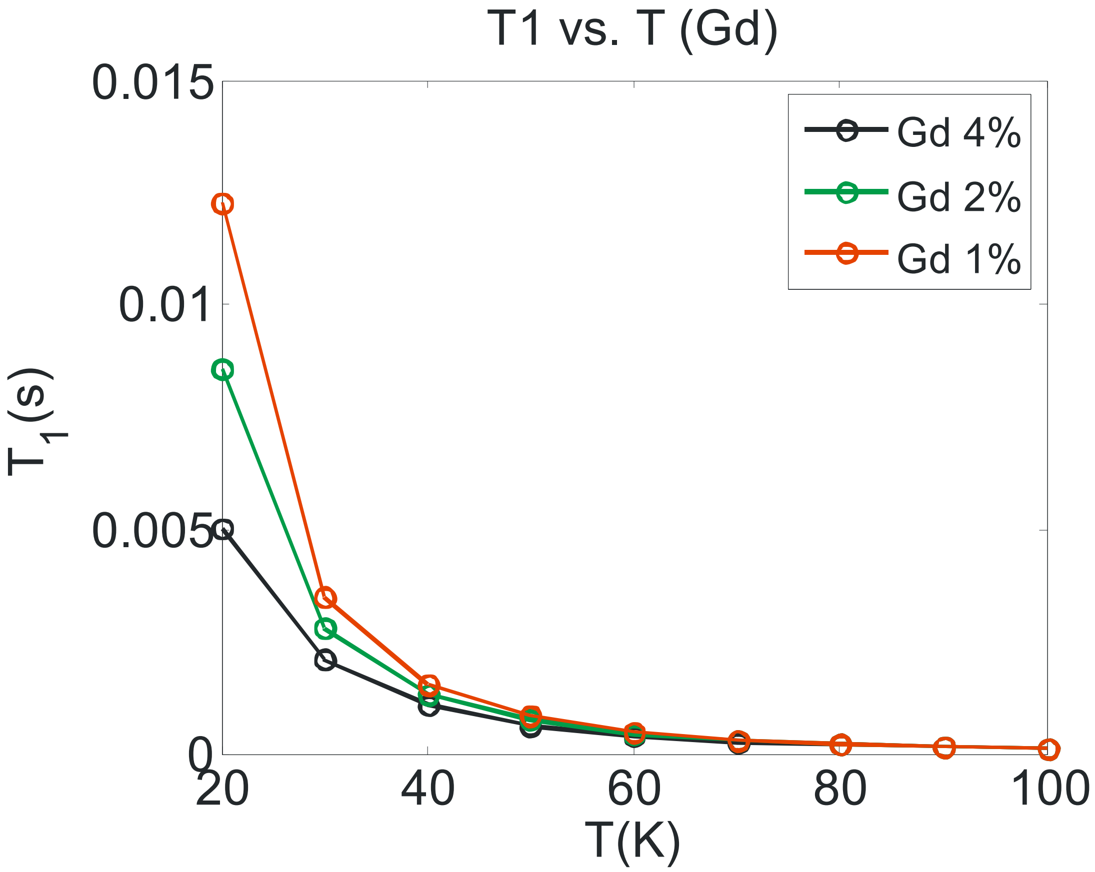

Figure 5.26: Relaxation time vs temperature curves for Gd^{3+}-loaded spin labelled AuNPs.

5.9 Conclusions

Water soluble nitroxide spin labelled AuNPs were prepared and then loaded with Dy^{3+} and Gd^{3+}. For this model system, the distance measurement data by DEER experiments were found in full agreement with the previous reported results[29] for model systems. But unfortunately, the relaxation enhancement studies of nitroxide by lanthanides (Dy^{3+} and Gd^{3+}) at the surface of gold nanoparticles were unexpected i.e. no significant relaxation enhancement was observed. It might be due to the interaction of nitroxide free electrons with the gold surface electrons.

5.10 References

1. J. Kim, Y. Piao and T. Hyeon, *Chem. Soc. Rev.*, 2009, **38**, 372-390.
2. P. Howes, M. Green, A. Bowers, D. Parker, G. Varma, M. Kallumadil, M. Hughes, A. Warley, A. Brain and R. Botnar, *J. Am. Chem. Soc.*, 2010, **132**, 9833-9842.
3. Y.-M. Huh, Y.-w. Jun, H.-T. Song, S. Kim, J.-s. Choi, J.-H. Lee, S. Yoon, K.-S. Kim, J.-S. Shin, J.-S. Suh and J. Cheon, *J. Am. Chem. Soc.*, 2005, **127**, 12387-12391.
4. J. Chen, F. Saeki, B. J. Wiley, H. Cang, M. J. Cobb, Z.-Y. Li, L. Au, H. Zhang, M. B. Kimmey, Li and Y. Xia, *Nano Lett.*, 2005, **5**, 473-477.
5. J.-H. Lee, Y.-w. Jun, S.-I. Yeon, J.-S. Shin and J. Cheon, *Angew. Chem. Int. Ed.*, 2006, **45**, 8160-8162.
6. J. R. Lakowicz, *Principles of Fluorescence Spectroscopy,* Springer, 2006, **3**, pp.1-3.
7. G. R. Choppin and D. R. Peterman, *Coord. Chem. Rev.*, 1998, **174**, 283-299.
8. J.-C. G. Bünzli, S. Comby, A.-S. Chauvin and C. D. B. Vandevyver, *J. Rare Earths*, 2007, **25**, 257-274.
9. J.-C. G. Bunzli and C. Piguet, *Chem. Soc. Rev.*, 2005, **34**, 1048-1077.
10. Catherine L. Davies, Nicholas G. Housden and A.-K. Duhme-Klair, *Angew. Chem. Int. Ed.*, 2008, **47**, 8856-8858.
11. J. R. Albani, *J. Fluoresc.*, 2007, **17**, 406-417.
12. M. Brust, M. Walker, D. Bethell, D. J. Schiffrin and R. Whyman, *J. Chem. Soc.-Chem. Commun.*, 1994, 801-802.

13. P. Ionita, A. Volkov, G. Jeschke and V. Chechik, *Anal. Chem.*, 2007, **80**, 95-106.

14. P. Ionita, J. Wolowska, V. Chechik and A. Caragheorgheopol, *J. Phys. Chem. C*, 2007, **111**, 16717-16723.

15. T. Teranishi, S. Hasegawa, T. Shimizu and M. Miyake, *Adv. Mater.*, 2001, **13**, 1699-1701.

16. S. Langereis, Q. G. de Lussanet, M. H. P. van Genderen, W. H. Backes and E. W. Meijer, *Macromolecules*, 2004, **37**, 3084-3091.

17. W. Cheng, S. Dong and E. Wang, *Angew. Chem. Int. Ed.*, 2003, **42**, 449-452.

18. E. Dulkeith, A. C. Morteani, T. Niedereichholz, T. A. Klar, J. Feldmann, S. A. Levi, F. C. J. M. van Veggel, D. N. Reinhoudt, M. Möller and D. I. Gittins, *Phys. Rev. Lett.*, 2002, **89**, 203002.

19. A. Aguila and R. W. Murray, *Langmuir*, 2000, **16**, 5949-5954.

20. J. R. Lakowicz, *Principles of Fluorescence Spectroscopy,* Springer, 2006, **3**, Ch. 8.

21. J. Massue, S. J. Quinn and T. Gunnlaugsson, *J. Am. Chem. Soc.*, 2008, **130**, 6900-6901.

22. A. Wokaun, H. P. Lutz, A. P. King, U. P. Wild and R. R. Ernst, *J. Chem. Phys.*, 1983, **79**, 509-514.

23. S. Mayilo, M. A. Kloster, M. Wunderlich, A. Lutich, T. A. Klar, A. Nichtl, K. Kürzinger, F. D. Stefani and J. Feldmann, *Nano Lett.*, 2009, **9**, 4558-4563.

24. O. Kulakovich, N. Strekal, A. Yaroshevich, S. Maskevich, S. Gaponenko, I. Nabiev, U. Woggon and M. Artemyev, *Nano Lett.*, 2002, **2**, 1449-1452.

25. H. Jäger, A. Koch, V. Maus, H. W. Spiess and G. Jeschke, *J. Magn. Reson.*, 2008, **194**, 254-263.

26. M. A. Hemminga and L. J. Berliner, *ESR Spectroscopy in Membrane Biophysics,* Springer, 2007, **27**, Ch. 1.

27. M. Pannier, S. Veit, A. Godt, G. Jeschke and H. W. Spiess, *J. Magn. Reson.*, 2000, **142**, 331-340.

28. M. A. Hemminga and L. J. Berliner, *ESR Spectroscopy in Membrane Biophysics,* Springer, 2007, **27**, Ch. 4.

29. G. Jeschke and Y. Polyhach, *Phys. Chem. Chem. Phys.*, 2007, **9**, 1895-1910.

Chapter 6: Conclusions and Proposed Future Work

Chapter 6: Conclusions and proposed future work

6.1 General conclusions

Gold nanoparticle based MRI contrast agents (CAs) were synthesized and characterised. The relaxation measurements showed that gold nanoparticle based CAs have slightly higher efficiency than the commercially available MRI contrast agent i.e. Gd-DTPA.[1] Due to promising multifunctionality features of gold nanoparticles, applicability of these nanoparticle based contrast agents for MRI as target specific agents was evaluated by attaching a recognition vector. The target-specific studies of multifunctional gold nanoparticle based CAs were successful.

In order to explore the moderate increase in relaxivity, EPR spectroscopy was used which confirmed that moderate increase in relaxivity was due to relatively fast tumbling of nanoparticle-attached Gd-DTPA chelates. The EPR results diverted the project to develop strategies for reducing mobility of the Gd-DTPA chelates at the nanoparticle surface. The immobilisation of Gd-DTPA chelates was increased by depositing layers of oppositely charged polyelectrolytes at the negatively charged surface of Gd-DTPA@AuNPs. The polyelectrolyte layers reduced mobility, which resulted in significant increase in relaxivity. The increase in ligand packing density at nanoparticle surface by increasing the size of nanoparticles was an alternative strategy which also influenced / increased the relaxivity significantly. Thus EPR measurements confirmed the previously reported[1-4] moderate increase in relaxivity by gold nanoparticle based contrast agents. Apart from Gd-based contrast agents, paramagnetic nitroxide radical based contrast agents were also prepared using gold nanoparticles as templates.

Several nitroxide radicals were attached at the gold nanoparticles surface to get nitroxide based ligand protected gold nanoparticles as MRI contrast agents. The redox behaviour of these nitroxide based contrast agents was studied *in vitro* using EPR spectroscopy. The EPR data showed that nitroxides at gold nanoparticle surface underwent chemical reduction slower as compared to free nitroxides which showed better efficiency of gold nanoparticle based redox sensitive contrast agents than free nitroxides. The relaxivity of nitroxide protected AuNPs was also found slightly higher than for free nitroxides.

Gold nanoparticles protected by DTPA based ligands were also studied for some other useful applications besides MRI contrast agents. They were studied as optical imaging contrast agents after replacing Gd^{3+} with other lanthanides such as Tb^{3+} and Eu^{3+}. However, fluorescence measurements of Tb and Eu-loaded AuNPs did not show any fluorescence, their fluorescence was quenched by gold nanoparticles. The nitroxide labelling of DTPA ligand protected AuNPs and then loading with various lanthanides (La^{3+}, Dy^{3+} and Gd^{3+}) provided the opportunity to test a useful (i.e. double electron electron resonance) EPR methodology.

The real clinical applications of gold nanoparticle based MRI contrast agents may be hampered due to several issues: e.g. their efficiency is not much higher than the small molecules based CAs, AuNPs based CAs will have a much higher cost. But the results regarding gold nanoparticle based contrast agents presented in this thesis will definitely pave the way for multifunctionality studies using other nanomaterials, supramolecular assemblies and other similar systems. For example, these results will definitely help further studies of mesoporous silica based contrast agents[5], which is much cheaper than gold, easy to synthesize and might have much higher efficiency than gold nanoparticle based CAs. However this work can be further extended to explore many other aspects, e.g. quenching of fluorescence of Tb-loaded AuNPs, very small increase in relaxivity of nitroxide protected AuNPs etc.

6.2 Proposed future work

As mentioned in the above section, the fluorescence of lanthanide-loaded AuNPs was found to be quenched by AuNPs. This quenching can be avoided by synthesising some new DTPA ligands with a long carbon tail as compared to DTPA ligand **5** or **6**. The long tail DTPA ligand will help to avoid the fluorescence quenching of lanthanide chelates at gold nanoparticle surface and thus lanthanide-loaded gold nanoparticles can be studied as optical imaging contrast agents (Figure 6.1).[6]

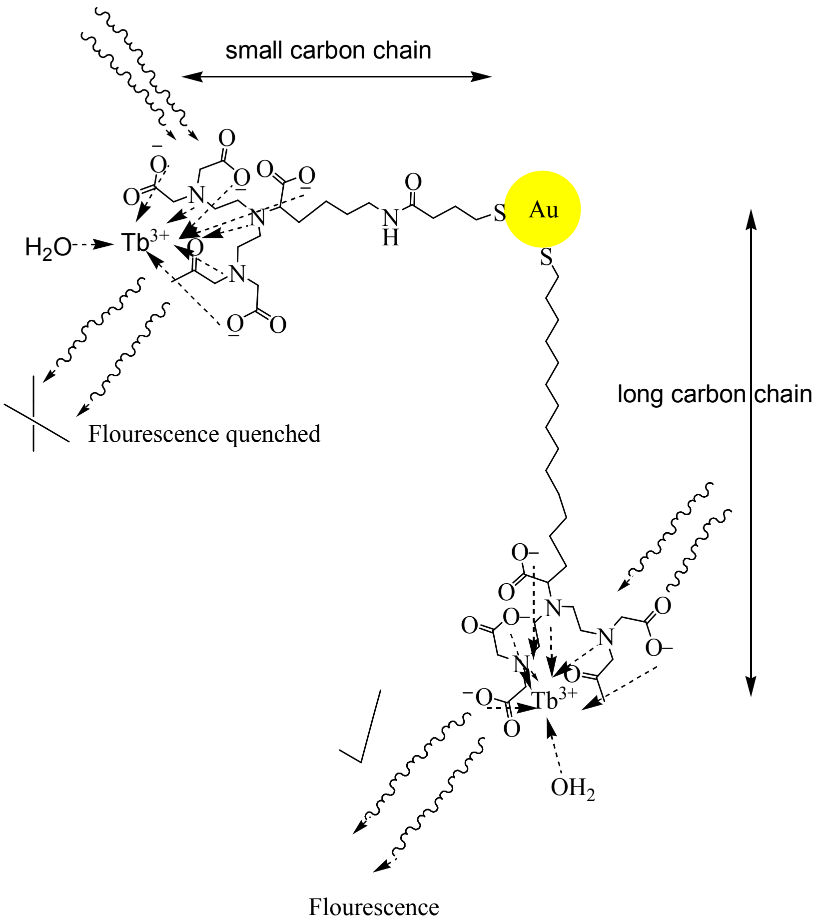

Figure 6.1:Tb-DTPA chelates at AuNPs surface with small and long carbon chain.

Secondly various methods for increasing efficiency (relaxivity as well as reducing behaviour) of nitroxide protected gold nanoparticles can be explored. For example after replacing the triphenylphosphine (PPh_3) molecules with dithiobis [succinimidylpropionate] (DSP) from triphenylphosphine protected gold nanoparticle (PPh_3@AuNPs), the DSP can be reacted with PAMAM dendrimers (G_0) along with amino-TEMPO to get nitroxide and PAMAM dendrimers protected gold nanoparticles. PAMAM dendrimers molecules will restrict the tumbling of nanoparticles attached nitroxides which will enhance the relaxivity. The insertion of dendrimer molecules in between nitroxides at nanoparticles will also help to increase the reduction period of nitroxides. Furthermore after attaching suitable biomolecules they can be *in vitro* and then *in vivo* studied for brain imaging as they might pass through blood brain barrier.

In chapter five, the paramagnetic radicals (i.e. nitroxides) and lanthanide ions (Dy^{3+}, Gd^{3+}, La^{3+}) were attached at the surface of gold nanoparticles and these nanoparticles were quite soluble in aqueous medium (i.e. water). DNP (dynamic nuclear polarisation), which is based on Nuclear Overhauser Effect[7] (discovered in 1953), is the phenomenon of NMR signals enhancement by electronic spin polarisation. The signal intensity of the nuclei under question can be enhanced significantly; for example, theoretically ^1H NMR signal intensity can be enhanced by a factor of 660. The gold nanoparticles with stable radicals and lanthanides at their surface can be utilised as model compounds for studying DNP phenomenon. The gold nanoparticles having more than one radical at their surface may prove better signal enhancer by electron spin polarisation phenomenon than monoradical. The relatively restricted tumbling of radicals as compared to free radicals at nanoparticle surface could play a significant role in DNP phenomenon.

6.3 References

1. P.-J. Debouttière, S. Roux, F. Vocanson, C. Billotey, O. Beuf, A. Favre-Réguillon, Y. Lin, S. Pellet-Rostaing, R. Lamartine, P. Perriat and O. Tillement, *Adv. Funct. Mater.*, 2006, **16**, 2330-2339.
2. C. Alric, J. Taleb, G. L. Duc, C. Mandon, C. Billotey, A. L. Meur-Herland, T. Brochard, F. Vocanson, M. Janier, P. Perriat, S. Roux and O. Tillement, *J. Am. Chem. Soc.*, 2008, **130**, 5908-5915.
3. M. Marradi, D. Alcantara, J. M. d. l. Fuente, M. L. Garcia-Martin, S. Cerdan and S. Penades, *Chem. Comm.*, 2009, 3922-3924.
4. J.-A. Park, P. A. N. Reddy, H.-K. Kim, I.-S. Kim, G.-C. Kim, Y. Chang and T.-J. Kim, *Bioorg. Med. Chem. Lett.*, 2008, **18**, 6135-6137.
5. K. M. L. Taylor, J. S. Kim, W. J. Rieter, H. An, W. Lin and W. Lin, *J. Am. Chem. Soc.*, 2008, **130**, 2154-2155.
6. J. Massue, S. J. Quinn and T. Gunnlaugsson, *J. Am. Chem. Soc.*, 2008, **130**, 6900-6901.
7. A. P. M. Kentgens, J. Bart, P. J. M. van Bentum, A. Brinkmann, E. R. H. Van Eck, J. G. E. Gardeniers, J. W. G. Janssen, P. Knijn, S. Vasa and M. H. W. Verkuijlen, *J. Chem. Phys.*, 2008, **128**, 1-24.

Chapter 7: Experimental

Chapter 7: Experimental

7.1 Materials and chemicals

All chemicals were purchased from Sigma-Aldrich if not stated otherwise. All solvents were purchased from Fisher Scientific International. All chemicals were used as received without further purification unless stated otherwise. Bio-beads S-XI (200-400 mesh) for gel permeation chromatography was purchased from Bio-Rad. The Sephadex gel LH-20 was supplied by GE Healthcare. Dithiobis(succinimidylpropionate) (DSP) was purchased from Apollo Scientific Ltd. TLC analysis was performed on Merck Silica Gel 60 F245 aluminium backed silica plates. Column chromatography was performed using silica gel 60 which was purchased from BDH. The dialysis membranes with MWCO 500 and 12-14 kDa were supplied by Spectrum Laboratories and Fischer Scientific, respectively.

7.2 Instrumentation / techniques

- ***NMR:*** ^{1}H and ^{13}C NMR spectra were recorded on JEOL ECX 270 MHz, ECX 400 MHz and ECS 400 MHz machines. Values of chemical shifts for ^{1}H NMR spectra are reported relative to internal standards i.e. $CHCl_3$ in $CDCl_3$ (7.26 ppm), CH_3OD in CD_3OD (3.49 ppm) and HOD in D_2O (4.79 ppm). Similarly, ^{13}C NMR peaks are referenced to the solvent peaks i.e. $CDCl_3$ (77.36 ppm) and CD_3OD (50.41 ppm). Spectral splitting parameters are represented as: s, singlet; t, triplet; q, quartet; m, multiple; br, broad.

- ***MS:*** Mass spectra were recorded on a Bruker micro-TOF with LCQ ion trap and ESI ion source.

- ***UV/Vis.:*** UV/Vis. spectra were acquired on a double beam Hitachi U-3000 spectrophotometer.
- ***IR:*** IR spectra were recorded on JASCO FT/IR-400 spectrometer.
- ***Fluorescence Emission Spectra:*** The fluorescence emission spectra were acquired on Hitachi F-4500 Flourimeter.

- ***EPR:*** The EPR spectra were recorded on Bruker EMX, ESP300E and JEOL JES-RE 1X spectrometers.
- ***TGA:*** The TGA analysis of all samples was performed on STA625 Thermal Analyzer.
- ***TEM:*** TEM analysis was carried out using FEI TECNI I2 electron microscope.
- ***Elemental Analysis:*** Elemental analyses were carried out by Microanalysis Service at Medac Ltd., (London).
- ***NMR Imaging:*** T_1 weighted images were acquired on a spin echo based RARE sequence on Bruker Avance II 600 MHz (14 T) NMR spectrometer with the GREAT 40 gradient system. Imaging parameters were: time of repetition (TR) 400.0 ms, time of echo (TE) 15.0 ms, the thickness of the slice 2.0 mm, MTX (matrix size) = 128 × 128, FOV (field of view) = 2.5cm × 2.5cm
- ***Relaxation Measurements:*** Relaxation measurements were carried out on Bruker AMX 300 MHz spectrometer at room temperature (298 K)
- ***Pulsed EPR (DEER) Measurements:*** Double electron-electron resonance measurements were carried on a Bruker EleXsys E680 X/W-band spectrometer in collaboration with Prof. Gunnar Jeschke at ETH Zurich, Switzerland.

Gold Nanoparticles Yield Calculations: The yield of AuNPs protected by various (thiol based) ligands was calculated by assuming the 3 / 1 : Au to ligand ratio.[1]

7.3 Experimental part for chapter 2

7.3.1 Synthesis of DTPA based ligand 6

7.3.1.1 Alkylation of ethanolamine by t-butyl protected bromoacetate (1)

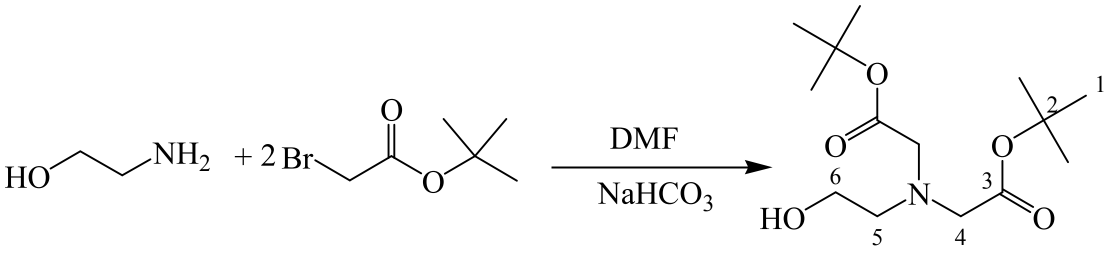

1

Compound **1** was synthesized by following the literature procedure.[2] To t-butyl bromoacetate (13.5 g, 69.2 mmol) dissolved in DMF (50 mL), $KHCO_3$ (7.68 g, 76.8 mmol) was added. The suspension was cooled to 0 °C and ethanolamine (0.92 mL, 15.16 mmol) was added over a period of 5 min. The reaction mixture was stirred for 30 min at 0 °C and for 22 h at room temperature. At the end of this period, diethyl ether (75 mL) and saturated aq. $NaHCO_3$ (50 mL) were added. The organic phase was separated from aqueous phase and organic phase was washed with saturated aq. $NaHCO_3$ (50 mL). The aqueous phases were combined and extracted with diethyl ether (75 mL) and organic phases were combined and washed with brine (75 mL). The organic phase was dried with anhydrous Na_2SO_4, and evaporated to get compound **1** as white solid. Yield 12.60 g (63 %).

^{1}H NMR ($CDCl_3$): δ (ppm) 1.38 (s, 18H, H^1), 2.84 (t, J 5.01 Hz, 2H, H^5), 3.41 (s, 4H, H^4), 3.48 (t, J 5.01 Hz, 2H, H^6).

^{13}C NMR ($CDCl_3$): 28.01 (C^1), 56.53 (C^5), 56.80 (C^6), 59.20 (C^4), 81.38 (C^2), 171.31 (C^3).

HR ESI-MS: m/z,$[M + H]^{1+}$, Calcd. for $C_{14}H_{28}NO_5$: 290.1962, Found: 290.1958

7.3.1.2 Bromination of compound 1

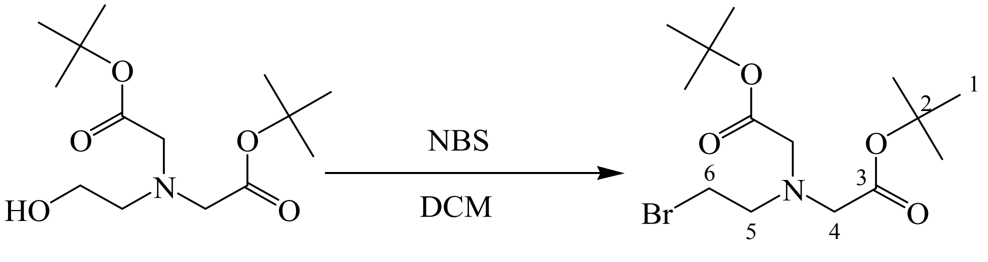

1 **2**

Compound **2** was synthesized from compound **1** by following the literature procedure.[2] Compound **1** (3.63 g, 12.56 mmol) was dissolved in DCM (50 mL). Ph_3P (3.29 g, 12.56 mmol) was added and solution was cooled to 0 °C. Solid N-bromosuccinimide (2.23 g, 12.56 mmol) was added portion wise over a period of 5 min. After the solution was stirred at 0 °C for 1.5 h, the evaporation of the solvent gave semisolid residue. The semisolid residue was triturated with diethyl ether (Et_2O) (100 mL) and resulting solid was removed by filtration. The ether phase was concentrated and then passed through a short silica column, eluting with ether (Et_2O). Evaporation of ether gave colourless oil as crude product. The crude product was purified by flash chromatography using silica gel as a stationary phase and n-hexane / Et_2O (3 / 1) as a mobile phase (R_f 0.35). Yield 3.25 g (73 %).

^{1}H NMR ($CDCl_3$): δ (ppm) 1.40 (s, 18H, H^1), 3.08 (t, J 7.42, 2H, H^5), 3.38 (t, J 7.42, 2H, H^6), 3.41 (s, 4H, H^4).

^{13}C NMR ($CDCl_3$): δ 28.21 (C^1), 30.33 (C^6), 56.54 (C^5), 56.70 (C^4), 81.34 (C^2), 170.58 (C^3).

HR ESI-MS: m/z $[M + H]^{1+}$, Calcd. for $C_{14}H_{27}BrNO_4$: 352.1118, Found: 352.1120

7.3.1.3 Alkylation of N-ε-CBZ-L-Lysine t-butyl ester hydrochloride by bromo derivative 2

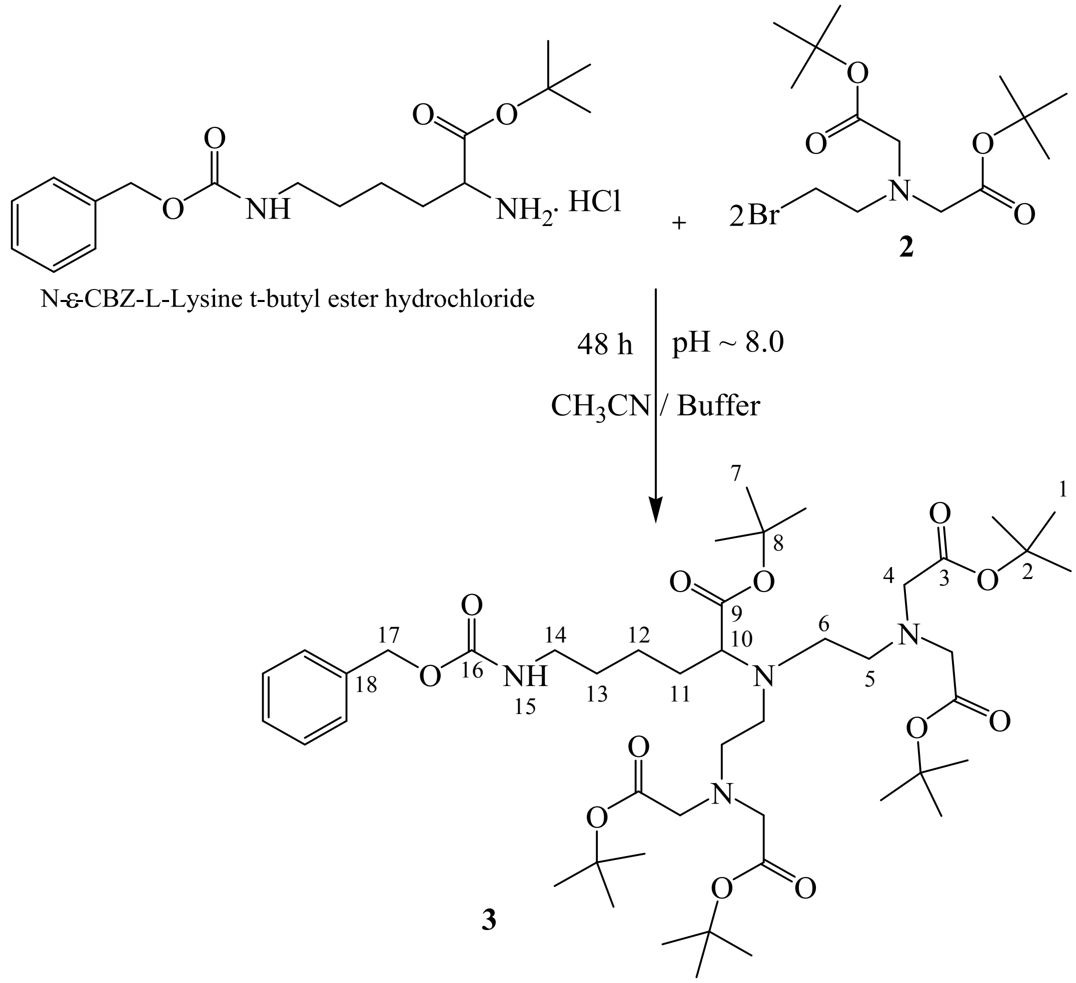

Compound **3** was synthesized according to literature procedure.[3] N-ε-CBZ-L-Lysine t-butyl ester hydrochloride (1.87 g, 5.01 mmol) was taken in a round bottom flask containing acetonitrile (10 mL). Compound **2** (4.50 g, 12.09 mmol) was added followed by phosphate buffer (2 M, 12 mL, pH 8.0) and the mixture was stirred for 2 h. After stirring, aqueous layer was replaced with fresh buffer solution and then stirred again for 48 h. The organic layer was separated from the aqueous layer. The aqueous layer was discarded and organic layer was concentrated to dryness by rotary evaporation. The crude material was purified by flash chromatography using silica gel as a stationary phase and EtOAc / n-hexane (1 / 2) as a mobile phase (R_f 0.51). Yield 3.15 g (72 %).

^{1}H NMR ($CDCl_3$): δ (ppm) 1.28-1.36 (m, 2H, H^{12}), 1.40 (s, 45H, H^1), 1.44-1.65 (m, 4H, H^{11}**,** H^{13}), 2.56-2.82(m, 8H, H^5, H^6), 3.15 (t, J 6.40 Hz, 2H, H^{14}), 3.22 (t, J 7.32 Hz, 1H, H^{10}), 3.40 (s, 8H, H^4), 5.04 (s, 2H, H^{17}), 5.12 (br, 1H, H^{15}), 7.20-7.29 (m, 5H, Ar^{18}-H).

^{13}C NMR ($CDCl_3$): δ (ppm) 23.31 (C^{12}), 28.11 (C^7), 28.25 (C^1), 29.45 (C^{11}), 40.81 (C^{14}), 50.16 (C^{13}), 53.53 (C^5), 55.90 (C^4), 60.34 (C^6), 63.86 (C^{10}), 66.36 (C^{17}), 80.71 (C^8), 80.75 (C^2), 127.91, 128.05, 128.39, 136.72 (Ar), 156.73 (C^{16}), 170.61 (C^3), 172.69 (C^9).

HR ESI-MS: m/z $[M + H]^{1+}$, Calcd. for $C_{46}H_{79}N_4O_{12}$: 879.5689, Found: 879.5684

7.3.1.4 Deprotection of DTPA-analogue 3

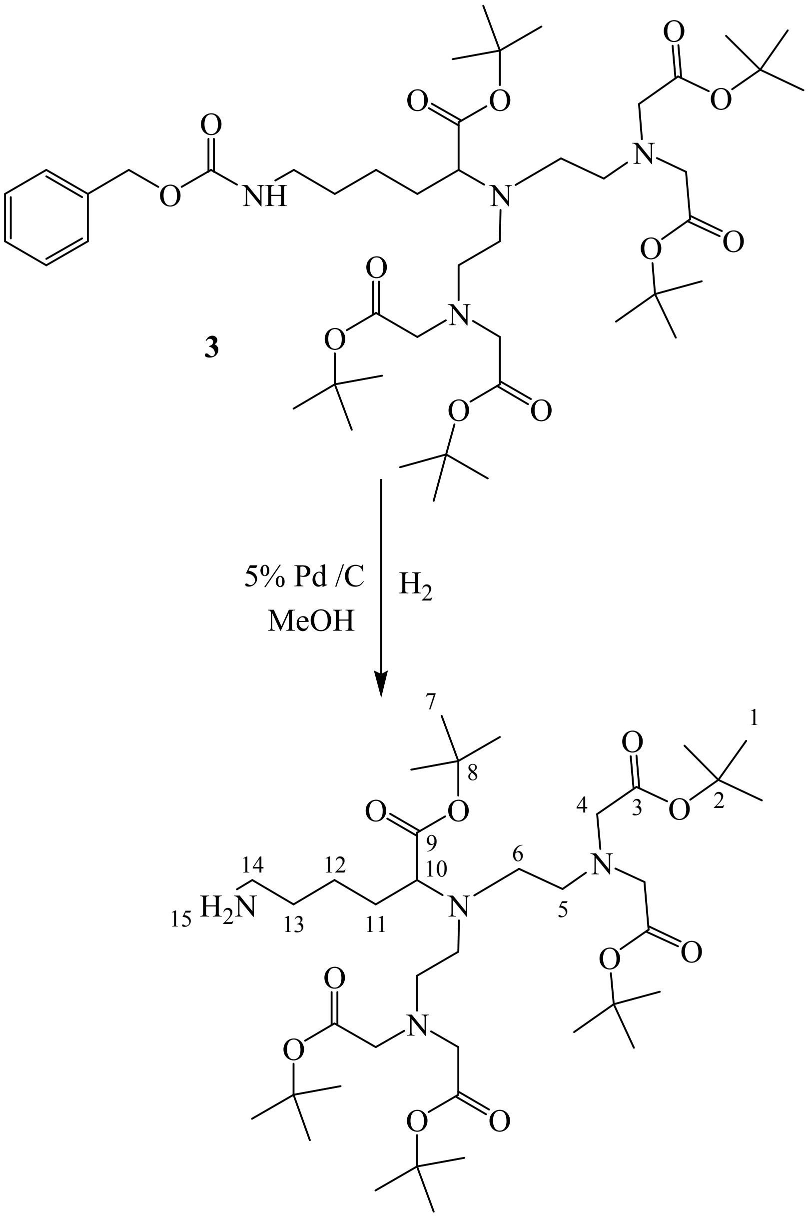

3

4

Compound **4** was synthesized according to literature procedure.[3] Compound **3** (1.0 g, 1.14 mmol) was taken in a 50.0 mL round bottom flask containing MeOH (25 mL). The 5% Pd on C (100.0 mg) was added and reaction mixture was flushed with nitrogen gas (3-4 times). The suspension was vigorously stirred for 4 h under hydrogen atmosphere at room temperature. The residue was filtered using sintered filter and evaporation of solvent gave a yellow coloured crude product. The crude product was purified by flash chromatography using MeOH with a few drops of Et_3N (R_f 0.28). Yield 0.525 g (62 %).

^{1}H NMR ($CDCl_3$): δ (ppm) 1.28-1.36 (m, 2H, H^{12}), 1.40 (s, 45H, H^1), 1.46-1.68 (m, 4H, H^{11}, H^{13}), 2.64-2.82 (m, 8H, H^5, H^6), 3.04 (t, J 7.13 Hz, 1H, H^{10}), 3.22 (t, 6.58 Hz, 2H, H^{14}), 3.40 (s, 8H, H^4).

^{13}C NMR ($CDCl_3$): δ (ppm) 23.20 (C^{12}), 28.25 (C^7), 28.35 (C^1), 29.61 (C^{11}), 32.00 (C^{13}), 40.81 (C^{14}), 50.60 (C^5), 53.60 (C^6), 56.10 (C^4), 64.05 (C^{10}), 80.90 (C^8), 81.00 (C^2), 170.78 (C^3), 172.80 (C^9).

HR ESI-MS: m/z [M + H] $^{1+}$, Calcd. for: $C_{38}H_{73}N_4O_{10}$ 745.5321, Found: 745.5332

7.3.1.5 Coupling of DTPA-analogue 4 with dithiobutyric acid

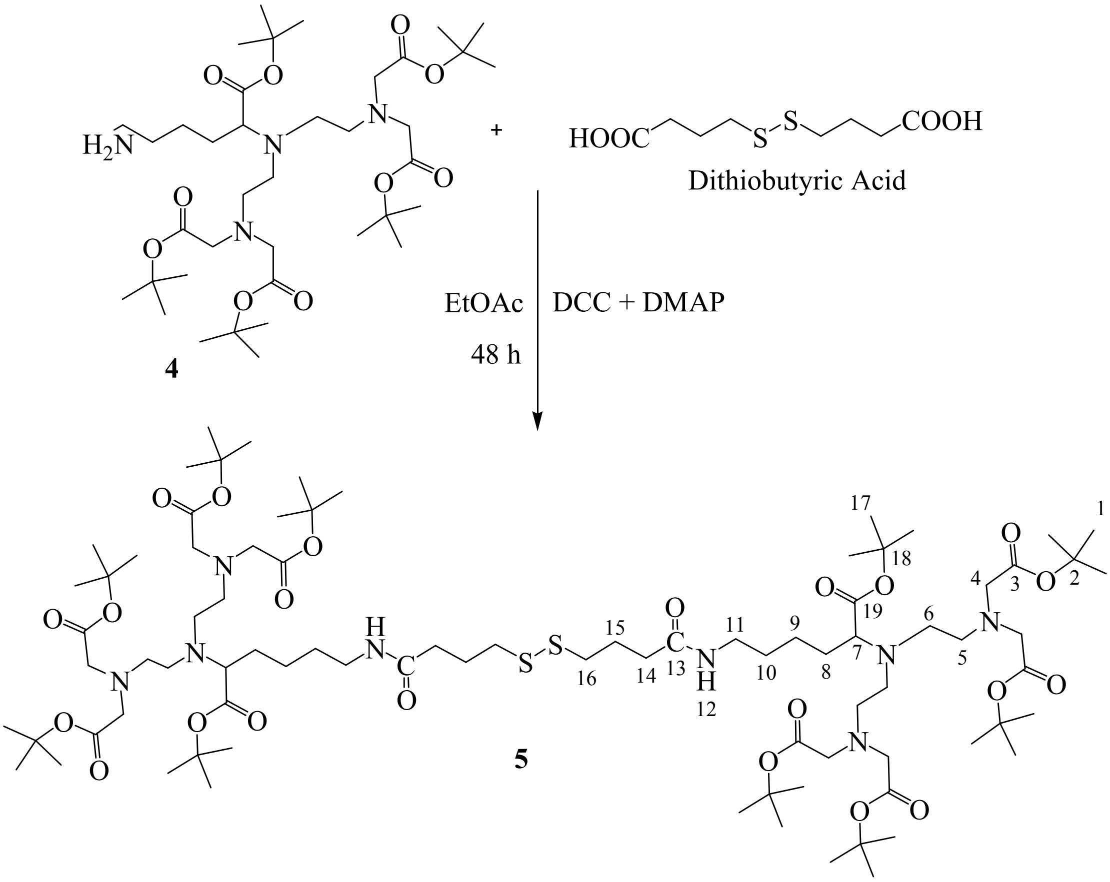

Compound **5** was synthesized using a standard peptide (DCC / DMAP) coupling method[4]. Compound **4** (0.453 g, 0.61 mmol) was taken in a 50 mL round bottom flask containing EtOAc (10 mL). Dithiobutyric acid (0.066 g, 0.277 mmol) was added and solution was cooled to 0 °C. Dicyclohexylcarbodiimide (DCC) (0.057 g, 0.277 mmol) and dimethylaminopyridine (DMAP) (0.034 g, 0.277 mmol) were added as a mixture of solids and solution was stirred for 48 h at room temperature. After stirring, the solid residues were removed by filtration and filtrate was evaporated to get a highly viscous yellow coloured crude product. The crude compound was purified by flash chromatography using silica gel as a stationary phase and ethyl acetate/n-hexane (2/1) as a mobile phase (R_f 0.65). Yield 0.545 g (53%). NMR spectrum assignment was done by comparison with similar compounds reported in the literature.[5]

^{1}H NMR (CDCl$_3$): δ (ppm) 1.40 (s, 90H, H^1), 1.17-1.64 (m, 12H, H^8, H^9, H^{10}), 1.90-2.02 (m, 4H, H^{15}), 2.26 (t, J 7.32 Hz, 2H, H^{14}), 2.56-2.70 (m, 16H, H^5, H^6), 2.76 (t, J 7.47 Hz, 4H, H^{16}), 3.23-3.16 (m, 6H, H^7 , H^{11}), 3.40 (s, 16H, H^4).

^{13}C NMR (CDCl$_3$): δ (ppm) 19.81 (C^9), 21.07 (C^{15}), 24.40 (C^1), 24.52 (C^{17}), 25.26 (C^8), 25.68 (C^{10}), 30.89 (C^{14}), 34.28 (C^{16}), 35.50 (C^{11}), 46.39 (C^5), 49.81 (C^4), 52.16 (C^6), 60.14 (C^7), 76.93(C^{18}), 77.06 (C^2), 166.89 (C^3), 168.24 (C^{19}), 168.95 (C^{13}).

HR ESI-MS: m/z $[M + H]^{2+}$, Calcd. for $C_{84}H_{156}N_8O_{22}S_2$: 846.5382, Found: 846.5379

7.3.1.6 Deprotection of t-butyl ester groups of DTPA based ligand 5

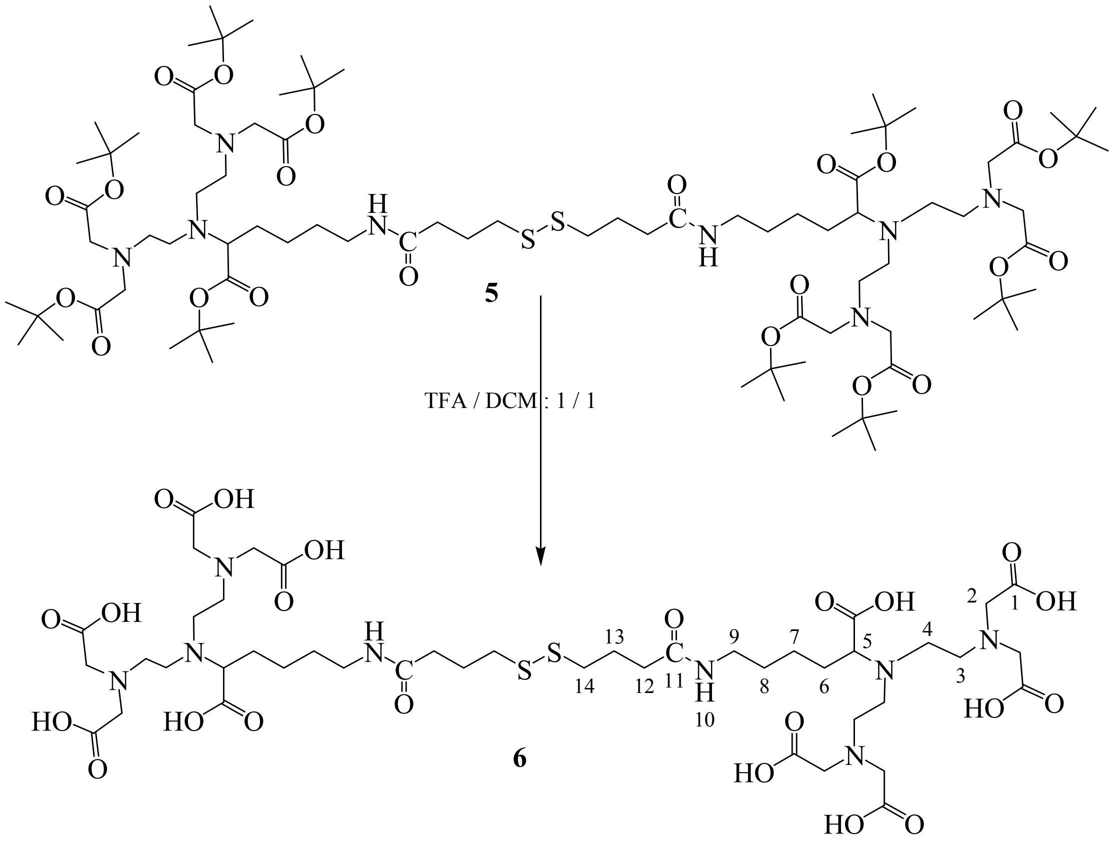

Compound **6** was obtained by deprotection of t-butyl ester groups of compound **5** using a modified literature procedure.[5] Compound **5** (117 mg, 0.069 mmol) was taken in a 25 mL round bottom flask. Trifluoroacetic acid (TFA) (1.0 mL) was added to the solution of compound **5** in dichloromethane (DCM) (1.5 mL). The reaction mixture was stirred overnight at rt. After overnight stirring, DCM and TFA were evaporated using rotary evaporator at rt. The crude product (compound **6**) was dissolved in water (10.0 mL), filtered and dialyzed using 500 MWCO dialysis tubing against deionised H_2O for 48 h. After dialysis, water was evaporated below 40 ^{o}C to get a white product. Yield 60.0 mg (77 %).

^{1}H NMR (D_2O): δ (ppm) 1.17-1.66 (m, 12H, H^6, H^7, H^8), 1.77-1.82 (m, 4H, H^{13}), 2.28 (t, J 7.01 Hz, 4H, H^{14}), 2.66 (t, J 7.01 Hz, 4H, H^{12}), 2.84-3.08 (m, 10H, H^4, H^5), 3.22-3.40 (m, 12H, H^3, H^9), 3.82 (s, 16H, H^2).

^{13}C NMR (D_2O): δ (ppm) 23.42 (C^7), 24.81 (C^{13}), 27.82 (C^6), 28.19 (C^8), 34.35 (C^{12}), 37.14 (C^{14}), 38.92 (C^9), 46.29 (C^4), 52.89 (C^3), 55.92 (C^2), 63.26 (C^5), 169.65 (C^1), 175.09 (C^{15}), 175.70 (C^{11}).

HR ESI-MS: m/z $[M-H]^{2-}$ Calcd. for $C_{44}H_{72}N_8O_{22}S_2$: 546.2107, Found: 546.2103

7.3.1.7 Synthesis of AuNPs stabilised by DTPA based ligand 6

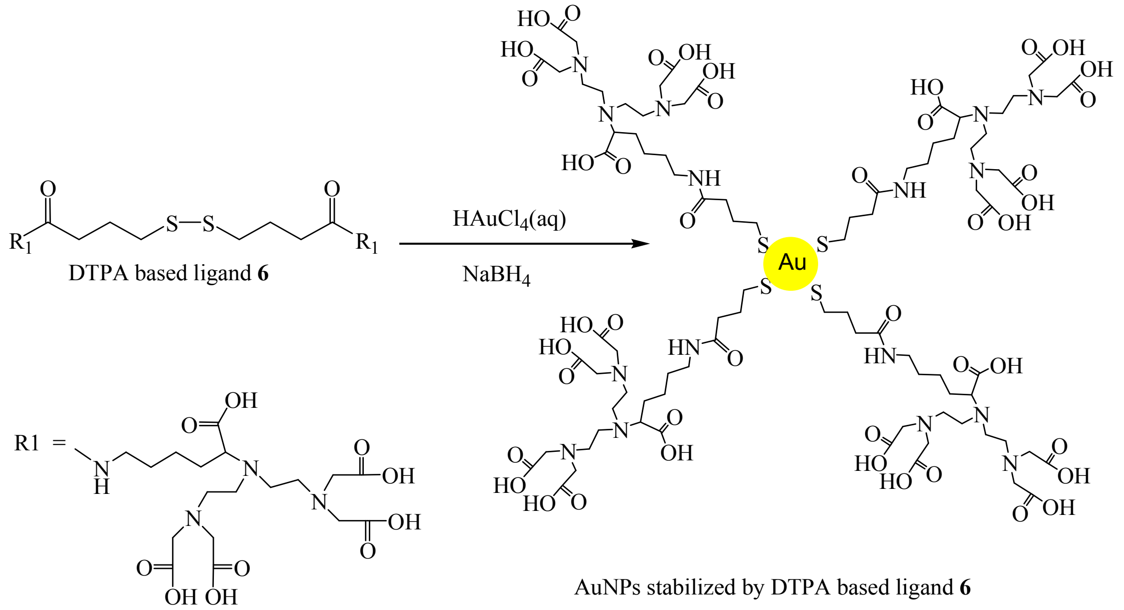

Gold nanoparticles stabilized by DTPA based ligand **6** were prepared by modification of a literature procedure.[6] A 1.0 % w/w solution of hydrogen tetrachloroauric acid trihydrate ($HAuCl_4 . 3H_2O$) (4.12 mL, 0.1 mmol) was taken in a 25 mL round bottom flask. To this flask, DTPA based ligand **6** (60 mg, 0.1 mmol) dissolved in deionised water (10.0 mL) was added. A freshly prepared aqueous solution of $NaBH_4$ (40 mg, 1.0 mmol) in deionised water (10.0 mL) was added immediately after the addition of ligand **6** to the flask. The colour of the stirring solution turned dark brown after the addition of sodium borohydride solution, which confirmed the formation of gold nanoparticles. After stirring for 10 min, water was evaporated below 40 °C using rotary evaporator. The excess ligand was removed by GPC (Sephadex gel G-100) column using aq 0.1M NaCl as eluent. The AuNPs were then dialysed against DI H_2O using 12-14 kDa MWCO tubing for o / n, and then water was evaporated below 40 °C to get solid AuNPs. Yield 35.0 mg. Characterisation of AuNPs protected by DTPA ligand **6** is shown in chapter 2 (section 2.3).

7.3.1.8 Complexation of gadolinium (Gd^{3+}) with DTPA@AuNPs

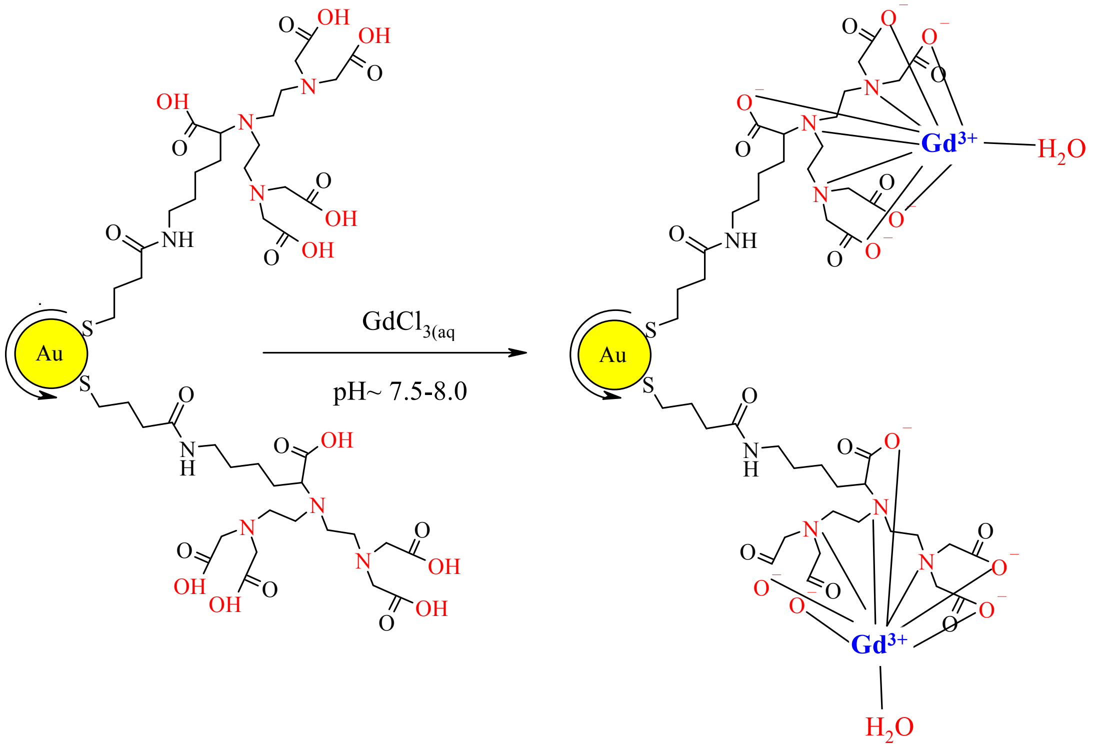

Gd-loaded AuNPs

Complexation of gadolinium (Gd^{3+}) with DTPA units of the ligand attached to gold nanoparticles was done by slightly modifying the literature procedure.[7] A 10.0 mL aqueous AuNPs (5.83mg, 3.92×10^{-3} mmol of DTPA units) was taken in a 50.0 mL round bottom flask. A 1.0 mM aqueous gadolinium chloride hexahydrate was added drop wise over a period of 10 min. The amount of Gd^{3+} was monitored by colorimetric titration using xylenol orange as an indicator (discussed in chapter 2, section 2.4.1). The reaction mixture was then stirred for further 30 min. Using aq (~1 mM) NaOH, the pH of the medium was kept slightly basic (7.5-8.0) during addition of Gd^{3+} to the colloidal solution of AuNPs. After addition of Gd^{3+}, water was evaporated below 40 °C to get a dark brown powder, the Gd-loaded AuNPs. The free Gd^{3+} ions were removed by dialyzing the aqueous solution of Gd-loaded AuNPs against deionised water for o/n using 12-14 kD MWCO dialyzing tubing. The water was evaporated below 40 °C using rotary evaporator to get solid Gd-loaded AuNPs. Yield 6.12 mg. Characterisation of Gd-loaded AuNPs is given in chapter 2 (section 2.4.3).

7.3.1.9 Synthesis of Gd-DTPA complex

Gadolinium-diethylenetriaminepentaacetic acid (Gd-DTPA) complex was prepared in an analogous procedure as described in section 7.3.1.8, from $GdCl_3$ (45 mL, 5.0 mM) and DTPA (50 mL, 5.0 mM).Yield 0.100 g (81%).

HR ESI-MS: m/z $[M - H]^{1-}$, Calcd. for $C_{14}H_{19}GdN_3O_{10}$: 547.0320, Found: 547.0336

7.3.2 Synthesis of biotin-terminated thiol (BTT)

Biotin-terminated thiol (BTT) was synthesized by a modified literature procedure.[8] NHS-$(PEO)_4$-biotin (1.17mg, 1.98×10^{-3} mmol) was taken in a 5.0 ml round bottom flask. To this flask, 19.44 mM solution of cysteamine in DMSO (0.1 mL, 1.98×10^{-3} mmol) was added. The flask was put under vacuum on a Schlenk line, to avoid any contact with air or moisture. Anhydrous DMSO (0.9 mL) and anhydrous DMF (1.0 mL) were then added carefully with pre-dried syringes. The reaction mixture was stirred overnight under the blanket of nitrogen at room temperature. The unreacted NHS-$(PEO)_4$-biotin was removed by dialysing against deionised water using 500 MWCO dialysing membrane. Water was evaporated using rotary evaporator to get purified BTT. Yield 1.03 mg (93 %).

HR ESI-MS: m/z $[M+H]^{1+}$ Calcd. for $C_{24}H_{47}N_4O_7S_2$: 567.2557, Found: 567.2517

7.3.3 Attachment of biotin-terminated thiol to the AuNP surface

Biotin-terminated thiol (BTT) was attached to the AuNPs surface using a modified literature procedure.[9] Gd-loaded AuNPs (3.0 mg, 5.06×10^{-5} mmol) were taken in a 5.0 mL round bottom flask. To this flask, 1.58 mM solution of BTT (60.0 µL, 9.45×10^{-5} mmol) in DMSO/DMF (1/1) mixture was added. The reaction mixture was stirred for overnight at room temperature. The unreacted BTT was removed by dialysis against deionised water for overnight using 12-14 kDa MWCO membrane, followed by water evaporation using rotary evaporator to get solid BTT-labelled AuNPs. Yield 2.05 mg (68 %).

7.4 Experimental part for chapter 3

7.4.1 Vanadyl complexation with DTPA@AuNPs

Vanadyl (VO^{2+}) was complexed with DTPA@AuNPs using a modified literature procedure.[10] The AuNPs stabilised by DTPA based ligand **6** (15.0 mg, 0.011 mmol of DTPA units) were taken in a 25 mL round bottom flask containing deionised H_2O (5.0 mL). A 5.0 mM $VOSO_4$ solution (0.75 mL, 3.71×10^{-3} mmol of VO^{2+}) was added drop wise to the stirred solution of AuNPs. After adding $VOSO_4$ solution to the AuNPs solution, the reaction mixture was stirred for further 10-15 min. Water was evaporated using rotary evaporator at ca. 40 °C to get solid VO-DTPA@AuNPs. Yield 11.35 mg.

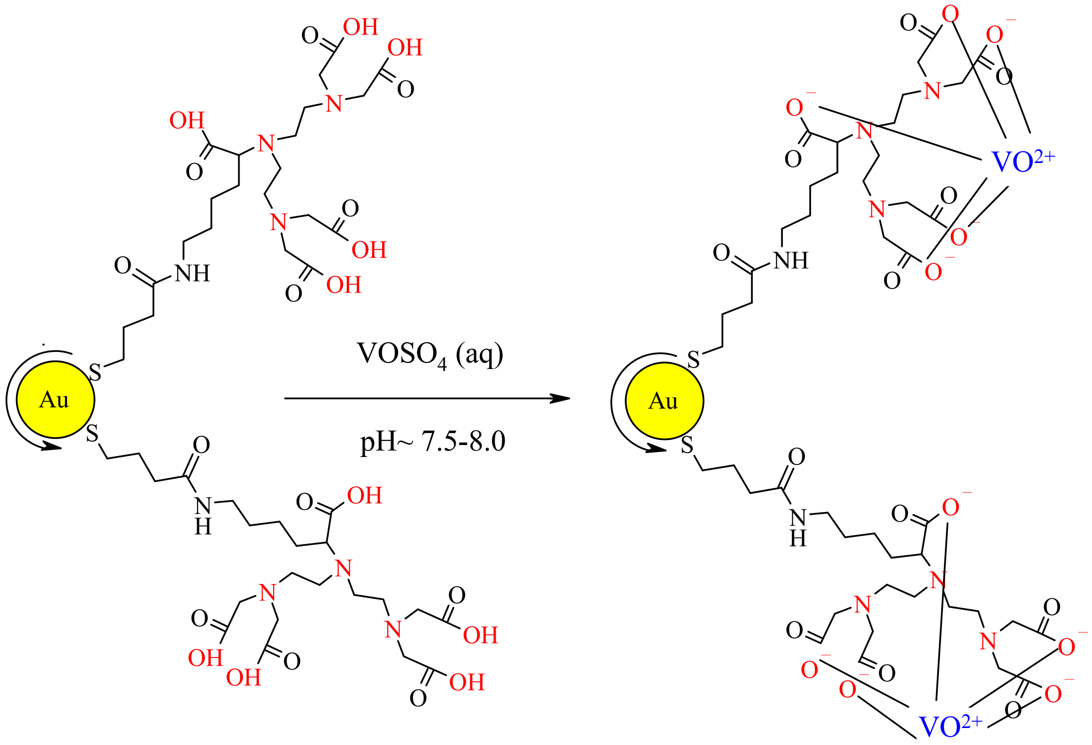

7.4.2 Synthesis of VO-DTPA

Vanadyl (VO^{2+}) chelate with DTPA was synthesised by an analogous procedure as described in section 7.4.1 from 5.0 mM DTPA solution (5.0 mL, 0.025 mmol) and freshly prepared 5.0 mM aq $VOSO_4$ (4.0 mL, 0.02 mmol). Yield 7.25 mg (78 %).

7.4.3 Growth of AuNPs (~4.0 nm)

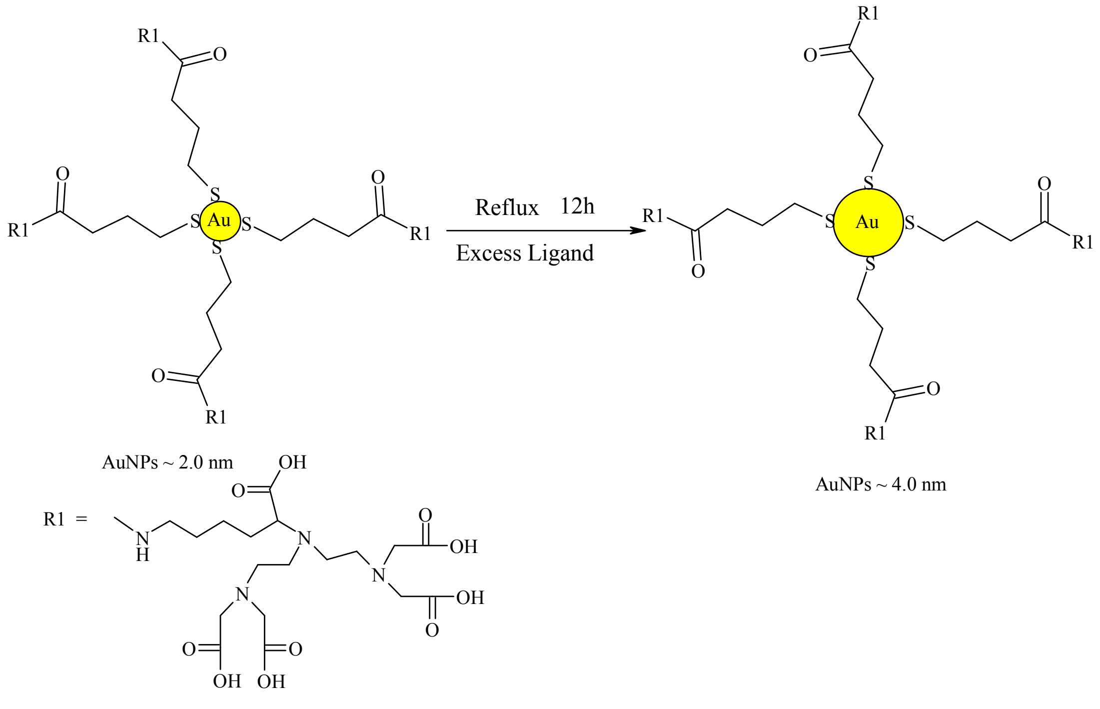

DTPA based ligand **6**

Small (2.0 nm) AuNPs protected by DTPA ligand **6** were grown into large (~ 4.0 nm) AuNPs using a modified literature procedure.[11-12] Freshly prepared crude small AuNPs (50 mg, ~2.0 nm) dissolved in deionised H_2O (25 mL) were taken in a 100.0 mL round bottom flask. To the aqueous solution of AuNPs, DMF (5.0 mL) was added. The aqueous solution of crude AuNPs (containing excess of DTPA ligand **6**) was refluxed for ca. 12 h. After refluxing, the solution was concentrated to ~100 mL by rotary evaporation. DMF was removed by dialysis against deionised H_2O using 12-14 kDa MWCO dialysis tubing. Water was evaporated using rotary evaporator at ca. 40 °C to get crude grown (4.0 nm) AuNPs. The crude grown (4.0 nm) AuNPs were purified by gel permeation chromatography using Sephadex gel (G 100) as a stationary phase and 0.1 M NaCl as a mobile phase. The purified grown AuNPs were dialysed for overnight against deionised H_2O to remove NaCl followed by water evaporation using rotary evaporator to get solid AuNPs (~ 4.0 nm). Yield 26 mg. Characterisation for grown (~4.0 nm) AuNPs is given in chapter 3 (section 3.4.1).

7.4.4 Growth of AuNPs (~6.0 nm)

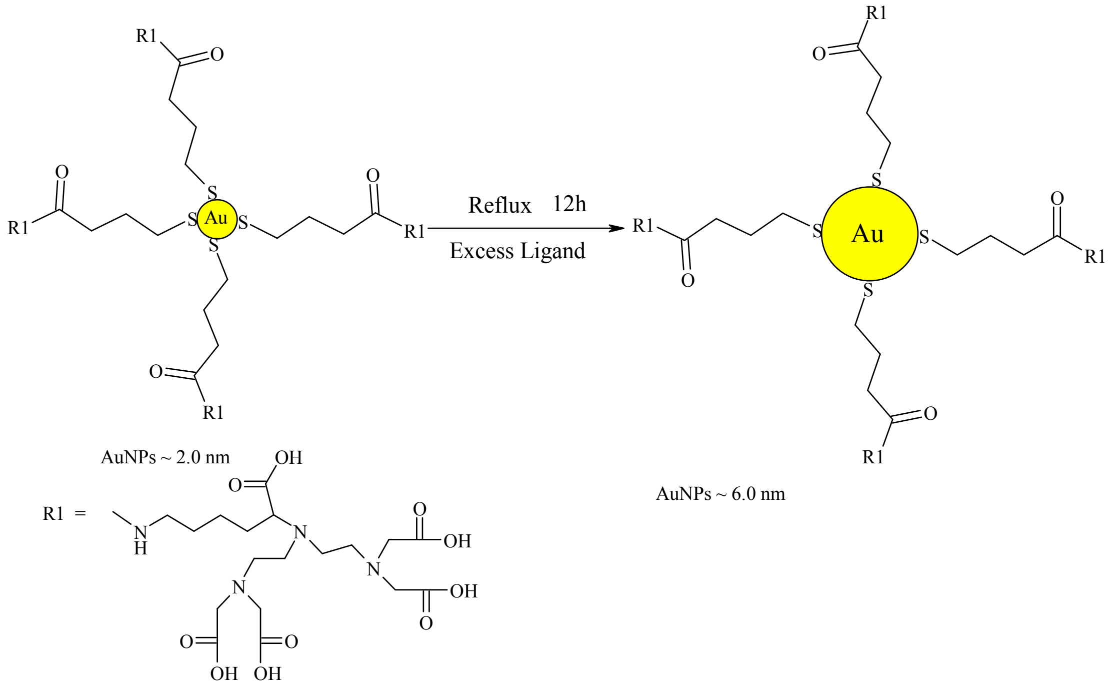

DTPA based ligand **6**

Small (~2.0 nm) AuNPs were grown into large (~ 6.0 nm) AuNPs in an analogous procedure as described in section 7.4.3 by refluxing of small AuNPs (50.0 mg) in an aqueous solution containing DMF (5.0 mL) for ca. 24 h. Yield 19 mg.

7.4.5 Formation of PEI layer around Gd-DTPA@AuNPs

Polyethyleneimine (PEI) layer around Gd-DTPA@AuNPs was formed using a modified literature procedure.[13] PEI with M_n ~ 423 was used. Gd-loaded AuNPs (5.5 mg, 4.00×10^{-3} mmol of Gd-DTPA units) were dissolved in deionised H_2O (~5.0 mL) in a 25 mL round bottom flask. To the stirred solution of AuNPs, a 27 mM aq PEI (60 µL, 0.016 mmol of NH^+) was added. The reaction mixture was stirred for further

10-15 min at rt. The excess of PEI molecules was removed by dialysis against deionised H_2O using 12-14 kDa dialysis tubing. Water was evaporated using rotary evaporator below 40 °C to get solid PEI-protected AuNPs.

7.4.6 Formation of PAMAM-dendrimer layer around Gd-DTPA@AuNPs

Poly (amidoamine) (PAMAM) layer around Gd-loaded AuNPs was formed by an analogous procedure as described in section 7.4.5, from Gd-loaded AuNPs (5.5 mg, 4.00×10^{-3} mmol of Gd-DTPA units) and 55.0 mM aq PAMAM G**0** (130.00 µL, 0.016 mmol of NH^+) and 2.0 mM aq PAMAM **G4** (108 µL, 0.016 mmol of NH^+).

7.4.7 Layer by layer assembly of PEI (M_n~1300) and PAA (M_n~1200)

Layer by layer (LBL) assembly of oppositely charged polyelectrolytes around negatively charged Gd-loaded AuNPs was carried out using an analogous procedure as described in section 7.4.5, from Gd-loaded AuNPs (10.0 mg, 6.69×10^{-3} mmol of Gd-DTPA units), 5.0 mM aq PEI **1** with M_n ~ 1300 (180 µL, 0.026 mmol of NH^+) and 5.0 mM aq PAA **1** with M_n~1200 (235 µL, 0.026 mmol of COO^- units). The same procedure was followed to form polyelectrolyte self assembly using larger polyelectrolytes i.e. PEI **2** (M_n~2000) and PAA **2** M_n~2100).

7.5 Experimental part for chapter 4

7.5.1 Synthesis of triphenyl phosphine protected AuNPs (PPh$_3$@AuNPs)

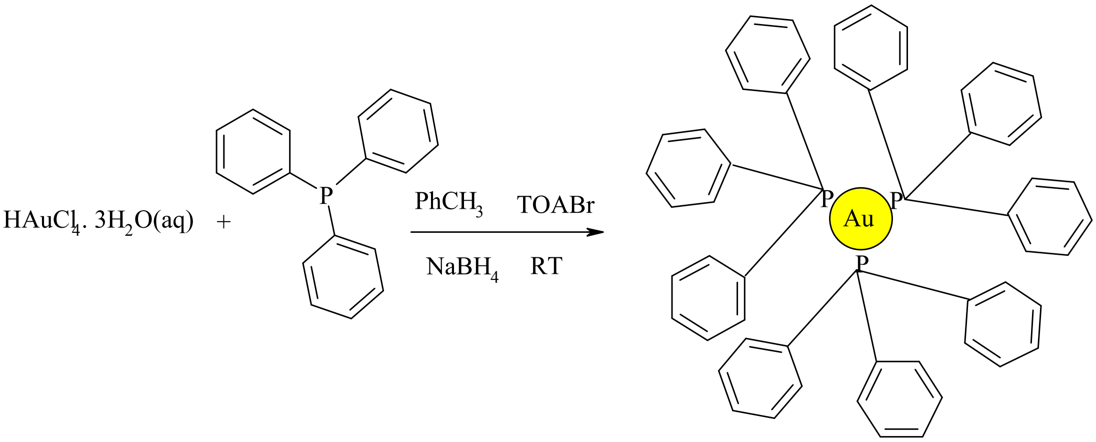

PPh$_3$ protected AuNPs

Triphenyl phosphine (PPh$_3$) protected AuNPs were prepared using the literature procedure.[14] A 1.0 % (w/w) aq solution of tetrachloroaurate trihydrate (5.0 mL, 0.127 mmol) was taken in a 50 mL round bottom flask. Tetraoctylammonium bromide (100 mg, 0.183 mmol) solution in toluene (5.0 mL) was added to the stirred gold solution. The reaction mixture was stirred for 5.0 min. The colour of the organic phase turned orange due to the transfer of gold from the aqueous phase to organic phase and the aqueous phase became colourless. Triphenyl phosphine (PPh$_3$) (130 mg, 0.496 mmol) was added as a solid to the above solution and the reaction mixture was stirred for further 2.0 min. A freshly prepared solution of NaBH$_4$ (130 mg, 3.42 mmol) in deionised H$_2$O (5.0 mL) was added to the stirred reaction mixture. The colour of organic phase turned from orange to dark brown within seconds. The reaction mixture was stirred for further 10-15 min. The organic phase was separated from the aqueous phase. The solvent (toluene) was removed using rotary evaporator at ~30-35^{o}C to get solid crude PPh$_3$ protected AuNPs. The crude AuNPs were purified by gel permeation chromatography using Bio-Beads SX-I gel (Bio-Rad) as a stationary phase and DCM as an eluent. Yield 54 mg.

7.5.2 Synthesis of AuNPs protected by nitroxide based ligand

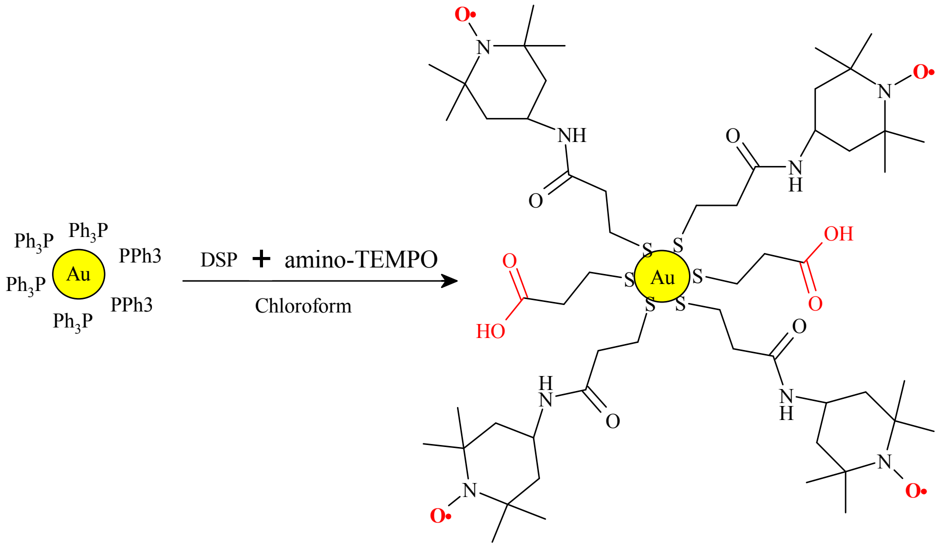

Nitroxide Protected AuNPs

The gold nanoparticles protected by TEMPO based ligand were prepared using a modified literature procedure.[15] The PPh_3 protected AuNPs (30.0 mg, 0.03 mmol of PPh_3) dissolved in chloroform (5.0 mL) were taken in a 25 mL round bottom flask. The temperature of the gold solution was raised to ~50 °C. To the stirred solution, dithiobis(succinimidylpropionate) (DSP) (124 mg, 0.31 mmol) solution in chloroform (5.0 mL) was added and the reaction mixture was stirred for 1.0 min at 50 °C. After 1 min, 4-amino-TEMPO (210 mg, 1.22 mmol) solution in chloroform (5.0 mL) was added. The reaction mixture was stirred at 50 °C for further 2 h. After stirring, the chloroform was evaporated using rotary evaporator to get crude AuNPs protected by TEMPO based ligand. The excess of free ligand molecules was removed by gel permeation chromatography using Sephadex LH-20 as a stationary phase and MeOH as an eluent. Yield 17.0 mg. Characterization of AuNPs protected by TEMPO based ligand is given in chapter 4 (section 4.3.1).

7.6 Experimental part of chapter 5

7.6.1 Synthesis of tryptophan based ligand 7

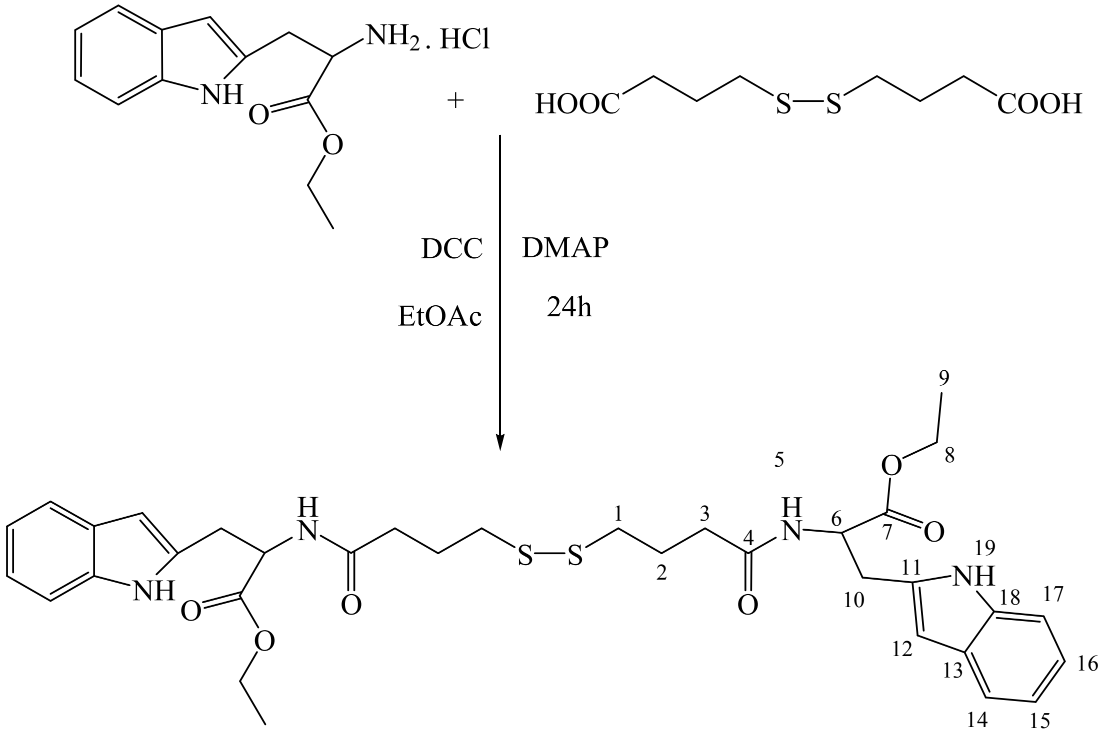

Tryptophan based ligand **7**

Tryptophan based ligand **7** was synthesised by a standard peptide coupling method.[4] L-tryptophan ethyl ester hydrochloride (0.51 g, 1.898 mmol) was taken in a 50 mL round bottom flask containing EtOAc (15.0 mL). To the stirred solution of tryptophan, dithiobutyric acid (0.200 g, 0.8403 mmol) was added. DCC (0.3964 g, 1.92 mmol) and DMAP (0.2355 g, 1.93 mmol) were added as a solid mixture to the above solution. The reaction mixture was then stirred for 48 h. After stirring, the solid residue was removed by filtration, and EtOAc was removed by rotary evaporation to get crude tryptophan based ligand **7**. The crude product was purified by flash chromatography using silica gel as a stationary phase and EtOAc/n-hexane (4/1) as an eluent (R_f 0.62). Yield 0.38 g (67%).

^{1}H NMR ($CDCl_3$): δ (ppm) 1.18 (t, J 7.05 Hz, 6H, H^9), 1.78-1.95 (m, 4H, H^2), 2.17 (t, J 7.05 Hz, 4H, H^1), 2.47 (t, J 7.90 Hz, 4H, H^3), 3.18-3.36 (m, 4H, H^{10}), 4.11 (q, 4H, J 7.05 Hz, H^8), 4.86-4.96 (m, 2H, H^6), 6.32 (d, J 7.80 Hz, 2H H^{12}), 6.88-7.18

(m, 4H, Ar-H^{15+16}), 7.29 (d, J 7.42 Hz , 2H, Ar-H^{17}), 7.50 (d, J 7.80 Hz , 2H, Ar-H^{14}), 8.95 (s+br, 2H, H^{5}).

^{13}C NMR ($CDCl_3$): δ (ppm) 14.10 (C^{9}), 24.50 (C^{2}), 25.20 (C^{3}), 34.20 (C^{1}), 52.80 (C^{10}), 61.40 (C^{8}), 109.60 (**Ar**-C), 111.60 (**Ar**-C), 118.30 (**Ar**-C), 119.20 (**Ar**-C), 121.90 (**Ar**-C), 123.10 (**Ar**-C), 127.60 (**Ar**-C), 136.10 (**Ar**-C), 171.90 (C^{4}), 172.10 (C^{7}).

HR ESI-MS: m/z [M + H] $^{1+}$, Calcd. for $C_{34}H_{43}N_4O_6S_2$: 667.2619, Found: 667.2640

7.6.2 Synthesis of AuNPs stabilised by DTPA ligand 5

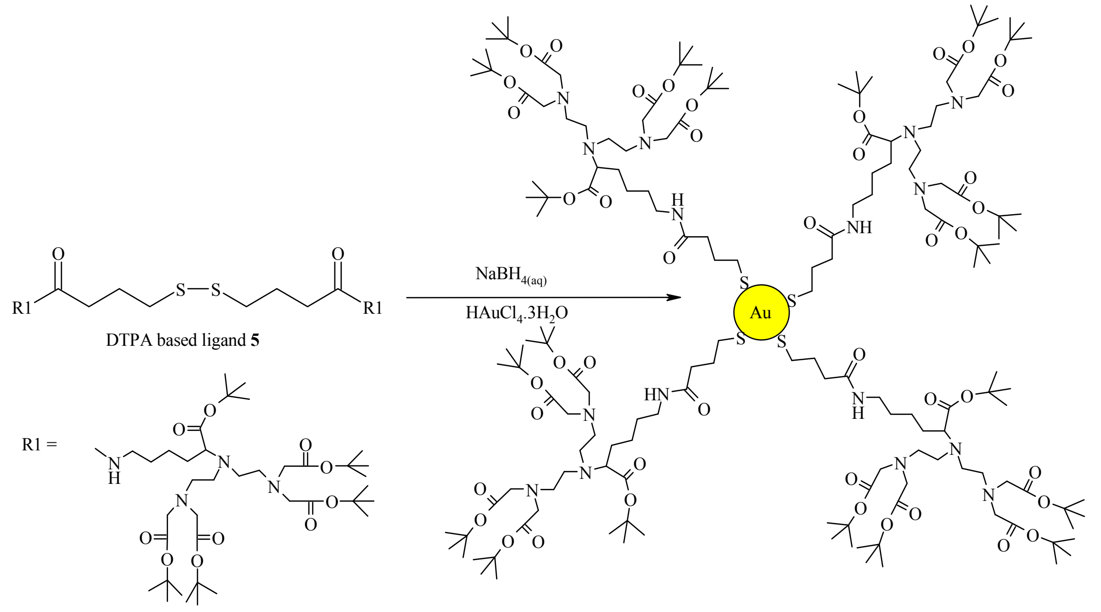

DTPA based ligand **5**

AuNPs stabilized by DTPA based ligand **5**

AuNPs stabilised by DTPA ligand **5** were synthesised by a modified Brust's biphasic method.[6] A 1.0 % (w/w) solution of hydrogen tetrachloroaurate trihydrate (5.0 mL, 0.127 mmol of Au) was taken in a 50 mL round bottom flask. Tetraoctylammonium bromide (347 mg, 0.635 mmol) solution in toluene (12.0 mL) was added to the stirred gold solution. The mixture was stirred for ca. 5.0 min until all Au (III) precursor had transferred to the organic phase. Visually, the colour of the aqueous phase turned from yellow to colourless, while the colour of the toluene phase became red brown. A 10 % (w/w) solution of DTPA ligand **5** (107 mg, 0.0635 mmol) in toluene was then added to the reaction mixture. A freshly prepared solution of $NaBH_4$ (48 mg, 1.27 mmol) in deionised H_2O (3.0 mL) was added 10 s after adding the ligand. Au (III) was reduced to Au (0) within seconds; the reaction mixture was stirred for further 10-15 min. The organic phase was separated from aqueous phase. The organic phase (toluene) was evaporated below 40 °C using rotary evaporator to give a dark brown residue, which was dissolved in a minimum amount of toluene and purified by gel permeation chromatography using Bio-Beads SX-I gel (Bio-Rad) as a stationary phase and toluene as an eluent. Yield 75 mg.

7.6.3 Ligand exchange of tryptophan based ligand 7 with AuNPs

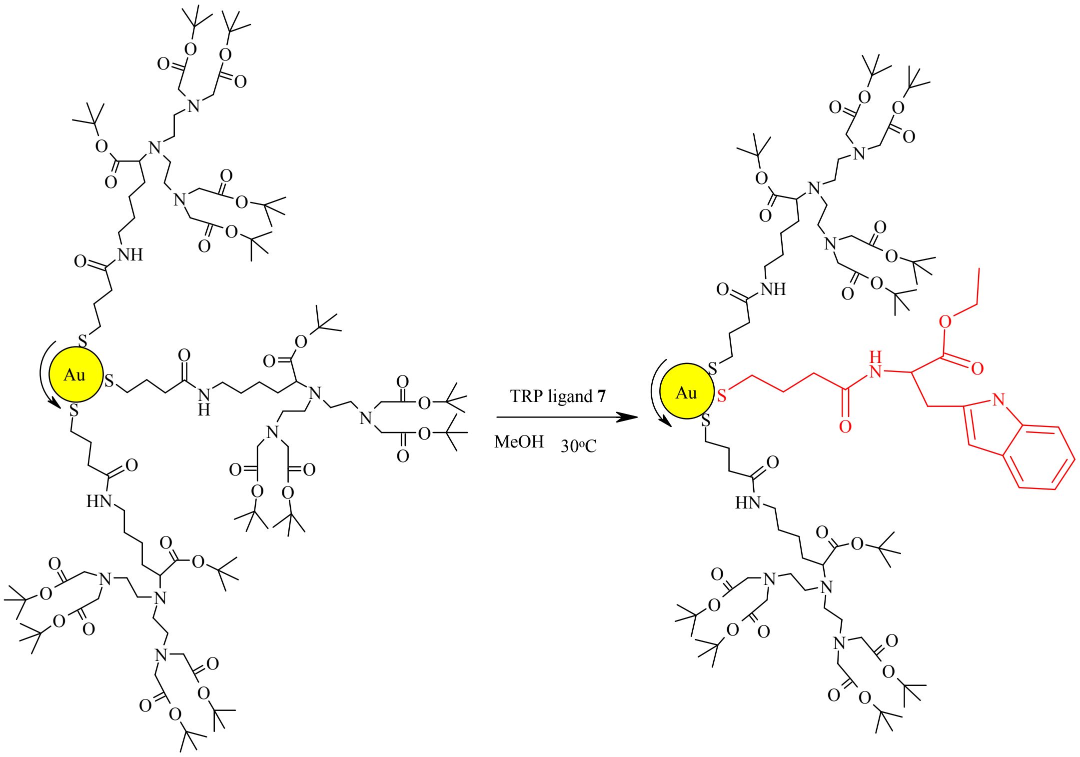

AuNPs stabilized by DTPA based ligand **5**

Tryptophan based ligand labelled AuNPs

The ligand exchange reaction with AuNPs protected by ligand **5** was carried out using a modified literature procedure.[16] AuNPs (10.0 mg, 4.73×10^{-3} mmol of DTPA units) were taken in a 25 mL round bottom flask containing MeOH (10.0 mL). To the stirred solution of AuNPs, a 1.0 mM solution of tryptophan ligand **7** in MeOH (0.8 mL, $7.85\ \times10^{-4}$ mmol) was added. The reaction mixture was stirred for overnight at 30 °C. The solvent was evaporated using rotary evaporator, and the

AuNPs labelled with tryptophan based ligand were purified by gel permeation chromatography using Bio-Beads SX-I gel (Bio-Rad) as a stationary phase and DCM as an eluent, followed by DCM evaporation using rotary evaporator to get solid tryptophan ligand labelled AuNPs. Yield 7.50 mg.

7.6.4 Deprotection of t-butyl ester groups of DTPA based ligand 5 and tryptophan ligand 7 at AuNP surface

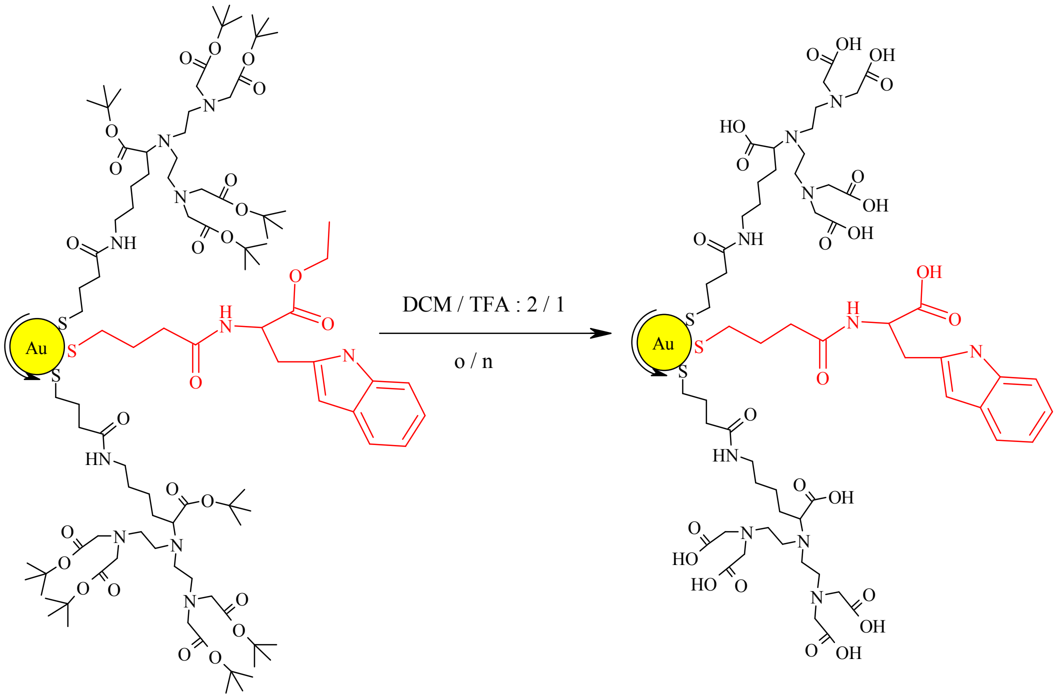

Deprotection of t-butyl ester groups of DTPA ligand **5** and tryptophan ligand **7** at AuNP surface was carried out using procedure described in section 7.3.1.6 from AuNPs (10.0 mg) and DCM / TFA (2 mL / 1 mL, respectively) under the blanket of N_2 atmosphere. The dialysis was carried out against deionised H_2O using 12-14 kDa MWCO dialysis membrane. Yield 6.0 mg.

7.6.5 Lanthanide (Tb^{3+} and Eu^{3+}) loading on AuNPs

The loading of lanthanides (Tb^{3+} and Eu^{3+}) was done by an analogous procedure as described in section 7.3.1.8 using tryptophan based ligand labelled AuNPs (10.0 mg, 5.30×10^{-3} mmol of DTPA units), a 5.0 mM $TbCl_3$ (1.0 mL, 5.0×10^{-3} mmol) and a

5.0 mM $EuCl_3$ (1.0 mL, 5.0×10^{-3} mmol). Yield: Tryptophan labelled Tb-loaded AuNPs 6.5 mg, Tryptophan labelled Eu-loaded AuNPs 7.01 mg.

7.6.6 Synthesis of Ln^{3+}-DTPA Chelates

Lanthanide (Tb and Eu-DTPA) complexes were prepared by an analogous procedure as described in section 7.3.1.8, from 5.0 mM aq DTPA (20.0 mL, 0.10 mmol) and 5.0 mM aq $TbCl_3$ (18.0 mL, 0.09 mmol of Tb^{3+}) and 5.0 mM aq $EuCl_3$ (18.0 mL, 0.09 mmol of Eu^{3+}) . Yield: Tb-DTPA 36.85 mg (78 %), Eu-DTPA 33.69 mg (69.0 %).

Tb-DTPA: HR ESI-MS m/z $[M - H]^{1-}$, Calcd. for $C_{14}H_{19}TbN_3O_{10}$: 526.0329, Found: 526.0326

Eu-DTPA: HR ESI-MS m/z $[M - H]^{1-}$, Calcd. for $C_{14}H_{19}EuN_3O_{10}$: 542.0278, Found: 542.0302

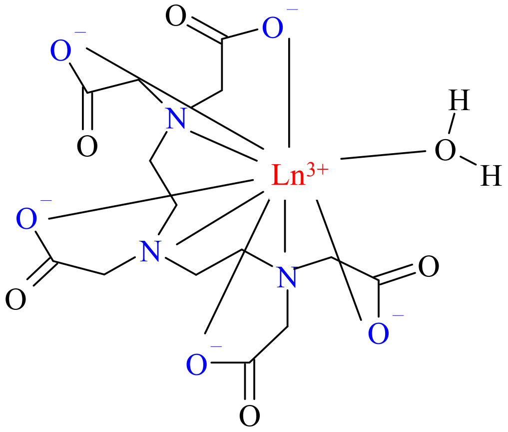

Ln^{3+} = Tb^{3+} & Eu^{3+}

7.6.7 Ligand exchange of Tb-DTPA chelates@AuNPs with 3-mercaptopropionic acid

Ligand exchange reaction was done by an analogous procedure as described in section 7.6.3, from tryptophan labelled Tb-loaded-AuNPs (8.0 mg, 4.24×10^{-3} mmol of DTPA units) and a 100.00 mM aq 3-mercaptopropionic acid (4.0 mL, 0.4 mmol). Yield 5.0 mg.

7.6.8 Treatment of tryptophan labelled Tb-loaded AuNPs with KI and I_2

The tryptophan labelled Tb-loaded AuNPs (5.0 mg) were taken in a 25 mL round bottom flask. To this flask, a solution of iodine (40 mg) and potassium iodide (900 mg) in MeOH (20 mL) was added. The AuNPs were destroyed immediately after the addition of iodine solution. The decomposition of the AuNPs was evident by their colour change from dark brown to yellow.

7.6.9 Synthesis of TEMPO based ligand 8 (TEMPO based spin label)

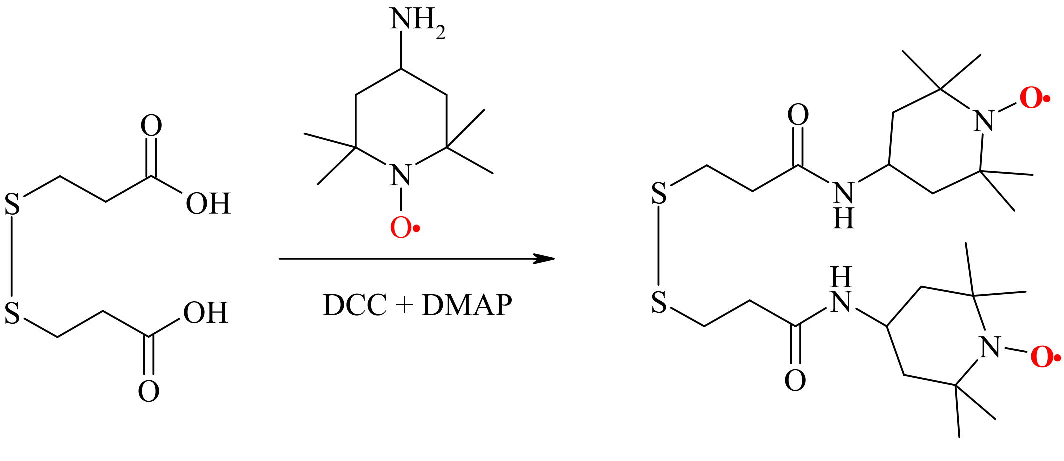

TEMPO based ligand **8**

TEMPO based ligand **8** was synthesised using a standard coupling method.[17] 3,3-Dithiodipropionic acid (0.105 g, 0.5 mmol) was taken in a 100 mL round bottom flask containing 5.0 mL of THF. DCC (0.227 g, 1.0 mmol) dissolved in DCM (5.0 mL) was added to the stirred solution. Then solution of 4-amino-TEMPO (0.172 g, 1.0 mmol) in DCM (5.0 mL) was added followed by DMAP (10.0 mg, 0.08 mmol). The reaction mixture was stirred for 72 h at room temperature. The mixture was then filtered and washed with acidified water (2×50 mL, 40.0 mL water + 10.0 mL conc.

HCl) and then immediately with 50 mL deionised H_2O. The organic phase was dried over anhydrous Na_2SO_4 and combined aqueous phases were extracted with DCM (3×10 mL). Solvent was removed and the product was purified by flash chromatography using silica gel as a stationary phase and DCM / MeOH (12 / 1) as eluent (R_f 0.42). Yield 130 mg (50 %).

HR ESI-MS: m/z $[M + H]^{1+}$, Calcd. for $C_{24}H_{45}N_4O_4S_2$: 517.2877, Found: 517.2861

7.6.10 Labelling of AuNPs by TEMPO based spin label 8

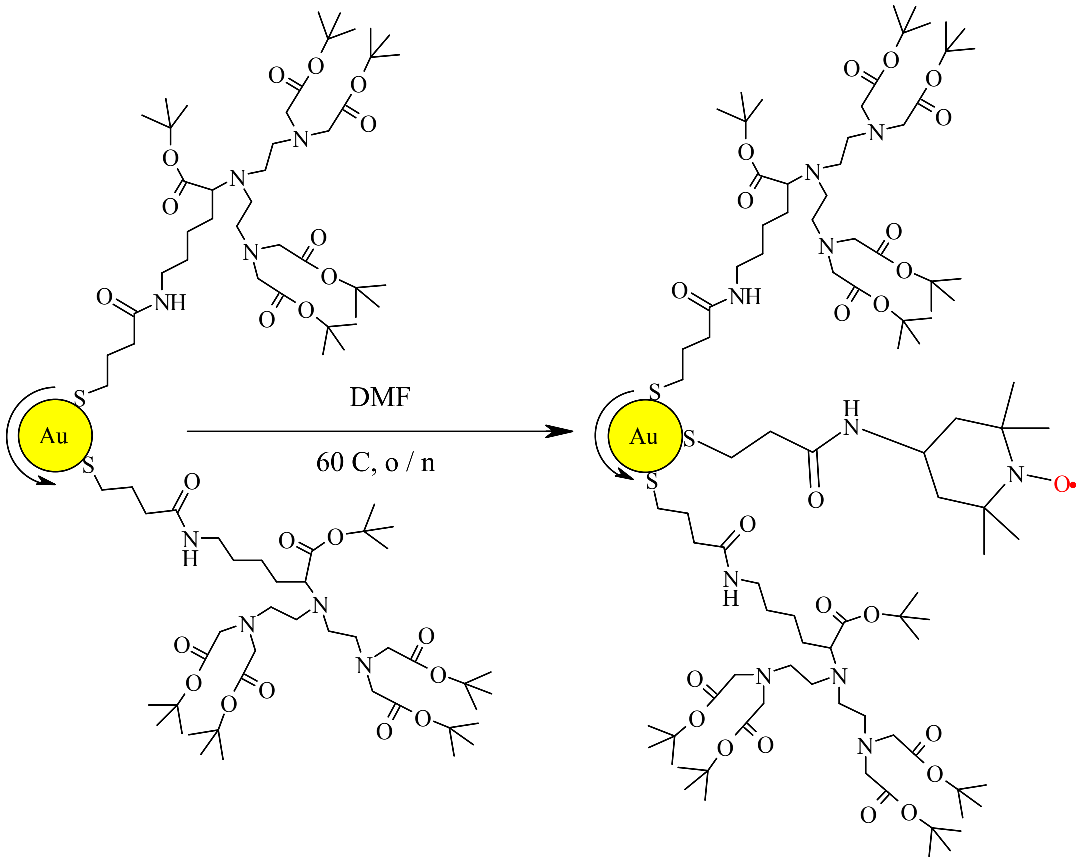

AuNPs protected by DTPA ligand **5**

AuNPs labelled with TEMPO based spin label **8**

The labelling of AuNPs protected by ligand **5** was done by ligand exchange method as described in section 7.6.3 from AuNPs (50.0 mg, 0.027 mmol of DTPA ligand molecules) and a 1.0 mM solution of spin label ligand **8** in DMF (4.5 mL, 4.43×10^{-3} mmol).Yield 34 mg.

7.6.11 Deprotection of t-butyl ester groups of DTPA ligand 5 at AuNP surface

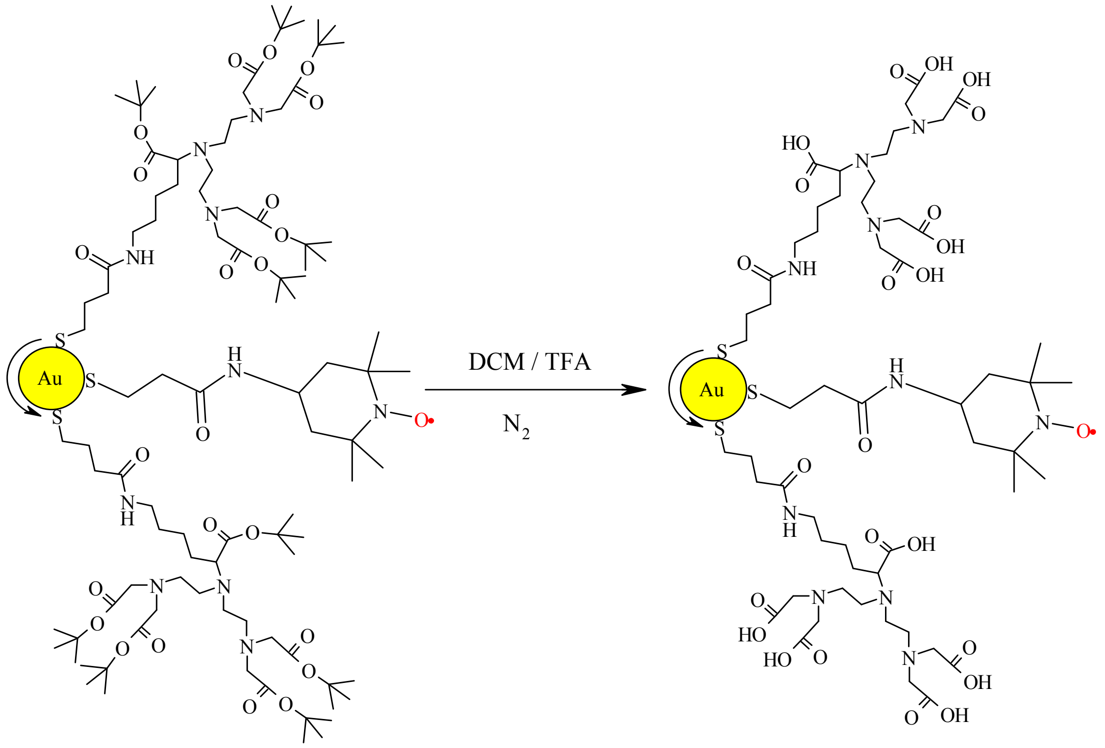

The AuNPs labelled with TEMPO based ligand 8 (10.0 mg) dissolved in DCM (2.0 mL) were taken in a 25 mL round bottom flask. The flask was closed with a septum (suba seal) and put under inert atmosphere. Under an inert atmosphere, TFA (1.0 mL) was syringed in. The reaction mixture was stirred for 4 h under the blanket of N_2 atmosphere. After stirring, DCM/TFA was evaporated at room temperature using rotary evaporator and the residual TFA was immediately quenched with 0.1 M NaOH. Deprotected spin labelled AuNPs were dialysed against deionised H_2O for overnight and then purified by gel permeation chromatography using Sephadex gel (G 100) as a stationary phase and deionised H_2O as an eluent. Yield 6.5 mg.

7.6.12 Lanthanide-loading on (ligand 8) spin labelled AuNPs protected by DTPA ligand

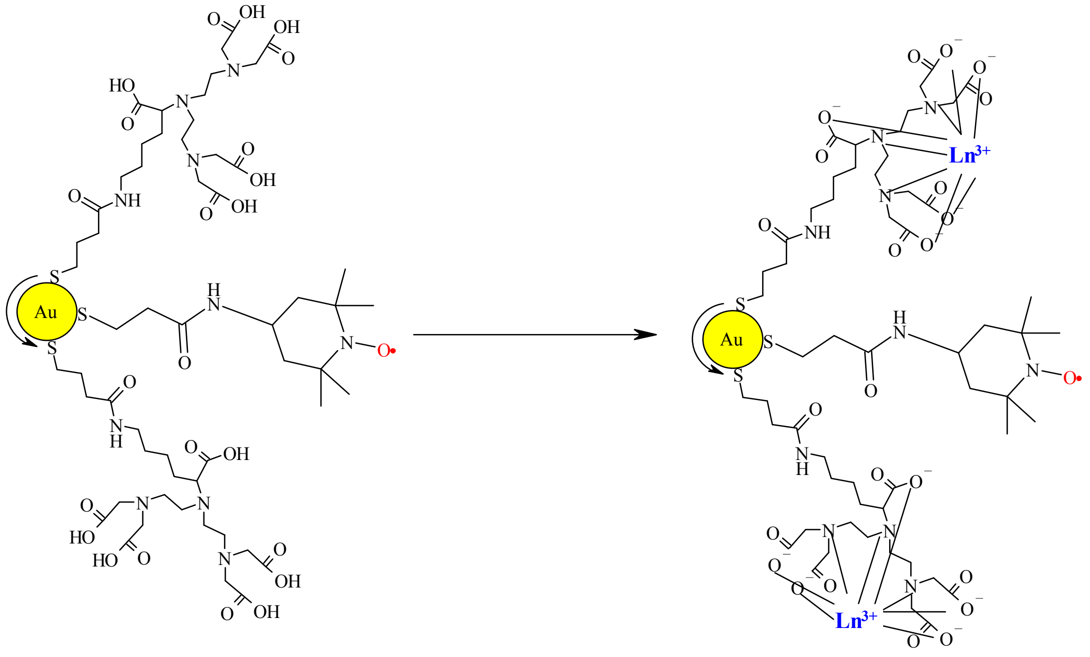

Ln^{3+} = Gd^{3+} , Dy^{3+} and La^{3+}

Lanthanides (Gd^{3+}, Dy^{3+} and La^{3+}) were loaded using a procedure as described in section 7.6.5 from spin labelled (by ligand **8**) AuNPs (15.0 mg) and a 1.0 mM solution of $GdCl_3.6H_2O$, $DyCl_3.6H_2O$ and $LaCl_3.7H_2O$). Yield (Gd-loaded-spin-labelled-AuNPs) 11.23 mg, (Dy-loaded-spin-labelled-AuNPs) 9.56 mg, (La-loaded-spin-labelled-AuNPs) 12.36 mg.

7.7 References

1. V. Chechik and R. M. Crooks, *Langmuir*, 1999, **15**, 6364-6369.
2. M. A. Williams and H. Rapoport, *J. Org. Chem.*, 1993, **58**, 1151-1158.
3. P. L. Anelli, F. Fedeli, O. Gazzotti, L. Lattuada, G. Lux and F. Rebasti, *Bioconjugate Chem.*, 1999, **10**, 137-140.
4. D. C. Johnson Ii and T. S. Widlanski, *Tetrahed. Lett.*, 2001, **42**, 3677-3679.
5. S. Langereis, Q. G. de Lussanet, M. H. P. van Genderen, W. H. Backes and E. W. Meijer, *Macromolecules*, 2004, **37**, 3084-3091.
6. M. Brust, M. Walker, D. Bethell, D. J. Schiffrin and R. Whyman, *J. Chem. Soc.-Chem. Commun.*, 1994, 801-802.
7. P. J. Debouttiere, S. Roux, F. Vocanson, C. Billotey, O. Beuf, A. Favre-Reguillon, Y. Lin, S. Pellet-Rostaing, R. Lamartine, P. Perriat and O. Tillement, *Adv. Funct. Mater.*, 2006, **16**, 2330-2339.
8. M. Chen, L. Guo, R. Ravi and P. C. Searson, *J. Phys. Chem. B*, 2005, **110**, 211-217.
9. A. K. Salem, M. Chen, J. Hayden, K. W. Leong and P. C. Searson, *Nano Lett.*, 2004, **4**, 1163-1165.
10. E. C. Wiener, F. P. Auteri, J. W. Chen, M. W. Brechbiel, O. A. Gansow, D. S. Schneider, R. L. Belford, R. B. Clarkson and P. C. Lauterbur, *J. Am. Chem. Soc.*, 1996, **118**, 7774-7782.
11. M. M. Maye, W. Zheng, F. L. Leibowitz, N. K. Ly and C.-J. Zhong, *Langmuir*, 1999, **16**, 490-497.
12. T. Teranishi, S. Hasegawa, T. Shimizu and M. Miyake, *Adv. Mater.*, 2001, **13**, 1699-1701.

13. W. Tong, C. Gao and H. Möhwald, *Polym. Adv. Technol.*, 2008, **19**, 817-823.

14. M. Conte, H. Miyamura, S. Kobayashi and V. Chechik, *J. Am. Chem. Soc.*, 2009, **131**, 7189-7196.

15. S. Durocher, A. Rezaee, C. Hamm, C. Rangan, S. Mittler and B. Mutus, *J. Am. Chem. Soc.*, 2009, **131**, 2475-2477.

16. P. Ionita, A. Caragheorgheopol, B. C. Gilbert and V. Chechik, *Langmuir*, 2004, **20**, 11536-11544.

17. P. Ionita, J. Wolowska, V. Chechik and A. Caragheorgheopol, *J. Phys. Chem. C*, 2007, **111**, 16717-16723.